Disk-Planet Interactions: Formation of Mean-motion Resonances in a Gaseous Protoplanetary Disk

Zijia Cui

A thesis submitted for the degree of
PhilosophiæDoctor (PhD)
prepared under the supervision of prof. dr hab. Ewa Szuszkiewicz

2022

Abstract

In this thesis, we investigate the formation of mean-motion resonances at the early stages of the evolution of planetary systems, when the forming or newly formed planets are still embedded in a gaseous protoplanetary disk. We focus on the systems containing the most numerous planets known till now, called super-Earths or mini-Neptunes. The planets evolving in a gaseous environment are subjects to the orbital migration due to disk-planet interactions. It is expected that, when the relative migration of two planets is convergent, than the capture into a mean-motion resonance can occur. Is this expectation always met? To answer this question, we employ a full two-dimensional hydrodynamic treatment of the disk-planet interactions, accompanied where possible with the analytic estimates, based on a simplified description of the interactions.

The first series of simulations, motivated by the observed orbital configuration of planets in the Kepler-29 system, is conducted with the aim to determine disk properties that favor a capture of two equal-mass super-Earths into the 9:7 second-order mean-motion resonance. We find that, a resonance trapping occurs during the convergent migration of planets, if one of the resonance angles at the moment of arrival at the commensurability assumes values in a so called window of capture. The width of such a window depends on the relative migration and circularization rates that are in turn determined by the disk parameters. The window is wide, if the relative migration rate is low, and it becomes narrower as the relative migration rate increases. If the migration rate is sufficiently high than the window will be closed and the capture will not take place. Here, we confirm the results of the previous studies and thanks to our full two-dimensional hydrodynamic treatment of the problem, applied to the second-order resonances for the first time, we are able also to extend the conclusions to the wider range of the initial eccentricities and the initial orbits of the planets. The masses of the super-Earths and the disk properties are chosen to ensure that the planets are not able to form the partial gaps along their orbits, and their migration can be regarded as classical type I migration.

The second series of simulations is motivated by the observational trend, seen in the distribution of the period ratios of planet pairs in the confirmed multi-planetary systems, that the period ratios prefer slightly larger values than the resonant ones. This trend is present regardless of the distance from which a planet pair orbits its parent star. We propose that, one of the reasons for what is seen in the distribution of the period ratios of planet pairs, may be the repulsion between planets due to wave-planet interactions. In the proposed picture, the transfer of the angular momentum carried by the waves to the other planet can lead to divergent migration, thus preventing the planets from being closely locked into any mean-motion resonance. Similar picture has been described in the literature in the case of the system of an inner giant planet and a super-Earth migrating in the exterior orbit, as well as

in the case of pairs of Saturn-like and Uranus-like planets. In this thesis, we confirm those findings, and demonstrate that repulsion between planets is effective also in the case of two super-Earths, if they are able to form partial gaps in the disk (their migration is not of type I) and if those gaps contain enough material to support angular momentum exchange with the planet. These two conditions for the effectiveness of the mechanism are formulated by us using simple analytical estimates describing wave-planet interactions. Using two-dimensional hydrodynamical simulations, we verify these conditions for a wide range of planetary masses and disk properties. Our results indicate that, if conditions favor the repulsion between two planets, we expect to observe planet pairs with their period ratios greater, often only slightly greater, than resonant values. Another possibility is that the commensurabilities will not form at all and therefore the resonances are not necessarily common.

Streszczenie

W niniejszej rozprawie, badamy procesy powstawania rezonansów ruchu średniego we wczesnych etapach ewolucji układów planetarnych, wtedy gdy wciąż formujące się lub już zupełnie uformowane planety zanurzone są w gazowym dysku protoplanetarnym. Koncentrujemy się na układach zawierających super-Ziemie lub mini-Neptuny, należące do najliczniejszej klasy planet odkrytych do tej pory. Planety ewoluujące w środowisku gazowym podlegają migracji orbitalnej wskutek oddziaływań pływowych pomiędzy dyskiem i planetą. Przewiduje się, że jeśli względna migracja dwóch planet jest zbieżna to planety te mogą schwytać się w rezonans ruchu średniego. Czy takie oczekiwania są zawsze spełnione? Odpowiedzi na to pytanie szukamy, wykorzystując dwuwymiarowe hydrodynamiczne modelowanie wzajemnych oddziaływań dysku protoplanetarnego i planet oraz, tam gdzie jest to możliwe, analityczne oszacowania oparte na uproszczonym opisie tych odziaływań.

Pierwsza seria symulacji, zainspirowana konfiguracją planet obserwowaną w układzie Kepler-29, jest prowadzona w celu określenia warunków panujących w dysku, które sprzyjają tworzeniu się rezonansu ruchu średniego drugiego rzędu 9:7 pomiędzy dwoma super-Ziemiami o tej samej masie. Znajdujemy, że schwytanie się planet w rezonans następuje podczas zbieżnej migracji, jeśli jeden z kątów rezonansowych, w momencie dotarcia do rezonansu przyjmuje wartość z tak zwanego "okna przechwycenia". Szerokość tego okna zależy od względnego tempa migracji i ukołowienia, które z kolei są określone przez parametry dysku. Okno przechwycenia jest szerokie, jeśli tempo względnej migracji jest niskie i ulega zwężeniu w miarę wzrostu tempa migracji. Jeśli tempo migracji jest wystarczająco wysokie, wtedy okno jest zamknięte i planety nie utworzą konfiguracji rezonansowej. Potwierdzamy tutaj wyniki poprzednich badań i, dzięki naszemu podejściu do problemu rezonansów drugiego rzędu z wykorzystaniem po raz pierwszy symulacji hydrodynamicznych, otrzymujemy wyniki w szerszym zakresie początkowych mimośrodów i wielkich półosi planet. Masy super-Ziem i parametry dysku zostały tak dobrane, aby zapewnić że planety nie są w stanie utworzyć obszaru o obniżonej gęstości powierzchniowej wzdłuż swoich orbit i ich evolucję w dysku możemy uważać na zgodną z klasyczną migracją I typu.

Druga seria symulacji jest zainspirowana obserwowanym trendem, widocznym w rozkładzie stosunków okresów par planet w układach wieloplanetarnych, w którym stosunki okresów przyjmują wartości trochę większe od rezonansowych. Tendencja ta jest obecna bez względu na odległość, w jakiej para planet obiega gwiazdę macierzystą. Proponujemy tutaj, że jedną z możliwych przyczyn tego faktu obserwacyjnego jest wzajemne odpychanie się planet wskutek oddziaływań pomiędzy dyskiem i planetami. W zaproponowanym scenariuszu, przekazanie momentu pędu poprzez fale gęstości wzbudzone przez jedną planetę drugiej planecie prowadzi do rozbieżnej migracji i tym samym uniemożliwia powstanie resonansu. Podobny mechanizm został

opisany w literaturze w przypadku par: gazowy olbrzym i super-Ziemia, dwie planety podobne do Saturna i dwie planety podobne do Urana. W niniejszej rozprawie, potwierdzamy te wyniki i dowodzimy, że wzajemne odpychanie się planet jest efektywne również w przypadku dwóch super-Ziem, jeśli są one w stanie usunąć część materii z obszarów wzdłuż swoich orbit (ich migracja nie jest klasyczną migracją I typu) i jeśli w tych obszarach pozostała jeszcze wystarczająca ilość gazu niezbędna do efektywnego przekazania momentu pędu planecie. Te dwa warunki na efektywność odpychania się planet uzyskujemy, wykorzystując uproszczony analityczny opis oddziaływań pomiędzy dyskiem i planetami. Za pomocą dwuwymiarowych symulacji hydrodynamicznych weryfikujemy wyprowadzone kryteria dla szerokiego zakresu mas i warunków panujących w dysku. Nasze wyniki wskazują na to, że jeśli warunki na wzajemne odpychanie się planet są sprzyjające to oczekujemy, że obserwowane stosunki okresów orbitalnych planet są większe, często tylko nieznacznie większe od rezonansowych, albo że w ogóle nie dochodzi do powstania rezonansu. Zatem rezonanse powstające na wczesnych etapach ewolucji układów planetarnych niekoniecznie muszą być powszechne.

Acknowledgements

First of all, I would like to express my deepest appreciation to my supervisor, prof. Ewa Szuszkiewicz, who offered me the opportunity to study the Planetary Astrophysics in Poland. Her patient guidance, enthusiasm and immense knowledge help me a lot in my research work and thesis writing. Besides that, she is also a good friend who is always ready to give advice and encouragement, as she has done during the whole period of my PhD study. Although the life is difficult, meeting with her is always one of the best things that ever happened to me.

Secondly, I'm deeply indebted to prof. John Papaloizou for all of his advices and suggestions, which are very valuable for guiding my research works. It is a great honor for me to have such a precious chance to work with him. I am grateful to prof. Franco Ferrari for his continuous support in the development of the computational techniques and computer facilities in the University of Szczecin. My sincere thanks also goes to my colleagues: Federico Panichi, Cezary Migaszewski and Kazuhiro Kanagawa for their stimulating discussions and insightful comments. I also extend my thanks to all the professors and staff who gave me courses or any assistance in the University of Szczecin.

I would like to acknowledge the support by Polish National Science Centre MAESTRO grant DEC-2012/06/A/ST9/00276. My research was performed at the University of Szczecin. Most of the simulations presented in this thesis were calculated on HPC cluster HAL9000 of the Computing Center of the Faculty of Mathematics and Physics, University of Szczecin. Some calculations preformed in the Chapter 5 of the thesis were accomplished under the support from DAMTP, University of Cambridge. I gratefully acknowledge all the people for their help of the technical assistance and the permission for access to computational facilities.

I would like to thank my friends whom I met in Poland: Tian Huang, Chunlian Li, Jinman Liang, Xiangling Kong, Yani Zhao, Zhiyin Luo and all others who helped me a lot during my study in Szczecin. I also appreciate their company for many beautiful moments which I never forget in my whole life.

Last but not the least, I would like to thank my parents: Yuelin Liu and Fengyu Cui for supporting me spiritually throughout all these years of my study in Poland. And to my grandpa, thank you so much for encouraging me when I was in depression. May you have rest and peace in another world.

Contents

Chapter 1

Introduction

The study of planets, planetary systems and the processes that form them has a long history which can be traced back to the ancient era. Five planets have been known to the ancients: Mercury, Venus, Mars, Jupiter and Saturn. They "wonder" through the nighttime sky against the background of the "fixed" stars. People observed their complicated motions with the naked eye and at the end of 16th century thanks to Tycho Brahe's careful quantitative studies were able to describe the planetary motion very well. However, describing does not necessary mean understanding. This came later, when Johannes Kepler succeeded with simple empirical laws to account for Brahe's data and Isaac Newton demonstrated that the Kepler's laws are straightforward consequences of the law of universal gravitation. While the first five planets in the Solar System had been viewed by civilizations for millennia, two others, Uranus and Neptune, have been discovered relatively recently in 18th and 19th centuries. The availability of the telescopes was essential but not the only reason for those achievements.

One and half century later, a new era has started. During the last thirty years, a wealth of planets outside our Solar System, orbiting other stars, have been discovered as a result of our understanding of physics laws and the capability to apply the most sophisticated observational techniques. Till now, more than 4000 planets have been confirmed by using ground-based observational facilities (e.g. ESO Very Large Telescope - VLT and Very Large Telescope Interferometer - VLTI) and operating space missions (e.g. Convection, Rotation & planetary Transits (CoRoT) [15, 40], Kepler [30], K2 [86], Transiting Exoplanet Survey Satellite (TESS) [183], CHaracterising ExOPlanet Satellite (CHEOPS) [26]). Therefore, there is no doubt that planetary systems are common in our Galaxy.

The results of new observations present a diversity of the architectures of planetary systems and a variety of planets residing in those systems. This gives us better chance than ever to find out more about the formation and evolution of planetary systems. It is therefore just a right time to contribute to this hot research topic in modern astrophysics and I am glad to be able to describe my own contribution in this thesis.

1.1 Architectures of multi-planetary systems

Our Solar System with its eight planets is not an exception. We know already more than 700 multi-planetary systems. They provide a unique laboratory for studying the planet formation and for constraining exoplanet demographics. First, let's have a closer look at the overall properties of the confirmed planets, no matter if they belong to a single or multi-planetary system.

1.1.1 Properties of the confirmed planets

In Figure 1.1 we display the planetary masses and radii versus orbital periods for all confirmed exoplanets discovered by various detection techniques till August, 2021. The left panel of the figure shows the planets with the determined masses and the right panel those with measured radii. The plotted points are coded by the method of detection in each particular case and the symbols used for that are described in the legend placed in the left panel. The symbols in the right panel have the same meaning. The majority of the planets shown in the figure have their orbital periods in the range between 1 to 10^4 days with the mass less than $20M_{\rm Jup}$ and the radius less than $20R_{\oplus}$. For comparison, the masses and radii of Jupiter, Neptune and Earth are indicated by the dashed horizontal lines.

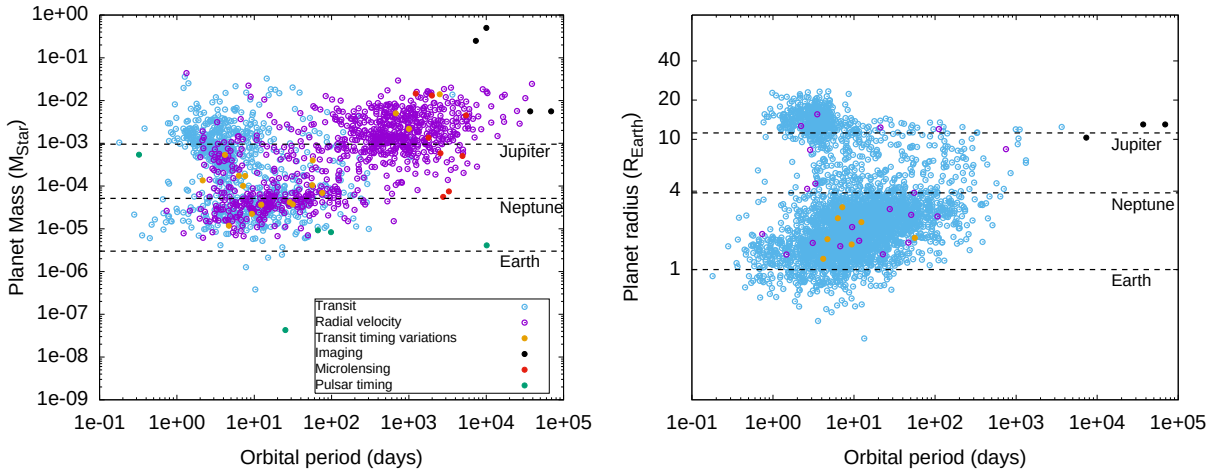

Figure 1.1: Planetary mass and radius as a function of the orbital period for the confirmed exoplanets - The detection methods for each planet are denoted by different colors and symbols. The dashed horizontal lines indicate the values of masses and radii of Jupiter, Neptune and Earth in the left and right panels, respectively. Data are obtained from NASA Exoplanet Archive.

In the radius-orbital period diagram (right panel), two populations of planets can be distinguished. The most numerous population is the one in which planets have their radii larger than the Earth's radius, but smaller than that of Neptune. Those small planets constitute more than half of the exoplanets discovered so far. Two names are used for planets belonging to this population: *super-Earths* and *mini-Neptunes* depending of their structures and compositions. The super-Earths are rocky planets similar in structure to our planet Earth [31] and mini-Neptunes

have a hydrogen-helium outer envelope, which make them being similar to Neptune [19]. Removing from this population all planets with their radii determined with the uncertainties larger than 5%, or differently taking into account only those, whose radii are known precisely, we will see that the radius distribution for such planets shows a bimodal character [64, 65, 203]. This property is called in the literature a planetary radius valley and it can imply a composition transition from rocky planets without H/He gaseous envelopes to planets with envelopes of a few percent in mass [116, 146]. Much effort is devoted to explain this observed valley from different point of views, such as the photoevaporation [147, 205] and core powered mass-loss [68, 75]. One difficulty is connected with the fact that currently we are only able to look at the largest and hottest planets. To characterize the smaller and cooler ones we shall wait for James Webb Space Telescope (JWST) and Atmospheric Remote-sensing Infrared Exoplanet Large-survey (ARIEL).

The second population of planets seen in the right panel consists of larger planets with their radii of the order of the Jupiter radius. Unlikely the giant planets in the Solar System, they have short orbital periods and are called as *Hot Jupiters*. The first extrasolar planet detected in orbit around a solar-type star 51 Pegasi is considered to be the prototype of this new family of Jovian planets [129]. It is important to stress here that the planets shown in the radius-orbital period diagram have been found mostly by the transit method (indicated by the light blue circles). The transit method uses photometry to provide accurate constraints on the size of detected planets. However, it is not free from the well-known observational biases. One of these is that it favors the detection of large planets with short periods. This fact must be taken into account, while interpreting the statistical properties of the confirmed planets.

In the mass-orbital period diagram (left panel), two distinct populations are still visible. There is a population of massive planets (with the mass of the order of the Jupiter mass) and a population of low-mass planets (with the masses between the Neptune and Earth masses). In this diagram we have a numerous set of planets discovered by the radial velocity method (Doppler spectroscopy). Major advantage of this method is its ability to place accurate constraints on a planet's mass. Second powerful tool to measure the masses of the planets is the transit-timing-variation method [1, 85, 114]. The massive planets in this diagram are characterized not only by the short periods, but now their periods cover the whole range from 1 till 10^4 days. Those massive planets, whose periods are larger than 200 days are often called as *Cold Jupiters*. And the prototype of this family is the Jupiter in our Solar System. The majority of the low-mass planets in this figure have the orbital periods from several days to one year. In summary, the observations show that close-in super-Earths (mini-Neptunes) are the most common exoplanets in our galaxy known to date. The statistics suggest that around 60% of stars possess one or more super-Earths [63, 166]. By considering the intrinsic multiplicity and inclination dispersion within planetary systems, this occurrence is reduced to 30% for the Solar-type stars [83, 224]. In my thesis we focus mainly on the low-mass planets with the masses between 2-10 Earth masses.

1.1.2 Configurations of the observed multi-planetary systems

The quest to characterize the planets provides the global properties such as the masses, sizes and orbital periods with better and better precision. We have shortly presented the most recent determinations of these characteristics in the previous subsection. The existence of planetary

systems with more than one planet orbiting around the host star gives us not only additional ways to characterize the planets (transit timing variations), but provides statistical observational features, which we can use to test our understanding about the processes of formation of the planetary systems. A particular attention should be brought to the occurrence of the mean-motion commensurabilities, because they can tell us about the conditions in which the shaping of the planetary systems take place. A number of multi-planetary systems are found to have planets near to or in the mean-motion resonances (MMRs), which means that the period ratios of planets are close or equal to ratios of small integers. For instance, the Kepler-9 system contains two planets with period ratio of 2.026 that is quite close to 2:1 [29]. Similar orbital configurations are found also in HD 128311 system consisting of two planets with the period ratio of 2.024 [187], as well as HD 155358 system with the period ratio of 2.017 [186]. The planet pairs in the systems close to the 3:2 resonance configuration have been observed in KOI-3503 system in which the period ratio of planet pair is 1.5024 [93]. And in KOI-1599 system, the two planets with the period ratio of 1.5021, have been confirmed to stay in the 3:2 MMR from the study of dynamical simulations [154]. The Kepler-50 system have two planets with the period ratio of 1.2002, which is almost equal to 5:4 [84] and the Kepler-36 system consisting of two planets with the period ratio of 1.17 very close to 7:6 [36]. Besides that, the planet pairs with the period ratios near to the second-order resonance commensurabilities have been discovered also in multi-planetary systems. Such examples can be seen in the Kepler-87 system that composed of two planets with the period ratio of 1.667 extremely close to 5:3 [142] and the system of Kepler-29 in which two planets have the period ratio of 1.2850 near to 9:7 [207]. It has been confirmed that the planet pair orbiting around Kepler-29 are trapped into the 9:7 MMR based on the analysis of numerical simulations [133]. Moreover, the multi-resonance configurations in a few planetary systems have been found such as the GJ 876 system in which three planets (two giants and one Uranus-mass planet) are in a resonant chain with the period ratios as 4:2:1 [184]. Another example is the three super-Earths in Kepler-60 system with the inner pair in a 5:4 commensurability and the outer pairs in a 4:3 commensurability [193]. By investigating the dynamical stability, these three planets are confirmed to stay in the 5:4:3 Laplace MMRs [74]. The longest resonant chain has been found in the TRAPPIST-1 system in which seven approximately Earth-sized planets are in a chain of near resonances. They are configured such that each triple of adjacent planets is in a Laplace resonance, namely e, b, c and d in a 8:5:3:2 Laplace resonance while c, d and e in a 4:3:2 Laplace resonance [67, 117].

The number of known multi-planetary systems allow us to analyze the frequency of the MMR occurrence in a statistical sense. Are these orbital commensurabilities common? By inspecting the orbital spacings in the multi-planetary systems discovered by the radial velocity technique, it was found that for the planet pairs with a total mass exceeding $1 M_{\rm Jup}$, there is a clustering near or in the 2:1 resonance that is unlikely to be a statistical coincidence [212, 214]. The statistical studies for the multi-planetary systems of low-mass planets discovered by *Kepler* show that the situation is a bit different from that observed in the systems discovered by the Doppler method. Figure 1.2 illustrates the distribution of the period ratios of planet pairs in the range of [1, 2.5] in the multi-planetary systems which have been confirmed till August, 2021. The planets shown in the figure are mainly detected by the transit method and have small masses with periods

shorter than a few hundred days. Within this sample, there is only a weak preference for the period ratios near the resonances and the majority of the observed planet pairs' period ratios are far from the resonant values [55, 112].

These findings were initially surprising because the Doppler systems had already shown some preference for the resonances between massive planet, and then the theoretical expectations for the evolution of the low-mass planets in the disk (type I migration) were such that the planet pairs would often be caught into the resonances as a result of convergent migration [106, 158].

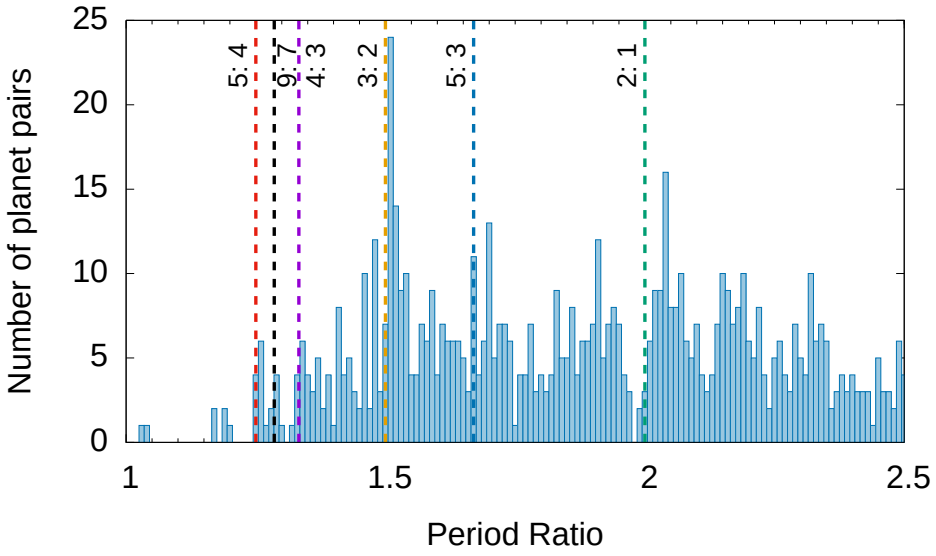

Figure 1.2: Histogram of the orbital period ratio of exoplanet pairs - The width of the bin is 0.01. Dashed vertical lines show the locations of MMRs' commensurabilities. The data for the periods of exoplanets are obtained from NASA Exoplanet Archive.

By observing the distribution of period ratios around the resonant values shown in Figure 1.2, a subtle feature can be seen that there appears to be a tendency to avoid the exact resonances [206], more precisely the period ratios prefer slightly larger than the resonant values, especially around 3:2 and 2:1 [55]. In particular, there is an excess of planet pairs with the period ratios around 1.52 and 2.02 and a deficit of pairs with the period ratios around 1.99. This finding was predicted as a consequence of tidal dissipation within the inner planet that would cause the orbits to spread apart [22, 42, 107, 113, 201, 216]. Apart from that, other mechanisms for explaining this performance have been proposed and studied in recent years (e.g. dynamical instability of tightly packed planetary chains [91, 143, 144, 182]), which will be reviewed in the following section.

In summary, the observations seem to indicate that although resonance configurations are found in some planetary systems, the commensurabilities are not common in the systems containing low-mass planets with the short periods. So the question still remains - why? Regardless different successful attempts to answer this question, mentioned above, the problem is not solved. We have got motivated to take a different approach and investigate how the low-mass planets migrate in the protoplanetary disk, how the resonance capture take place and whether such

a configuration is maintained during its further evolution in the disk or not considering the fundamental processes acting between disk and planet.

1.2 Protoplanetary disks

In the previous section we have presented the observed properties of the already formed planets and the mature systems in which they reside. However, in order to understand how the planetary systems form and evolve we need to look back at the early phases when the protoplanets, planetary cores or even already formed planets are still embedded in the protoplanetary disk. Such observations are challenging, but thanks to the recent progress in the observational techniques, it is possible to detect not only many interesting sub-structures in the disks situated in nearby star forming regions, as for example the axisymmetric rings, gaps, inner cavities and spirals, but also to catch the protoplanet in act of its formation. The recent confirmed example of the protoplanet forming in the disk is a young massive object within the gap of the transition disk around PDS 70 [98]. The sub-structures in the disks are frequently observed over a wide range of ages and masses of stellar hosts [4, 5, 87, 115]. One of the explanations for their formation is the interactions between the planets and the disks, in which they are embedded [53, 87]. This interpretation has a strong theoretical foundation. A planet with the sufficient mass can develop a clear annular gap, which could be observed as a ring in the disk [71, 103, 109, 110]. Moreover, the giant planets in multi-planetary systems can form a cavity in a wide radial range in the disk [44, 222], and may excite vortices or eccentric modes that generate strong azimuthal asymmetric structures such as arcs in the disk [12, 101, 223]. In addition, some studies pointed out that a super-Earth size planet is able to create the annular substructures in a low-viscosity disk as well [14, 46]. The disk-planet interactions which are the subject of this thesis enter the stage in which the theoretical predictions can be finally verified by the high resolution observations.

The story about the planet formation should start much earlier than the phase of planets embedded in the protoplanetary disk, namely starting from a molecular cloud where the stars form. This is because, the star and planet formation should be considered side by side as a sequence of processes, coupled strongly to each other, leading to the formation of a complete planetary system (a star with planets, asteroids and comets). Molecular clouds consist mainly of gas, but also dust in small quantities is present there (roughly one percent of the mass of the cloud is in the form of sub-micron dust particles). The clouds must be sufficiently dense (density should be bigger than 10^2 hydrogen nuclei per cubic centimeter) in order to form stars. Within dense clouds there are denser regions called "dense cores". In some of those dense cores, the conditions are sufficient to initiate the process of collapse in which the gravitational force of the gas overcomes the gas pressure. As a result of this process, a protostar is formed. The newly formed protostar continues to accrete matter from its surroundings. Some of the accreting material spreads out into a disk in accordance with the conservation of angular momentum. The angular momentum is transferred away from the protostar and the matter is flowing towards it. It is not the only way in which the angular momentum is removed from the system. The protostellar outflows and jets are often observed in the young stellar objects. They extract efficiently the angular momentum from the system. Numerical models (both magnetic and

non-magnetic) of the collapsing molecular cores show that disks form within 10^4 yrs [88, 221]. After roughly 1 Myr counting from the beginning of the gravitational collapse, we can expect to have a pre-main sequence star and a circumstellar disk (a classical T Tauri star if the mass of the central star is in the range of 1-2 $M_\odot$ or a Herbig Ae/Be star if the stellar mass is in the range of 2-10 $M_\odot$). At this stage, the disk contains only a few percent of the central stellar mass and the processes of planet formation already operate in there [211]. Such disks are called protoplanetary. However, recent observations suggest that planet formation may begin already at the protostellar stage [33, 80]. More investigations are needed to resolve this important issue. The lifetime of the protoplanetary disks is estimated to be equal to 1-10 Myrs on the basis of the disk occurrence rates in stellar clusters, for which we know the ages [79, 164]. The disk material will disperse during that time, one part will be accreted onto the star, another one onto planets and still another one will be lost due to the disk wind [52]. The outcome of this stage of the evolution is a new planetary system, namely a young star with the planets and planetesimals orbiting around it. The evolution of the system continues further for hundreds of Myrs on account of the collisions between planets and planetesimals.

1.2.1 Properties of protoplanetary disks

Knowing the properties of the disks is crucial since on them depends whether the planets will form in the disks at all, what kind of planets will form there and what the planetary system architectures will be. In the last decade, the detailed information on the disk structures has been provided by the Atacama Large Millimeter/submillimeter Array (ALMA) and the Very Large Telescope Interferometer (VLTI), the instruments able to probe the solids and gas in the disks with high spatial resolution and sensitivity. These observations give us fundamental insights into the mass distribution, dynamics and evolution of protoplanetary disks. It is worth to discuss here shortly the most important disk properties with the aim to put in the context the results presented in this thesis. The detail description of the observations of protoplanetary disk structures is given in [6].

Protoplanetary disk structure

A typical protoplanetary disk in classical T Tauri stars consists of an inner purely gaseous disk, extending from a few stellar radii to the dust sublimation radius, and an outer disk of gas and dust, whose outer edge ranges from 100 AU to more than 1000 AU depending on the object. The truncation of the inner edge of the disk at typically a few stellar radii from the stellar surface happens due to the stellar magnetic field. The process of dust sublimation determines the outer rim of the dust-free disk. The dust sublimation radius depends on the stellar luminosity, dust sublimation temperature and the ratio of the absorption efficiencies of the dust of the incident field and of the reemitted one [135]. The study in [165] argues that for their sample of T Tauri stars, the dust-free inner part of the disk extends from 0.03 to more than 0.4 AU. The investigations of the conditions present in the inner protoplanetary disks are possible thanks to the high sensitivity and a very good spatial frequency coverage of the GRAVITY instrument of the Very Large Telescope Interferometer (VLTI). In order to probe the outer part of the disk, we need to apply different observational techniques. The disk geometry can be characterized

by using the scattered stellar radiation on small dust grains (less than or equal to 1μm in size) observed in the near and mid-infrared continuum. The dust disk is optically thick at these wavelengths, so the intensity of scattered light is not related to the column density but to the amount of stellar light received by the layer. The column density of the dust and also its temperature can be determined from the thermal emission of bigger dust grains (with a size of the order of 1 mm) detected in the (sub-)millimeter continuum, if the dust is optically thin at these wavelengths, as it is often the case. More information about the surface of the gas layer is provided by the spectral lines observed both in the infrared and at radio wavelengths. They probe specific gas tracers such as gas or molecular transitions. Observationally, estimates of the size of the gaseous disk are based on the extent of CO submillimeter rotational emission. Gas disk sizes have now been measured consistently for a significant number of disks [8].

The mass of a protoplanetary disk is one of the most difficult properties to constrain. Most of the solids in the disks are in the form of millimeter and larger sized dust grains, which are not mixed well with the gas. For that reason, the measurements of the mass of dust and gas components must be done separately and different methods should be used for that. Several recent studies have succeeded in evaluating the dust mass. One of the examples is the investigation of a complete sample of protoplanetary disks in the young Lupus star-forming region, observed by the Atacama Large Millimeter/submillimeter Array (ALMA), in which it was possible to constrain the solid mass and get $M_{\rm s} \sim 0.2 M_{\oplus}$ [7, 8]. The measurements of the mass of the gas, which is the dominant constituent of the disk material, is much more difficult to perform. It is because the emission of the main ingredient of a gaseous disk, molecular hydrogen, is weak, pratically below the detection limit in most regions of a disk. One way to evaluate the mass of the gas is to measure the mass of the dust and then to calculate the gas mass by assuming gas mass/dust mass = 100. Another way is to use other molecules as a proxy of the molecular hydrogen. A good observational strategy is to consider two independent mass tracers, namely CO and HD to overcome the difficulties [35]. Regardless from the big effort directed towards the measurements of the gas mass in the protoplanetary disks, we know relatively small number of objects for which it has been done with a high level of confidence. Among those are TW Hya [27, 202], DM Tau and GM Aur [130], and more recently HD 163296 [94]. The masses of the disks in these objects are in the range between $6 \times 10^{-3} M_{\odot}$ and $2 \times 10^{-1} M_{\odot}$. Those values are consistent with the masses evaluated from the typical accretion rates onto the T Tauri stars ($10^{-8} M_{\odot}$/year) and the lifetime of the disk. The simple evaluation is done under the assumption that the accretion rate is approximately constant during the lifetime of these objects.

The surface density distribution of dust and gas can be determined from the observations, performing spatially resolved measurements of the mass tracers, mentioned above. However, such measurements are facing the same difficulties as those present in the evaluation of the disk mass. There are some promising ideas to overcome the problems [175, 199], but more and better quality data are needed.

The thermal structure of a disk is also connected to the tracers of the disk material. It controls the molecular excitation conditions, the vertical location of the scattering surface and the spectral line and continuum intensities. One of the most common ways to get an insight into the temperature distribution is the classical approach of modeling the spectral energy distribution

(SED) in infrared. This approach consists in assuming the density and opacity distribution, simulating the propagation of energy through the disk, generating synthetic observables to compare with the data and finally iterating the model till the best agreement with the observed quantities. It can be found that temperatures range from 1000 K in the inner (0.1 AU) disk down to 10 K in the outer (100 AU) disk [3].

Our discussion can be summarized by presenting a typical disk model obtained by [3], which matches disk observations:

$$\Sigma(r) = 300\ (r/\mathrm{AU})^{-1}\ \mathrm{g \cdot cm^{-2}} \tag{1.1}$$

$$T(r) = 280\ (r/\mathrm{AU})^{-0.5}\ \mathrm{K} \tag{1.2}$$

$$\Omega(r) = 2 \times 10^{-7} (r/\mathrm{AU})^{-1.5}\ \mathrm{s^{-1}} \tag{1.3}$$

where $\Sigma(r)$ is the disk surface density at the distance r from the central star defined as the mass density integrated in the direction perpendicular to the disk plane at r, $T(r)$ is the temperature profile, and $\Omega(r)$ is the angular velocity of the disk. It is a model of the protoplanetary disk rotating around a solar mass star, extending from 0.07 to 200 AU and having the mass equal to 0.04 $M_\odot$.

One can derive from this model other useful characteristics of the disk, which will be used in this thesis. Adopting the isothermal sound speed as $c_s = \sqrt{P/\rho}$, where P and ρ are the gas pressure and mass density respectively, and assuming the vertical hydrostatic equilibrium to define the disk vertical scale height $H = c_s/\Omega$, we have:

$$c_s(r) = 10^5 (r/\mathrm{AU})^{-0.25}\ \mathrm{cm \cdot s^{-1}}, \tag{1.4}$$

$$H(r) = 5 \times 10^{11} (r/\mathrm{AU})^{1.25}\ \mathrm{cm}, \tag{1.5}$$

$$\frac{H(r)}{r} = 0.03 (r/\mathrm{AU})^{0.25}. \tag{1.6}$$

It is convenient to stress the connection between the sound speed c_s and the pressure scale height H, namely $c_s \propto T^{1/2}$ and $H \propto (Tr^3/M_*)^{1/2}$.

1.2.2 Protoplanetary disk evolution

There are several physical processes that drive the evolution of the protoplanetary disks. One of the best studied is accretion. The typical accretion rates observed in T Tauri stars are of the order of $10^{-8} M_\odot$/yr [3]. The matter can be accreted onto the star if it loses its angular momentum, so to explain the observed rates we need to know how the angular momentum is removed from the disk, keeping in mind that the angular momentum is a conserved quantity. One way to remove the angular momentum is to transport it radially outwards in the disk as it is the case in the simple geometrically thin viscous disk model. Another way is to transport it vertically away in a magnetized wind. Recently, the vertical transport attracts a lot of attention due to its high efficiency. In the case of the viscous accretion, we expect to observe an increase of the size of the disk in time. It is because while most of the mass in the disk moves inward, some material should move outward. This phenomenon can be used to distinguish between the

radial and vertical angular momentum transport, as we do not expect any increase in size of the disk in the case of a magnetized wind.

The mechanism by which angular momentum is transported in the protoplanetary disk is still a matter of debate. This is a reason why most viscous evolution models still use the α parametrization introduced by [191] for the kinematic viscosity $\nu = \alpha H c_s$, where H is the pressure scale height of the disk (an upper limit for the mixing length of the gas) and c_s is the isothermal sound speed (an upper limit for the turbulent velocity of the gas). The value of α can be constrained by studies of the evolution of the stellar accretion rate [81] or by detailed studies of individual systems [88]. These methods typically yield $\alpha \sim 10^{-2}$, with large uncertainties. The most widely accepted mechanism is the magnetorotational instability (MRI), a linear, ideal magentohydrodynamics (MHD) instability found in rotating sheared flows [17]. Classical models of turbulence driven by the MRI predict $\alpha \approx 0.001 - 0.1$ [6]. However, it is known that the non-ideal effects present in protoplanetary disks strongly affect this instability [16].

The evolution of the protoplanetary disks affects critically the process of planet formation. In the commonly used α-disk paradigm, the disk is turbulent by the assumption. However, if it is not the case and the accretion is driven by magnetized wind, the flow is likely to be laminar [16]. Several attempts to measure turbulence in the protoplanetary disks indicate also a low level of turbulence (e.g. [50, 58, 59, 60, 89, 172, 198, 199]). The lack of turbulence will change the outcome of vertical and radial settling, coagulation and disruption efficiency of the large dust grains (larger than 10 μm). Moreover, also the orbital migration of planets in the turbulence-free environment might be different from the migration processes investigated till now. The first study, which consider the effects of the wind stress on the planet migration has been performed in [99]. The state of the art in our understanding of orbital migration is the subject of the next section.

1.3 Disk-planet interactions – orbital migration in a protoplanetary disk

The main focus of this thesis is on the consequences of disk-planet interactions in multi-planetary systems. In order to place our results in the context of the knowledge already acquired, we present here shortly relevant developments and the state-of-the-art of this subject leaving important details for the next chapter.

The transfer of angular momentum and energy between a disk and a perturber (satellite, star, planet) embedded in it has been investigated back in the late seventies and early eighties of the previous century in the seminal papers [70, 71, 109]. At that time the only known planetary system was our own. Therefore, it is no wonder that the simple analytical models considered at that time were first discussed in connection with planetary rings, accretion disks in close binary systems and satellite systems. Despite of the fact that [71] have applied their results also to the interaction of Jupiter with the protoplanetary nebula, the fast development of the field started only after the first extrasolar planets were discovered.

A forming or already formed planet embedded in a protoplanetary gaseous disk exchanges the angular momentum and energy with the material in the surrounding disk mainly due to the

gravitational interaction. This results in the significant changes in the orbital elements of the planet, especially in its semi-major axis, and we say that the planet migrates in the disk. The migration can occur toward or away from the central star, depending on the mass of the planet and the physical conditions of this part of the disk where the planet is located. The disk-planet interactions can, if the planet is sufficiently massive, modify substantially also the structure of the disk and contribute to its evolution. The most recent review on the planet migration has been presented by [162].

Three main regimes of the orbital migration (classified as type I, type II and type III) have been studied in details, starting from the analytical investigations and continuing with the numerical simulations, gradually improving in time the models of the protoplanetary disks, with which the (proto)planets interact.

The regime of type I migration characterizes by weak disk-planet interactions, which means that the planet embedded in the disk does not perturb the disk structure significantly. In this regime, the planet migrates due to the angular momentum transport determined by the sum of the torques exerted on the planet from the density waves and the material in the corotation region.

A sufficiently massive planet is able to form a clean density gap around its orbit. In this case the perturbation of the disk caused by the planet is very strong. The planet migration is significantly influenced by the formation of the gap, namely it becomes slower than it would be without the gap formation. If the gap is clean and stationary, the disk is separated into two parts: the inner disk and the outer disk, which both repel the planet towards the center of the gap. As a consequence, the planet is locked in its gap and the gap must migrate along with the planet. Therefore, the expected migration speed of the planet corresponds to the radial velocity of the gas in a viscous unperturbed disk $v_r = -(3/2)\nu/r$, which is independent of the planet's mass and the aspect ratio of the disk. This regime of disk-planet interaction in which clean gap opening planets are locked to the viscous evolution is known as type II migration [210]. If the planet mass is larger than the local disk mass, namely $\pi r_p^2 \Sigma_p \lesssim m_p$, the inertia of the planet begins to be important and resists the viscous driving, which leads to the migration speed of the planet being slower than the viscous gas drift speed [10, 90, 103, 179, 195]. A substantial fraction of the viscous timescale is needed in order to reach the type II migration rate in typical low turbulent viscosity disks [190]. Therefore, it is important to model the planet motion before it actually happens. There are numerous recent studies describing the initial planet evolution towards the type II migration (e.g. [48, 50, 51, 96, 185]) showing that it can be faster or slower than type II migration rate, depending on the ratio between the disk's surface density and the mass of the planet.

For the intermediate-mass planets (in the range from sub-Saturnian to Jovian mass), capable to form a partial gaps in sufficiently massive disks, the migration can be very fast. This is known as type III migration or runaway migration [123]. The mechanism in this case relies on the asymmetry of the surface density distribution in the co-orbital region formed as a result of the planet migration in the disk. This asymmetry causes very efficient loss of the angular momentum by the planet and in the consequence its migration becomes faster. The faster migration leads to more pronounced asymmetry and in turn makes the migration even faster. Due to this runaway

process a planet can fall onto its parent star after no more than few hundreds orbital periods. In principle, type III migration can be either inward or outward, so in this latter case the planet can survive this phase of evolution.

To summarize, although several physical models have been put forward to describe the migration of the planets with different masses in the disk, the actual migration of a planet in a variety of conditions present in the protoplanetary disks still needs to be investigated. Particular points relevant for our studies will be presented in Chapter 2.

1.4 Orbital migration in a protoplanetary disk – formation and evolution of resonance configurations

The distribution of period ratios of the planetary pairs in the confirmed multi-planetary systems shown in Figure 1.2 indicates the presence of the resonance configurations. The most common configurations seem to be those corresponding to period ratio 3:2, but also those with the ratio 2:1 are observed. There are 32 resonance or near-resonance systems listed in [196]. Many more have been found by then by Kepler, TESS and ground-based facilities. The existence of the mean-motion commensurabilities provides a framework for testing various evolutionary scenarios leading to the formation of the observed planetary systems. The fact that the resonances are not as common as suggested by some of the simple models, tells us a lot about the way in which the planets migrate or to be more precise in which they do not migrate. Not less interesting is an attempt to investigate the migration histories of the individual systems. This will allow to constrain some of the assumptions of the disk models.

1.4.1 Resonance capture in planetary systems

The orbital migration is a consequence of disk-planet interactions and, in the situation when two or more planets are embedded in the protoplanetary disk, can lead to the formation of the special dynamical states between planets named mean-motion resonances or mean-motion commensurabilities [39, 71, 103]. The mean-motion commensurabilities in the Solar System are known and have been the subject of intensive studies since eighteenth century. The best example is the Laplace resonance between three satellites of Jupiter, namely Io, Europa and Ganymede. Their mean-motions n_{Io}, n_{Europa} and n_{Ganymede}, defined as $n_i = 2\pi/P_i$, where P_i is the orbital period of the satellite and the index i indicate the name of the satellite, obey the relation $n_{\mathrm{Io}} - 3n_{\mathrm{Europa}} + 2n_{\mathrm{Ganymede}} = 0$. The two-body resonances are also present in our planetary system, for example the 3:2 commensurability between Neptune and Pluto. In this thesis we concentrate on two-body resonances in the extrasolar planetary systems.

How can the migration bring two planets orbiting around the star in the protoplanetary disk into the resonance configuration? The migration increases the mobility of planets in the disk. They can move around changing the location of their orbits relative to each other. If the mutual separation between the planets increases then the planet-planet interactions are weak and the resonance capture cannot happen. This is the situation when the migration is divergent. So, for the resonance capture to take place, the migration must be convergent, which means that the mutual separation between planets decreases. When the orbital periods ratio of two planets is

approaching a resonance commensurability, the planet-planet interaction becomes stronger due to the periodic perturbations and the orbital eccentricities are excited. The convergent migration is the necessary condition, but not the sufficient one. The planets must not cross the resonance too fast, namely the migration timescale should be longer than the libration timescale associated with the resonance width [192]. This dependence of the resonance capture on the migration rate gives us the opportunity to get an insight about the efficiency of disk-planet interactions from the observation of the resonant planetary systems. It is an additional argument, stressing the point why the study of the orbital commensurabilities are so important. We are aware that the tidal interaction between star and planets plays also a significant role in the formation of MMRs in planetary systems [69, 163, 220]. However, in this thesis we will focus on the resonance captures and their maintenance caused by the disk-planet interaction.

The analytical formulation of the capture probability was firstly proposed in the framework of the circular restricted three-body problem in which a massive planet is assumed to orbit the central star on a circular trajectory and perturbs a massless test particle [219]. The capture probability for the first and second-order resonances can be expressed as a function of the rescaled eccentricity J_0 and rescaled migration rate $|d\beta/dt|$ of a test particle and it has been shown in Figure 1.3 adopted from [138]. The contours marked in red indicate the levels of the capture probability, starting from the white region those are 99, 75, 50, 25 and 1 percent probabilities. It can be seen from this figure that the first-order resonance is assured for small initial eccentricities and migration rates (white region). The capture will not take place if the eccentricities are low, but the migration rates are high (black region). For high eccentricities ($J_0 > 1.3$) the capture is probabilistic, unless the migration rate is very high (in such a case the capture is impossible). The situation is similar for second-order resonances. However, it it worth to point out that for the certain capture the migration rates for second-order resonances must be significantly lower than in the case of first-order resonances. Moreover, the transition from certain to probabilistic capture for the low migration rates occurs at $J_0 = 0.8$ instead of $J_0 = 1.3$ as for the first-order resonances. As an example indicate by green crosses in Figure 1.3, the location of a particle with the eccentricity equal to 0.01 migrating towards an Earth-mass planet orbiting a solar mass star at 1 AU, with the rate of 1 AU/Myr. This migration rate is too fast for the capture into the 2:1 resonance to take place, but the capture into any of subsequent resonances, namely the 3:2, 4:3 an so on is more likely.

The restricted three-body problem is a surprisingly good approximation for quite a few important applications. However, it could be verified only after relaxing the restricted assumptions and moving into the physical domain of the unrestricted elliptic three-body problem, which considers the two bodies with finite masses and eccentricities (e.g. [23], [217], [167], [218]).

The formation and evolution of the first-order resonance configurations for planets migrating in the disk have been extensively investigated by N-body and hydrodynamical calculations, in which the orbital migrations of planets are calculated based on the action of tidal torques. The full two-dimensional hydrodynamic simulations and N-body simulations were firstly used to study the 2:1 resonance trapping in the system around GJ 876 [106, 192]. The migration of two low-mass planets in the disk with different planetary masses and disk parameters in hydrodynamic simulations show that the planets can become locked in a first-order MMR as

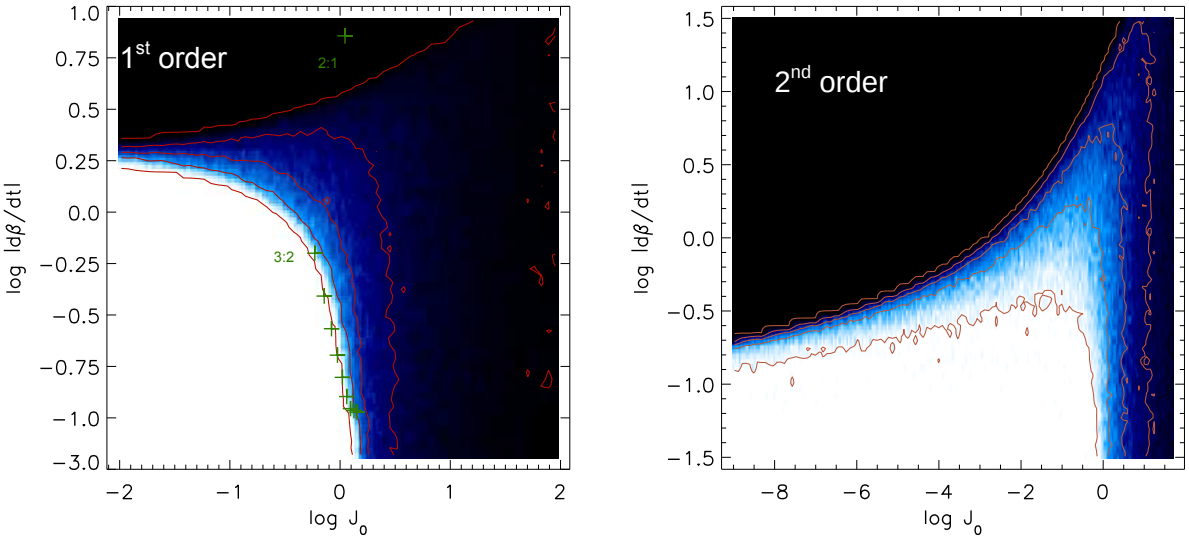

Figure 1.3: Capture probability for first and second-order resonances in a restricted three-body problem - The quantity J_0 is a rescaled eccentricity while the $|d\beta/dt|$ is a rescaled migration rate of the test particles. See text for more details. The figure is adopted from Figure 2 in [138].

a result of convergent migration [158]. The first-order resonance trapping for the planet pairs with different masses (from super-Earth like mass to giant mass) during convergent migration in the protoplanetary disk are examined by N-body simulations and two or three-dimensional hydrodynamic simulations in other works [2, 37, 39, 168, 170].

The capture into the second-order resonance in planetary systems have also been studied numerically. The numerical experiments for two planets with giant masses reveal that the higher order commensurabilities are favored when either one of the planet is massive, or the inner planet begins with a significant orbital eccentricity [140]. By adopting different migration parameters in N-body simulations of two low-mass planets, the migration parameters of migration rate and circularization rate which can induce the formation of second-order resonances have been constrained [133, 215]. The results of the N-body simulations show that the resonance capture requires slow convergent migration of the planets with sufficiently large circularization time and small pre-resonance eccentricities. However, for a system with comparable mass planets and higher initial eccentricities, the probabilistic trapping for second-order resonances has also been observed [217].

1.4.2 The evolution of the resonance configurations

In the early stages of the planetary system evolution, when the gas is still present in the disk, the planets can be captured in a MMR as a result of the convergent migration caused by the disk-planet interactions if all necessary conditions are satisfied (previous subsection). It is difficult to expect that in every protoplanetary disk the conditions will be just right for the capture to take place. Moreover, the formation of the resonance configuration at this early stage does not guarantees that the commensurability will be maintained in its further evolution. Indeed, there

are number of circumstances when the resonance will not form or it will not survive till the stage of a mature system, in which most of the confirmed planetary systems are found. One of the examples, already mentioned in the previous sections is the turbulence present in the disk (e.g. [17, 32, 82, 141, 152, 169, 177, 181]). Another example involves an evolution of the disk with a realistic opacity in which several regions of the divergent migration are formed in the disk [131]. There is no strong reason to expect that the orbital period ratios distribution of observed planet pairs should be dominated by the occurrence of mean-motion resonances. However, a significant number of planet pairs close to the resonance, especially the 3:2 and 2:1 MMRs, is of great interest and justifies further investigations.

It can be noticed that there is some trend for the planet period ratios to group not at the position of nominal commensurability, but slightly to the right of this position. This observational feature has been extensively investigated (e.g. [22, 41, 107, 113, 160, 161]) in the context of the tidal effects induced by the interactions between the central star and planets, operating after the disk has dispersed. It was found that when the planets orbit very close to the star than they move away from exact commensurabilities with the increased period ratios. The significant differences between the observational distributions of the period ratio among the most close-in and the farthest planetary systems is also a strong argument in favor of the tidal dissipation scenario [42].

However, it has been identified also the repulsion mechanism to account for the departure from resonances or more generally for the forestallment of the attainment of commensurabilities, which does not depend on the distance from the star. This considers the effects of the density waves excited by one of the planets on the other one. When the propagating density waves excited by one planet dissipate in the co-orbital region of the other planet, the angular momentum carried by the waves is transferred to the horseshoe region and then to the planet through horseshoe drag. And the additional torque is applied to change the migration rate of the planet in the disk. Consequently, the planets may evolve away from the resonance configuration or even cannot reach the MMRs.

Such mechanism was firstly noticed in a system consisting of a giant planet in an interior orbit and a super-Earth with a larger orbital period. The results of hydrodynamic simulations show that the inward migration of the super-Earth in a gaseous disk can be reversed under the outward propagating density waves excited by the inner giant planet. As a result, the planet pairs cannot be locked into 2:1 MMR. The local shearing box simulations indicate that the angular momentum transferred to the disk material via the density waves of the giant planet and then communicated to the low-mass planet through co-orbital dynamics, which can halt or even reverse the inward migration of the super-Earth [174].

The similar effect has been found in the system of two Saturn-like planets as well as two Uranus-like planets. In the second case the planets with $m_1 = 15M_\oplus$ and $m_2 = 13M_\oplus$ are found to be captured into the 3:2 MMR first and then leave away from it during the divergent migration, which is illustrated in Figure 1.4. The contour plot in the right panel shows that two planets open partial gaps in their co-orbital region where the material inside has interaction with the wakes emitted from each other. The study pointed out that such wake repulsion mechanism due to wake-planet interactions requires some non-linearity in planetary corotational regions,

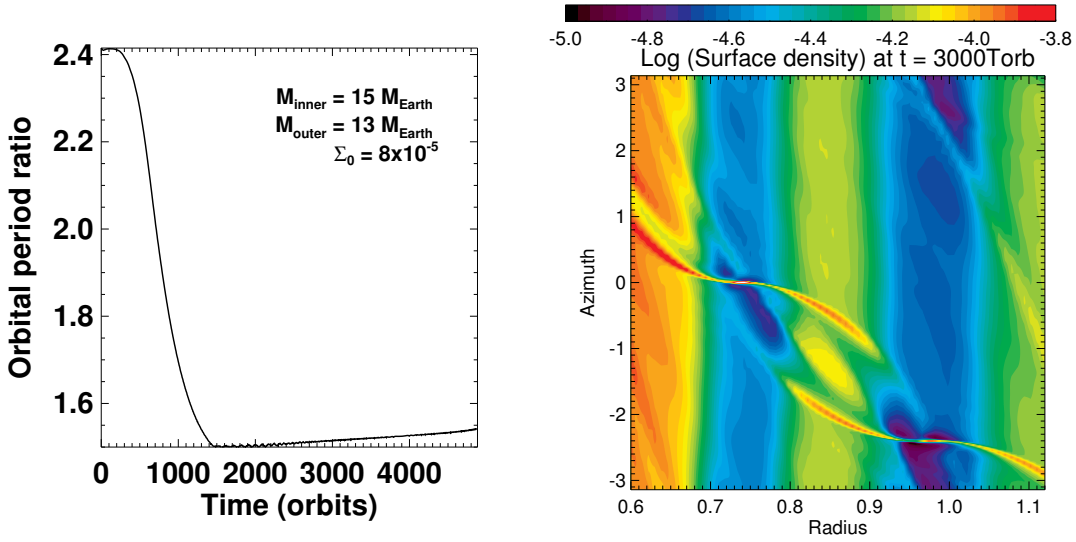

Figure 1.4: Migration of two planets in the Uranus's mass range - Left : evolution of the period ratio of two planets with $M_{\rm inner} = 15M_{\oplus}$ and $M_{\rm outer} = 13M_{\oplus}$; Right: the surface density contour of the disk in the vicinity of two planets at 3000 orbits. The figures are adopted from Figure 7 in [21].

which means that it cannot work efficiently in type I migration regime. Moreover, considering that the material in the co-orbital region of the planets needs to be remained in order to have dynamic interaction with the density wakes, the gap opened by the planets should not be totally cleaned. Accordingly, two conditions for the efficient wake-driven repulsion mechanism need to be considered: First, the donor planet should be a partial or a deep gap-opening planet; Second, the recipient planet could be a partial gap-opening planet or a type I migrating planet [21]. Similar behavior has been observed in the case for studying the migration of planet pairs which are able to form a partial gap in the disk. The results of hydrodynamic simulations show that the planet pairs trapped into the MMRs at the early phase of evolution can depart from the resonance at later times due to the gap formation process [97].

1.5 Thesis overview

The aim of my thesis is to investigate the establishment and maintenance of mean-motion resonances in the early stages of evolution of planetary systems, it means at the time when the forming planets are still embedded in a gaseous protoplanetary disk. The disk-planet interactions, which take place at that time, are of high level of complexity. As we have already discussed, the knowledge about one of the consequences of these interactions, namely the orbital migration, is substantial, but far from being complete. Moreover, we are aware that the simple disk models used in most of the studies do not include all relevant physics. Therefore a caution is needed in any attempt to interpret the observational data. However, the robust features in the observational properties of the planetary configurations, like for example occurrence of the mean-motion resonances, open a possibility to learn more about the migration itself and uncover, at least partially, the history of the formation of planetary system architectures.

Motivated by this fact, we focus our study on disk-planet interactions in a system of two low-mass planets embedded in a gaseous protoplanetary disk. Our conclusions are based on the simple two-dimensional hydrodynamic disk models, but our findings might be extended onto more general physical situations.

In the previous sections we have indicated the relevant background information in order to put the results of this thesis in a wider perspective. We have reported shortly what is known about the observed properties of the confirmed planets, the structure and evolution of protoplanetary disks and the observed resonance configurations. In Chapter 2 we set up the stage for our investigations. Chapter 6 contains the summary and outlook of our studies. The main results of this thesis are presented in Chapters 3 – 5 and here we highlight them briefly.

1.5.1 What are the conditions in which the low-mass planets embedded in the protoplanetary disk can be captured in the second-order mean-motion resonances?

Higher-order resonances between low-mass planets in extrasolar systems are less common that the first-order ones, but a number of planet pairs are found to be very close to the second-order mean-motion commensurabilities. Particularly intriguing is the system Kepler-29, in which the orbital period ratio of two planets is extremely close to the nominal value of the 9:7 MMR [54]. The existence of such a system has inspired us to have a closer look at the second-order mean-motion resonances (Chapter 3). Specially because at the time we have started our investigations, it was not sure whether the pair of planets in Kepler-29 is indeed in this resonance. Later on the dynamical architecture of this planetary system has been constrained, performing transit timing variation analysis [92] and demonstrating that the planets are in the 9:7 resonance configuration [133]. The masses of the planets have been evaluated to be in the super-Earth range. In our studies we show how such configurations may form and whether we expect to find more of them in the future.

The previous studies on the second-order resonance captures have been performed in the framework of the semi-analytical models and N-body calculations. We will take one step further and for the first time apply full two-dimensional hydrodynamic simulations to perform a detailed study of the 9:7 resonance capture for two equal-mass super-Earths embedded in the protoplanetary disk. We also make a comparison between the results of our hydrodynamic simulations with those obtained in previous works by more restricted methods. This provides the information about the range of parameters for which the simple methods can be used without necessity to implement computationally expensive simulations.

1.5.2 Is it true, considering just disk-planet interactions, that the slow convergent migration of two low-mass planets will inevitable lead to the resonance configuration?

The observations show that the resonance configurations are not so often, as was previously thought, in multi-planetary systems of low-mass planets. A number of mechanisms to explain this has been put forward (see Section 1.4.2). Among them, there is one which is of particular interests here, namely the repulsion of the planets, due to the wake-planet interactions [21, 174].

The discussion about this mechanism started after it has been shown that the inward migration of the super-Earth can be reversed due to the effect of the outward propagating density waves excited by a giant planet [173, 174]. Very similar results have been obtained later in the case of two Saturn-like and two Uranus-like planets [21]. However, as we have already pointed out, the most numerous planets around other suns are super-Earths and mini-Neptunes. How efficient is this mechanism for the lower mass planets?

Before going to the case of two super-Earths we reexamine the orbital evolution of the super-Earth under the influence of the density waves of a Jupiter-size planet in the inner part of the disk (Chapter 4). The aim is to confirm the main reason for the outward migration of the super-Earth using FARGO3D code in this case (Chapter 2) instead of NIRVANA, as it was done in [21]. Moreover, the dependence of the efficiency of wave-planet repulsion mechanism on the mass of the inner planet is determined in more detail, using the whole sequence of inner planet masses.

The common expectation was that this effect is too small for the super-Earths to be of any importance. Our intuition was telling something different, so the best approach is to find out who is right. This is done in Chapter 5, where we not only demonstrate that the mechanism is efficient even for the planets in the super-Earth mass range, but we also provide the conditions which must be satisfied for the low-mass planet pairs to be repelled efficiently in the protoplanetary disk.

Chapter 2

Setting the stage

In this thesis we investigate the formation of mean-motion resonances as a consequence of the migration of two planets embedded in a gaseous protoplanetary disk. One way to approach the problem is to use two-dimensional hydrodynamic simulations to calculate the protoplanetary disk evolution and the migration of the planets under the disk-planet interactions. This is exactly the way we adopt.

First, we formulate the problem giving the basic equations. This will allow to extend our discussion from Chapter 1 about the disk-planet interactions, placing more technical description here in order to make our results reported in Chapters 3 – 5 easy to read and understand. The computational tools and a numerical setup of our simulations are also presented. In addition, more details about the different types of planet migration are given in the last section of this chapter.

2.1 Formulating the problem in the hydrodynamical approximation

The gaseous protoplanetary disk considered in our studies can be treated as a continuous medium, and its evolution in time is described by the equations of fluid dynamics.

2.1.1 Basic fluid dynamics for ideal gas

The state of a continuous fluid at a certain time can be described by the velocity $\vec{v}(\vec{r},t)$, pressure $p(\vec{r},t)$ and mass density $\rho(\vec{r},t)$. For simplicity, we consider the ideal fluid and neglect the chemical and nuclear reactions, ionization and recombination inside of it.

Equation of continuity

The *continuity equation* has the form:

$$\frac{\partial \rho}{\partial t} + \vec{\nabla} \cdot (\rho \vec{v}) = 0 \tag{2.1}$$

where ρ is the mass density, $\vec{v}$ is the velocity of the fluid element. This equation expresses the conservation of mass in a volume of fluid.

Equation of motion

For the fluid only considering the pressure acting on it, according to Newton's second law of motion, the *Euler's equation* has a form:

$$\frac{\partial \vec{v}}{\partial t} + \vec{v} \cdot \vec{\nabla} \vec{v} = -\frac{\vec{\nabla} p}{\rho}. \tag{2.2}$$

Depending on the problem under consideration, the accelerations generated by the additional forces can be put in the right hand side of this equation. For instance, if the gravitational force is present in the investigated problem than the Euler's equation will have a form:

$$\frac{\partial \vec{v}}{\partial t} + \vec{v} \cdot \vec{\nabla} \vec{v} = -\frac{\vec{\nabla} p}{\rho} - \vec{\nabla} \Phi \tag{2.3}$$

where Φ is the gravitational potential. The gravitational force can be imposed by an external mass. Moreover, the fluid itself could also generate the gravitational field, which should be computed self-consistently. This equation represents the conservation of momentum.

We remark that the continuity Equation (2.1) and Euler's Equation (2.3) are not sufficient to constrain all physical quantities (ρ, p and $\vec{v}$) presented in these equations. In order to close this set of equations for describing the dynamics of the fluid, more information about the relations between those variables are required. Before going further with this argument, let us include into the equation of motion another very important effect, namely the viscosity.

2.1.2 Equation of motion in viscous fluid

In the discussion above, we only consider the forces acting on the fluid due to the pressure and gravity, which is valid in the case if the molecular mean free path $\lambda \to 0$. However, in a more realistic case with finite λ, the random motion of molecules in a fluid causes the particle exchange between the adjacent fluid elements, which leads to the additional momentum and energy transfer in this process. Such dissipative processes are related to the molecular viscosity.

In a viscous fluid, the continuity equation has the same form of Equation (2.1). However, the Euler's equation (2.3) should be modified, adding the forces associated with the molecular viscosity into its left hand side. Therefore, the Euler's equation for the viscous flow reads

$$\frac{\partial \vec{v}}{\partial t} + \vec{v} \cdot \vec{\nabla} \vec{v} = -\frac{\vec{\nabla} p}{\rho} + \frac{1}{\rho} \vec{\nabla} \sigma - \vec{\nabla} \Phi. \tag{2.4}$$

where σ is the viscous stress tensor, related to the velocity gradients.

It is important to stress that Equation (2.4) is derived for the fluid under the effects of the molecular viscosity. However, such effects are far too weak in order to account for the required angular momentum transport in the disk. In the classic α-disk model, a more effective viscosity generated by the turbulence in the disk is thought to be able to dominate the evolution of the protoplanetary disk [191]. Therefore, equation of motion in this model is written as

$$\frac{\partial \vec{v}}{\partial t} + \vec{v} \cdot \vec{\nabla} \vec{v} = -\frac{\vec{\nabla} p}{\rho} - \vec{\nabla} \Phi + \vec{f_\nu} \tag{2.5}$$

where $\vec{f_\nu}$ represents the viscous force per unit mass associated with the kinematic viscosity resulting from the disk turbulence.

In this way we obtain the continuity equation (2.1) and the equation of motion (2.5) for the ideal gas in a viscous disk. In numerical simulations, these two formulae are applied to calculate the gas evolution in the protoplanetary disk. As we have already mentioned, the equations we have presented till now are not sufficient in order to model the disk evolution - more constrains are needed. This brings us to the third macroscopic law of conservation, namely the energy conservation.

2.1.3 Energy equation

The structure and evolution of the protoplanetary disk can be calculated from the continuity, momentum and energy equations. We have dealt with the two first equations already. Now it is time for the energy equation, which can be written as follows [155]:

$$C_V \rho \left[\frac{DT}{Dt} - (\gamma - 1) \frac{T}{\rho} \frac{D\rho}{Dt} \right] = D_\nu + H_e - \nabla \cdot \vec{F}. \tag{2.6}$$

where C_V is the constant volume specific heat per unit mass of the disk gas, T is the temperature, γ is the adiabatic index, H_e is the external heating rate per unit volume and $\vec{F}$ is the radiative flux. The function D_ν denotes the viscous dissipation per unit volume, but it can also include ohmic dissipation, if relevant. The symbol D/Dt is the Lagrangian derivative and is defined as

$$\frac{D}{Dt} = \frac{\partial}{\partial t} + \vec{v} \cdot \vec{\nabla}.$$

In few particular simple cases, there is no need to solve full energy equation. Instead, one can close the set of the hydrodynamic equations with the appropriate equation of state.

Equation of state

The pressure p and density ρ of a fluid element can be connected with each other by the equation of state. It is often assumed that the gas in a protoplanetary disk can be well approximated as an ideal gas, for which equation of state has the form

$$p = \frac{k \rho T}{\mu m_H} \tag{2.7}$$

where T is the temperature, k is the Boltzmann constant and μ is the mean molecular weight (average mass per particle in units of the mass of a hydrogen atom m_H).

In the simplest case, one can assume that T is constant, which leads to $p \propto \rho$. This is dubbed as *isothermal gas*. In this case, the Equation (2.7) can be written as follows

$$p = c_s^2 \rho \tag{2.8}$$

where c_s is the isothermal sound speed and it reads

$$c_s^2 = \frac{kT}{\mu m_H} = \text{constant}. \tag{2.9}$$

Another interesting case is the locally isothermal equation of state. The disk temperature is not radially uniform, as in the globally isothermal fluid, but it remains fixed at each individual radius. It means that all excess energy generated by, for example, compression, viscous dissipation or shocks can be radiated away efficiently, thereby keeping the temperature profile fixed.

To bridge simple locally isothermal fluid with the more realistic full radiation-hydrodynamical situation one can apply the adiabatic equation of state. The equation of state for the ideal adiabatic gas is related to the internal energy, which gives

$$p = e\rho(\gamma - 1) = C_V T\rho(\gamma - 1) \tag{2.10}$$

where e is the specific internal energy (energy per unit mass) and γ is the adiabatic index with $\gamma = C_P/C_V$, namely the ratio of specific heats at constant pressure and constant volume. Now, the pressure depends also on the temperature, so the energy equation has to be solved as well. The adiabatic sound speed is given by

$$c_s^2 = \gamma \frac{kT}{\mu m_H} \tag{2.11}$$

which is not a constant but depending on T.

2.2 Numerical setup

The aim of our work in this thesis is to study the formation of the resonance configurations for planet pairs embedded in a protoplanetary disk. Therefore we consider a system of two planets with masses m_1 (inner planet) and m_2 (outer planet) orbiting in a gaseous disk around the central star with the mass M_*. The unit of mass in the calculations is adopted to be the mass of the central star. Now, we go on describing the disk models and numerical setups adopted in our simulations.

2.2.1 Disk model

A typical protoplanetary disk can be approximated as being a geometrically thin and rotating with the angular velocity Ω, close to the Keplerian one. For this reason, we adopt a two-dimensional vertically integrated disk model in a cylindrical polar coordinate system (r, ϕ, z). The origin of the system is located at the central star which is regarded as a point mass. The disk model is described by the continuity equation and the Euler's equation, which in this particular representation are as follows:

$$\frac{\partial \Sigma}{\partial t} = -\vec{\nabla} \cdot (\Sigma \vec{v}) \tag{2.12}$$

and

$$\frac{\partial \vec{v}}{\partial t} + \vec{v} \cdot \vec{\nabla}\vec{v} = -\frac{1}{\Sigma}\vec{\nabla}P - \vec{\nabla}\Phi + \vec{f_\nu} \tag{2.13}$$

where P is the vertically integrated pressure, Σ and $\vec{v}$ respectively denote the surface density of the disk and the velocity, while Φ is the gravitational potential and $\vec{f_\nu}$ is the viscous force per unit mass.

In almost all the simulations, we adopt a locally isothermal equation of state, where the vertically integrated pressure is expressed as $P = \Sigma c_s^2$ with the sound speed c_s related to the pressure scale height of the disk H through $c_s = (H/r)(GM_*/r)^{1/2}$. The aspect ratio of the disk defined as $h = H/r$ is assumed to be constant in the simulation, which leads to $c_s \propto r^{-\beta}$ with $\beta = 1$. Thus the power-law index of the radial temperature profile is equal to -1. Whenever relevant we investigate how this particular equation of state may influence our results, in order to show the robustness of our findings. Therefore, we also apply the adiabatic equation of state, in which the pressure is given by $P = (\gamma - 1)e\Sigma$. Moreover, we run the simulation using the optically thick disk with constant angular momentum flux (Chapter 5). The energy equation in those simulations is calculated as follows

$$\frac{\partial e}{\partial t} + \vec{\nabla} \cdot (e\vec{v}) = -P\vec{\nabla} \cdot \vec{v} + Q^+\Sigma - Q^-\Sigma \tag{2.14}$$

where e is now the internal energy per unit area. Q^- and Q^+ are the heating and cooling functions defined as

$$Q^- = (2\sigma T_e^4)/\Sigma \tag{2.15}$$

where σ is the Stefan-Boltzmann constant and T_e is the effective temperature, and

$$Q^+ = \nu r^2 \left(\frac{d\Omega}{dr}\right)^2. \tag{2.16}$$

An ideal equation of state is used to close the hydrodynamics equations

$$P = \frac{k\Sigma T}{\mu m_H}. \tag{2.17}$$

The internal energy per unit area is linked to the temperature through

$$e = \frac{kT}{\mu m_H(\gamma - 1)}. \tag{2.18}$$

The self-gravity of the disk is neglected in our simulations since the masses of the disks adopted in our work are sufficiently low. We have validated this assumption by performing additional calculations described in Chapter 5, as a response to the concern expressed in [13]. The action of an effective kinematic viscosity ν in the disk is modeled by applying the turbulent viscosity. In the majority of our simulations shown in this thesis, a constant kinematic viscosity ν is adopted in units of $r_1^2(GM_*/r_1^3)^{1/2}$.

To start the simulations, we initialize the equilibrium model of the disk and then put the planet as a perturber into the disk. We do not keep the planet on the fixed orbit, but we allow the planet to move according to the forces acting on it. The initial disk surface density profiles adopted are specified for each set of calculations presented in the next chapters. The standard outflow boundary conditions are applied at the disk boundaries in all simulations, which extrapolates the surface density and Keplerian velocity profiles across the boundary region of the disk. Moreover, where relevant, the wave-killing zones operate in the computational domains connecting to the inner and outer boundaries of the disk for damping the disturbances near the mesh radial boundaries [43].

2.2.2 Planets

The planets are initially located at r_1 (inner planet) and r_2 (outer planet) from the central star in circular or eccentric orbits depending on the investigated case. The unit of length is taken to be the initial orbital radius of the inner planet r_1. The inclination of the planetary orbit is set to zero for both planets considered here.

The orbital evolution of a planet is calculated due to the gravitational interactions with the disk, other planet present in the system, and the central star. When working out the force per unit mass on each planet, there is in addition to the contribution due to direct gravitational interaction, and indirect term that arises on account of the acceleration of the origin of the coordinate system that is constrained to be centered on the star. The time unit in which we follow the evolution is the initial orbital period of the inner planet P_1.

To avoid the singularity of the gravitational potential at $r = 0$, the softening parameter is introduced [43] and the modified potential of a planet with mass m_p has the form of:

$$\psi_p = -\frac{Gm_p}{\sqrt{r^2 - 2rr_p\cos(\phi - \phi_p) + r_p^2 + b^2 r_p^2}} \tag{2.19}$$

where (r_p, ϕ_p) are the coordinates of the planet in radial and azimuthal directions while b is the softening parameter which is adopted to mimic the vertical extent of the disk. Selecting the correct value of the softening parameter b is important for calculating the orbital evolution of the planet. Smaller softening parameter generally lead to stronger torques and faster migration. In this thesis, we concentrate on studying the migration of low-mass planets. Therefore, the value of b is taken to be $0.3h - 0.6h$ [56, 125, 127, 152].

We use two independent hydrodynamic codes to calculate the evolution of two low-mass planets in gaseous protoplanetary disks. One is an early MHD version of the code NIRVANA [225] and the other one is a widely used code FARGO3D [24]. This allows us to check the robustness of our numerical results and confirm the outcome of other authors' calculations performed in the past by only one of those codes. In addition, a fast Eulerian transport algorithm has been applied in FARGO3D code, enables to speed up the computational time significantly [120]. It is particularly valuable, as the long term evolution considered in this thesis is computationally expensive. More details about numerical setups and models will be given together with the discussion of the results in Chapters 3 – 5.

2.3 Planet migration in a protoplanetary disk

In Chapter 1 we have introduced briefly three main regimes of the orbital migration. Here, we will give more details about the migration, concentrating on those aspects which will be useful later on for the presentation and discussion of our results.

A planet embedded in a protoplanetary disk, orbiting around the central star exchanges its angular momentum with the material in the disk. The change of the angular momentum of the planet J_p, due to the disk-planet interaction, can be written as follows

$$\frac{dJ_p}{dt} = \Gamma_p \tag{2.20}$$

where Γ_p is the z-component of the total torque (z is the vertical coordinate of the cylindrical polar coordinate system (r, ϕ, z)). The torque acting on the planet, responsible for this exchange, is generated by the asymmetries in the disk density caused by the presence of the planet (see Figure 2.1). There are two contributions to the torque, Γ_p, acting on the planet. One is from the spiral density waves excited in the disk by the planet and propagating through the disk: the inner spiral is leading while the outer one is trailing. Note that the planet orbits the central star counterclockwise (see the left panel of Figure 2.1). The interior and exterior waves exert on the planet a positive and negative torques, respectively. The net torque from the density waves acting on the planet depends on the balance between these two torques. The second contribution comes from the gas in the corotation region of the planet, showing a characteristic asymmetry in the density distribution in front and behind the planet. In this way the material near the orbit of the planet that executes horseshoe turns generates an additional torque (see the right panel of Figure 2.1). The planet migration depends on the sum of the torques exerted from the density waves and the material in the corotation region.

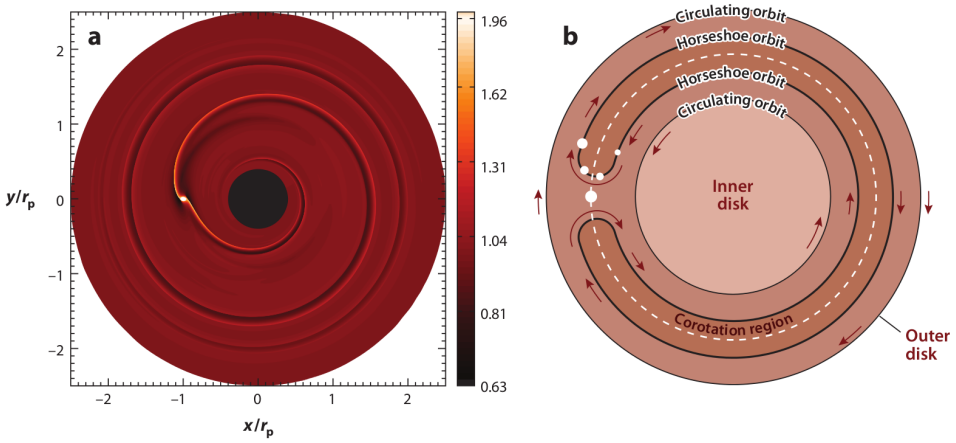

Figure 2.1: Perturbation of the gaseous disk caused by a low-mass embedded planet - Left: the contour plot of the disk surface density perturbed by a planet with the mass of 10 $M_\oplus$ orbiting counterclockwise on a circular orbit around the central star, which is located in the center of the plot. The planet is embedded in a disk with a constant initial density. Right: the motion of the gas in the vicinity of the planet. The motion is denoted by red arrows in a reference frame rotating with the planet. The horseshoe region is indicated by the dark brown color. The figure is taken from Figure 19 in [104]. See text for more details.

Using the angular momentum for a planet with mass m_p on a circular orbit in the form:

$$J_p = m_p r_p^2 \Omega_p \tag{2.21}$$

where r_p is the distance from the planet to the central star and Ω_p is the angular velocity of the planet in its orbit, and assuming that the planet angular velocity is Keplerian, namely $\Omega_p = \Omega_K = \sqrt{GM_*/r_p^3}$, we can define the migration timescale as

$$\tau_{mig} \equiv \frac{r_p}{\dot{r}_p} = \frac{1}{2}\frac{J_p}{\Gamma_p}. \tag{2.22}$$

In order to describe the way in which planets migrate we will use both the migration timescale and the migration rate of the planet, which is determined by $1/\tau_{mig}$. Studies of the migration processes require the knowledge of the torque Γ_p acting on the planet. In a flat two-dimensional disk, which will be used in this thesis, Γ_p can be written as follows

$$\Gamma_p = -\int \Sigma(\vec{r_p} \times \vec{F})_z ds \tag{2.23}$$

where Σ represents the surface density of the disk, $\vec{r_p}$ indicates the location of the planet, $\vec{F}$ is the gravitational force per unit mass acting between the planet and an infinitesimal surface element of the disk ds. The integration is performed over all surface elements in the disk. It is important to stress this again that here, for simplicity, we consider the planets on circular orbits.

The best approach to determine the torque acting on the planet and in consequence the way in which planet migrates is to use full non-linear hydrodynamic simulations. In this thesis we adopt such an approach. However, other approaches, as the linear approximation, proved being very useful in understanding the nature of the complex interactions responsible for the evolution of the planet motion. For that reason we will give here the most relevant results coming from the analytical considerations.

The classification of the migration modes started from the two well defined cases, namely *type I migration* and *type II migration*, based on the strength of the disk-planet interactions. If the interactions between planet and disk are not able to decrease the surface density in the co-orbital region of the planet significantly than we have type I migration. This may occur if the mass of the planet embedded in the typical protoplanetary disk is low (for example few Earth masses). Instead, if the interactions are strong enough to change significantly the surface density profile close to the planet, so a gap is formed in the disk than the planet migration differs from type I migration. In the ideal case, when the gap is clean and stationary, this is called the type II migration. This can take place if the planet mass is sufficiently massive. For typical protoplanetary disks, the planet should have at least the mass of the Jupiter to be able to open a clean gap. The situation is more complicated if the gap is partially opened, which means that it is not clean. The migration of a partial gap-opening planet is intensively investigated now. The effects of this type of migration will be discussed in Chapters 4 – 5.

2.3.1 Low-mass planet migration: type I migration

A planet with a sufficiently low mass embedded in a protoplanetary disk is not able to form a significant density depletion in its co-orbital region. Therefore, we can perform the linear analysis for the determination of the torque acting on the planet. Let's assume that the unperturbed disk is axisymmetric and rotates around the central star with the Keplerian angular velocity $\Omega(r) = \Omega_K = \sqrt{GM_*/r^3}$. If the planet is on a circular orbit, than its gravitational potential ψ_p, defined as

$$\psi_p = -\frac{Gm_p}{\sqrt{r^2 - 2rr_p\cos(\phi - \phi_p) + r_p^2}} \tag{2.24}$$

is periodic in azimuth and can be expanded in a Fourier series in the form of

$$\psi_p(r,\phi,t) = \sum_{m=0}^{\infty} \psi_m(r)\cos\{m[\phi-\phi_p(t)]\} \tag{2.25}$$

where ϕ_p at the planet position is equal to $\Omega_p t$ and Ω_p is the angular velocity of the planet, while ψ_m is the potential coefficient for each azimuthal mode number m. The total torque exerted by the disk on the planet (see Equation (2.23)) can be also written as [103]

$$\Gamma_p = -\int \Sigma(\vec{r}_p \times \vec{F})_z ds = \int \Sigma(\vec{r}_p \times \nabla\psi_p)_z ds = \int \Sigma \frac{\partial \psi_p}{\partial \phi} ds \tag{2.26}$$

where Σ represents the surface density of the disk, $\vec{F}$ is the gravitational force per unit mass acting on a disk surface element ds. Based on Equation (2.25), the strongest perturbations are generated at the particular resonant locations where the frequency of an individual potential Fourier component $m(\Omega(r)-\Omega_p)$ is equal to a natural oscillation frequency in the disk [28]. Therefore, the torque from the disk acting on the planet can be calculated by summing over the torques exerted at each resonant location in the disk [70, 197, 210].

If the effects of the disk pressure and its self-gravity can be neglected, the locations of the resonances can be easily found and described by the equality $m(\Omega(r)-\Omega_p)=0$ or $m(\Omega(r)-\Omega_p)=\pm\kappa(r)$ where $\kappa^2(r)=(2\Omega(r)/r)d(r^2\Omega(r))/dr$ is the epicyclic frequency, the characteristic frequency of the particle oscillations in the disk. It is worth noticing that for the Keplerian disk, $\kappa(r)=\Omega_K(r)=\sqrt{GM/r^3}$. The place in which the local angular velocity of the disk material is equal to the angular velocity of the planet indicates the location of the so called corotation resonance. This resonance occurs inside the corotation region (horseshoe region) indicated by the dark brown color framed by the solid line, marked "horseshoe orbit" in Figure 2.1. Instead, two other resonant conditions, namely $\Omega(r)=\Omega_p \pm \kappa(r)/m$ correspond to Lindblad resonances: an inner Lindblad resonance (with the plus sign) located inside the orbit of the planet and an outer Lindblad resonance (with the minus sign) occurring outside the planet orbit. The radial locations of the Lindblad resonances in a Keplerian disk are derived by taking $\kappa(r)=\Omega_K(r)$, which gives

$$r_L = \left(\frac{m}{m\pm 1}\right)^{2/3} r_p. \tag{2.27}$$

If the effects of the disk pressure cannot be neglected, the condition for the Lindblad resonance should be modified as

$$m(\Omega(r)-\Omega_p) = \sqrt{\kappa^2(r)(1+\xi^2)} \tag{2.28}$$

where $\xi \equiv mc_s/(\Omega r)$. Thus in this case the locations of both inner and outer Lindblad resonances are shifted inward [159, 210]. Taking $m\to\infty$ and $c_s = H\Omega$, the Lindblad resonances is found to pile up at

$$r_L = r_p \pm \frac{2H}{3}. \tag{2.29}$$

At these locations the disk flow relative to the planet becomes sonic. Therefore they are those places from where the density waves are originated [73]. This phenomenon is known as the torque cut-off [11, 71].

2.3.1.1 Lindblad torques

Density waves are launched at Lindblad resonances in the disk and transfer the angular momentum between the planet and the disk. The planet gains and loses angular momentum from the disk at the inner and outer Lindblad resonances, respectively. Thus the net torque generated by density waves can be obtained by summing the contributions from all Lindblad resonances, which is dubbed as *differential Lindblad torque* [70, 71].

The theoretical Lindblad torques exerted on the disk via the density waves can be calculated analytically from solving the wave excitation problem in the linear approximation by using the WKB method [70, 109, 111]. In that approximation, the analytic expression for the Lindblad torque arising from the component of the potential with azimuthal mode number m acting on the planet is obtained as

$$\Gamma_m^{\rm LR} = \frac{{\rm sign}(\Omega_p - \Omega)\pi^2\Sigma}{3\Omega\Omega_p\sqrt{1+\xi^2}(1+4\xi^2)}\Psi^2 \tag{2.30}$$

with

$$\Psi = r\frac{d\psi_m}{dr} + \frac{2m^2(\Omega-\Omega_p)}{\Omega}\psi_m \tag{2.31}$$

where the expression has to be evaluated at the location of the resonance $r = r_L$ [11, 70, 156, 210]. Then the total inner and outer Lindblad torque are derived by summing over all Lindblad resonances with different m as

$$\Gamma_{\rm OLR(ILR)} = \sum_{m=1(2)}^{+\infty} \Gamma_m^{\rm OLR(ILR)} \tag{2.32}$$

where $\Gamma_{\rm ILR}$ and $\Gamma_{\rm OLR}$ are referred to one-sided Lindblad torques which scale with h^{-3} [210]. And the differential Lindblad torque is the sum of the total inner and outer Lindblad torques. In general, the differential Lindblad torque is negative since the outer Lindblad resonances lie closer to the planet than the inner ones. Therefore, the planet is driven by the Lindblad torque to migrate inward.

The expressions of the Lindblad torque in the three-dimensional isothermal disk has been obtained analytically based on the linear analysis, which gives the form as [197]

$$\Gamma_{\rm L,iso}/\Gamma_0 = -(2.34 - 0.10\alpha) \tag{2.33}$$

with

$$\Gamma_0 = \left(\frac{m_p}{M_*}\right)^2\left(\frac{1}{h}\right)^2\Sigma_p r_p^4\Omega_p^2 \tag{2.34}$$

where Σ_p indicates the unperturbed disk surface density at the planet's position r_p. The normalization factor Γ_0 reflects the scaling of the torque determined by the disk physical properties.

In two-dimensional calculations, the gravitational potential of the planet ψ_p needs to be smoothed by taking a softening parameter b for avoiding singularities since the planet is typically treated as a point mass, as we have already pointed out (see Equation (2.19)). If the adopted value of b is appropriate, the results obtained in two-dimensional calculations are consistent with

three-dimensional ones. The Lindblad torque in an adiabatic disk with such smoothing is given by [150]

$$\gamma\Gamma_{\mathrm{L,adia}}/\Gamma_0 = -(2.5 + 1.7\beta - 0.1\alpha)\left(\frac{0.4}{b/h}\right)^{0.71} \tag{2.35}$$

where γ is the adiabatic index while α and β are the power law exponents in the surface density Σ and temperature T dependence of the radial coordinate, namely $\Sigma \propto r^{-\alpha}$, $T \propto r^{-\beta}$.

2.3.1.2 Corotation torques

For low-mass planets embedded in the disk, the corotation torque exerted on the planet by the material in its co-orbital region can be calculated applying the linear theory in the same way as for the Lindblad torque. It has been done originally for the planet-satellite system by [70]. They have found that

$$\Gamma_m^{\mathrm{CR}} = \frac{m\pi^2\psi_m}{2r(d\Omega/dr)}\frac{d}{dr}\left(\frac{\Sigma}{B}\right) \tag{2.36}$$

where $B = \kappa^2/(4\Omega)$ denotes the second Oort's constant. By definition B is the z-component of the vorticity (circulation) of the flow $(\vec{\nabla}\times\vec{v})|_z$ divided by 2, and in consequence $2B/\Sigma$ is the specific vorticity, which sometimes is also called the vortensity. The torque expressed by Equation (2.36) should be evaluated at the corotation radius $r = r_C$. To obtain the total torque, it is sufficient to sum the contributions from all values of m.

The formula for the corotation torque in three-dimensional isothermal disk obtained from linear analysis has the form of [197]

$$\Gamma_{\mathrm{C,iso}}/\Gamma_0 = 0.64(1.5 - \alpha). \tag{2.37}$$

It can be noticed that for the disk model with the surface density $\Sigma \propto r^{-3/2}$, we obtain $\Gamma_{\mathrm{C,iso}} = 0$. Thus, for such models the only contribution to the total torque is the differential Lindblad torque.

The linear corotation torque in the two-dimensional softened gravity approach for the adiabatic disk is obtained as [150]

$$\gamma\Gamma_{\mathrm{C,adia}}/\Gamma_0 = 0.7\,(1.5 - \alpha)\left(\frac{0.4}{b/h}\right)^{1.26} - 1.4\left(\frac{\xi}{\gamma}\right)\left(\frac{0.4}{b/h}\right)^{1.26} + 2.2\xi\left(\frac{0.4}{b/h}\right)^{0.71} \tag{2.38}$$

where $\xi = \beta - (\gamma - 1)\alpha$ is the power law exponent in the specific entropy profile, which has the form $\propto r^{-\xi}$.

The total torque exerted from the disk acting on the planet can be calculated by summing over the Lindblad torque and the corotation torque and the type I migration rate for low mass planet can be derived. From the linear calculations by taking into account three-dimensional effects, the type I migration time is given as [197]

$$\tau = (2.7 + 1.1\alpha)^{-1}\frac{M_*}{m_p}\frac{M_*}{\Sigma_p r_p^2}h^2\Omega_p^{-1}. \tag{2.39}$$

Based on that, for an Earth-mass planet around a solar mass star at $r = 1$ AU in a disk with $\Sigma = 1700\ \mathrm{g\cdot cm^{-2}}$ and $h = 0.05$, we derive the migration time $\tau \sim 1.6\times10^5$ yrs. Moreover, the formula of Equation (2.39) indicates that τ is inversely proportional to the planet mass m_p. It

infers that the migration of the planets with higher mass should be faster than the lower mass planets. Therefore, in the type I migration regime, the more massive planet can arrive to the regions closer to the central star in the early stage of the evolution before the disk is dispersed.

2.3.1.3 The horseshoe drag

For low-mass planets and large viscosity, the corotation torque, described in the previous subsection behaves as expected from linear theory. However, when the viscosity becomes small enough, the horseshoe turns in the corotation region take place, which means that the fluid elements in the vicinity of the planet execute the U-shaped turns along with the horseshoe orbit as it is shown in the right panel of Figure 2.1. In the presence of horseshoe turns, the linear corotation torque is replaced by *horseshoe drag* (nonlinear co-orbital torque) introduced by [208]. The angular momentum can be exchanged between the planet and the co-orbital disk material at each U-turn. Summing over the contributions from each of the horseshoe U-turns, we can calculate the total horseshoe drag [208]. A non-zero net torque will result if a persistent asymmetry between the two U-turns exist. The strength of this asymmetry depends on the radial gradients of specific vortensity and entropy across the horseshoe region [20, 148, 208]. The expression of the horseshoe drag can be written as [208]

$$\Gamma^{\rm HS} = \frac{3}{4}\left(\frac{3}{2}-\alpha\right) x_s^4 \Sigma_p \Omega_p^2 \tag{2.40}$$

where x_s is the radial half-width of the horseshoe region. In a number of the numerical studies it has been shown that x_s in a two-dimensional disk can be expressed in the form [20, 125, 148]

$$x_s = C(\epsilon) r_p \sqrt{\frac{m_p/M_*}{h}} \tag{2.41}$$

with $C(\epsilon)$ a factor of order unity and ϵ the smoothing length defined as $\epsilon = br_p$. In general, the horseshoe drag is more efficient to slow down the inward migration of low-mass planets than the linear corotation torque. In specific cases, the horseshoe drag even can overwhelm the Lindblad torque, forcing the planet migrate outward.

The horseshoe drag is found to be very sensitive to the disk viscosity and thermal properties in the vicinity of the planet [126]. Based on the physical arguments and two-dimensional numerical results, the expression for the horseshoe drag in the adiabatic disk is obtained as [150]

$$\gamma\Gamma_{\rm HS,adia}/\Gamma_0 = 1.1\left(\frac{0.4}{b/h}\right)(1.5-\alpha) + \frac{\xi}{\gamma}\left(\frac{0.4}{b/h}\right)\left(10.1\sqrt{\frac{0.4}{b/h}} - 2.2\right) \tag{2.42}$$

where the first term on the right hand side is the vortensity-related component and the second term corresponds to the entropy-related component.

Unlike the inner and outer parts of the disk, there is no density waves involved for transferring the angular momentum in the horseshoe region. Thus the angular momentum exchanged between the material and the planet is finite in the corotation region. As a result, the horseshoe drag will be saturated, namely it can be largely reduced or even vanished [209]. Sustaining the horseshoe drag requires a flow of angular momentum supplied into the horseshoe region, which

can be achieved by the action of viscosity. The optimal level of desaturation occurs when the viscous diffusion time scale across the horseshoe region $\tau_\nu = x_s^2/\nu$ is shorter than the libration time of the material near the outer edges of the horseshoe region, $\tau_{\rm lib} = (8\pi r_p)/(3\Omega_p x_s)$ [72, 121, 122, 145]. However, if the viscosity is too high, τ_ν is short and comparable to the time for the gas undergoing a horseshoe U-turn. Then the horseshoe streamlines are strongly disrupted by the viscosity and the horseshoe drag becomes weaker. When the viscosity continue to increase, the horseshoe drag will approach the linear corotation torque [122, 148, 151].

2.3.2 Migration of planets, which are able to form at least a partial gap in the disk

If the planet is sufficiently massive to modify the initial disk surface density profile, the gravitational interactions between the planet and the disk cannot be treated any longer in the linear approximation, as in the case of low-mass planets discussed in the previous subsection. As a consequence of the disk-planet interaction, a gap is formed and the planet will migrate differently.

2.3.2.1 Gap formation

For a sufficient massive planet, the density wave turns into a shock in its vicinity. The angular momentum can be deposited locally due to the dissipation of the shocks and the viscosity. The material inside the planet orbit loses the angular momentum while the material outside it gains the angular momentum. As a result, the material is repelled from the vicinity of the planet and a gap is formed in the disk. During the process of the gas being removed, the gap becomes deeper and wider. Meanwhile, the gradients of the disk's surface density profile at the edges of the gap become steeper. This leads to the enhancement of the disk's viscous torque. When the density gradient is steep enough that the viscous torque is able to balance the torque exerted by the planet on the same annulus of the disk, the gap reaches a steady state and its profile does not changing significantly [38, 204]. The depth and width of the gap depend on the disk properties and the mass of the planet.

For opening a gap, the tidal torque should be able to balance or overwhelm the viscous torque, which gives the viscous criterion that $q > q_{\rm viscous} \equiv 30\pi\alpha h^3$ with $q = m_p/M_*$. On the other side, the Hill sphere of the planet should be larger than the disk scale height, which derives the pressure criterion: $q > q_{\rm thermal} \equiv 3(H/r)_p^3 = 3h_p^3$ [111]. These two conditions have been combined into a single criterion, which is obtained by two-dimensional hydrodynamic simulations with the form of [38]:

$$\frac{3}{4}\frac{H}{r_H} + \frac{50\nu}{q r_p^2 \Omega_p} \lesssim 1. \tag{2.43}$$

where r_H is the Hill radius of the planet defined as $r_H = r_p(q/3)^{(1/3)}$. This gives an estimate of the minimum mass of the planet for opening a gap with bottom density less than 10% of the background disk density. Further studies about the analysis of tidal induced shocks in the disk indicates that a strong shock is not necessary for gap opening process and the low-mass planet is also able to open a gap in an inviscid disk [178]. Moreover, the numerical simulations show

that a planet with several times of Earth mass also can open a gap in a thin viscous disk even if the Hill radius is smaller than the disk scale height [47].

The gap structure has been investigated recently by using hydrodynamic simulations [47, 66, 95]. The depth of the gap is usually described as the ratio between the surface density of the disk at the position of the planet perturbed by the planet Σ_{min} and the unperturbed value Σ_{un}. It can be derived from considering the balance between the viscous angular momentum flux and the torque from the outer disk (or the inner disk), which gives the form of [49, 95]:

$$\frac{\Sigma_{min}}{\Sigma_{un}} = \frac{1}{1 + 0.04K} \tag{2.44}$$

where K is a coefficient with the form of

$$K = q^2 h^{-5} \alpha^{-1} \tag{2.45}$$

with the aspect ratio h is taken at the planet's position r_p and α is the viscosity parameter in the α disk model. This formula has a good agreement to the numerical results when K is large or small but the deviations become larger if $K \sim 10 - 1000$ due to the non-linear effects [49].

2.3.2.2 Type II migration

The planet migration is profoundly influenced by the formation of the gap. One of the reasons is that the corotation torques are less important since the density in the co-orbital region is largely reduced. For a very massive planet that is able to open a very wide gap, the Lindblad torques are also reduced, which slows down the planet migration.

It should be noticed that type II migration is an idealized planetary migration model, difficult to verify by the direct numerical calculations, as it requires to follow the evolution of the migrating planet for several viscous timescales, which is a challenge. The type II migration is characterized by the formation of a clean gap, it means that at least 90% of gas has been removed from the region along the orbit. The planet stays in the center of the gap and feels no torque from the disk. The planet migration rate follows the viscous speed. However, in a more realistic situation, the disk is not separated completely into two parts by the gap. Therefore, the migration of the massive planet in the disk can differ from the type II migration, at least in the initial phase of the evolution before reaching the final state after several viscous timescales.

2.3.2.3 Migration of planets able to form a partial gap

Numerical simulations show that the radial velocity of the massive planet does not follow exactly the viscous accretion speed. If the planet mass is larger than the disk mass, namely $\pi r_p^2 \Sigma_p \lesssim m_p$, the disk cannot push the planet efficiently and the migration speed of the planet is slower than the speed of the viscous flow [10, 90, 179, 195]. On the other side, the gas is found to be able to pass through the gap during the planet migration. It has been pointed out that the planet should still feel the gravitational torque in the gap after reaching a steady state [38]. For the massive planet in a low-viscosity disk, the passage of gas through the gap is negligible because the gap is wider than the horseshoe region of the planet. In that case, as the planet migrate inwards, the gap is refilled from the outer disk, which enhances the viscous torque and makes

the migration rate of the planet faster than the viscous speed [185]. Recent studies indicate that the migration rate of the planet able to form a partial gap depends on the ratio between the disk surface density and the planet mass, the aspect ratio and also the viscosity [48, 50, 51, 185].

For a wide range of the disk parameters (the disk aspect ratio spans from 0.03 to 0.07 and the viscosity from 10^{-3} to 10^{-2}) and the planet masses (in the range from 5×10^{-6} to 10^{-3}) have shown that the planet migration slows down as the surface density of the bottom of the gap decreases [96]. They have derived an empirical formula of the torque exerted on the planet in the form

$$\Gamma_{\rm total} = \frac{\Gamma_{\rm L} + \Gamma_{\rm C} \exp(-K/K_t)}{1 + 0.04K} \tag{2.46}$$

where the values of the Lindblad and corotation torques in the locally isothermal case are given by [150]

$$\Gamma_{\rm L}/\Gamma_0 = -(2.5 + 1.7\beta - 0.1\alpha) \left(\frac{0.4}{b/h}\right)^{0.71} \tag{2.47}$$

$$\Gamma_{\rm C}/\Gamma_0 = 1.1 \left(\frac{0.4}{b/h}\right) (1.5 - \alpha) + 2.2\beta \left(\frac{0.4}{b/h}\right)^{0.71} - 1.4\beta \left(\frac{0.4}{b/h}\right)^{1.26}. \tag{2.48}$$

The exponential coefficient of $\Gamma_{\rm C}$ indicates the cutoff of the corotation torque, and K_t is related to the gap depth for which the corotation torque is ineffective. The above expressions for the Lindblad and corotation torques in the locally isothermal case can be obtained from Equations (2.35), (2.38) and (2.42) by taking the limit $\gamma \to 1$ and invoking infinitely efficient thermal diffusion. Under such assumptions, the linear Lindblad torque is given by Equation (2.35) with γ set to 1. The corotation torque is the sum of the second and third terms in Equation (2.38), with $\gamma = 1$ and $\xi = \beta$, and the first term in Equation (2.42).

2.3.3 Dynamic torque on migrating planet: Type III migration

Most of the formulae of the torques discussed in this chapter are obtained under the assumption that the planet is kept on a fixed orbit. When the planet is allowed to migrate in the disk, it may experience dynamical torques, which are related to its migration rate.

For the intermediate-mass planet (in the range from sub-Saturnian to Jovian mass), the migration can be very fast in periods of time under appropriate conditions, which is known as *type III migration* or *runaway migration* [123]. This fast migration relies on co-orbital torques which is proportional to the migration rate of the planet in the disk. Depending on the sign of this dynamical torque, there is a possibility of a positive feedback loop. In principle, type III migration can be either inward or outward. Considering the case that a planet migrates inward (similar analysis can be done for the outward migration case), the material trapped in the horseshoe orbits will be carried by the planet in its Hill sphere. Therefore, the planet must exert a negative torque on this material while the material exerts a positive torque on the planet, which will slow down its inward migration. Considering this feedback, the mass contained within the horseshoe region needs to be moderate for obtaining the rapid migration.

There are two conditions required for the occurrence of type III migration [123]. First, a partial gap should be formed in the planetary location in order to generate a co-orbital mass deficit. Second, the co-orbital mass deficit should satisfy the condition $\delta m \simeq m_p'$, where m_p' is

the sum of the planet mass and the mass in its Hill sphere. When migration runs away, the drift rate grows exponentially until reaching the so-called fast regime. And then, the drift rate settles to a finite, large value, which defines the regime of type III migration.

For the low-mass planet, its migration in the disk can also be affected by the dynamic corotation torques in particular cases [153, 171]. Unlike the classical type III migration, low-mass planets do not perturb the surface density distribution significantly, but still a "mass" deficit can arise if there is a radial gradient in vortensity in the disk. Therefore, the sign of dynamic corotation torque acting on the low-mass planet depends on the background vortensity gradient. And the feedback on the planet migration could be either positive or negative. In the disk with mass a few times more massive than $2 \times 10^{-3} M_{\odot}$ at 10 AU, the effects of dynamic corotation torque may have a significant impact on the planet migration.

The presented here overview of the concepts as well as the analytical and semi-analytical results about the planetary orbital migration is by no means complete or comprehensive. Our aim was to introduce those aspects of the subject, which will be helpful in showing and discussing the outcome of our investigations, which we are going to do in the next chapters.

Chapter 3

Capture of super-Earths into second-order mean-motion resonances: the 9:7 commensurability

This Chapter is based on the paper written by Zijia Cui, John C. B. Papaloizou, and Ewa Szuszkiewicz, "On the 9:7 Mean Motion Resonance Capture in a System of Two Equal-mass Super-Earths", published in The Astrophysical Journal, 872:72 (15pp), 2019.

There are numerous investigations dedicated to the first-order commensurabilities, which occur in planetary systems at locations where the ratio of the two orbital periods can be expressed as $(p+1)/p$, with p being an integer [34, 37, 100, 140, 158, 192]. As can be seen in Figure 1.2, the first-order commensurabilities between two low-mass planets are more common than the second-order resonances, for which the ratio of the orbital periods is given by $(p+2)/p$. Recently, however, several second-order mean-motion commensurabilities have been observed, for example 5:3 or 9:7, and the question about their origin becomes relevant. In particular, the commensurability in the Kepler-29 system has attracted our attention, because in this system the orbital period ratio of two low-mass planets is extremely close to 9/7 [54]. Our aim here is to determine the disk properties that favor a capture in the 9:7 resonance in a system of two equal-mass super-Earths embedded in a gaseous protoplanetary disk. To reach our objective, we apply, for the first time, full two-dimensional hydrodynamic simulations. The analytical and N-body approaches made till now to the similar problems were used as tests in the regimes of their applicability.

3.1 Motivation: Why 9:7?

We have already anticipated in the introduction to this chapter that there is one very interesting system: Kepler-29 with two low-mass planets having the orbital period ratio extremely close to 9/7, namely 1.28566 as determined by [54] in the confirmation paper. The dynamical architecture of this planetary system has been constrained based on the TTV analysis in [84, 92], but the

existence of the resonance configuration was still a matter of debate, when we started to think about modeling this system. Being close to the commensurability naturally provides a strong indication that the system, indeed, contains the resonant pair of planets. However, the indication does not mean that it is actually true, so further analysis was needed. Our attempts to obtain the resonance configuration in the Kepler-29 system using the hydrodynamical simulations motivated our colleagues to have a closer look at the assumed resonance in this system and they have concluded that the planets most likely are in the resonance configuration [132]. This result strengthens our stimulus for studying the formation of the second-order resonances in the early phases of the planetary system evolution. Most recently, the new analysis shows that the period ratio of Kepler-29 b and c is slightly lower than determined by [92], namely 1.28495 and the masses of the planets have been respectively evaluated to be $5.0M_{\oplus}$ and $4.5M_{\oplus}$ [207]. The new period ratio is more distant from the 9:7 exact commensurability, compared with its original determination, but still it is very close to 9/7. Moreover, non-zero eccentricity of the planetary orbits in this system, supports the conclusion that planets should be locked in the 9:7 MMR [93].

Apart from the Kepler-29 system, which was our strongest motivation for the study presented in this thesis, some other planets might be also locked in this particular second-order resonance. To find out such systems we have performed a search in NASA Exoplanet Archive. In the histogram of the orbital period ratios for confirmed *Kepler* planet pairs shown in Figure 3.1, we illustrate the statistics of the planet pairs around the 5:4, 9:7, and 4:3 MMRs. The bin size is equal to 0.01 that corresponds approximately to the mean value of the libration widths evaluated for those three resonances for the planets with the super-Earth mass. As it can be

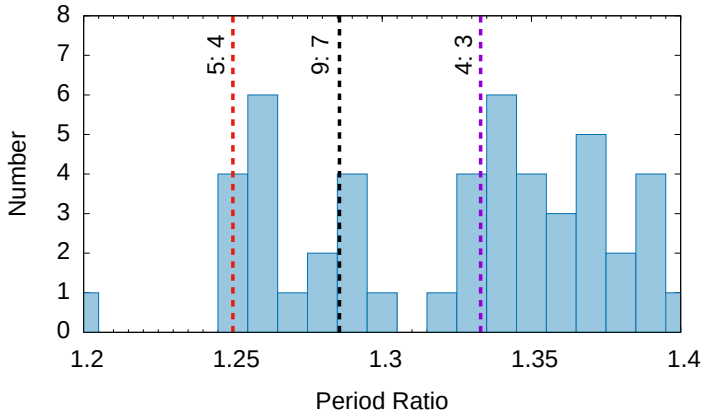

Figure 3.1: Histogram of confirmed *Kepler* planet pairs with period ratios around 9:7 MMR - The width of the bin is 0.01. Dashed vertical lines from the left to right indicate the locations of 5:4, 9:7, and 4:3 resonance commensurabilities, respectively. Observed planetary periods data are taken from NASA Exoplanet Archive (as of August, 2021).

seen in Figure 3.1, six planet pairs are found, for which the orbital period ratios are near the 9:7 commensurability. Four of them have period ratios slightly larger than 9:7 while another two have them a little bit less than 9:7. The detailed information about those planet pairs are given in Table 3.1.

Table 3.1: Planet pairs with the period ratios near the 9:7 resonance

System	Confirmed Planet	Planet Pair	Periods (days)	Deviation from 9:7	References
Kepler-29	2	Kepler-29b Kepler-29c	10.3397 13.2861	0.0008	[207]
Kepler-417	2	Kepler-417b Kepler-417c	12.3309 15.9425	0.0072	[136]
Kepler-431	3	Kepler-431b Kepler-431c	6.8025 8.7034	0.0063	[136]
Kepler-37	4	Kepler-37d Kepler-37e	39.7920 51.1960	0.0009	[76]
Kepler-1542	4	Kepler-1542b Kepler-1542e	3.9512 5.1012	0.0053	[136]
Kepler-33	5	Kepler-33e Kepler-33f	31.7848 41.0281	0.0051	[136]

Only two systems listed in Table 3.1: Kepler-29 and Kepler-417 are composed of two planets. All others have more planets than two: Kepler-431 contains three, Kepler-37 and Kepler-1542, four and Kepler-33 five planets, so the formation of the 9:7 resonance in those systems might be affected also by the presence of other planets. In the Kepler-37 system, the planets d and e are extremely close to the 9:7 MMR [76]. However, the existence of planet e was, and still is, questioned in [18, 118] and [180]. If the planet e does exist, the 9:7 resonance in the Kepler-37 system will form more complex resonance configuration together with the 3:1 commensurability between planets b and d. The conclusion from our search is clear: There are not many examples of the second-order 9:7 mean-motion resonances. Is there Kepler-29 an exception? The answer to this question can be found by understanding the conditions for the resonance capture.

3.2 Previous studies

The second-order resonance capture has been investigated in the past in the framework of semi-analytic models and N-body calculations. Those studies have provided very useful guidelines and testbeds for our studies. The hydrodynamic simulations, that we have employed here for the first time, have to be able to reproduce the results obtained in the restricted range of applicability of the methods used in the previous works and to give the results for more general situations not accessible by other means.

A variety of aspects of the formation and evolution of the second-order resonances has been covered by the previous studies. The resonance capture probability as a function of planetary masses, initial eccentricities of the orbits and migration parameters has been investigated in [176] using a simple planar restricted three-body Hamiltonian model. Later on, this work has been confirmed and extended in [138]. It has been found that the probability of the second-order resonances capture depends on the migration rate and initial eccentricity of a test particle. In particular, it has been shown that the second-order resonance capture cannot occur for

high migration rates, and the capture probability decreases for higher eccentricities of the test particle. Besides that, they have also concluded that test particles can be captured by more massive planets at higher initial eccentricities and relative migration rates than the less massive ones. An interesting result has been obtained for the capture into the 3:1 MMR in [62] using the algebraic mapping of the averaged planar restricted three-body problem. They have found that the resonance capture occurs at discrete windows of initial eccentricities for fast migration rates. The locations of those windows depend on initial resonance angles while their widths on the relative migration rates. This work indicates the regimes in which the capture phenomenon is not probabilistic.

The migration parameters that can induce the second-order resonance captures were constrained in the N-body calculations performed for the two low-mass planets, with the wide range of the masses, migrating in a protoplanetary disk in [215]. The capture and stability of second-order resonances for migrating planet pairs with comparable masses and very low initial eccentricities have been studied in [217]. They have found that the second-order resonance capture for such planets requires the slow convergent migration with sufficiently large circularization time and small pre-resonance eccentricities. Finally, [133] has used the N-body approach with the particular parametrization of the migration rates to study in great details the structure of the 9:7 resonance and the conditions for the maintenance of this commensurability.

Here, we investigate the formation of a second-order resonance in a two-planet system by applying full two-dimensional hydrodynamic simulations to treat the disk-planet interactions in more rigorous way. However, there is a price to pay for that, unlike the case of the first-order resonances, where the evolution of the commensurability can be followed for a sufficiently long time, before and after the capture, the numerical calculations presented in this work are limited to the close vicinity of the 9:7 resonance. There are two reasons why we could not follow the evolution for much longer and they both are computational in nature.

The first reason is connected with a very low migration rate, which has to be used in the simulations in order to guarantee that the time for planets to cross the resonance is longer than the inverse libration frequency, which can be estimated as [215]

$$n_1 - (9/7)n_2 \sim 4.2 \times 10^{-5}(m_1/M_\oplus)(M_\odot/M_*)n_2 \tag{3.1}$$

Therefore, the relative migration rate is equal to

$$-d(a_2/a_1)/dt < [4.2 \times 10^{-5}(m_1/M_\oplus)(M_\odot/M_*)]^2 n_2 \tag{3.2}$$

which gives a condition that the migration time should exceed $10^6 - 10^7$ yrs. Here n_1, a_1 and n_2, a_2 are the mean motions and semi-major axes of the inner and outer planets respectively while m_1 is the mass of the inner planet. Such a low migration rate leads to a very small change in the semi-major axis during the typical length of our calculations, namely 10^4 orbits. This stopped us from starting our simulations far away form the resonance. Otherwise we will be not able to follow evolution of the planets till their arrival at the commensurability, as the time of such calculation will be prohibitively long.

The second cause is the eccentricity damping taking place during the planet evolution in the disk. As it is well known in a non-adiabatic regime, which is considered in this work, a

second-order resonance capture is possible only if the eccentricity of the orbit is nonzero [62]. To achieve that, the planets need to arrive at the resonance before the initial eccentricity will be damped completely, which means that the system can only migrate for a time comparable to the circularization time.

Both reasons mentioned above explain why we have focused only on the orbital evolution of the planets in the last stages of capture into the resonance. Now, we move on and present the numerical setup of the hydrodynamic simulations, used to determine the disk properties that favor a capture of two low-mass planets into the 9:7 MMR.

3.3 Disk model and numerical setup

We consider a system of two equal-mass planets embedded in a gaseous protoplanetary disk and orbiting a central star. The gas in the disk is modeled by adopting a locally isothermal equation of state with $P = \Sigma c_s^2$. The aspect ratio $h = H/r$ is assumed to be constant and thus the fixed temperature has the profile of $T(r) \propto r^{-1}$ [188, 200]. We remark that the migration rates of the low-mass planet cannot be significantly affected by the particular choice of the equation of state since the torques acting on the planet with the mass adopted in our calculations are similar in fully radiative and locally isothermal disks considered in this study [102]. The self-gravity of the disk is discarded.

The system of units in the numerical simulation has been described in Section 2.2. We take the central stellar mass M_* equal to the Solar mass $M_\odot$ and the initial position of the inner planet $r_1 = 1$ AU. Therefore the time unit for the numerical simulations is 1 yr.

We assume that at least the inner planet's eccentricity has been excited to a nonzero value during the early orbital evolution in order to fulfill the necessary condition for the resonance trapping into a second-order resonance of the nonzero eccentricity as mentioned before. If not stated differently, the inner planet is initially located in an eccentric orbit with the eccentricity of $e_1 = 0.005$ while the outer planet is put into a circular orbit. In the simulations, if the initial eccentricity of a planet is not zero than the planet is located at the pericenter of its orbit, namely its initial semi-major axis is $a_i = r_i/(1 - e_i)$, where $i = 1, 2$ denotes the inner and outer planets respectively. The initial position of the outer planet r_2 is chosen to let the initial orbital period ratio of two planets be equal to 1.2865, which is slightly larger than 9:7. In this work, we simply assume that the planets arrived at these positions during the previous stage of the evolution without considering how such configuration was actually formed.

For the low-mass planet undergoing the type I migration, its migration time is inversely proportional to the planet mass and the disk surface density (see Equation (2.39)) [197]. Considering that in this work the planets have the equal masses, a particular initial surface density profile $\Sigma(r)$ with a central cavity has been adopted to guarantee the convergent migration of two planets in the early stages of the evolution. In the outer part of the disk the surface density profile is uniform, while in the inner part of the disk, the surface density increases linearly with the distance from the star. The adopted initial surface density profile $\Sigma(r)$ has the form

$$\Sigma(r) = \begin{cases} \Sigma_0 r & \text{for} \quad r_{\min} < r < 1.1, \\ 1.1\Sigma_0 & \text{for} \quad 1.1 \leq r < r_{\max} \end{cases} \tag{3.3}$$

where Σ_0 is a scaling parameter of the disk surface density while $r_{\rm min}$ and $r_{\rm max}$ represent the inner and outer boundaries of the computational domain in the radial direction. In the simulations, the inner planet is initially put in the inner part of the disk having a positive gradient density profile while the outer planet is inserted in the outer part of the disk with a flat disk surface density profile. In this way, the inner planet migrates slower relative to the outer planet due to the difference in the corotation torque action and the convergent migration can take place [149], which is a necessary condition for the capture into MMRs [100, 140].

In this work, we use the hydrodynamic code NIRVANA to solve the continuity and Navier-Stokes equations with the aim to follow the evolution of the disk [225]. The effective viscosity generated from turbulence is modeled by adopting a constant kinematic viscosity ν [139]. The computational domain in the radial direction extends from $r_{\rm min} = 0.33$ to $r_{\rm max} = 3.0$ with open boundaries and in the azimuthal direction covers the whole range of angles, ϕ, from zero to 2π. The numerical resolution is chosen based on the results of a series of convergence tests. It was shown that with doubling of the resolution in each coordinate direction, the circularization rates remain the same and the relative migration rate may be changed up to a factor of two. Although this was found to have the effect of mapping simulations with different disk parameters at lower resolution, it will not change the final conclusions of this work obtained from an ensemble of simulations. Hence, as a compromise between specific numerical accuracy and improved statistical significance of our results, the resolution adopted in the simulations is 384×512 for the computational domain in radial and azimuthal directions, respectively.

Here, we consider the system with the masses of both planets in the super-Earth range. The gravitational potential of the planets is smoothed by a softening parameter of $b = 0.45h$. For the disk aspect ratio with the value of $h = 0.045$ adopted in the simulations, the planets are not able to open partial gaps and their orbital migration is expected to be in the type I regime.

3.4 Formation of the 9:7 resonance for two equal low-mass planets in a disk

In this section, first, we determine the theoretical expectation for the relation between the eccentricities, circularization and migration times for a pair of low-mass planets trapped in the second-order resonance due to disk-planet interactions. Then we perform a series of the hydrodynamic simulations for two equal-mass planets ($m_1 = m_2 = 3M_\oplus$) embedded in a protoplanetary disk in order to check the consistency of the numerical results with the predictions derived using the semi-analytic approach.

3.4.1 Semi-analytic solution for two planets in the 9:7 resonance

The semi-analytic solution for two planets in a second-order resonance undergoing migration and orbital circularization have been discussed in previous works (e.g. [215] see also Section 1.4.1). The relation between the planets' migration and circularization rates as well as eccentricities, to be expected in such a system, has been derived in [215]. Based on their results, we can estimate the eccentricity ratio of planets captured in the 9:7 MMR and the libration width of the 9:7 MMR for two equal-mass planet system.

3.4.1.1 Conservation of angular momentum and energy

We consider two planets with masses of m_i (i = 1, 2 for inner and outer planet respectively). Their semi-major axes and eccentricities are denoted as a_i and e_i. The total angular momentum of the system of two planets is given by [140, 215]

$$\begin{aligned} J = J_1 + J_2 &= m_1\sqrt{GM_*a_1(1-e_1^2)} + m_2\sqrt{GM_*a_2(1-e_2^2)} \\ &= m_1\sqrt{GM_*a_1(1-e_1^2)}\cdot\left[1+\frac{m_2\sqrt{a_2(1-e_2^2)}}{m_1\sqrt{a_1(1-e_1^2)}}\right] \end{aligned} \tag{3.4}$$

and the total energy E of two planets has the form of

$$E = -\frac{GM_*m_1}{2a_1} - \frac{GM_*m_2}{2a_2} - m_2R = -\frac{GM_*m_1}{2a_1}\left(1+\frac{m_2}{m_1}\frac{a_1}{a_2}\right) - m_2R, \tag{3.5}$$

where m_2R is the interaction energy with R being the disturbing function. The contribution of the interaction energy is small and will be neglected in further consideration. If the planets are already in the resonance than the semi-major axis ratio a_2/a_1, e_1 and e_2 for two planets are nearly constant and the self-similar migration can be assumed. In [140], it has been shown that for self-similar migration induced by the interactions with the disk, we can write the following

$$\begin{aligned} \frac{dJ}{dt} &= J_1\frac{1}{2a_1}\frac{da_1}{dt}\left[1+\frac{m_2\sqrt{a_2(1-e_2^2)}}{m_1\sqrt{a_1(1-e_1^2)}}\right] \\ &= -\left(\frac{m_1\sqrt{GM_*a_1(1-e_1^2)}}{\tau_{mig,1}} + \frac{m_2\sqrt{GM_*a_2(1-e_2^2)}}{\tau_{mig,2}}\right) = T \end{aligned} \tag{3.6}$$

where the total torque $T = T_1 + T_2$ is the sum of the torques from the disk acting on each planet, while $\tau_{mig,i} = -2a_i/\dot{a_i}$ for planet i with $i = 1, 2$. The conservation of total energy gives

$$\frac{dE}{dt} = \frac{GM_*m_1}{2a_1^2}\frac{da_1}{dt}\left(1+\frac{m_2a_1}{m_1a_2}\right) = -D \tag{3.7}$$

where $D = D_1 + D_2$ is the total orbital energy loss rate induced by tides. It is related to the torques acting on the planets and the circularization times (defined as $\tau_{c,i} = -e_i/\dot{e_i}$) through

$$D = \frac{GM_*m_1e_1^2}{a_1(1-e_1^2)\tau_{c,1}} + \frac{GM_*m_2e_2^2}{a_2(1-e_2^2)\tau_{c,2}} - \frac{n_1T_1}{\sqrt{1-e_1^2}} - \frac{n_2T_2}{\sqrt{1-e_2^2}} \tag{3.8}$$

with $n_i = \sqrt{GM_*/a_i^3}$ for $i = 1, 2$ denoting the mean motion for each planet. Combining Equations (3.6), (3.7) and (3.8) we obtain

$$\begin{aligned} &\frac{1}{m_1m_2}\left(\frac{m_1a_2e_1^2}{\tau_{c,1}(1-e_1^2)} + \frac{m_2a_1e_2^2}{\tau_{c,2}(1-e_2^2)}\right) = \\ &\frac{a_2^{3/2}\sqrt{(1-e_2^2)} - a_1^{3/2}\sqrt{(1-e_1^2)}}{m_2\sqrt{a_2(1-e_2^2)} + m_1\sqrt{a_1(1-e_1^2)}}\left(\frac{1}{\tau_{mig,2}} - \frac{1}{\tau_{mig,1}}\right). \end{aligned} \tag{3.9}$$

This is the relation between e_1, e_2, $\tau_{c,1}$, $\tau_{c,2}$, $\tau_{min,1}$ and $\tau_{mig,2}$ for two planets captured into the resonance.

3.4.1.2 Ratio of the eccentricities of two planets captured in the 9:7 resonance

When the planets are captured in the 9:7 resonance, all the 9:7 resonance angles librate. The resonance angles are defined as:

$$\begin{aligned}\phi_1 &= 9\lambda_2 - 7\lambda_1 - 2\varpi_1,\\ \phi_2 &= 9\lambda_2 - 7\lambda_1 - 2\varpi_2,\\ \phi_3 &= 9\lambda_2 - 7\lambda_1 - \varpi_1 - \varpi_2.\end{aligned} \tag{3.10}$$

where λ_1 and λ_2 are the mean longitudes while ϖ_1 and ϖ_2 are the longitudes of the pericenters of the inner and outer planets, respectively.

Denoting $\beta = \phi_3 - \phi_1$, we can calculate the rate of change of β in the form:

$$\frac{d\beta}{dt} = \frac{d\phi_3}{dt} - \frac{d\phi_1}{dt} = \frac{d\varpi_1}{dt} - \frac{d\varpi_2}{dt} \tag{3.11}$$

with the variation of the longitude of the pericenter given by [137]

$$\frac{d\varpi_1}{dt} = \frac{\sqrt{1-e_1^2}}{n_1 a_1^2 e_1}\frac{\partial R_1}{\partial e_1}, \qquad \frac{d\varpi_2}{dt} = \frac{\sqrt{1-e_2^2}}{n_2 a_2^2 e_2}\frac{\partial R_2}{\partial e_2} \tag{3.12}$$

where $R_1 = R_D G m_2/a_2$ and $R_2 = R_D G m_1/a_2$. Here R_D is the direct part of the disturbing function that can be expanded into the Fourier series in terms of λ_i and ϖ_i, $i = 1, 2$. To discuss the 9:7 resonance with $9n_2 \sim 7n_1$, we retain terms containing λ_1 and λ_2 only in the combination $\theta_j = 9\lambda_2 - 7\lambda_1$ in R_D. Thus the retained part of R_D takes the form of

$$R_D = \sum_{n,i} F_i^n \cos(n\theta_j - i\varpi_1 + (i-2n)\varpi_2) \tag{3.13}$$

where n is a non-negative integer and i is a positive or negative integer. By considering the terms up to fourth order in the eccentricity, the form of R_D is taken as (from Appendix A in [215])

$$\begin{aligned}R_D =& F_0^0 + F_1^0\cos(\varpi_2 - \varpi_1) + F_2^0\cos 2(\varpi_2 - \varpi_1) + F_2^1\cos(\theta_j - 2\varpi_1) +\\ & F_1^1\cos(\theta_j - \varpi_2 - \varpi_1) + F_0^1\cos(\theta_j - 2\varpi_2) + F_3^1\cos(\theta_j + \varpi_2 - 3\varpi_1) +\\ & F_{-1}^1\cos(\theta_j + \varpi_1 - 3\varpi_2) + F_4^2\cos(2\theta_j - 4\varpi_1) + F_3^2\cos(2\theta_j - 3\varpi_1 - \varpi_2) +\\ & F_2^2\cos(2\theta_j - 2\varpi_1 - 2\varpi_2) + F_1^2\cos(2\theta_j - \varpi_1 - 3\varpi_2) + F_0^2\cos(2\theta_j - 4\varpi_2)\end{aligned} \tag{3.14}$$

where

$$
\begin{aligned}
F_0^0 &= f_0 + (e_1^2 + e_2^2) f_2 + e_1^4 f_4 + e_1^2 e_2^2 f_5 + e_2^4 f_6, \\
F_1^0 &= e_1 e_2 f_{10} + e_1^3 e_2 f_{11} + e_1 e_2^3 f_{12}, \\
F_2^0 &= e_1^2 e_2^2 f_{17}, \\
F_2^1 &= e_1^2 f_{45} + e_1^2 e_2^2 f_{47} + e_1^4 f_{46}, \\
F_1^1 &= e_1 e_2 f_{49} + e_1^3 e_2 f_{50} + e_1 e_2^3 f_{12}, \\
F_0^1 &= e_2^2 f_{53} + e_1^2 e_2^2 f_{54} + e_2^4 f_{55}, \\
F_3^1 &= e_1^3 e_2 f_{68}, \\
F_{-1}^1 &= e_2^3 e_1 f_{69}, \\
F_4^2 &= e_1^4 f_{90}, \\
F_3^2 &= e_1^3 e_2 f_{91}, \\
F_2^2 &= e_1^2 e_2^2 f_{92}, \\
F_1^2 &= e_1 e_2^3 f_{93}, \\
F_0^2 &= e_2^4 f_{94}.
\end{aligned}
\tag{3.15}
$$

The forms of f_i and $f_{i,j}$ are presented in Appendix B of [137].

Substituting Equation (3.12) and Equation (3.13) into Equation (3.11), we obtain

$$
\begin{aligned}
\frac{d\beta}{dt} &= \frac{\sqrt{1-e_1^2}Gm_2}{n_1 a_1^2 a_2 e_1}\frac{\partial R_D}{\partial e_1} - \frac{\sqrt{1-e_2^2}Gm_1}{n_2 a_2^3 e_2}\frac{\partial R_D}{\partial e_2} \\
&= \sum_{n,i}\left[\frac{\sqrt{1-e_1^2}Gm_2}{n_1 a_1^2 a_2 e_1}\frac{\partial F_i^n}{\partial e_1} - \frac{\sqrt{1-e_2^2}Gm_1}{n_2 a_2^3 e_2}\frac{\partial F_i^n}{\partial e_2}\right]\cos\Psi_i^n
\end{aligned}
\tag{3.16}
$$

where $\Psi_i^n = n\theta_j - i\varpi_1 + (i-2n)\varpi_2 = (2n-i)\phi_3 - (n-i)\phi_1$. Considering that under the assumption of the self-similar migration, ϕ_1 and ϕ_3 librate respectively around π and zero and do not differ much from those values, we can set $d\beta/dt$ equal to zero. Our numerical calculations performed for the planets trapped in the 9:7 MMR confirmed the validity of this assumption. Thus Equation (3.16) changes to

$$
\sum_{n,i}\left(\frac{\sqrt{1-e_1^2}m_2}{n_1 a_1^2 a_2 e_1}\frac{\partial F_i^n}{\partial e_1}\right)\cos\Psi_i^n = \sum_{n,i}\left(\frac{\sqrt{1-e_2^2}m_1}{n_2 a_2^3 e_2}\frac{\partial F_i^n}{\partial e_2}\right)\cos\Psi_i^n. \tag{3.17}
$$

Making use of F_i^n given by Equation (3.15), applying the relation $n_1^2 a_1^3 = n_2^2 a_2^3$ to Equation (3.17) and retaining only the terms in eccentricities of the order not higher than two, we can write the following:

$$
\frac{m_2}{n_2 a_2 e_1}(2f_2 e_1 - f_{10} e_2 - 2f_{45} e_1 + f_{49} e_2) = \frac{m_1}{n_1 a_1 e_2}(2f_2 e_2 - f_{10} e_1 + f_{49} e_1 - 2f_{53} e_2) \tag{3.18}
$$

with f_i and $f_{i,j}$ having the form [137]

$$\begin{aligned}
f_2 &= \frac{1}{8}[-4j^2 + 2\alpha D + \alpha^2 D^2]A_j \\
f_{10} &= \frac{1}{4}[2 + 6j + 4j - 2\alpha D - \alpha^2 D^2]A_{j+1} \\
f_{45} &= \frac{1}{8}[-5j + 4j^2 - 2\alpha D + 4j\alpha D + \alpha^2 D^2]A_j \\
f_{49} &= \frac{1}{4}[-2 + 6j - 4j^2 + 2\alpha D - 4j\alpha D - \alpha^2 D^2]A_{j-1} \\
f_{53} &= \frac{1}{8}[2 - 7j + 4j^2 - 2\alpha D + 4j\alpha D + \alpha^2 D^2]A_{j-2}
\end{aligned} \tag{3.19}$$

where $D = d/d\alpha$ and $A_j = b^{(j)}_{\frac{1}{2}}(\alpha)$ which is the Laplace coefficient with the definition of

$$\frac{1}{2}b^{(j)}_s(\alpha) = \frac{1}{2\pi}\int_0^{2\pi} \frac{\cos j\psi d\psi}{(1 - 2\alpha\cos\psi + \alpha^2)^s}. \tag{3.20}$$

For the 9:7 resonance, we take $j = 9$ and $\alpha = a_1/a_2 = (7/9)^{2/3}$. Accordingly, we need to calculate $DA_7, D^2A_7, DA_8, D^2A_8, DA_9, D^2A_9, DA_{10}$ and D^2A_{10} to obtain the values of $f_i, f_{i,j}$ from Equation (3.19). The derivation of the Laplace coefficients DA_j and D^2A_j can be performed using the relations [194]

$$\begin{aligned}
DA_j &= Db^{(j)}_{\frac{1}{2}}(\alpha) = \frac{1}{2}(b^{(j-1)}_{\frac{3}{2}} - 2\alpha b^{(j)}_{\frac{3}{2}} + b^{(j+1)}_{\frac{3}{2}}) \\
D^2A_j &= D^2b^{(j)}_{\frac{1}{2}}(\alpha) = \frac{1}{2}(Db^{(j-1)}_{\frac{3}{2}} - 2\alpha Db^{(j)}_{\frac{3}{2}} + Db^{(j+1)}_{\frac{3}{2}} - 2Db^{(j)}_{\frac{3}{2}})
\end{aligned} \tag{3.21}$$

with

$$Db^{(j)}_{\frac{3}{2}}(\alpha) = \frac{3}{2}(b^{(j-1)}_{\frac{5}{2}} - 2\alpha b^{(j)}_{\frac{5}{2}} + b^{(j+1)}_{\frac{5}{2}}) \tag{3.22}$$

Therefore, the calculation of f_i and $f_{i,j}$ comes down to computing the values of the Laplace coefficients A_j numerically. The calculated values of the related A_j are given in Table 3.2.

Table 3.2: Numerical values of the Laplace coefficients

i	5	6	7	8	9	10	11	12
$b^{(i)}_{\frac{1}{2}}$	-	-	0.2215	0.1754	0.1395	0.1113	-	-
$b^{(i)}_{\frac{3}{2}}$	-	17.1391	15.1686	13.3629	11.7259	10.2538	8.9386	-
$b^{(i)}_{\frac{5}{2}}$	689.3854	649.2006	607.0159	563.9777	521.0064	478.8312	438.0032	398.9299

Placing the numerical values of the appropriate coefficients f_i into the Equation (3.18) we have

$$\frac{m_2}{n_2 a_2 e_1}(-35.4257e_1 - 39.9985e_2) = \frac{m_1}{n_1 a_1 e_2}(-42.819e_2 - 46.3847e_1). \tag{3.23}$$

Considering the case of the equal-mass planets captured in the 9:7 MMR, we set $m_1 = m_2$ and $(n_1/n_2)^2 = (a_2/a_1)^3 = (9/7)^2$ into Equation (3.23) and obtain the ratio of the eccentricities for the two equal-mass planets captured in the 9:7 MMR, which is $e_1/e_2 \sim 0.96$. It is important to stress here that this result has been derived retaining only the first order terms in eccentricity in Equation (3.17) and therefore it is valid for the planets on the low eccentricity orbits.

3.4.1.3 Libration width of the 9:7 resonance

In the case of the first-order resonance capture, the resonance angles may librate even when the period ratios differ significantly from the exact commensurability. For higher order resonances, the planets need to be much closer to the commensurability in order to observe the resonance angles to librate. The libration width for the 9:7 MMR for small eccentricities is given by [215]

$$|n_1/n_2 - 9/7| \sim 4.2 \times 10^{-5}(m_1/m_\oplus)(M_\odot/M_*) \tag{3.24}$$

For the system of planets with larger eccentricities, departures from the strict commensurability may be larger and the libration width can be estimated following the derivation given by [137] and reported in [215] for the 9:7 commensurability, in the form

$$|n_1/n_2 - 9/7| \sim 2.6 \times 10^{-3} \left(\frac{e_1}{0.1}\right) \sqrt{\left(\frac{m_1}{m_\oplus}\right)\left(\frac{M_\odot}{M_*}\right)}. \tag{3.25}$$

3.4.2 Capture into the 9:7 resonance: hydrodynamic simulations

Here we present our results of the hydrodynamic simulations of the evolution of two planets with $m_1 = m_2 = 3M_\oplus$ migrating convergently in the gaseous protoplanetary disk towards the 9:7 MMR. In this simulation, the disk parameters are adopted as follows: $\Sigma_0 = 2 \times 10^{-5}$ and $\nu = 1 \times 10^{-6}$. Considering two reasons mentioned in Section 3.2, the initial eccentricities of two planets are set to be $e_1 = 0.005$ and $e_2 = 0$ while the initial orbital period ratio of the planets is taken to be 1.2865, which is slightly larger than 9:7.

The evolution of the period ratio of two planets, their eccentricities e_1, e_2, the angle between the apsidal lines defined as $\Delta\varpi = \varpi_2 - \varpi_1$ as well as the resonance angles ϕ_1, ϕ_2 and ϕ_3 defined in Equation (3.10) are shown in Figure 3.2. We can see that after a short period of convergent migration with relative migration rate of $\dot{a}/a \sim 0.96$ Myr^{-1}, two planets arrive at the 9:7 resonance at $t \sim 1700$ yrs. After that, their period ratio oscillates around the 9:7 commensurability till the end of the calculation. When the resonance capture occurs, e_2 is excited from zero to 0.004 and then evolves together with e_1 showing similar behavior. In the final stage of the calculation, both eccentricities are oscillating around equilibrium values with e_2 slightly larger than e_1. At the same time, $\Delta\varpi$, ϕ_1 and ϕ_2 librate around π while ϕ_3 librates around zero. During the whole calculation, two planets migrate slowly without opening partial gaps in the disk.

The evolution of the disk surface density $\Sigma(r)$ is illustrated in Figure 3.3. The initial $\Sigma(r)$ defined as in Equation (3.3) is denoted by the dashed purple line. The profiles at $t = 1250$ yrs (green solid line) and $t = 15000$ yrs (yellow solid line), drawn in this figure, represent the disk surface density distributions before and after the resonance entrance. The positions of the planets are indicated by black solid circles. Comparing $\Sigma(r)$ in these two moments of time, we note that the surface density has decreased significantly at the latest time due to the viscous evolution and mass loss through the open boundaries of the computational domain. But this is not the case at the time when the planets are captured into the resonance.

As can be seen in Figure 3.3, the planets do not perturb the disk significantly during the evolution, meaning that there is no sign of the partial gaps formation along the planet's orbits.

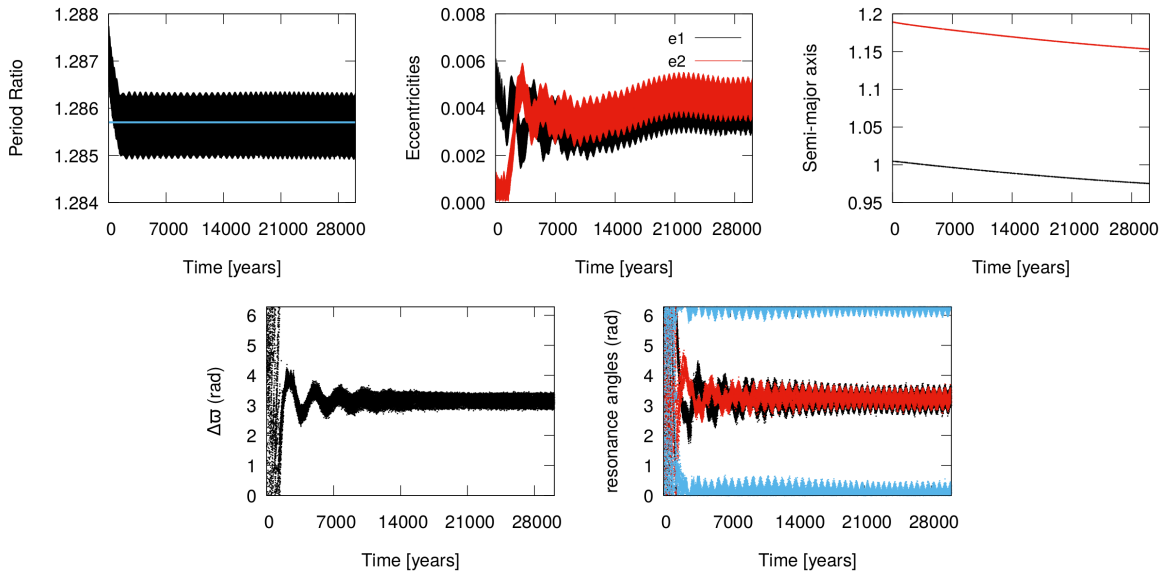

Figure 3.2: Results of the hydrodynamic simulation for the 9:7 resonance capture in the two equal low-mass planet system - The upper panels show, from left to right, the evolution of the period ratio, the eccentricities e_1, e_2 and the semi-major axes. The blue horizontal solid line in the upper leftmost panel shows the position of the 9:7 resonance commensurability. The lower panels show the evolution of $\Delta\varpi$ (left panel) and the resonance angles ϕ_1 (black), ϕ_2 (red) and ϕ_3 (blue) (right panel).

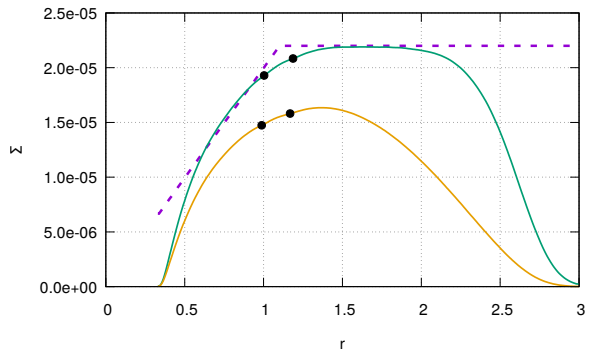

Figure 3.3: Evolution of the disk surface density in the simulation for the two equal low-mass planet system - The azimuthally averaged surface density profile of the disk at $t = 0$ (dashed purple line), $t = 1250$ yrs (green solid line) and $t = 15000$ yrs (yellow solid line) in the simulation shown in Figure 3.2. The black solid circles denote the positions of two planets.

Table 3.3: The parameters and migration times of two planets

Time (yrs)	planet	α_p	r_p	$\Sigma_p(r_p^2/M_*)$	$\tau_{\rm typeI}$ (Myr)	$\tau_{\rm fit}$ (Myr)
1250	Inner	-0.55	1.003	1.929×10^{-5}	0.89	0.90
	Outer	-0.31	1.187	2.084×10^{-5}	0.94	0.64
15000	Inner	-0.47	0.988	1.474×10^{-5}	1.09	1.02
	Outer	-0.29	1.168	1.581×10^{-5}	1.20	1.01
30000	Inner	-0.40	0.975	9.530×10^{-6}	1.67	1.31
	Outer	-0.18	1.153	1.005×10^{-5}	1.76	1.68
Averaged value	Inner	-	-	-	1.22	1.08
	Outer	-	-	-	1.30	1.11

This indicates that the migration of both planets should be in the regime of type I migration. It needs to be noticed that although the Lindblad torques are in the linear regime, the corotation torques are not [149]. When the corotation torques are unsaturated as expected here, they will be underestimated in a linear calculation. Nonetheless, the migration rates obtained in the linear calculation should be correct to order of magnitude unless there is a near balance between corotation and Lindblad torques [149].

To verify that, we calculate the timescale for type I migration $\tau = r_p/(-\dot{r_p})$ in the linear regime according to [197],

$$\tau = (2.7 + 1.1\alpha)^{-1} \frac{M_*}{M_p} \frac{M_*}{\Sigma_p r_p^2} \left(\frac{c_s}{r_p \Omega_p}\right)^2 \Omega_p^{-1} \tag{3.26}$$

where α is the slope of the disk surface density profile defined as $\Sigma \propto r^{-\alpha}$, Ω_p denotes the angular velocity and Σ_p is the value of the disk surface density at the planet's position r_p. The values of α, r_p and Σ_p for two planets obtained at $t = 1250, 15000$ and 30000 yrs in the simulation are given in Table 3.3, together with the type I migration time $\tau_{\rm typeI}$ for each planet calculated according Equation (3.26). Besides that, at the same moments of time, we evaluate the migration time $\tau_{\rm fit} = a_i/(-\dot{a_i})$ (i=1, 2 for inner and outer planet respectively) by fitting the results of the calculations in the 100 yrs intervals around each of those three moments of time. The migration times obtained in this way are also given in the table. Comparing the values in the last row of Table 3.3, we conclude that the migration time from our numerical simulations are reasonably close to the values calculated from Equation (3.26), which indicates that the planets indeed migrate in the type I regime.

The relation between migration rates and eccentricities of two planets captured in a resonant configuration has been derived and is given in Equation (3.9). For the comparison with the results predicted by the semi-analytic considerations, we need to measure the values of e_1, e_2 as well as τ_c, τ_{mig} for each planet in the simulation and then check if they satisfy the relationship provided in Equation (3.9). First, we obtain $a_1 = 0.992$, $a_2 = 1.17308$, $e_1 = 0.00265$ and $e_2 = 0.00326$ from the simulation after $t = 11000$ yrs when the planets are already in the 9:7 resonance. Then, we measure the $\tau_{c,i} = -e_i/\dot{e_i}$ and $\tau_{mig,i} = -2a_i/\dot{a_i}$ for each planet by fitting the numerical results in the interval of $t = 11000 \pm 100$ yrs, which gives $\tau_{c,1} = 4.70 \times 10^3$ yrs, $\tau_{c,2} = 3.39 \times 10^3$ yrs, $\tau_{mig,1} = 1.75 \times 10^6$ yrs and $\tau_{mig,2} = 1.64 \times 10^6$ yrs. By inserting these

numbers into the two sides of Equation (3.9), we get 5.41×10^{-4} and 5.70×10^{-4} for the left and right hand sides, respectively. The comparison shows that the relation between those parameters in the simulation is consistent with the one predicted in the semi-analytic approach.

Next we compare the ratio of the eccentricities of two planets in the simulation with the value predicted by Equation (3.17). In the final stage of the simulation, we can see that ϕ_1 librates around π and ϕ_3 librates around zero while the final values of e_1 and e_2 are very close to zero. As derived before, for such case with $m_1 = m_2$ and very small eccentricities, the ratio of eccentricities of two planets is expected to be $e_1/e_2 \sim 0.96$, which is in a good agreement with the result of the simulation.

To summarize, we have demonstrated that, in this simulation, two equal-mass super-Earths are trapped into the 9:7 MMR after a short period of convergent migration in the protoplanetary disk with $\Sigma_0 = 2 \times 10^{-5}$ and $\nu = 1 \times 10^{-6}$. Moreover, the behaviors of their orbital parameters in the 9:7 MMR are consistent with our expectations based on the semi-analytic solution. Now, we are very well prepared to run a series of simulations by adopting various disk parameters to investigate the conditions of the 9:7 resonance capture.

3.5 Conditions for the 9:7 resonance capture

In this section we explore the conditions for the 9:7 resonance capture in a system of two equal-mass planets with $m_1 = m_2 = 3M_\oplus$ migrating in a protoplanetary disk. For that aim, we analyze the orbital evolution of two planets in a series of simulations performed with the different disk parameters Σ_0, ν and/or initial positions of planets.

In those simulations, the orbital evolution of two planets embedded in the disk is followed for a period of time longer than the time needed for the planets to arrive at the 9:7 resonance from their initial positions. Two different results are expected: the planets can be captured in the resonance or pass through it (hereafter dubbed as "capture" and "fail" cases, respectively). It is possible that not all of the resonance capture in our "capture" cases are permanent since we do not continue our simulations for sufficiently long time to check it. Therefore, the conclusions obtained here based on our simulations are valid for the planets being trapped into the 9:7 MMR at least temporarily.

3.5.1 A 9:7 resonance survey

We calculate the orbital evolution of two planets migrating in the protoplanetary disks starting from the same initial configuration adopted in the typical simulation shown in Section 3.4.2, namely the initial period ratio of 1.2865, $e_1 = 0.005$ and $e_2 = 0$. We run 82 simulations by taking the surface density scaling parameter Σ_0 in the range of $[2 \times 10^{-5}, 6 \times 10^{-5}]$ and the viscosity ν in the interval of $[10^{-6}, 10^{-5}]$. The results of these simulations are illustrated in a form of a map in the top panel of Figure 3.4 in which the "capture" and "fail" cases are denoted by the black solid and empty circles, respectively. The value of Σ_0 adopted in each simulation is shown in the horizontal axis while that of ν is indicated by the line, with the given color, which connects all the circles, for which the same value of viscosity has been used in the calculations (see the legend in the figure).

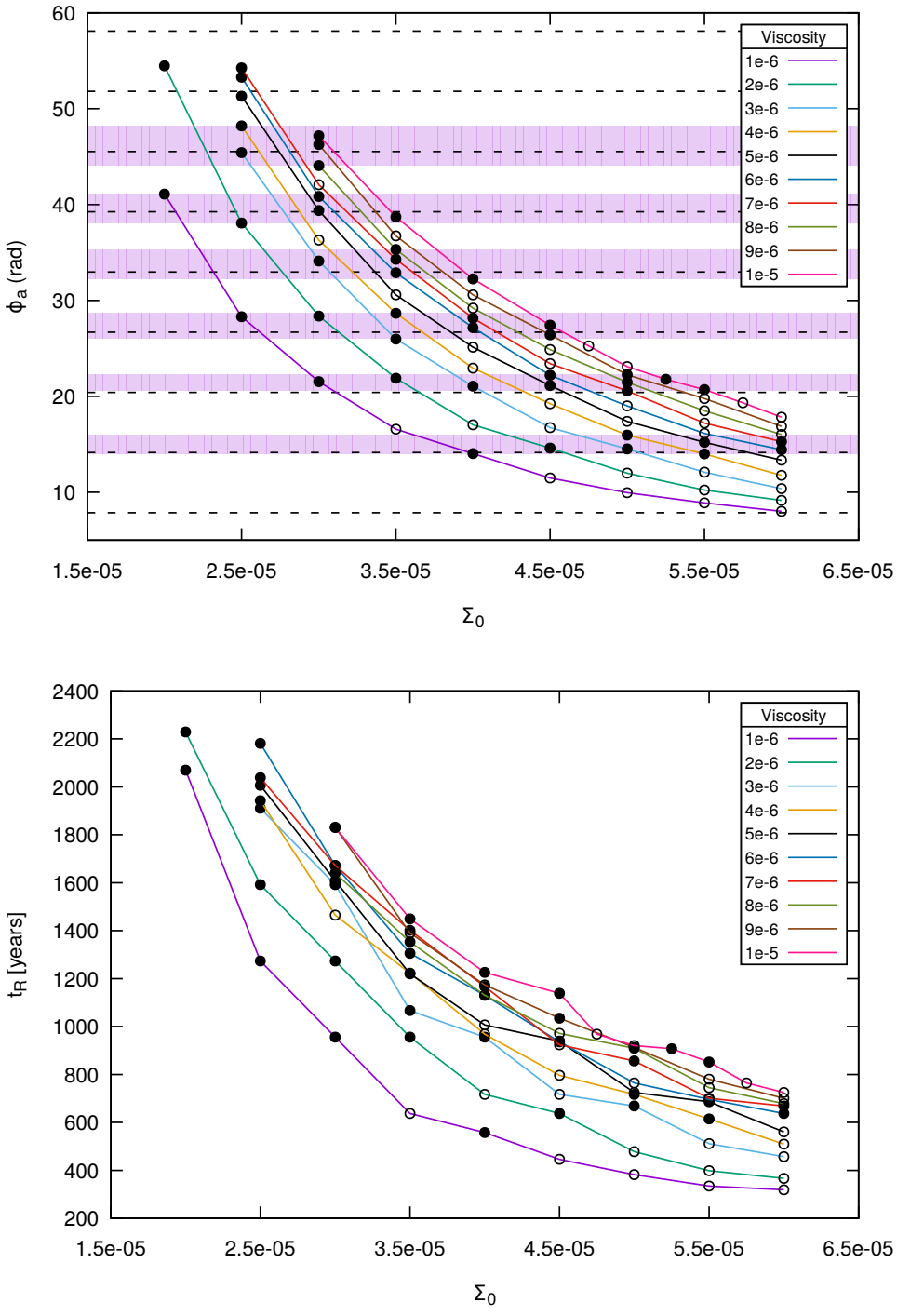

Figure 3.4: A 9:7 resonance survey for a system of two equal low-mass planets - Top: the accumulated resonance angle ϕ_a obtained by adopting different Σ_0 and ν in the simulations. The black solid and empty circles indicate the "capture" and "fail" cases, respectively. The dashed horizontal lines indicate the positions of ϕ_a with $\phi_{\rm entry} = 3\pi/2$. Bottom: The results of the same simulations showed in top panel, but now instead of plotting the surface density on the vertical axis we give the time in which the planets travel from the initial location to the entrance of the 9:7 resonance, t_R. (The data for drawing this figure are given in Table A.1.) See text for more details.

The most interesting quantity in the map, and at the same time somewhat intriguing, placed on the vertical axis, is ϕ_a - the accumulated resonance angle. We introduce this completely new quantity to describe a particular regularity observed in our calculations, connected with the resonance angles and the time of the arrival at the commensurability. There was no better way to express what we saw in the simulations. The idea to define such a quantity was inspired by the paper of [62] about the 3:1 resonance. The definition of the accumulated resonance angle is as follows:

$$\phi_a = 2\pi N_{\mathrm{rot}} + (2\pi - \phi_{\mathrm{entry}}) \tag{3.27}$$

where ϕ_{entry} is the value of ϕ_1 at the moment when planets enter into the 9:7 MMR and N_{rot} is a number of full rotations from zero to 2π performed by the resonance angle ϕ_1 in the period of time starting from the beginning of the simulation till the arrival of planets at the 9:7 MMR. The time of arrival at the 9:7 resonance is determined as the moment in which the resonance angles begin to librate. It happens when the period ratio reaches the upper boundary of the libration width of the 9:7 resonance (see Section 3.4.1). According to Equation (3.24), the libration width of the 9:7 MMR for low mass planets with small eccentricities ($e_1 \lesssim 0.003$) can be calculated as $P_2/P_1 - 9/7 \sim 1.26 \times 10^{-4}$. This implies that ϕ_1 should start to librate when the period ratio of planets reaches the value 1.2858.

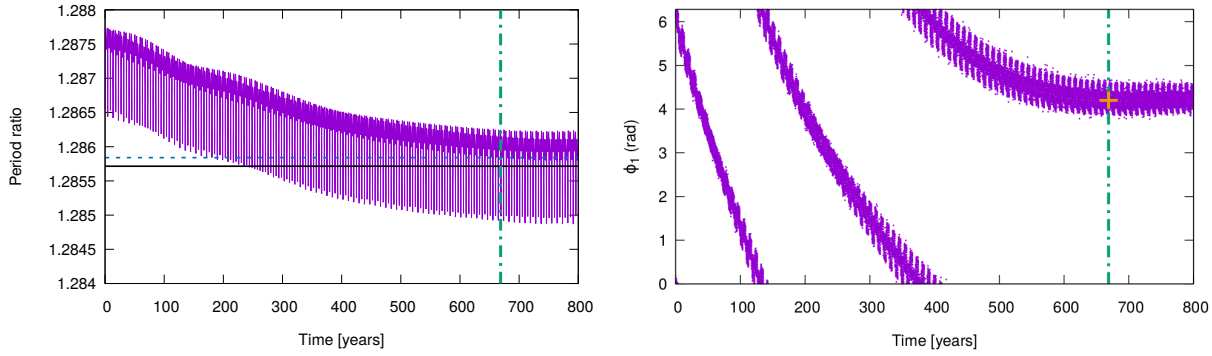

Figure 3.5: An example for calculating ϕ_a - Evolution of period ratio (left panel) and ϕ_1 (right panel) in the simulation with $\Sigma_0 = 4.5 \times 10^{-5}$ and $\nu = 2 \times 10^{-6}$. The dashed blue horizontal line in left panel denotes the position of $P_2/P_1 = 1.2858$. The dashed-dotted green vertical line in both panels represents the time when the period ratio is equal to 1.2858. The orange cross in the right panel indicates the value of ϕ_{entry} in this simulation.

The best way, to understand how the ϕ_a has been constructed and calculated, is to give an example. Let's take the results of the calculation with $\Sigma_0 = 4.5 \times 10^{-5}$ and $\nu = 2 \times 10^{-6}$ for that purpose. The evolution of the period ratio and the resonance angle ϕ_1 in this simulation are shown in Figure 3.5. The upper limit of the libration width of the 9:7 MMR ($P_2/P_1 = 1.2858$) is represented by the dashed blue horizontal line in the left panel. The period ratio of the evolving planets gets this particular value at the time indicated in the same panel by the dashed-dotted green vertical line, which is the time of the entrance to the resonance. Now, we would like to find out what is the value of ϕ_1 at the entrance time. To achieve that, we can simply draw the evolution in time of the resonance angle in this calculation as it is shown in right panel of Figure 3.5 and read the value (denoted by the orange cross in the right panel) at the time

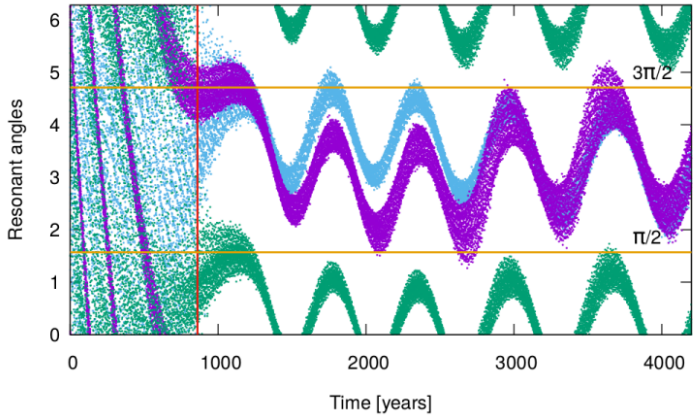

Figure 3.6: Evolution of the 9:7 resonance angles when arriving at the 9:7 MMR - Evolution of the 9:7 resonance angles ϕ_1 (violet), ϕ_2 (blue) and ϕ_3 (green) in the simulation with $\Sigma_0 = 5 \times 10^{-5}$ and $\nu = 7 \times 10^{-6}$. The red vertical line indicates the time when the period ratio of planets reaches the value of 1.2858.

indicated by the dashed-dotted green vertical line (the same in both, left and right panels). The value of ϕ_1 at the entrance time we call $\phi_{\rm entry}$. Before reaching the entrance to the resonance, the ϕ_1 has performed two full rotations from zero to 2π, so this gives $N_{\rm rot} = 2$. According to Equation (3.27), the accumulated resonance angle in this simulation is equal to $\phi_a = 14.65$ *rad*.

To illustrate a general picture of the evolution of the resonance angles when the planets entering into the resonance, we show the results for a "capture" case in the simulation with $\Sigma_0 = 5 \times 10^{-5}$ and $\nu = 7 \times 10^{-6}$ in Figure 3.6. The time necessary for the period ratio of planets reaching 1.2858 is indicated by the red vertical line in the figure. We can see that when the planets arrive at the upper boundary of the 9:7 MMR, ϕ_1 (denoted by the violet dots) started to librate around $3\pi/2$, which is just the value of $\phi_{\rm entry}$ in this case. However, along with the time evolution, the libration center of ϕ_1 moves to the value π, so the libration center is not necessarily the same as $\phi_{\rm entry}$. In addition, we also note that when the resonance capture occurs, the other resonance angles ϕ_2 and ϕ_3 begin to librate together with ϕ_1.

Following Equation (3.27), we calculate the values of ϕ_a in all 82 simulations and illustrate the results in the top panel of Figure 3.4. It can be seen that the values of ϕ_a for the "capture" cases are distributed in the particular regions indicated by the violet stripes in the (Σ_0, ϕ_a) plane. We emphasis that the "capture" cases located in the same violet stripe region have ϕ_a with the same value of $N_{\rm rot}$. From the bottom stripe to the top one, $N_{\rm rot}$ increases from 2 to 7. We do not draw in this figure the violet stripe region for the "capture" cases which have $\phi_a > 50$ with $N_{\rm rot} = 8$, because the number of simulations is not sufficient to infer the width of this region in a satisfactory way. It can be noticed that the resonance capture occurs most likely if the value of $\phi_{\rm entry}$ is close or equal to $3\pi/2$. This can be inferred from the fact that the dashed black lines indicating the positions of ϕ_a with $\phi_{\rm entry} = 3\pi/2$ are located inside or close to the boundary of the violet stripe regions. The violet stripe regions contain those pairs (Σ_0, ϕ_a) for which the capture into the 9:7 resonance is going to happen. However, we cannot say that the resonance capture is certain if ϕ_a for the evolving pair of planets is placed in these regions.

This limitation is due to the finite resolution of sampling in the parameter space, which can be done in such a survey. More simulations could reveal that the stripe regions are not continuous, but they contain the whole structure of the much narrower regions. This point requires further studies.

From the top panel of Figure 3.4, we also notice that with larger values of ϕ_a, the capture regions are wider, although again one should be aware of the fact that the statistics is not high. When ϕ_a is large enough, the capture regions could span the whole range of angles from zero to 2π and the probability of the resonance capture becomes 100%. Such situation corresponds to orbital evolution of two planets with a very low relative migration rate. On the other hand, we do not find any capture regions with $\phi_a < 13.33$ in the map. In those cases, the relative migration rate of the planets is quite high and the capture probability is rather low or even zero. However, as already pointed out we cannot exclude the situation that there are some very narrow capture regions which cannot be seen in this map due to the limited sampling resolution in this survey.

On the basis of the results shown in the top panel of Figure 3.4, it is possible to predict with high probability the outcome of the simulations, namely whether the planets will be locked or not into the 9:7 resonance, using the values of accumulated resonance angle, which can be translated into the disk parameters, such as Σ_0 and ν.

Introducing the new quantity, namely the accumulated resonance angle, we have stated that we could not find any better way to describe what we saw in the calculations. In fact, we did make quite a lot of thoughts about it and we even try another quantity, to get more robust picture of the 9:7 resonance capture. However, the results were not as good as what we have just presented. We illustrate this point giving a specific example. In the bottom panel of Figure 3.4 we show how our map in (Σ_0, ϕ_a) will change if we replace ϕ_a with t_R that denotes the time when the planets enter into the 9:7 MMR. The picture looks qualitatively similar, however, although there is a tendency that the time t_R increases with the viscosity, the regularity is not as clear as that observed in the map with ϕ_a shown in the top panel. Moreover, there is no information directly related to the resonance angles, and the regions with "capture" cases appear distorted.

The results presented in Figure 3.4 can also be discussed in terms of dynamical parameters that describe the orbital evolution of planets in a protoplanetary disk due to disk-planet interactions, namely the relative migration rate and the circularization rate. They are defined as $\dot{a}/a = \dot{a_1}/a_1 - \dot{a_2}/a_2$ and $-\dot{e_1}/e_1$ respectively, where a_1, a_2 are the semi-major axes of the inner and outer planets and $a = a_2/a_1$. We determine the initial values of these quantities by fitting the numerical results in the early stage of the evolution in the time interval [0, 160] yrs. Since the initial values of the relative migration rate $\dot{a}/a$ and the circularization rate $-\dot{e_1}/e_1$ are determined by the disk parameters of Σ_0 and ν, the results of the simulations also can be expressed in terms of these two physical quantities.

In order to facilitate the comparison with Figure 3.4, we present the relative migration time $T_m = a/\dot{a}$ and the circularization time $T_e = -e_1/\dot{e_1}$ on the vertical and horizontal axes instead of the relative migration rate and the circularization rate. The relations between the disk parameters (Σ_0, ν), T_m, T_e and the accumulated resonance angle ϕ_a in the results of the simulations are illustrated in Figure 3.7. The values of ν adopted in the simulations are indicated

by those curves with different colors as in Figure 3.4. The solid and empty circles represent the "capture" and "fail" cases, respectively. The circles which are plotted on the same grey curve show the results of simulations by adopting the same values of Σ_0. From the right to left, the value of Σ_0 increases from 2×10^{-5} to 6×10^{-5}.

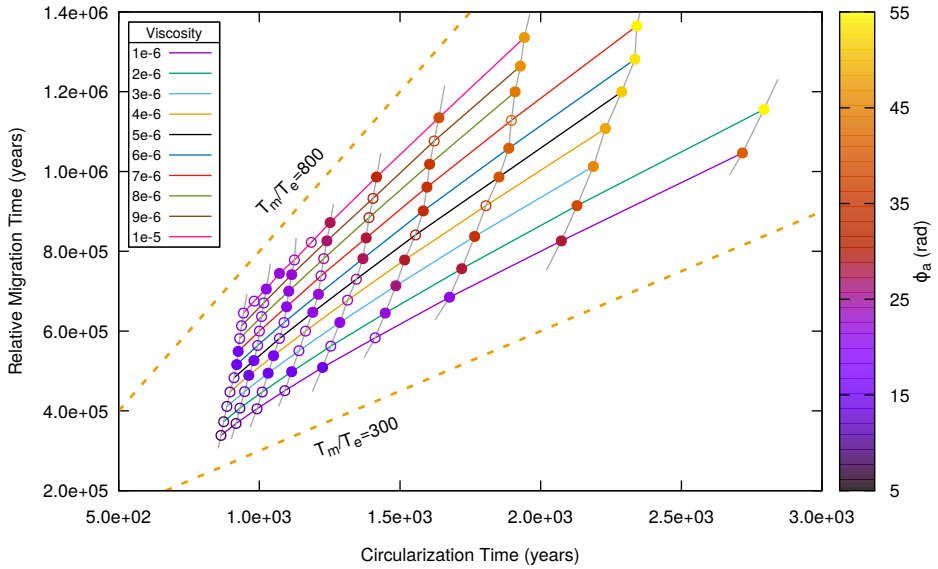

Figure 3.7: Dynamical parameters in the early stage of the simulations in the 9:7 resonance survey - The value of ϕ_a, the circularization time $T_e = -e_1/\dot{e}_1$ and the relative migration time $T_m = a/\dot{a}$ obtained in the simulations shown in Figure 3.4. The value of ν adopted in the simulations is indicated by the different colors of the curves. The circles connected by the same grey curve represent the simulations with the same Σ_0. From right to left, the values of Σ_0 increases from 2×10^{-5} to 6×10^{-5}]. (The data for drawing this figure are given in Table A.1.)

From the results shown in Figure 3.7, we find that in the disk with higher surface density and lower viscosity, the values of T_e and T_m for evolving planets are smaller, which means that $-\dot{e}_1/e_1$ and $\dot{a}/a$ are larger. Moreover, there is no "capture" case in the regime with $T_m < 0.48$ Myrs, which corresponds to the relative migration rate larger than 2.07 Myr^{-1}. When T_m is in the range of $[0.49, 0.55]$ Myrs, we obtain 8 "capture" cases with $2.8 < \phi_{\rm entry} < 4.8$, which are located in the first bottom "capture" region of ϕ_a in the top panel of Figure 3.4. Besides that, other wider regions of ϕ_a for the "capture" cases can be found in particular regimes with low relative migration rates and circularization rates. It can be noticed that the occurrence of 9:7 resonance depends on both T_m and T_e instead of only one of them.

To see how the $\phi_{\rm entry}$ depends on the relative migration rate and the circularization rate in the survey, we draw the $\phi_{\rm entry}$ as a function of these two dynamical parameters in two panels of Figure 3.8. The location of $\phi_{\rm entry} = 3\pi/2$ is denoted by a dashed horizontal line in each panel. In the left panel, we find that for the specific values of the relative migration rate, the "capture" cases are located in the particular region. Moreover, the width of this region is narrower for simulations with higher relative migration rates. Since the planets arrive at the 9:7 MMR sooner with larger relative migration rate $\dot{a}/a$, the accumulated resonance angle ϕ_a is directly determined by this quantity. As a result, the value of ϕ_a is larger in the simulations

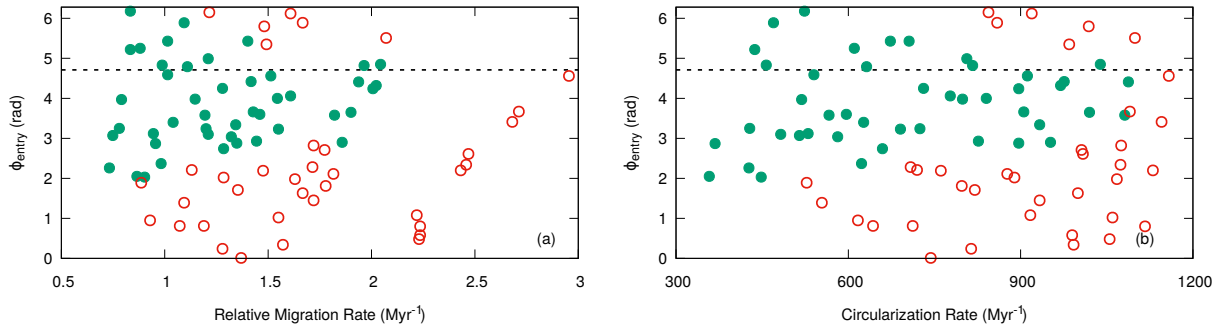

Figure 3.8: Relation between $\phi_{\rm entry}$ and dynamical parameters in the 9:7 resonance survey - The values of $\phi_{\rm entry}$ as a function of relative migration rate and circularization rate for simulations in the 9:7 survey are illustrated in the left and right panels, respectively. The green solid circles indicate "capture" cases while the red empty circles represent "fail" cases. The position of $3\pi/2$ is indicated by the dashed horizontal line in two panels. (The data for drawing this figure are given in Table A.1.)

with lower relative migration rate, which favor the capture into the 9:7 resonance. A similar trend can also be observed in the right hand panel of Figure 3.8, which shows that the "capture" region becomes smaller with the increased circularization rate. Therefore, we infer that capture into the 9:7 resonance can occur with $\phi_{\rm entry}$ in a region whose range should depend on both $\dot{a}/a$ and $-\dot{e_1}/e_1$.

3.5.2 Comparison to semi-analytic models and N-body calculations

Considering a restricted three-body problem, the capture probability for a second-order resonance has been obtained in [138]. In their study, for a system composed of an inner test particle and an outer planet, the eccentricity of the inner test particle e_1 and the relative migration rate $\dot{a}/a$ are rescaled to dimensionless quantities according to

$$J_1 = k \left(\frac{m_2}{M_\oplus}\right)^{-1} \left(\frac{M_*}{M_\odot}\right) e_1^2 \quad \text{and} \tag{3.28}$$

$$\dot{\beta} = l \left(\frac{m_2}{M_\oplus}\right)^{-2} \left(\frac{M_*}{M_\odot}\right)^{3/2} \left(\frac{a_1}{1\text{AU}}\right) \left(\frac{a_2}{1\text{AU}}\right)^{1/2} \left(\frac{\dot{a}/a}{\text{Myr}^{-1}}\right). \tag{3.29}$$

For the 9:7 resonance capture, $k = 125717$ and $l = 143.877$. In addition, the rescaled dimensionless quantities for an unrestricted two-planet system are also given as (in the Appendix A2 in [138])

$$J_1' = \frac{3[(2-j)^2 + (m_1/m_2)\alpha_0^2 j^2]}{32(m_2/M_*)\alpha_0 f_{45}} e_1^2 \tag{3.30}$$

$$\dot{\beta}' = \frac{3(j-2)a_1^{1/2}(\dot{a}/a)}{16(m_2/M_*)^2 \alpha_0^2 f_{45}^2} \tag{3.31}$$

where $j = 9$, $\alpha_0 = (7/9)^{2/3}$ and $f_{45} = 14.3866$ for the 9:7 resonance. Here e_1 represents the inner planet's eccentricity.

We would like to compare the results of our hydrodynamic simulations in the 9:7 resonance survey (in which $m_1 = m_2 = 3M_\oplus$, the initial eccentricities $e_1 = 0.005$ and $e_2 = 0$) to the results of the 9:7 resonance capture in a restricted three-body problem considered in [138] (shown in the right panel of Figure 1.3). To do that, first we calculate J_1' and $\dot{\beta}'$ for each simulation in our survey by taking the values of the eccentricities and the relative migration rates at the time when the planets enters into the 9:7 MMR. Next we assume the equivalences $J_1' \equiv J_1$ and $\dot{\beta}' \equiv \dot{\beta}$, and then obtain new values of e_1 and $\dot{a}/a$ from Equation (3.28) and Equation (3.29). In this way the eccentricity e_1 and relative migration rate $\dot{a}/a$ in our simulations are rescaled to be able to compare with those in a system consisting of a planet and a test particle in [138].

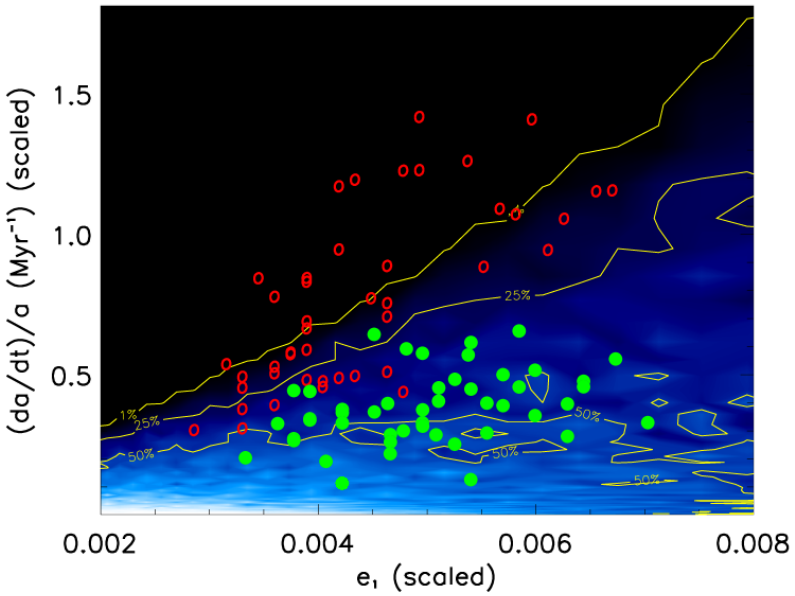

Figure 3.9: Comparison of the capture probabilities obtained in our hydrodynamic simulations and in the restricted three-body approach - Results of simulations with the initial $e_1 = 0.005$ and $e_2 = 0$ presented in the (rescaled eccentricity, rescaled relative migration rate) plane. The green solid and red open circles represent the "capture" and "fail" cases respectively. The contour plot shows the capture probability for the 9:7 resonance in a system of a test particle and planet with mass of $3M_\oplus$, which is taken from [138]. The contour lines for 1%, 25% and 50% are indicated by yellow lines.

We draw the results of our simulations for the 9:7 resonance survey with the rescaled e_1 and $\dot{a}/a$ on the contour plot showing the 9:7 resonance capture probability given in [138] obtained in a restricted three-body problem with the mass of the outer planet to be $3M_\oplus$ and the mass of the central star equal to the mass of the Sun. The contour plot for the capture probability obtained in their study is presented in Figure 3.9 in which the regions with capture probability of 50%, 25% and 1% are indicated by yellow contour lines. The results of our hydrodynamic simulations are represented by green solid and red open circles, which indicate the "capture" and "fail" cases, respectively. From the figure, we can see that all "capture" cases are located inside the region with capture probability larger than 1%. Moreover, all except one of them are inside the region with the capture probability larger than 25%. We also found that when the

rescaled relative migration rate is higher than 0.7 Myr^{-1}, the planets pass through the resonance in the simulations. In the region with low relative migration rate (rescaled $\dot{a}/a < 0.7\mathrm{Myr}^{-1}$), planets are captured into the 9:7 MMR more easily if their eccentricity is higher. Based on this comparison, we confirm that the results of our survey by using hydrodynamic simulations are consistent with the results illustrated in the contour plot for the second-order resonance capture probability obtained in [138].

The conditions for a second-order resonance capture in a system of two comparable low mass planets have been investigated in [217]. According to the analysis based on a restricted three-body problem, for the capture into a second-order resonance to happen, the migration timescale T'_m, the eccentricity damping timescale T'_e and the eccentricity of the inner planet, when enters the resonance, e_0 must satisfy:

$$T'_e \gtrsim \frac{P_1}{8\pi\mu}, \quad T'_m \gtrsim \frac{P_1}{8\pi\mu^2}\ln\frac{\mu}{e_0^2}, \quad e_0 \lesssim \mu^{1/2} \tag{3.32}$$

where $T'_e = T_{e,1} = -e_1/\dot{e_1}$ and $T'_m = 1/(1/T_{m,2} - 1/T_{m,1})$ with $T_{m,i} = -(\dot{a_i}/a_i + 2e_i^2/T_{e,i})^{-1}$. Here $T_{e,i}$ is the circularization time for planet i, with $i = 1, 2$ denoting the inner and outer planets respectively and $\mu = (m_1 + m_2)/M_*$. Inserting the values of the parameters adopted in our simulations into Equation (3.32), we obtain the conditions for the resonance capture to be $T_e \gtrsim 2.2 \times 10^3$ yrs, $T_m \gtrsim 3.3 \times 10^8$ yrs and $e_0 \lesssim 0.0042$. Comparing with the results shown in Figure 3.7, we can see that the relative migration rates in our simulations for the 9:7 resonance survey are much higher than the conditions derived in [217]. According to their conclusion, the resonance capture in our simulations are not expected to be certain, which is consistent with the results of our survey.

As we mentioned before, considering the orbital circularization due to disk-planet interactions, a second-order resonance capture requires non-zero initial eccentricities. Therefore, we can determine what is the minimal initial value of the eccentricity for the resonance capture to occur in our simulations. Based on the results of the calculations by taking the initial $e_2 = 0$ and different values of e_1, the minimum initial value of e_1 for which we obtained the 9:7 resonance capture was 0.002. In the simulation with initial $e_1 = 0.001$, the planets pass through the 9:7 resonance, because e_1 decreases to the value very close to zero before the planets arrive at the resonance. In other words, the initial eccentricity did not survive the planet journey from the initial position to the entrance of the resonance, or to put it differently, the initial eccentricity of the inner planet orbit lost against circularization.

3.5.3 Dependence of the 9:7 resonance capture on the initial orbit of outer planet

In all simulations included in the 9:7 resonance survey discussed in Section 3.5.1, our calculations start from the same planet configuration, namely the initial positions of inner and outer planets are taken to be $r_1 = 1$ and $r_2 = 1.18885$. In order to obtain a more general picture of 9:7 resonance capture, we investigate whether and how the outcome of our simulations depends on the initial configuration. For that purpose, we present here the results of the simulations with the same disk and planet parameters as before but different initial location of the outer planet,

r_2. We choose three simulations from the survey which are the "capture" cases with the adopted disk parameters given in Table 3.4. For each case we recalculate the orbital evolution of the planets starting from various initial values of r_2. In order to maintain the relative migration rate and circularization rate similar to the values in the previous simulations, we change the initial value of r_2 in a small range of distances around its original value, that is [1.18865, 1.18915].

Table 3.4: Disk parameters adopted in selected simulations from the 9:7 resonance survey

Case	Σ_0	ν	color
1	4×10^{-5}	3×10^{-6}	Purple
2	5.5×10^{-5}	4×10^{-6}	Green
3	4.5×10^{-5}	5×10^{-6}	Blue

The results of the simulations starting from the different r_2 are presented in Figure 3.10. The solid and empty circles indicate the "capture" and "fail" cases. The colors of the circles show the results of the simulations with the disk parameters given in Table 3.4). The red dashed-double dotted line indicates the initial r_2 adopted in the previous simulations and thus three points located on this line represent the outcome of the original simulations from the survey (the purple and blue points on the red dashed-double dotted line overlap each other). In this figure, we also draw the capture regions of ϕ_a indicated by the violet regions which are identical to those in Figure 3.4.

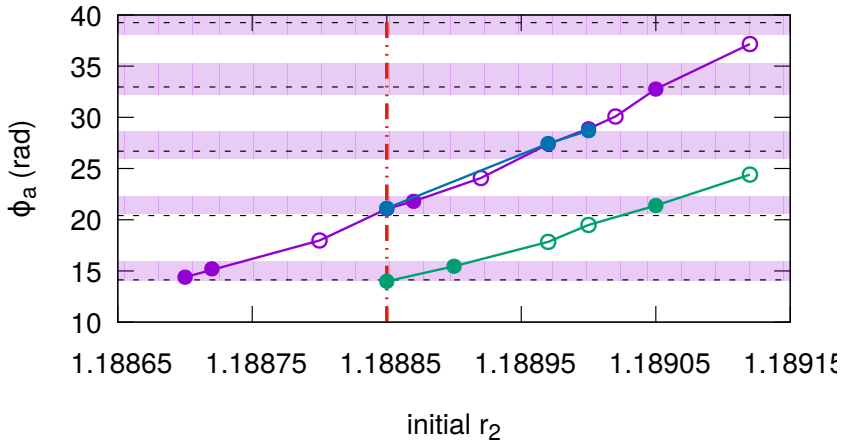

Figure 3.10: Results of simulations with different initial position of the outer planet - Changes of the accumulated resonance angle ϕ_a depending on the initial orbital radius of the outer planet r_2 for three simulations with the disk parameters shown in Table 3.4. The solid and empty circles represent the "capture" and "fail" cases, respectively. The violet strips indicate the capture regions as shown in Figure 3.4. The red dashed-double dotted vertical line denotes the initial $r_2 = 1.18885$ as adopted in the simulations in the 9:7 resonance survey.

As can be seen in Figure 3.10, for the same disk parameters, the values of ϕ_a increases (decreases) with larger (smaller) values of the initial r_2. It is not surprising that the values of ϕ_a in the new simulations are different from that obtained in the original ones, because the values

of ϕ_{entry} and N_{rot} have changed due to the different initial r_2 adopted in the simulations. This dependence of ϕ_a on r_2, in principle, could influence our results. However, it is easy to noticed that the solid circles are located in the violet regions, determined in the 9:7 resonance survey given in Figure 3.4, and the open ones are placed in between. It means that the outcome of the simulations is exactly as predicted, namely if the ϕ_a has a value lying inside one of the violet stripes than the resonance capture will take place, otherwise the planets will pass through the resonance. We can say even more, as from the results of the new simulations for case 1 (purple) and case 3 (blue), we note that the relation between ϕ_a and r_2 is very similar. This leads to the conclusion, that for other simulations with the same accumulated resonance angle but different disk parameters, the results should have the same dependence on r_2.

3.5.4 Trajectories in the ($e_1\cos\phi_1$, $e_1\sin\phi_1$) plane

In the framework of the restricted three-body problem, the particle's Hamiltonian curve can be drawn in the ($\sqrt{2\Phi}\cos\phi$,$\sqrt{2\Phi}\sin\phi$) plane, where $\sqrt{2\Phi}$ is a scaled eccentricity of the particle and ϕ is its resonance angle [137]. Similarly, we consider the case of a 9:7 resonance capture for two equal-mass planets and plot the trajectory in the ($e_1\cos\phi_1$, $e_1\sin\phi_1$) plane in order to describe the motion of the inner planet undergoing the 9:7 resonance capture during its migration.

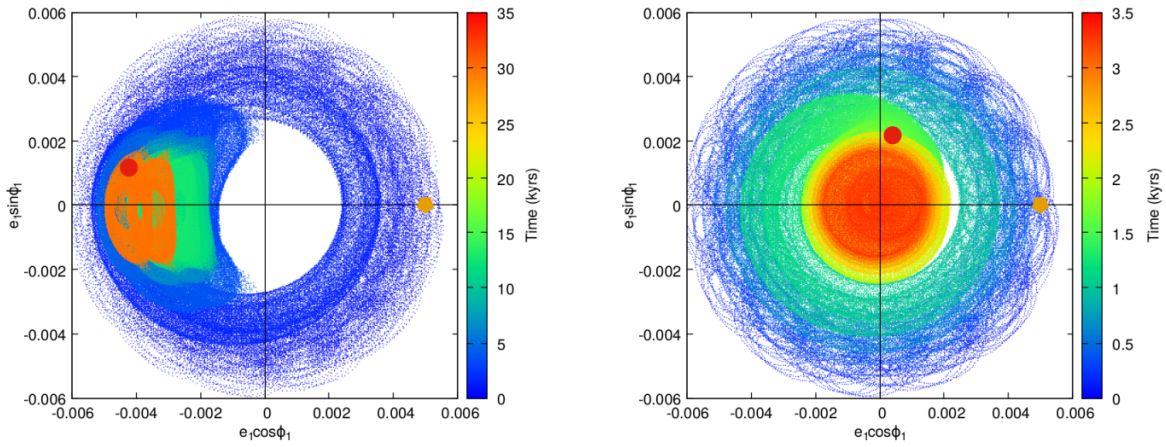

Figure 3.11: Trajectories in the ($e_1\cos\phi_1$, $e_1\sin\phi_1$) plane in a "capture" and "fail" cases in the 9:7 resonance survey - The left panel shows the track in the simulation with $\Sigma_0 = 2\times10^{-5}$ and $\nu = 1\times10^{-6}$ while the right panel in the simulation with $\Sigma_0 = 3\times10^{-5}$ and $\nu = 4\times10^{-6}$. The orange pentagons denote the initial positions of the system and the red circles indicate the positions when the systems arrive at the 9:7 MMR.

We choose two simulations from the 9:7 resonance survey and draw the trajectory in the ($e_1\cos\phi_1$, $e_1\sin\phi_1$) plane in Figure 3.11. The left panel shows the track of the inner planet in a "capture" case with $\Sigma_0 = 2\times10^{-5}$ and $\nu = 1\times10^{-6}$ while the right panel presents a "fail" case with $\Sigma_0 = 3\times10^{-5}$ and $\nu = 4\times10^{-6}$. In both simulations we take the initial $e_1 = 0.005$ and $\phi_1 = 0$, that is why the track of the inner planet starts from the position $(0.005, 0)$, which is indicated by an orange pentagon in both panels. The trajectory initially rotates clockwise due to the circulation of ϕ_1. Then the radial distance of the curve from the origin is getting smaller, because eccentricity e_1 is decreasing (the eccentricity damping due to the planet-disk

interaction). After the planet arrival at the resonance, which is denoted by the red circles in both panels, the behaviors of the trajectories in two cases, presented in this figure, become different. In the "capture" case, the resonance angle ϕ_1 begins to librate while e_1 increases. Thus the trajectory oscillates in the region with $e_1 \sin\phi_1 = 0$ and $e_1 \cos\phi_1 < 0$, which indicates that ϕ_1 is librating around π. In the "fail" case shown in the right panel, the planets pass through the resonance. Therefore, the resonance angle ϕ_1 is circulating while e_1 is decreasing. Accordingly, the track rotates and moves towards the origin.

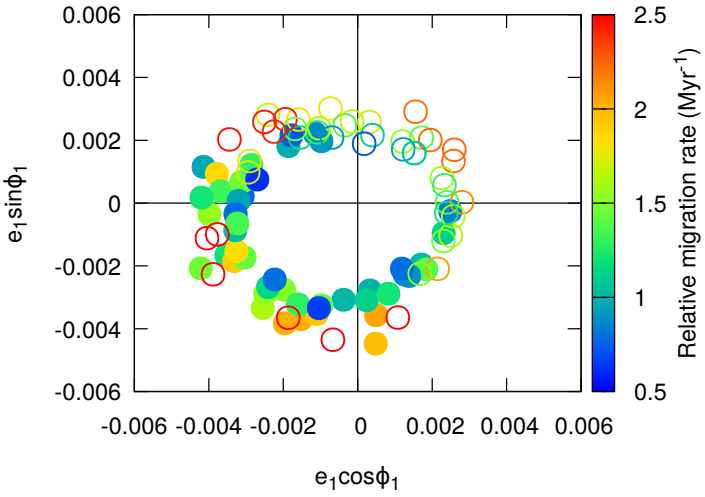

Figure 3.12: The entry location in the ($e_1\cos\phi_1$, $e_1\sin\phi_1$) plane for the simulations in the survey of the 9:7 resonance - The entry locations in the ($e_1\cos\phi_1$, $e_1\sin\phi_1$) plane for the runs shown in Figure 3.4 with relative migration rate smaller than 2.5Myr^{-1}. The solid and empty circles indicate the "capture" cases and the "fail" cases respectively (see text for more details).

Comparing these two plots, we note that the system can enter into the resonance from different points in the plane. To explore the dependence of the results on the location of the resonance entrance, we show the entry positions in all simulations for the 9:7 resonance survey in Figure 3.12 with relative migration rates smaller than 2.5Myr^{-1}. It can be noticed that in the first quadrant (related to $\phi_1 \in [0, \pi/2]$), there are only "fail" cases denoted by the empty circles with different relative migration rates. Most of the "capture" cases tend to enter the resonance from the third quadrant (related to $\phi_1 \in [\pi, 3\pi/2]$) including the cases with fast migrating planets that are indicated by the orange solid circles. For the "capture" cases with slower migrating planets represented by the blue and green solid circles, the entrances are also located in the second and fourth quadrants. On the other hand, the "fail" cases with high migration rates indicated by the red empty circles are distributed in all quadrants.

Based on the above discussion, we note that there is an entrance into the 9:7 MMR in the plane, which must be found by the evolving planets in order to be locked in this resonance. The existence, width and the location of this entrance depend on physical parameters such as the relative migration rate and the circularization rate, which can also be seen in Figure 3.8.

3.6 Resonance capture with different initial eccentricities

In previous sections, we presented the results of simulations of the orbital evolution of two equal-mass planets with very low initial eccentricity of the inner planet, $e_1 = 0.005$, and zero eccentricity of the outer planet, $e_2 = 0$, migrating in a protoplanetary disk. The next question to be asked is how the resonance capture conditions will change if planets will have significantly higher initial eccentricities. To address this question we perform a series of hydrodynamical calculations with various disk parameters and planets on the more eccentric orbits.

3.6.1 Capture on the 9:7 resonance with high eccentricities

Here, we discuss the results of the simulations of the system containing two planets evolving in the protoplanetary disk with the aim to determine how the 9:7 resonance capture conditions depend on the values of the initial eccentricities of the planets. Two sets of the initial eccentricities are adopted in the simulations: $e_1 = 0.015$, $e_2 = 0$ and $e_1 = 0.025$, $e_2 = 0.015$. As a consequence of higher initial eccentricities, the planets arrive at the 9:7 resonance with higher eccentricities than those considered in previous simulations presented in Section 3.5.1.

3.6.1.1 Results of simulations with $e_1 = 0.015$ and $e_2 = 0$

First, we explore the 9:7 resonance capture in a system of two equal-mass planets ($m_1 = m_2 = 3M_\oplus$) with initial eccentricities $e_1 = 0.015$ and $e_2 = 0$ migrating in a protoplanetary disk. The results of a typical simulation with $\Sigma_0 = 2 \times 10^{-5}$ and $\nu = 1 \times 10^{-6}$ are shown in Figure 3.13. We can see that the planets arrive at the 9:7 resonance at $t \sim 1400$ yrs as a result of a short period of convergent migration with the relative migration rate of $\dot{a}/a \sim 0.79$ Myr^{-1}. Then, the planets are captured into the 9:7 resonance, the eccentricity e_2 is excited and the period ratio of the planets oscillates around the 9:7 resonance commensurability. In the last stage of the calculation, both e_1 and e_2 are oscillating around 0.004 while $\Delta\varpi$ is found to librate in the range of [3.2, 5.1]. The resonance angles ϕ_1, ϕ_2 and ϕ_3 librate around 2.8, 4 and 0.2, respectively. Compared with the results shown in Figure 3.2, the values of eccentricities in the final stage of the calculations are very similar, but the librating centers of the resonance angles and $\Delta\varpi$ are shifted from zero or π. What's more, the amplitudes of the oscillations of the period ratio, eccentricities, and resonance angles are larger in this simulation.

Next we present a series of simulations in which Σ_0 is taken in the range of $[4.5\times10^{-5}, 6\times10^{-5}]$ and ν in the range of $[1 \times 10^{-6}, 7 \times 10^{-6}]$. As reported in Section 3.4.1, for the planets with high eccentricities $e_1 \gtrsim 2 \times 10^{-3} \left[(m_1/M_\oplus)(M_\odot/M_*)\right]^{1/2}$, the libration width of the 9:7 resonance can be estimated using Equation (3.25). Taking $e_1 = 0.012$ (which corresponds to the eccentricity of the inner planet when the planets arrive at the 9:7 resonance) and putting into Equation (3.25), we obtain the upper boundary of the 9:7 MMR $P_2/P_1 \sim 1.2863$. The values of ϕ_a in these simulations are determined when the period ratio reaches that value.

The results of those simulations are shown in Figure 3.14 as a function of the disk parameters and ϕ_a. The solid and empty circles represent the "capture" and "fail" cases, respectively. The locations of these circles allow to define, in the same way as it has been done in 3.5.1, the regions (red stripes), where the resonance captures takes place. The lowest region includes the resonance

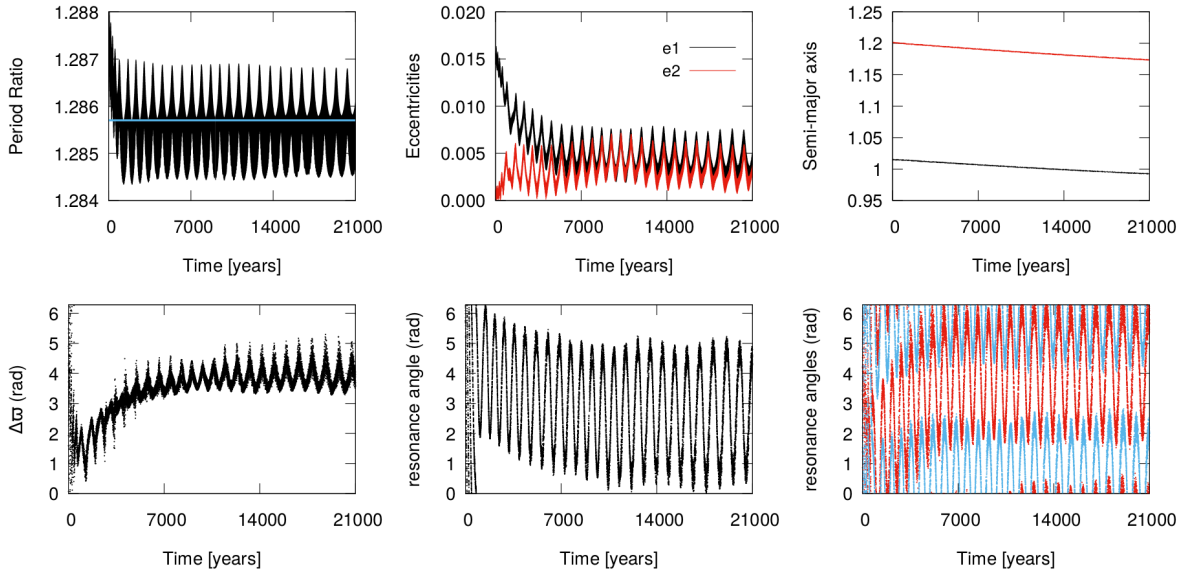

Figure 3.13: Results of a simulation with $e_1 = 0.015$ and $e_2 = 0$ - Top panels: evolution of the period ratio (left), eccentricities e_1, e_2 (middle), and the semi-major axes (right) for the simulation with $\Sigma_0 = 2 \times 10^{-5}$ and $\nu = 1 \times 10^{-6}$. The horizontal solid line in the top left panel shows the 9:7 resonance commensurability. Bottom panels: from left to right, $\Delta\varpi$, the resonance angle ϕ_1, and the resonance angle ϕ_2 (red) together with the resonance angle ϕ_3 (blue) in the simulation.

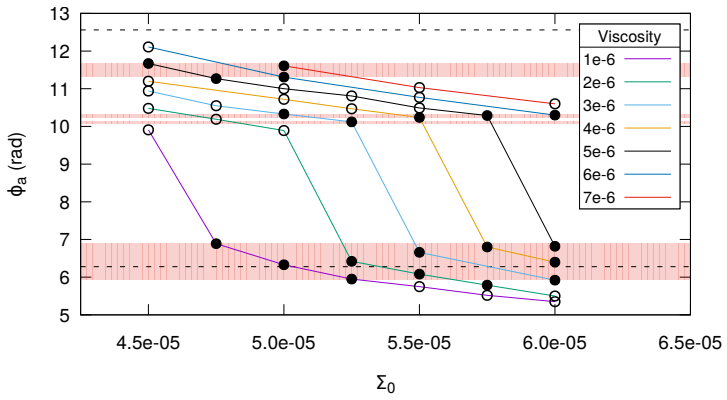

Figure 3.14: Results of the simulations with initial $e_1 = 0.015$ and $e_2 = 0$ by adopting different disk parameters - Accumulated resonance angle ϕ_a as a function of Σ_0, and ν in the simulations with initial $e_1 = 0.015$ and $e_2 = 0$. The solid and empty circles indicate "capture" and "capture" cases, respectively. The dashed line indicates the location of ϕ_a with $\phi_{\rm entry} = 2\pi$. Red regions represent the ranges of ϕ_a where the 9:7 resonance capture takes place. (The data for drawing this figure are given in Table A.2.)

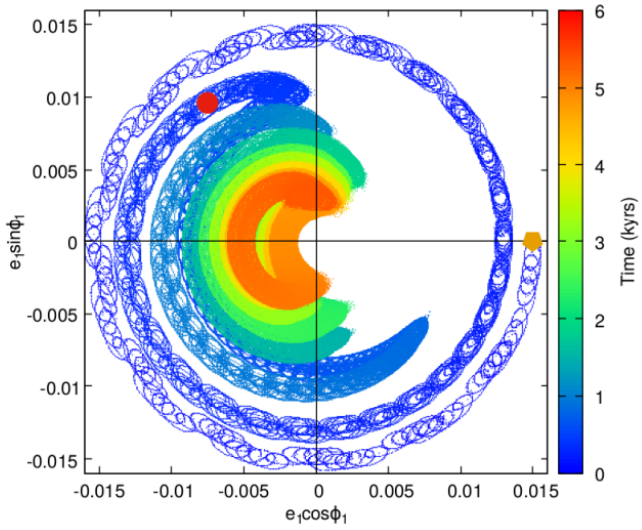

Figure 3.15: Trajectory of the system in the ($e_1\cos\phi_1$, $e_1\sin\phi_1$) plane for a "capture" case with initial $e_1 = 0.015$ and $e_2 = 0$ - The track in the simulation with $\Sigma_0 = 5 \times 10^{-5}$, $\nu = 3 \times 10^{-6}$. The symbols have the same meanings as those in Figure 3.11.

entry at $\phi_{\rm entry} = 2\pi$, which is represented by a dashed line. There are other three narrow red stripe regions in the upper part of the figure. Making the comparison with Figure 3.4, we find that for the simulations with the same disk parameters, the planets with initial $e_1 = 0.015$ are captured in the 9:7 resonance, while those with initial $e_1 = 0.005$ are not. Moreover, we found several narrow capture regions in the interval $[2\pi, 4\pi]$ in this figure. This is in contrast to the simulations shown in Figure 3.4, where only one continuous region is present for the capture in any of 2π intervals.

In order to describe the motion of the planet in a calculation for a "capture" case with higher initial eccentricities, we draw the track of the inner planet in the simulation with $\Sigma_0 = 5 \times 10^{-5}$ and $\nu = 3 \times 10^{-6}$ in the ($e_1\cos\phi_1$, $e_1\sin\phi_1$) plane in Figure 3.15. We can see that the track rotates clockwise before arriving at the resonance, the eccentricity of the inner planet, e_1, decreases, which results in a reducing rotating radius of the trajectory in the plane. The location where the planets enter into the 9:7 resonance is indicated by the red circle in the plane. In the final stages, the track of the planet is restricted to a small region colored by dark orange, corresponding to the situation that the planets are locked in the 9:7 resonance.

3.6.1.2 The survey with $e_1 = 0.025$ and $e_2 = 0.015$

In the previous section we have discussed the effects of the increase (by a factor of three) of the eccentricity of the inner planet on the occurrence of the resonance capture. Here, we consider a system of two equal-mass planets ($m_1 = m_2 = 3M_\oplus$) with even higher initial eccentricity of the inner planet, namely $e_1 = 0.025$ and nonzero eccentricity of the outer planet, $e_2 = 0.015$. The results of the calculation with the following disk parameters: $\Sigma_0 = 3 \times 10^{-5}$ and $\nu = 5 \times 10^{-6}$ are illustrated in Figure 3.16. As it can be seen in this figure, at the beginning of the simulation, when the planets migrate convergently, the eccentricities e_1 and e_2 damp very fast. $\Delta\varpi$ initially

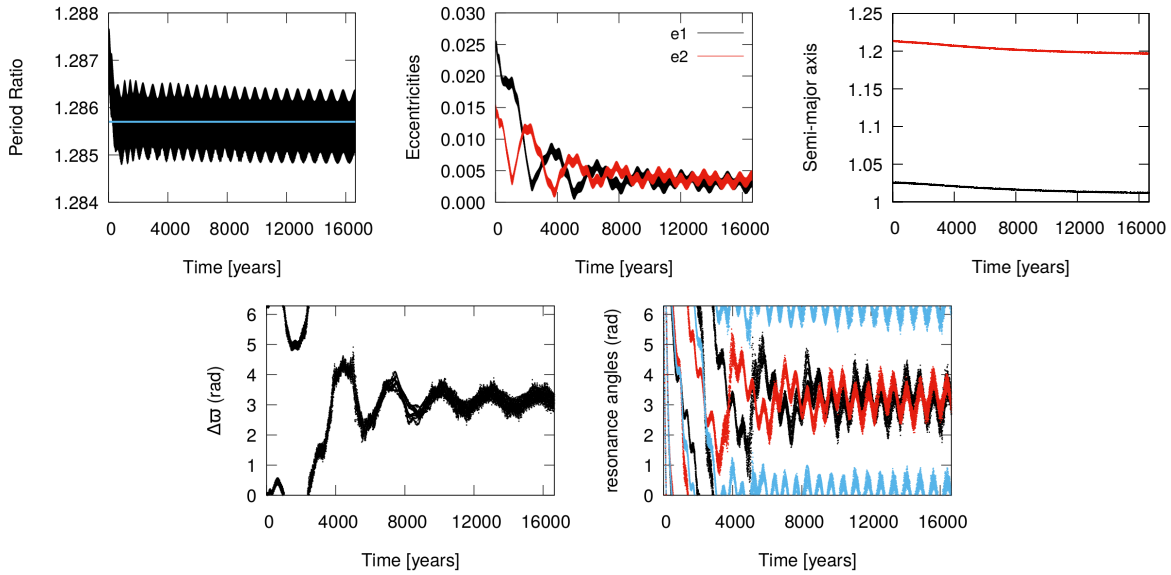

Figure 3.16: Result of a simulation with $e_1 = 0.025$ and $e_2 = 0.015$ - Top panels: evolution of the period ratio (left), eccentricities e_1, e_2 (middle), and the semi-major axes (right) in the simulation with $\Sigma_0 = 3 \times 10^{-5}$ and $\nu = 5 \times 10^{-6}$. The horizontal solid line in the top left panel shows the 9:7 resonance commensurability. Bottom panels: from left to right, $\Delta\varpi$ and the resonance angles ϕ_1 (black), ϕ_2 (red), and ϕ_3 (blue).

oscillates around zero and all the resonance angles circulate until $t \sim 600$ yrs, while, the period ratio of two planets is approaching the 9:7 MMR. Next the planets enters and stay in this commensurability till the end of the calculation. At $t \sim 6000$ yrs, the center of libration of $\Delta\varpi$ moves to π and all the resonance angles begin to librate. e_1 and e_2 tend to the equilibrium values with small amplitude of oscillations. At the end of the calculation, both eccentricities are oscillating around 0.004 and $\Delta\varpi$ is librating around π. The final values of all parameters are similar to those obtained in the simulation shown in Figure 3.2.

The results of the simulations with initial $e_1 = 0.025$ and $e_2 = 0.015$, in which Σ_0 is taken in the range of $[1.5\times10^{-5}, 4\times10^{-5}]$ and ν in the range of $[1\times10^{-6}, 8\times10^{-6}]$ are shown in Figure 3.17. The value of ϕ_a is determined in each simulation at the moment of time when semi-major axis ratio reaches 1.1829. This value is calculated according Equation (3.25) setting $e_1 = 0.02$ (the eccentricity is taken at the moment of the 9:7 resonance entry in those simulations). The ϕ_a in the "capture" cases define the particular regions, which are indicated by green stripes. One of them is still close to $\phi_{\rm entry} = 3\pi/2$ represented by the dashed horizontal line in this figure. At least two narrow regions for capture are found in the interval $[2\pi, 4\pi]$, which is similar to the situation illustrated in Figure 3.14.

3.6.2 Dependence on the initial eccentricities: summary

In order to reveal the influence of the initial eccentricities, adopted in the simulations, on the capture regions of ϕ_a, we present the results from three groups of simulations with different

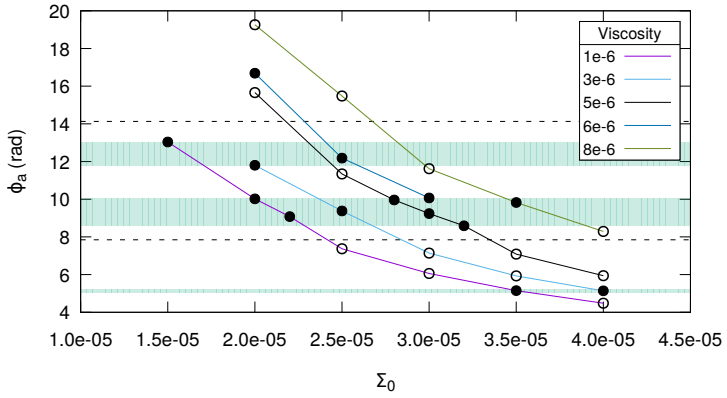

Figure 3.17: Results of the simulations with initial $e_1 = 0.025$ and $e_2 = 0.015$ obtained by adopting different disk parameters - Accumulated resonance angle ϕ_a as a function of Σ_0 and ν in the simulations with initial $e_1 = 0.025$ and $e_2 = 0.015$. The solid and empty circles show the "capture" cases and "fail" cases, respectively. Dashed lines indicate the position of ϕ_a with $\phi_{\rm entry} = 3\pi/2$. Green regions represent domains of ϕ_a where the capture takes place. (The data for drawing this figure are given in Table A.3.)

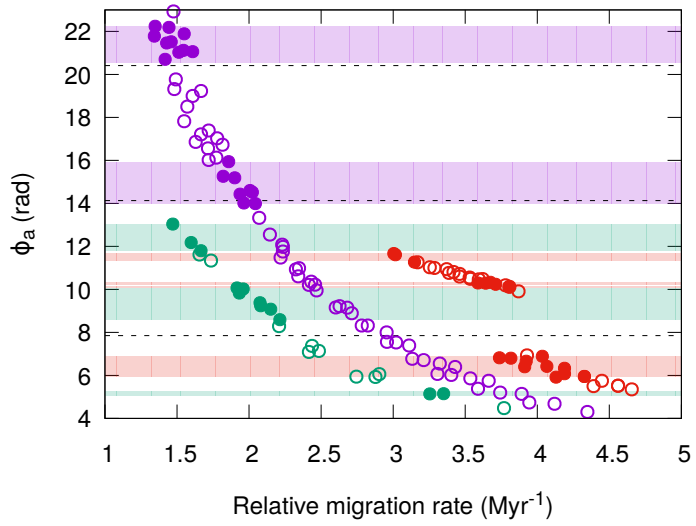

Figure 3.18: Relation between ϕ_a and the initial relative migration rate in all the surveys performed here in order to investigate the 9:7 resonance capture - Relation between ϕ_a and the initial relative migration rate in the simulations. The solid circles indicate the "capture" cases, and the empty circles indicate the "fail" cases. The results of simulations with initial $e_1 = 0.005$ and $e_2 = 0$ are indicated by violet color. Red circles represent the cases in which initial $e_1 = 0.015$ and $e_2 = 0$. Green circles denote the simulations that start with $e_1 = 0.025$ and $e_2 = 0.015$. The capture regions for each group of simulations are indicated with the same color-coding. The values of ϕ_a for which $\phi_{\rm entry} = 3\pi/2$ are indicated by dashed lines. (The data for drawing this figure are given in Table A.1,A.2 and A.3.)

initial eccentricities in the $(\dot{a}/a,\ \phi_a)$ plane in Figure 3.18. The solid circles represent "capture"

cases and the empty circles represent the "fail" cases. The circles and capture regions indicated by the violet color denote the results of the simulations with initial $e_1 = 0.005$ and $e_2 = 0$. The results of another two groups of simulations with higher initial eccentricities are indicated by the red and green colors as before. The positions of ϕ_a with $\phi_{\rm entry} = 3\pi/2$ are also shown in the figure by the dashed horizontal lines.

From the Figure 3.18, we note that ϕ_a increases with smaller relative migration rate. For the results illustrated with the violet color, a scatter in ϕ_a appears with a fixed relative migration rate once this is less than 2 Myr^{-1}, which infers that the influence of the circularization rate on the evolution of ϕ_1 is playing a role in this region. On the other hand, it can be seen that the capture regions for simulations by adopting different initial eccentricities are located in different areas in the figure. In the region with $\phi_a < 8$, the "capture" cases appear with high relative migration rates. Moreover, there is no violet stripes but several red and green stripes are found in that region. It infers that for simulations with high relative migration rate, larger initial eccentricities may lead to a higher probability for the planets being locked into the 9:7 MMR. In addition, we also note that the distance between neighboring violet regions is larger than for the green and red ones. As mentioned above, planets with low initial eccentricities can be captured in 9:7 resonance with $\phi_{\rm entry}$ in only one window, while for planets with high initial eccentricities, there are several discrete capture windows in full 2π range of ϕ_1.

3.7 Summary of the main results

In this chapter, we investigated the 9:7 resonance capture in a system of two low-mass planets ($m_1 = m_2 = 3M_\oplus$) migrating in a gaseous protoplanetary disk towards a central star with the mass of our Sun. For the first time, full two-dimensional hydrodynamic simulations have been used in order to determine the disk properties which favor the formation of this second-order mean-motion commensurability. The disk model considered in the simulations were described by the surface density profile parameterized by Σ_0 and the kinematic viscosity ν. Our approach allowed us to find out such values of Σ_0 and ν, for which the planets will be trapped (at least temporarily) in the 9:7 commensurability. Moreover, we confirmed the general picture of the 9:7 resonance capture observed in previous works [133, 138, 176, 217] and provided a description of the process which leads to the resonance trapping in terms of one of the resonance angles having to be located in a particular range at the particular time, namely when planets enter the resonance.

Let us highlight now the most interesting specific results discussed in this chapter.

- In our hydrodynamic simulations with initial $e_1 = 0.005$ and $e_2 = 0$, the existence of several capture regions have been demonstrated in (Σ_0, ν) parameter space (see Figure 3.4). We found that the resonance capture can occur when the accumulated resonance angle ϕ_a (relating to the evolution of ϕ_1 from the beginning till entering into the resonance) lies in a particular range (the capture window, as we called it) and the width of this range depends on the dynamical parameters (such as the relative migration rate and the circularization rate) which can be determined by Σ_0 and ν (see Figure 3.8). Our findings are similar to

the results obtained in [62], which shows that for a system of a giant planet and a small asteroid, the occurrence of the 3:1 resonance capture depends on the initial values of the resonance angle and $\Delta\varpi$.

- The criterion for the occurrence of the resonance capture derived in our survey is consistent with the conclusions obtained in [138], which shows that the resonance capture probability for a restricted three-body problem depends on the migration rate and the initial eccentricity of the test particle. In our work, the distribution of "capture" and "fail" cases in the 9:7 resonance survey corresponds to their result in the rescaled (e_1, $\dot{a}/a$) plane (see Figure 3.9).

- We also have investigated how the 9:7 resonance capture depends on the initial orbits of the system, by changing the initial semi-major axis of the outer planet. The changes of the value of a_2, we have made, do not significantly affect the relative migration rate or circularization rate in the simulations. However, they do influence the time required to reach the resonance. This in turn, may alter the value of the resonance angle at the entrance to the commensurability and at the end also the value of ϕ_a. Therefore, the results of the simulations may be different as far as the window of the resonance capture is concerned (see Figure 3.10). A similar conclusion obtained through N-body simulations can be found in [133].

- In addition, we explore how the resonance capture depends on the initial eccentricities based on two groups of simulations by adopting higher initial eccentricities with $e_1 = 0.015$, $e_2 = 0$ as well as $e_1 = 0.025$, $e_2 = 0.015$ (see Section 3.6). We found that several discrete windows for the occurrence of the resonance capture in these two cases are distributed over the full 2π region (see Figures 3.14 and 3.17).

- Comparing the results of the simulations starting from the same orbital period ratio but with different initial eccentricities of the planets, we found that for high relative migration rates in the range of $3.0-4.5$ Myr^{-1}, the planets can be captured in the 9:7 resonance with the higher initial eccentricities (see Figure 3.18). This is consistent to the results illustrated in the right panel of Figure 1.3 which infers that the capture probability for the second-order resonance in a restricted three-body problem increases with higher eccentricities when the migration rate is very high [138].

In this chapter, we have studied the 9:7 resonance capture in a system of two equal-mass super-Earths. For the disk parameters adopted in our simulations, the planets are not able to open partial gaps, so the migration of the planets in a protoplanetary disk is considered to be in the type I regime. Other effects such as the density wave propagation or wake-planet interactions which may prevent the resonance capture do not arise in presented here simulations. However, those effects could be significant in the simulations, if the favorable conditions in the protoplanetary disk are met. Such situation will be investigated and discussed in Chapter 5.

Chapter 4

Wave-planet interactions in a young two-planet system: super-Earth and its more massive interior planetary companion

In the previous chapter we have investigated the 9:7 mean-motion resonance capture in a system of two low-mass planets embedded in a protoplanetary disk. As we have pointed out, the second-order commensurabilities are not very common in observed planetary systems and we have explained why. Put simply, the conditions, which must be satisfied in order to form such a configuration are very difficult to meet. It is true, regardless of the fact that for the disk parameters adopted in those simulations, the planets were not able to form even the partial gaps along their orbits, which means that their migration due to the disk-planet interactions could be considered as type I migration (see Section 2.3.1). This is a very well studied regime of the migration and often it is assumed that whenever planets have sufficiently low mass, one can adopt this approximation, without taking into account the fact that even low-mass planets can affect the conditions in the disk. Such assumption led, for example, to the expectation that the first-order mean-motion resonance configurations should be very frequent, which is not the case, as we have discussed in the introduction to this thesis. They are of course more common that the second-order ones, but not as frequent as what is predicted from a simple migration model for type I migration. In the situation when the planets are able to open at least the partial gaps in the disk, other effects such as the density wave propagation or wake-planet interactions may affect the process of the resonance capture. In this chapter, we show in the framework of a simple disk model, following the migration of a super-Earth in the exterior orbit and its more massive planetary companion in the interior one, why we should not expect a very large number of first-order mean-motion commensurabilities, as an outcome of the disk-planet interactions during the early evolution of planetary systems. One reason for that is a repulsion between two planets induced by the wave-planet interactions taken place in a protoplanetary disk. The operation of this mechanism will be discussed in the present chapter.

4.1 Inspiration from the previous works

In [174] it has been shown that the inward migration of the super-Earth could be stopped or even reversed due to the wave-planet interactions, as a result of the angular momentum transfer by the outgoing density waves excited by an inner giant planet to an outer super-Earth. The question, which easily comes in mind is: How massive must be the inner planet in order to make such stopping or reversal efficient? In particular, we would like to know whether the repulsion mechanism will work in a system of two super-Earths embedded in the disk. Before going to the final answer about the two super-Earths (which will be given in the next chapter) we perform a systematic study of this process in the two-planet system embedded in the protoplanetary disk with the super-Earth on the outside and its more massive planetary companion on the inside, varying the mass of the inner companion in the range of $[8M_{\oplus}, M_{\rm Jup}]$. Our strategy is as follows, first, we revisit the calculation done with NIRVANA code in [174] for the system: super-Earth and Jupiter, using FARGO3D code and then we explore the efficiency of the mechanism decreasing the mass of the inner planet. This approach provides the independent confirmation of the results presented in [174] and the determination of the strength of the effect as a function of the inner planet mass. The outcome of this study will bring us closer to our final aim, namely to the case of two super-Earths migrating in the disk.

In the introduction of the thesis, we have shown the distribution of the period ratios of planet pairs in the range of [1, 2.5] in all multi-planetary systems which have been confirmed till August, 2021 (see Figure 1.2) and we have commented that the observations seem to indicate that although resonance configurations are found in some planetary systems, the commensurabilities are not common. It is interesting to see how this picture will change if we limit the choice of the planet pairs to those considered in this chapter, namely those which have at least one super-Earth, defined for this purpose as a planet with the mass $m_p \leq 10M_{\oplus}$. Being aware that a number of planets, detected by the transit method, with known mass is not large, we have used the mass-radius relation in the form $m_p/M_{\oplus} = 2.7(r_p/R_{\oplus})^{1.3}$ [213] to increase the statistics. Assuming that the maximum mass for a planet to be called a super-Earth is $m_p = 10M_{\oplus}$, we have found that the corresponding maximum value of the radius is $r_p = 2.738R_{\oplus}$. Thus the planet pairs containing at least one planet with radius $r_p \leq 2.738R_{\oplus}$ are also taken into account. In order to exclude the pairs in which the architectures are affected by the tidal effects from the central stars, we require that the periods of both planets are larger than 10 days [160, 161]. The histogram of the period ratios of the planet pairs, which satisfy the above conditions is illustrated in Figure 4.1. We can see that in such subset of the planetary systems, the period ratio distribution is similar to the one illustrated in Figure 1.2. The reason for excluding from our considerations those planetary pairs, which are too close to their host stars is dictated by the fact that tidal star-planet interactions are very effective in bringing about the departure from the strict mean-motion commensurabilities, expected as a result of migration in the protoplanetary disk (see Section 1.4.2). Here, in this chapter, we study a repulsion mechanism which operates regardless of the distance from which a planet pair orbits its parent star, namely a wave-planet repulsion mechanism due to the effects of the density waves excited by one of the planets on the other one when they are migrating in a protoplanetary disk (see Section 1.4.2).

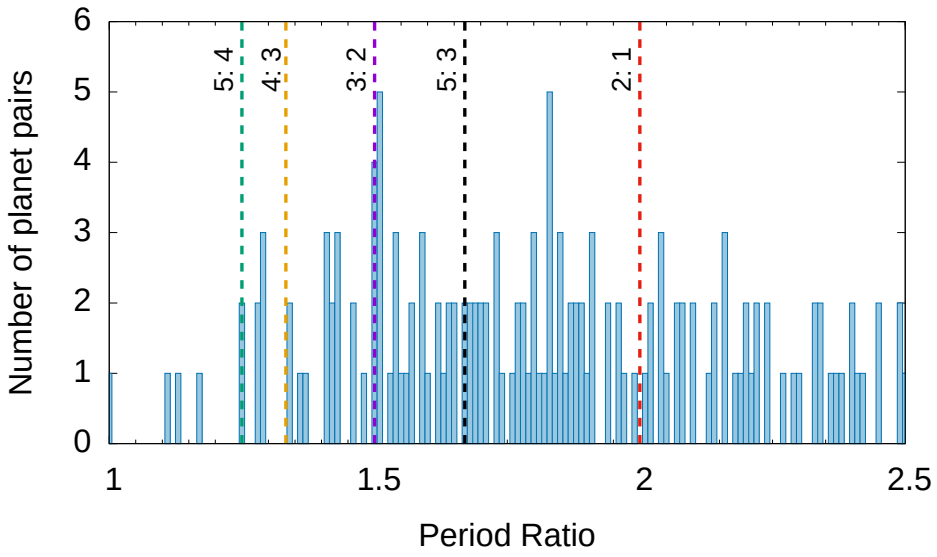

Figure 4.1: Histogram of the orbital period ratios of planet pairs containing at least one super-Earth - Statistics of the orbital period ratios for planet pairs containing at least one planet with the mass $m_p \leq 10M_\oplus$ or the radius $r_p \leq 2.738R_\oplus$. The periods of both planets are larger than 10 days. The width of the bin is 0.01. Dashed vertical lines indicate the locations of MMR's commensurabilities. The data for the periods of exoplanets are obtained from NASA Exoplanet Archive.

According to this mechanism, the migration of the planet is affected by the angular momentum transfer into the planet horseshoe region through the density waves excited by the other planet. If this mechanism works efficiently, the repulsion between two planets can take place and lead to the planet evolution away from the MMRs or prevent the planets to get sufficiently close to each other to form the commensurability.

4.2 Disk model and numerical setup

We consider a system of two planets orbiting a central star embedded in a protoplanetary disk. The mass of the outer planet in all simulations is equal to $5.5M_\oplus$ and the mass of the inner planet is different in each calculation and takes a value in the range of $[8M_\oplus, M_{\rm Jup}]$. A locally isothermal equation of state is adopted, which gives the vertically integrated pressure expressed as $P = \Sigma c_s^2$. The aspect ratio of the disk $h = H/r$ is assumed to be constant. The self-gravity of the disk is neglected in the calculations.

The units of mass, length and time used in the simulations are respectively, the mass of the central star, the initial position of the inner planet and its initial orbital period, as described in Section 2.2. Following the study of [174], we take the central mass to be the solar mass $M_\odot$ and we initialize the inner planet at $r_1 = 5.2$ AU, which gives the time unit to be the orbital period of Jupiter in the Solar System.

In most of the simulations, we adopt a power law disk surface density initialized as $\Sigma = \Sigma_0 r^{-\alpha}$ with $\Sigma_0 = 6 \times 10^{-4}$ and $\alpha = 1/2$. The effects of turbulence is modeled by a constant kinematic

viscosity and its value is taken as $\nu = 2 \times 10^{-6}$. The aspect ratio is assumed to be $h = 0.03$ in order to obtain relatively strong density waves launched by the giant planet in a thin disk [174].

In this work, we use the numerical hydrodynamic code FARGO3D [24] to follow the disk and planet evolution. The computational domain in the radial direction extends from $r_{\rm min} = 0.3$ to $r_{\rm max} = 2.4$ and covers the whole 2π region in azimuth. The resolution in the calculations is 800 cells in the radial direction and 1024 cells in the azimuthal direction. A standard outflow boundary conditions are used and the wave killing-zones located at the inner and outer radial boundaries are applied [43]. The reference frame is set to be rotating with the Keplerian frequency at the location of the super-Earth. The gravitational potential of the planets is smoothed by the softening parameter b which is equal to $0.6h$.

If not stated differently, two planets are initially located in circular orbits with the radial positions of $r_1 = 1$ and $r_2 = 1.62$, respectively, which gives the period ratio of 2.06. Therefore, the system of two planets lies just outside the 2:1 MMR at the beginning of the simulations. We do not consider the formation process of this configuration, but simply assume that it is the outcome of the previous stages of the evolution. Putting the super-Earth initially at 1.62 in the disk extending from 0.3 till 2.4 can raise doubts in regard to the accuracy of the migration rates calculated for the super-Earth, as our choice of the disk size excludes the 2:1 Lindblad resonance from the simulations to start with (Equation (2.27)). This point has been checked carefully and will be illustrated and discussed together with the presentation of the results of the simulations in the next section. It is also important to stress that the size of the disk has been adopted as a compromise between the sufficient grid resolution and the reasonable computational time necessary to reach the aim of this study.

4.3 Migration of a super-Earth in the presence of an interior Jupiter-mass planet

In this section, we discuss, on the basis of our simulations, the orbital evolution of a system composed of a giant planet and a super-Earth, both embedded in a gaseous protoplanetary disk. The initial ratio of the semi-major axes of the planetary orbits is taken to be 1.62, just outside the 2:1 MMR, as it has been stated in the previous section. The inner and outer planets have their masses equal to $M_{\rm Jup}$ and $5.5M_{\oplus}$, respectively.

First, we consider two planets migrating in the disk with $\Sigma_0 = 6 \times 10^{-4}$, which is the value taken in [174]. The evolution of period ratio of two planets and their semi-major axes, obtained in our simulation, is shown in the top row of Figure 4.2. As it can be seen from this figure, after a short period of rapid divergent migration, the planets migrate convergently, while both planets migrate inwards in the disk. At $t \sim 350$ orbits, the inward migration of the super-Earth changes the direction to outwards, which leads to the relative divergent migration of planets since the giant planet continues to migrate inwards. The planets start to move away from the 2:1 MMR, instead of coming closer. During next 800 – 900 orbits of the evolution the outward migration of the super-Earth slows down and the gas giant migrates as before, so the distance between the planets grows, but slower. Finally, at $t \sim 1300$ orbits, the super-Earth begins to migrate inward again and at around $t \sim 2000$ orbits, the period ratio of planets reaches ~ 2.5

with the approximate zero relative migration rate. One of the possible interpretation of this to happen is that with the growing distance between planets, the outgoing density wave excited by the Jupiter-mass planet is weaker and a kind of the steady-state situation is reached. In this simulation, we illustrate how planets approaching the commensurability can fail to be trapped in the resonance, because of the repelling mechanism between the planets operating in the disk, found in [174].

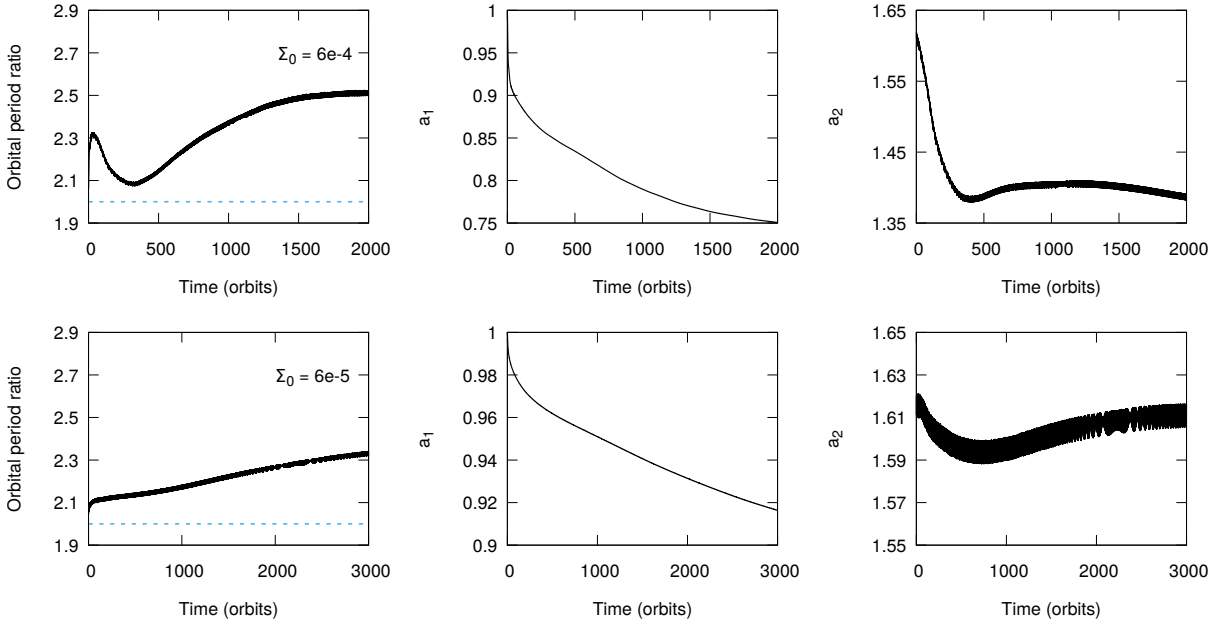

Figure 4.2: Results of the simulations of the system of an inner giant planet and an outer super-Earth migrating in the disk - Results of the simulations with Σ_0 equal to 6×10^{-4} (top row) and 6×10^{-5} (bottom row). Evolution of the period ratio of two planets and their semi-major axes are shown in each row from the left to right, respectively. The dashed horizontal line in the left panels indicates the position of the 2:1 commensurability.

To investigate this case further, we run another simulation for the same planet pair embedded in the disk with much lower surface density, namely $\Sigma_0 = 6 \times 10^{-5}$. The results of this calculation are illustrated in the bottom row of Figure 4.2. Here, both planets migrate slower, as expected, and the period ratio increases from the beginning till the end of the simulation. The relative migration of planets is always divergent. During this calculation, the giant planet migrates always inwards, while the super-Earth migrates inwards only till 600 orbits and then migrates outwards. Comparing this outcome to the case with higher Σ_0, the inward migration of the super-Earth is reversed at the position with larger a_2. The results of both simulations indicate that the repulsion between planets is efficient, regardless of the difference in the value of the surface density, and prevents the capture into the 2:1 resonance. This is consistent with the findings presented in [173], where NIRVANA code has been employed.

Using FARGO3D code, we confirmed the results obtained in [174] for the system containing the super-Earth and the Jupiter-mass planet in the interior orbit, now it is time to explore the efficiency of the repulsion mechanism decreasing the mass of the inner planet. Before moving to

the new series of the simulations, to gain more insights into the interpretation of the numerical results presented here, it is worth to perform few additional test calculations, the results of which will be discussed next.

4.3.1 Migration of a super-Earth in the presence of an interior non-migrating Jupiter-mass planet

From the results presented in Figure 4.2, it is easy to notice that the migration rate of the interior planet affects the orbital evolution of the exterior super-Earth. To eliminate this effect, it is convenient to fix the giant planet in its initial orbit during the whole calculation. In this way, we can explore how the migration of the super-Earth is driven by the torques exerted by the disk and the giant planet without considering its drift in the disk. Hence, we run a new simulation with the same parameters as in the case shown in the top row of Figure 4.2, but switching off the gravitational torque exerted by the disk on the giant planet. In this case, the giant planet only feels the torque from the super-Earth, which is not able to drive its migration efficiently.

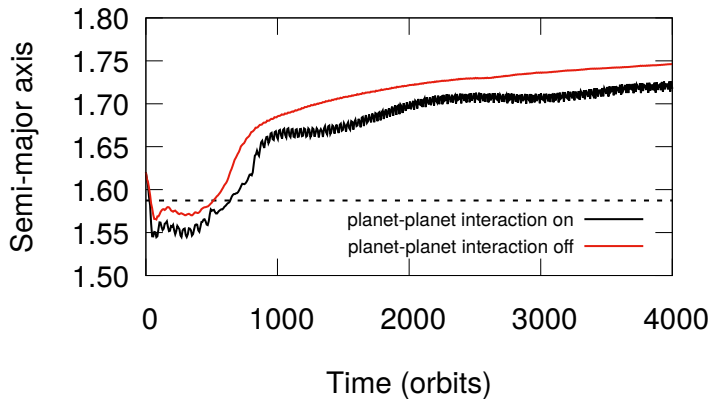

Figure 4.3: Migration of a super-Earth in the presence of an interior non-migrating giant planet in the disk - Evolution of the semi-major axis of the super-Earth in the simulations with an inner giant planet in which the torque from the disk acting on the giant planet is excluded. The results of the simulations with and without the planet-planet interactions are indicated by the black and red lines, respectively. The dashed horizontal line indicates the position of the 2:1 resonance commensurability with the inner giant planet.

The evolution of the semi-major axis of the super-Earth in the simulation with the non-migrating giant planet is shown in Figure 4.3, which is indicated by the black line. We can see that the inward migration of the super-Earth is changed to be outward after a short period of time, similarly to the results obtained in the case of the migrating Jupiter-mass planet (see top right panel of Figure 4.2). Therefore, the outcome of the simulations with migrating and non-migrating gas giants are qualitatively the same. Of course, the details of the evolution are different, which is not surprising, because fixing the Jupiter-mass planet in its initial orbit leads to faster relative migration of the planets. That is why, in this case, the planets pass through the 2:1 commensurability, while the super-Earth migrates inward. Next, at around $a_2 \sim 1.55$

the super-Earth stops for a short period of time and at $t \sim 400$ orbits the super-Earth migrates rapidly outward till $t \sim 750$ orbits. After that, starting at $t \sim 1000$ orbits, the super-Earth migrates slowly outwards till the end of the simulation.

The migration of the super-Earth is dominated by the disk-planet interactions, which can be easily checked, performing an additional simulation with the planet-planet interactions switched off. We show the results of such calculation in Figure 4.3, where the semi-major axis of the super-Earth is indicated by the red line. It is clear that the migrations of the super-Earth in both simulations are similar to each other, except that the outward migration of the super-Earth is smoother in the case of the planet-planet interaction absence. Hereafter, in order to concentrate on the disk-planet interactions, and encouraged by the outcome of this test, we will exclude planet-planet interactions in the simulations.

In the next calculation we verify how the outcome of the simulations depends on the extent of the computational domain. In all the simulations discussed till now the disk extends from 0.3 till 2.4 in the radial direction. In the calculation with the non-migrating Jupiter with the planet-planet interactions switched off, the super-Earth semi-major axis evolves in the range of $1.75 > a_2 > 1.58$. It means that during the whole simulation the outer 2:1 Lindblad torque does not contribute to the total torque acting on the planet. As we have already anticipated in the previous section, it is very important to check whether and how this numerical setup influences the results. For this purpose, we run a test simulation in which the outer boundary of the disk is extended to $r_{\max} = 2.9$ ensuring that the outer 2:1 Lindblad torque is included. To keep the same number of grid points in the length unit, the resolution in this test simulation is changed to 1024×1000 in the azimuthal and radial directions, respectively.

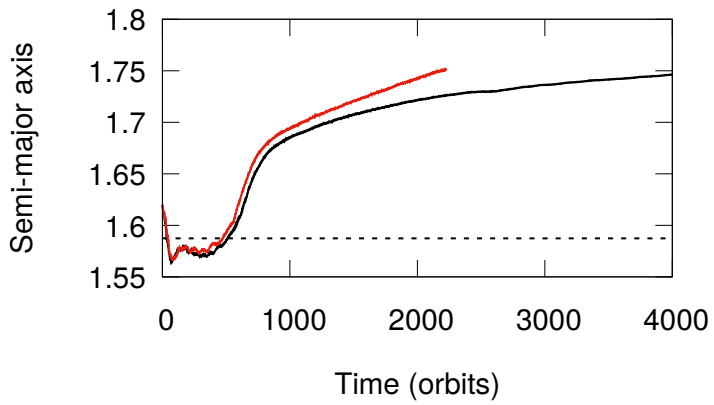

Figure 4.4: Migration of a super-Earth depending on the size of radial computational domain - Evolution of the semi-major axis of the super-Earth in the disks with their radial extents corresponding to [0.3, 2.4] (black line) and [0.3, 2.9] (red line). The dashed horizontal line indicates the position of the 2:1 resonance commensurability with the inner planet. The position of the commensurability is shown here just to guide an eye, as in those simulations the planet-planet interactions are not included.

The comparison of the results, obtained for two mentioned above computational domains, is given in Figure 4.4. The significant quantitative change manifests itself only in the phase of the outwards migration of the super-Earth. Therefore, we confirm that using a short radial

computational domain, to save the expensive computational time, will not change the general picture of the super-Earth's evolution, which is its outward migration.

4.3.2 A closer look at a super-Earth migration in the presence of a non-migrating Jupiter with planet-planet interactions switched off

Here, we describe in full details the evolution of the super-Earth in the presence of a non-migrating Jupiter, with the planet-planet interactions switched off. The semi-major axis of the super-Earth as a function of time is indicated by the red line in Figure 4.3. To make the description easier, we zoom in on the particular phases of this evolution, defined by giving the name and the duration of each phase in the following way:

- inward migration: from 0 to 80 orbits;
- halted migration: from 80 to 400 orbits;
- rapid outward migration: from 400 to 750 orbits;
- slowing down outward migration: from 750 to 2000 orbits;
- steady outward migration: from 2000 to 4000 orbits.

4.3.2.1 Evolution of the super-Earth semi-major axis

The semi-major axis evolution of the super-Earth in each of those phases has been illustrated in Figure 4.5. The super-Earth migrates inwards in first 80 orbits. At $t \sim 40$ orbits, the super-Earth passes from above through the location corresponding to the 2:1 commensurability with the inner planet. We refer here to the location corresponding to the 2:1 commensurability and not to the commensurability itself, because we describe the results of the calculations in which the planet-planet interactions are switched off. Later on, between 80 and 400 orbits, the super-Earth practically does not migrate, its evolution has been halted at around $a_2 \sim 1.57$. Next, during the period of $[400, 600]$ orbits, the super-Earth begins to migrate outward and passes from below through the location of the 2:1 commensurability. The outward migration of the super-Earth continues till the end of the calculations, first, from 600 to 750 orbits, it is a rapid evolution, then in the time range of $[750, 2000]$ orbits, the super-Earth slows down. Finally, after 2000 orbits, the outward migration speed of the super-Earth is nearly constant.

4.3.2.2 Evolution of the disk surface density

We have just shown how the super-Earth evolves in the disk in the presence of the Jupiter-mass planet as a result of the disk-planet interactions. In order to have a full picture about the processes, which lead to such evolution, it is mandatory to analyze how the disk properties changes in time. We expect that the disk surface density will be strongly perturbed by the giant planet, which is able to open a gap along its orbit.

To investigate the disk evolution, we draw the azimuthally averaged surface density of the disk $\Sigma(r)$ and its contour plot at t = 64, 350, 637 and 3185 orbits in Figure 4.6. The first

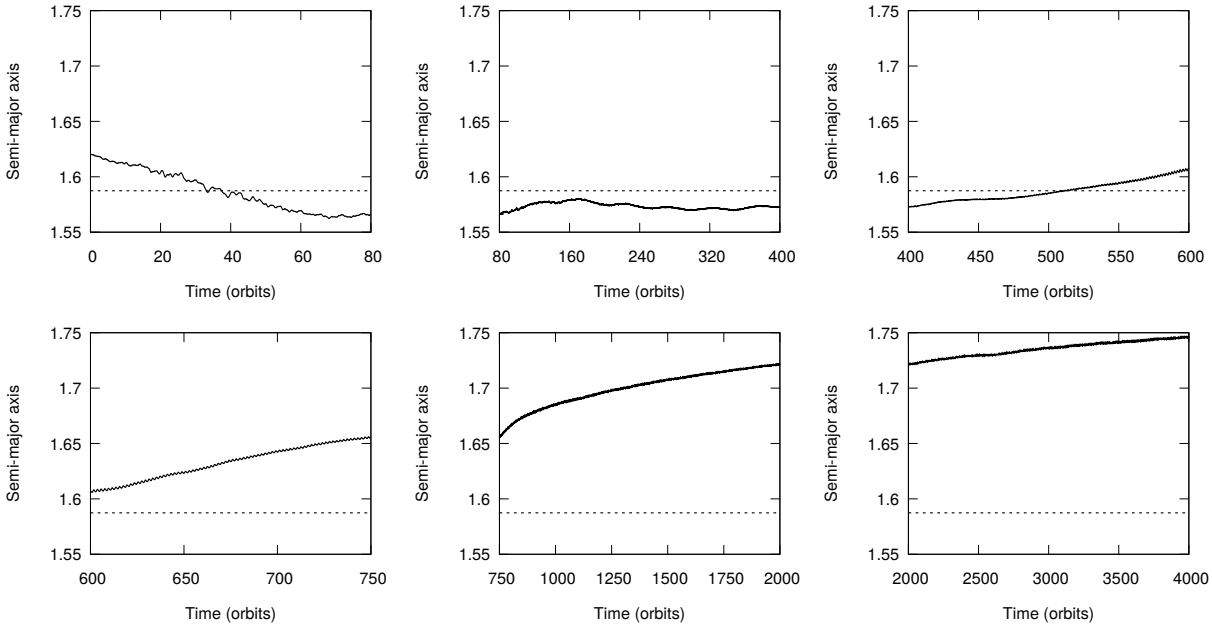

Figure 4.5: Zoomed in the orbital evolution of the super-Earth shown in Figure 4.3 - Evolution of the semi-major axis of the super-Earth in five particular phases: inward migration (first panel in the top row), halted migration (second panel in the top row), rapid outward migration (third panel in the top row and the first one in the bottom row), slowing down outward migration (second panel in the bottom row) and steady outward migration (third panel in the bottom row). The dashed horizontal line in the panels indicates the position of the 2:1 commensurability with the giant planet.

moment of time (t = 64 orbits) is chosen during the inward migration of the super-Earth, the second (t = 350 orbits) when the planet does not migrate (halted migration), the third (t = 637 orbits) during the rapid outward migration, the forth and the last one (t = 3185 orbits) is taken in the steady outward migration phase. All those phases have been introduced in Section 4.3.2.1. In the inward migration phase (top row), we can see the gap in the process of formation along the giant planet orbit. The surface density drops significantly in the co-orbital region of the giant planet. At this moment, the super-Earth is located outside the gap and the slope of the surface density at the super-Earth position, α_p, is negative. The related contour plot shows that the density waves of the giant planet are sufficiently strong to perturb the disk in a vicinity of the super-Earth. In the phase of halted migration (second row), a clean gap is formed around the giant planet orbit. The super-Earth approaches the outer edge of the gap while the density waves of the giant planet sweep through the whole disk. In the rapid outward migration phase (third row), the width of the gap is getting wider, and the position of the super-Earth remains near the outer boundary of the gap but α_p becomes positive. The density waves excited by the inner giant planet continue to propagate through the disk, as in the previous phase. In the steady outward migration phase (bottom row), the gap around the giant planet orbit is very wide, the surface density of the disk at the super-Earth position is lower and the disk surface density profile is flatter than in the previous phases while the density waves are weaker.

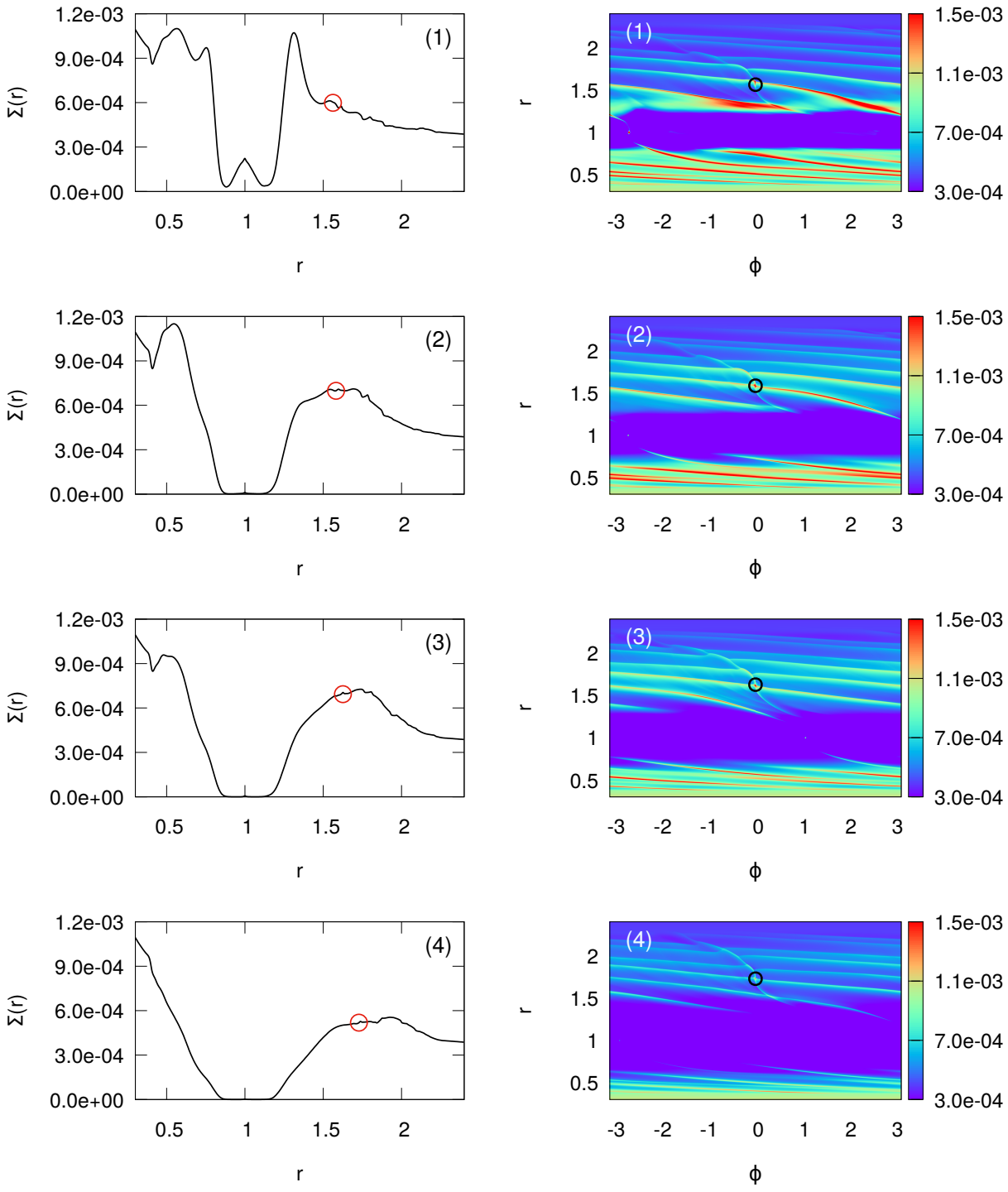

f

Figure 4.6: Evolution of the disk surface density in each phase of the super-Earth migration - From top to bottom: the profile (left) and the contour plot (right) of the disk surface density at t = 64, 350, 637 and 3185 orbits. The position of the super-Earth is indicated by red and black empty circles in the left and right panels, respectively.

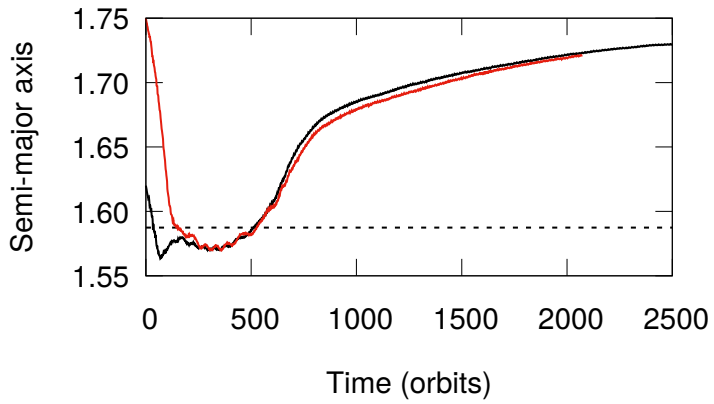

Figure 4.7: Evolution of the semi-major axis of the super-Earth with different initial positions - The black line and red line indicate the numerical results, obtained with the initial location of the super-Earth r_2 equal to 1.62 and 1.75, respectively. The dashed horizontal line indicates the position of the 2:1 commensurability with the inner giant planet.

The early evolution of the disk is dominated by the process of a gap formation along the giant planet orbit (see the top row of Figure 4.6). The gap formation stage is relatively short in comparison with the typical lifetime of the protoplanetary disk. That is why, a strong dependence of the planetary evolution on this particular stage will decrease the predicting power of our findings. To make sure that this is not the case, we run a new simulation in which the initial position of the super-Earth is changed to $r_2 = 1.75$. By doing that, we arrange that the super-Earth will arrive close to the giant planet at the time when the gap formation is almost completed. The results of this new simulation is shown by the red line in Figure 4.7, together with the results of the original case indicated by the black line, when the initial position of the super-Earth was $r_2 = 1.62$. It is easy to notice that after $t \sim 400$ orbits, the evolution of the semi-major axis of the super-Earth in two simulations is similar, which means that the outward migration is not sensitive to details of the early gap opening process.

Another interesting question to be answered is the following: When does the gap evolution reach a quasi-equilibrium state? In other words, we would like to know when the gap profile will be approximately constant in time. For this purpose, we draw in Figure 4.8 the disk surface density profiles $\Sigma(r)$ every 500 orbits covering the whole duration of the simulations. The slow decrease of the surface density values, seen during the evolution is due to the open boundary conditions applied in the simulation. It can be observed that, the shape of the gap does not change significantly after 2000 orbits, which indicates that the quasi-equilibrium state is reached around that time. This can nicely explain the steady outward migration of the super-Earth after $t \sim 2000$ orbits.

To find out how the super-Earth will migrate in the situation when the giant planet gap is in its quasi-equilibrium state from the very beginning of the simulation, we start a new calculation with only the gas-giant present in the disk. Then, after 2000 orbits when the steady-state gap profile is reached, we include the super-Earth in the calculation at r_2 equal to 1.62. The semi-major axis evolution of the super-Earth is illustrated in the left panel of Figure 4.9 (black line).

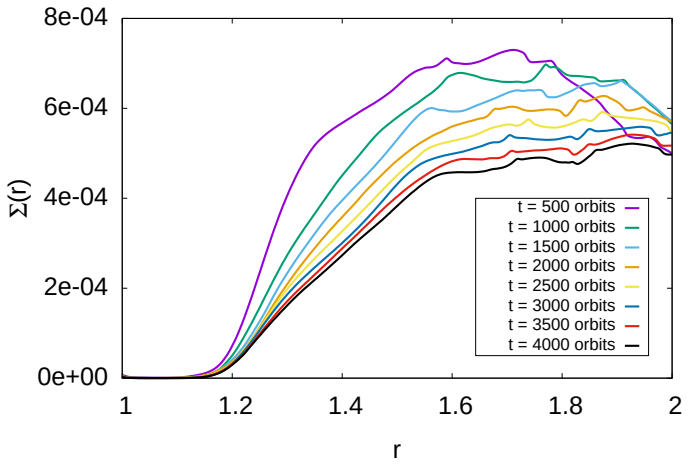

Figure 4.8: Evolution of the disk surface density towards the quasi-equilibrium state - The azimuthally averaged disk surface density in the range of [1, 2] every 500 orbits during the whole simulation preformed in Figure 4.3 indicated by the red line.

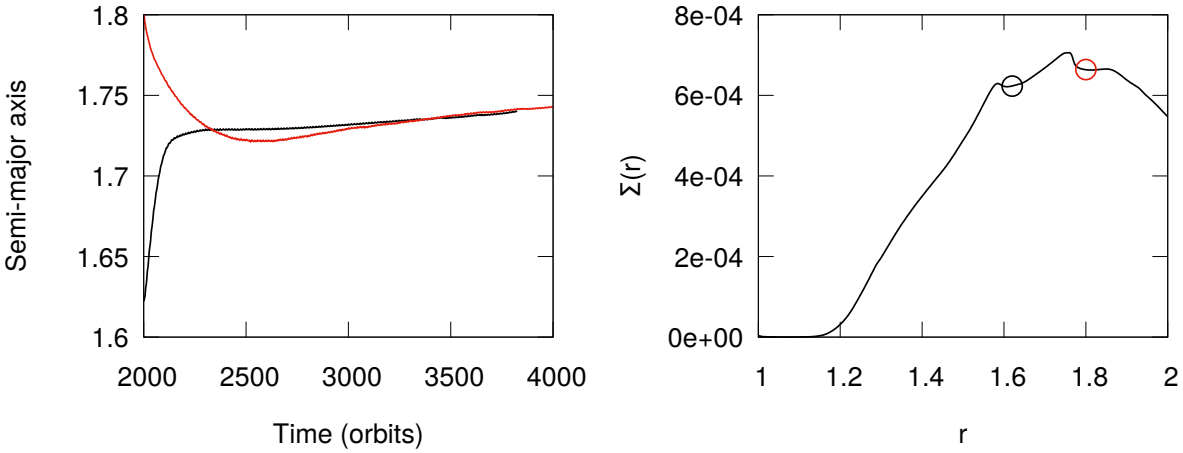

Figure 4.9: Evolution of the semi-major axis of the super-Earth in the disk with a gap already formed by the giant planet - Left: The migration of the super-Earth starting its evolution at $a_2 = 1.62$ (black line) and at $a_2 = 1.8$ (red line) in the disk with the already existing gap, formed by the gas giant, which has been kept for 2000 orbits in its initial orbit at $a_1 = 1$. Right: The surface density profile $\Sigma(r)$ at t = 2000 orbits before the super-Earth is put into the disk. The black and red circles denote the initial positions of the super-Earth with $a_2 = 1.62$ and 1.8, respectively.

We can see that the super-Earth after a short period of fast outward migration, lasting roughly 100 orbits and bringing the planet to $a_2 \sim 1.73$, undergoes slowly outward migration. In the right panel of Figure 4.9, we illustrate the $\Sigma(r)$ at t = 2000 orbits and the position where the super-Earth is inserted at that time. We note that its initial position is located in this part of the disk, where the slope of the surface density is positive (black empty circle in the right panel of Figure 4.9), which might explain the rapid outward migration of the super-Earth in this case.

We perform a similar calculation by inserting the super-Earth at $a_2 = 1.8$. Now, the initial position of the super-Earth is located in this part of the disk, where the slope of the surface density profile is negative (red empty circle in the right panel of Figure 4.9). The evolution of the semi-major axis of the super-Earth in this case is denoted by the red line in the left panel of Figure 4.9. At the beginning, the super-Earth migrates inward, however, after arriving at $a_2 \sim 1.72$, it starts its evolution outward. Comparing the results of the two just described cases to the one illustrated in Figure 4.3, we find that the outcome of all those calculations is similar. Therefore, we confirm that the outward migration of the super-Earth seen in the simulations is not driven by the formation and further evolution of the gap curved by the giant planet in the disk.

In Figure 4.6 (right panels) we illustrate the density waves propagation through the disk in which the super-Earth is embedded. As demonstrated in [174], the angular momentum transfer through the density waves excited by the giant planet is able to stop or reverse the inward migration of the super-Earth in the exterior orbit. The outward propagating density waves excited by the inner planet dissipate in the co-orbital region of the outer planet. During this process, the angular momentum carried by the density waves is transferred to the horseshoe region of the outer planet and then to the planet itself through the horseshoe drag. Therefore, an additional torque has been supplied, which is able to affect the migration of the outer planet in the disk. The full analysis of the mechanism itself will be covered in the next chapter in the case of two super-Earths migrating in the disk. Here, just to summarize, we confirmed the results of [174] and presented few test calculations, which will be useful in further discussion. The last part of this chapter we would like to dedicate to the systematic study of the efficiency of the repulsion mechanism as a function of the mass of the interior planet.

4.4 Migration of a super-Earth in the presence of an interior planet with the mass less than that of Jupiter

The aim of this section is to check whether the inward migration of the super-Earth can be reversed in the disk with an inner planet less massive than Jupiter due to the repulsion mechanism described in the previous section. To reach this aim, we perform the simulations with exactly the same numerical setup as the one used for the case of the interior Jupiter, keeping the disk properties and the mass of the super-Earth unchanged. To guarantee the convergent migration at the beginning of the simulations, the gravitational torque exerted by the disk on the inner planet is not calculated, as we assumed in the first simulation in Section 4.3.1. In this way, the inner planet can only feel the super-Earth but not the disk, so it is practically a non-migrating planet.

4.4.1 Evolution of the semi-major axes of two planets

Following the case of the system with an inner Jupiter-mass planet considered in Section 4.3.1, we run a sequence of simulations in which the outer planet has the mass of $m_2 = 5.5M_\oplus$ while the inner planet mass is taken to be $m_1 = 100M_\oplus, 60M_\oplus, 40M_\oplus, 20M_\oplus$ and $8M_\oplus$, respectively. The adopted disk parameters in all the simulations are as follows: $\Sigma_0 = 6 \times 10^{-4}$, $h = 0.03$ and $\nu = 2 \times 10^{-6}$.

The evolution of the semi-major axis ratio a_2/a_1 in the simulations with different m_1 are shown in the top panel of Figure 4.10. As the inner planet does not interact with the disk (the disk-planet interaction for the inner planet is excluded from the calculation), only the super-Earth migrates and this is a reason for which the relative convergent migration is the same in all those cases.

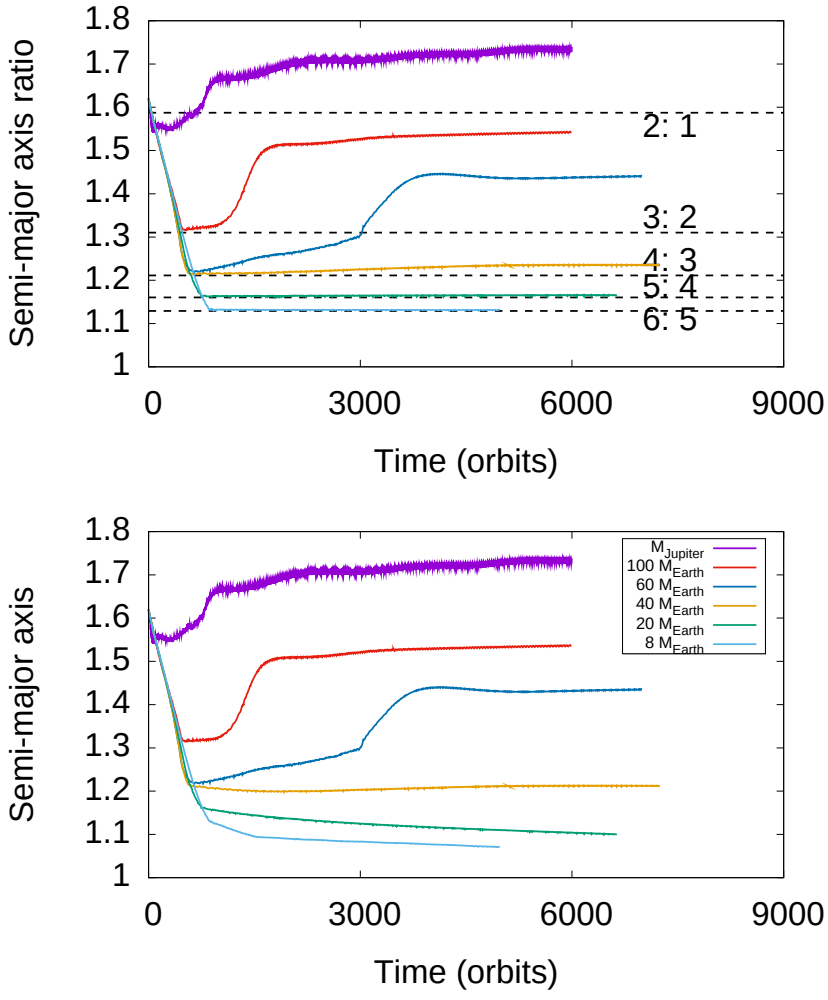

Figure 4.10: Results of simulations with different masses of inner planet - Evolution of the semi-major axis ratio of two planets (top panel) and the semi-major axis of the super-Earth (bottom panel) in the simulations with different m_1. The positions of the first-order resonances are indicated by dashed horizontal lines in the top panel.

The case of $m_1 = M_{\rm Jup}$ has already been discussed in Section 4.3.1. The planets first passed through the 2:1 MMR and then, they have the divergent migration with the semi-major axis ratio increasing rapidly from 1.55 to 1.67, in connection to the passage from below through the 2:1 resonance. After that the a_2/a_1 increases slower and at the end of the calculation the planets are located far away from the 2:1 commensurability. In the cases of $m_1 = 100M_\oplus$ and $60M_\oplus$, two planets arrive at the 3:2 and 4:3 MMRs, respectively. Subsequently, the planets leave the MMRs as a result of divergent migration and arrive at the location between the 2:1 and 3:2 commensurabilities. The planets, which arrived at the 3:2 commensurability ($m_1 = 100M_\oplus$), soon after their arrival, start to leave the resonance and undergo shortly lasted very rapid outward migration. Similar behavior can be seen, when a pair containing the planet with the $60M_\oplus$, on its way out of the 4:3 resonance, cross the 3:2 commensurability from below. In the case of $m_1 = 40M_\oplus$, the divergent migration also occurs after the planets arrive at the 4:3 resonance. However, in this case the semi-major axis ratio a_2/a_1 increases so slowly that even at the final phases of the simulation the planets are still close to the position of the 4:3 resonant value. For the inner planets with even lower masses, namely for $m_1 = 20M_\oplus$ and $8M_\oplus$, the period ratio of two planets maintains the value around the 5:4 and 6:5 commensurabilities, respectively, from the moment of the capture till the end of the simulations. It is also interesting to notice a general trend, that for the less massive inner planet the super-Earth is able to get closer to the inner planet. This explains why the planets enters different MMRs for the different masses of the inner planet, regardless of the fact that initially the relative migration rate is similar in all cases.

In the bottom panel of Figure 4.10, we illustrate the semi-major axis evolution of the outer planet in each simulation. Compared with the result shown in the top panel, it can be noticed that the evolution of a_2 is similar to a_2/a_1 except for the cases with $m_1 = 20M_\oplus$ and $8M_\oplus$. The similarity is due to the fact that the inner planet in the simulations with $m_1 \geq 40M_\oplus$ practically does not migrate (a_1 is close to 1), because its interaction with the disk is switched off. However, in the cases of $m_1 = 20M_\oplus$ and $8M_\oplus$, after arriving at the MMRs, the super-Earth and the inner planet migrate together inward being locked in the MMR.

To verify whether the resonance capture in the last three cases, namely for $m_1 = 40M_\oplus$, $20M_\oplus$ and $8M_\oplus$, actually took place, we present the resonance angles for the 4:3, 5:4 and 6:5 MMRs respectively in Figure 4.11. It is clear from the figure that in the case of $m_1 = 40M_\oplus$, both the 4:3 resonance angles librate with increasing amplitudes, which indicates that the system is slowly leaving the 4:3 MMR due to the divergent migration. In the case of $m_1 = 20M_\oplus$, the 5:4 resonance angles librate around π and zero from 800 orbits till the end of the calculation at 5000 orbits. However, it is not entirely convincing that this resonance will be maintained. Much longer calculations are required in order to give here a definitive answer. In the case of $m_1 = 8M_\oplus$, the 6:5 resonance angles begin to librate at $t \sim 800$ orbits and after $t \sim 1500$ orbits, they librate around $3\pi/2$ and zero, respectively. Till the end of the simulation, the libration amplitude remains roughly constant. Therefore, we conclude that in all three cases the planets are trapped in the different MMRs, but for the 4:3 commensurability the capture is clearly temporary, for the 5:4 the commensurability is long lived or permanent and finally for the 6:5 the resonance is most likely permanent.

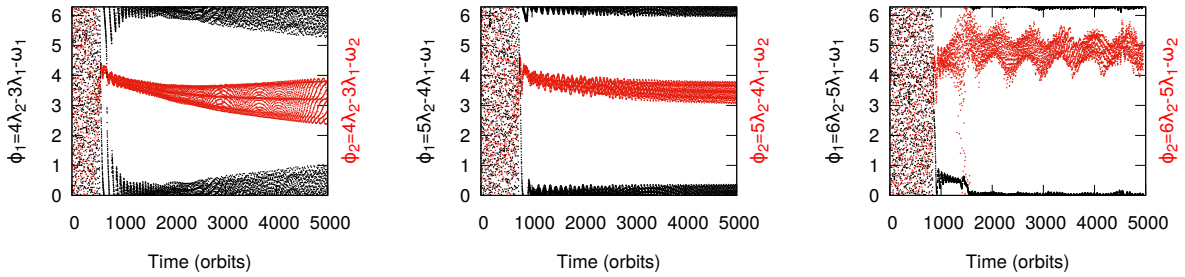

Figure 4.11: Resonance angles in the simulations with different masses of inner planet - From left to right, the inner planet's mass in each case is $40M_\oplus$, $20M_\oplus$ and $8M_\oplus$.

4.4.2 Evolution of the surface density of the disk

The interpretation of this picture will be easier after examining the disk surface density distributions in all the simulations. The surface density profiles have been modified notably due to the presence of the planets in the disk. In Figure 4.12 we show the azimuthally averaged surface density profile and the positions of two planets at $t = 5000$ orbits, which is a moment of time towards the end of the simulations when a_2/a_1 in each case evolves slowly. The planet with $m_1 = M_{\rm Jup}$ opened a wide clean gap along its orbit and the super-Earth is located at the extension of the wide gap right wing in the positive slope of the surface density profile. The inner planets with lower masses are not able to open such a gap in the disk, but they carved the partial gaps in their co-orbital regions. In particular, the deep partial gaps are formed in the cases of $m_1 = 100M_\oplus$ and $60M_\oplus$, in both situations $\Sigma_{min}/\Sigma_{un} \lesssim 10\%$, where Σ_{min}/Σ_{un} is the ratio of the value of the surface density at the bottom of the gap to the corresponding value of the surface density in the unperturbed disk. The position of the inner planet in all cases is slightly shifted from its original position $r_1 = 1$ in each simulation except in the case with $m_1 = M_{\rm Jup}$. The inner planets less massive than the Jupiter are pushed inward due to the planet-planet interactions. This effect is stronger when the planets enter into or passing through the MMRs.

Our findings presented in Figures 4.10, 4.11, 4.12 indicate three kinds of the outcomes:

1. $m_1 = M_{\rm Jup}, 100M_\oplus$ and $60M_\oplus$: the gap formed by the inner planet is very deep and the super-Earth is located at the right wing of the gap carved by the inner planet. The slope of the surface density distribution at the super-Earth location is positive. The planets are not trapped in any MMR. The super-Earth migrates outward.

2. $m_1 = 40M_\oplus$: the partial gap is deep and the super-Earth is very close to the edge of the gap. The planets enter the 4:3 resonance and stay there for the whole duration of the simulation, but the evolution of the resonance angles indicates that this resonance will not be maintained. The super-Earth migrates very slowly outward.

3. $m_1 = 20M_\oplus$ and $8M_\oplus$: the partial gaps are not deep, especially the one for the case of $8M_\oplus$ and the super-Earths are located inside the partial gaps of the inner planets. For

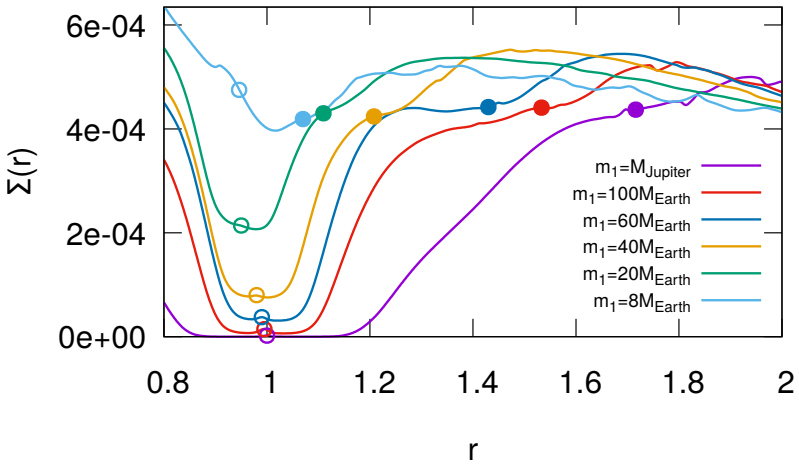

Figure 4.12: Comparison of the disk surface density profile in the simulations with different masses of the inner planet - The azimuthally averaged surface density profile in simulations with different masses of the inner planet at $t = 5000$ orbits. The positions of the inner and outer planets are indicated by empty and solid circles, respectively.

the pair with the more massive inner planet it is less notable, as the super-Earth has just entered into the gap of the interior companion. Instead, for the pair with less massive inner planet there is no doubt that both planets reside in one common gap. In both cases, the planets are locked in the MMRs till the end of the calculation and the super-Earths migrate inward. The case of $m_1 = 20M_\oplus$ is less convincing, as we have already mentioned.

The results of these simulations indicate that there is a strong dependence of the efficiency of the repulsion between planets on the mass of the interior planet. Less massive inner planets affect less the super-Earth in the exterior orbit. It is clear especially for the pairs with $m_1 \leq 40M_\oplus$, which form more compact configurations. Therefore, it is more likely that the planets will end up in the common gap, as it is a case for the pair with $m_1 = 8M_\oplus$. It has been shown already in [21] that in the case of the common gap formation the repelling mechanism is not efficient.

4.5 Summary of the main results

The main results discussed in this chapter can be summarize as follows:

- Using FARGO3D code, we confirmed the results obtained in [173] and [174] that the repulsion mechanism works efficiently in the pair of planets consisting of an inner Jupiter-size planet and an outer super-Earth embedded in the protoplanetary disk (Section 4.3). The repulsion mechanism operating in the system prevents planets from the 2:1 MMR capture. Revisiting this problem was important, because it this way, the same physical effect has been attained with two different numerical codes, namely FARGO3D and NIRVANA, increasing the confidence about the outcome of the calculations.

- We extended the previous study to the systems with the inner planet less massive than Jupiter in Section 4.4. For the cases of $m_1 \geq 40M_\oplus$, the outer planet migrates outward, and the planets are not trapped in any long lasting MMR, as a result of the relative divergent migration. When $m_1 \leq 20M_\oplus$, the planets arrive at and stay in the MMRs till the end of the calculations (see Figure 4.10). In these two cases the repulsion between planets is not effective, because planets are located in one common gap.

In this chapter, we have demonstrated that the migration of an exterior super-Earth under the effect of the density waves, excited by a more massive interior planet in a thin protoplanetary disk, can be slowed down or reversed, if the planets do not form a common gap. We have shown few good examples how the density waves affect the formation of the resonances. In Chapter 3 we have considered the formation of the second-order mean-motion resonances in the system of two super-Earths embedded in the protoplanetary disk, in which they were not able to open a partial gap. Here, we have analyzed the capture in the first-order MMRs, but in the case of an exterior super-Earth and an interior more massive planet evolving in the disk, in which only the interior planet is able to open a gap. The exterior super-Earth with the mass equal to $5.5M_\oplus$, used in our simulations, slightly perturbs the disk, but only the shallow decrease of the surface density can be seen in the absence of the second planet. When two planets are present in the disk, it is not possible to identify this very shallow gap in the surface density profile, due to the density waves excited by the interior planet traveling through the region of the disk where the super-Earth is located. Now, the question, which remain to be answered is: Does the repulsion mechanism will work in a system of two super-Earths embedded in the disk in which they are capable of opening a partial gap? The answer will be given in the next chapter, together with the discussion of the consequences for the formation of the mean-motion commensurabilities.

Chapter 5

Wave-planet interactions in a young two-planet system: a pair of super-Earths

This Chapter is based on the paper written by Zijia Cui, John C. B. Papaloizou, and Ewa Szuszkiewicz, "On the importance of wave planet interactions for the migration of two super-Earths embedded in a protoplanetary disk", published in The Astrophysical Journal, 921:142 (28pp), 2021.

In Chapter 4, we investigated the orbital evolution of the planet pairs consisting of an outer super-Earth and an inner planet with the mass taken in the range from Jovian to super-Earth's values. We found that, for the adopted disk (h=0.03) and the outer planet mass equal to $5.5M_{\oplus}$, the wave excited by a sufficiently massive inner planet, interacting with the outer planet, make a resonant trapping unlikely. However, in the case of two super-Earths, the evolution led to the formation of the 6:5 MMR and a common gap, in which both planets were located. Here, we analyze in more detail the repulsion mechanism in a pair of two super-Earths, which are able to open partial gaps along their orbits. We give the conditions to be satisfied for the effective action of the repelling between two super-Earths and discuss how the formation of the resonances can be affected by that.

5.1 Inspiration from the previous works

As we have already discussed, the wave-planet repulsion mechanism works efficiently for the super-Earth and its more massive interior planetary companion, if the evolution of this pair of planets is not leading to the common gap formation. [21] extended the study of [174], concerned with the super-Earth and Jupiter-mass planet, to the cases of two planets with comparable masses, namely the pairs of the Saturn-like and Uranus-like planets. The choice of the disk parameters has been constrained by the requirement that at least one of the planets is able to open a partial gap in the disk. Indeed, they found that the disk-driven repulsion, described in Chapter 4, leading to the divergent migration of the planets, is efficient in both considered by their cases. However, the observations show that close-in super-Earths (mini-Neptunes) are the

most common exoplanets in our galaxy known to date. That is why we focus here on the low-mass planets with the masses between 2-10 Earth masses. It is important to stress, that the migration of planets, which are able to form a partial gap has attracted a lot of attention (e.g. [48, 51, 96, 97]). To know how such planets migrate is crucial for understanding the formation of mean-motion resonances. In this chapter, we study the orbital evolution of two super-Earths embedded in a thin protoplanetary disk by employing two-dimensional hydrodynamic simulations. Using the knowledge gained from the previous studies, we arrange for the conditions in the disk to ensure that the planets are able to open partial gaps along their orbits. We will explore whether and under what conditions the wave-planet repulsion mechanism, responsible for the divergent migration and preventing planets from being trapped into the MMRs, is operational in the case of two super-Earths embedded in the protoplanetary disk.

Our motivation for this study is also reinforced by the observations. Some planet pairs composed of two super-Earths have been found with period ratios near to but slightly larger than the first-order resonance values. One of the examples is the Kepler-59 system, which is composed of an inner planet with the mass of $5.3M_{\oplus}$ and an outer planet with the mass of $4.6M_{\oplus}$. The planetary orbital period ratio in this system is 1.5141, which is slightly larger than 3:2 commensurability [189]. Another case is the Kepler-128 system in which the masses of the inner and outer planets are respectively equal to $0.77M_{\oplus}$ and $0.9M_{\oplus}$ with the period ratio to be 1.5112 [77]. Besides that, some planet pairs in two-planet systems are found in the vicinity of other first-order resonances. For instance, the planets in the system of Kepler-177 are close to the 4:3 commensurability [78], two super-Earths in the Kepler-307 system are near the 5:4 resonance [92] and in the system of Kepler-36, the period ratio of two super-Earths is very close but slightly larger than 7:6 [36]. The detailed information of those planets are given in Table 5.1. Considering that both planets in those systems have periods larger than 10 days, the tidal effect is not the reason for the departure from the exact commensurabilities [160, 161]. To explain the formation of such orbital configurations in those systems, we explore the hypothesis that the cause for the absence of the exact commensurabilities is the efficient wave-planet repulsion mechanisms similar to that presented in the previous chapter.

Table 5.1: Two-planet systems with the period ratios near the first-order resonances

System	Planet pair	Periods (days)	Mass (M_*)	MMR	Deviation	Refers
Kepler-59	Kepler-59b	11.8715	1.10×10^{-5}	3:2	0.0141	[189]
	Kepler-59c	17.9742	1.02×10^{-5}			
Kepler-128	Kepler-128b	15.090	2.12×10^{-6}	3:2	0.0112	[77]
	Kepler-128c	22.804	2.48×10^{-6}			
Kepler-177	Kepler-177b	35.860	1.90×10^{-5}	4:3	0.0445	[207]
	Kepler-177c	49.409	4.79×10^{-5}			
Kepler-307	Kepler-307b	10.4208	2.46×10^{-5}	5:4	0.0045	[92]
	Kepler-307c	13.0729	1.20×10^{-5}			
Kepler-36	Kepler-36b	13.8683	1.11×10^{-5}	7:6	0.0028	[207]
	Kepler-36c	16.2187	2.07×10^{-5}			

5.2 Physical model and numerical setup

We consider a system of two low-mass planets, orbiting a central star, embedded in a two-dimensional protoplanetary disk. A locally isothermal equation of state, with the vertically integrated pressure given as $P = \Sigma c_s^2$, is adopted in most of the simulations. The aspect ratio of the disk, h, is assumed to be constant. We preform also a calculation with an adiabatic equation of state where P is given by $P = (\gamma - 1)e\Sigma$, in order to verify how the outcome of the simulations depends on the assumed equation of state. Moreover, we consider a viscous disk model, in which the temperature is determined by the balance between local heating and cooling and which supports a constant angular momentum flux. The self-gravity of the disk is neglected in the simulations, but also this assumption will be checked and its consequences discussed.

The system of units in the numerical simulations are the same as given in Section 2.2. We take the initial position of the inner planet at $r_1 = 1$ AU and the central mass to be the solar mass $M_\odot$. Therefore, the time unit in the simulations is 1 yr. However, our numerical results can be scaled to other values of r_1 and M_*.

In the simulations, both planets are initially put in circular orbits. The inner and outer planets are initialized at $r_1 = 1$ and $r_2 = 1.48$, respectively. Their masses are in the super-Earth mass range.

To guarantee the convergent migration of two super-Earths in the early stages of their orbital evolution, we adopt a particular initial disk surface density profile $\Sigma(r)$ in most of our simulations. The initial disk surface density distribution contains a central disk cavity and have a form

$$\Sigma(r) = \begin{cases} 1.25\Sigma_0 r - 0.25\Sigma_0 & \text{for} \quad r_{\min} < r < 1, \\ \Sigma_0 r^{-\alpha} & \text{for} \quad 1 \leq r < r_{\max} \end{cases} \tag{5.1}$$

where Σ_0 is a scaling disk surface density parameter while $r_{\min}$ and $r_{\max}$ represent the inner and outer boundaries of the computational domain, respectively. If not stated differently, $\Sigma_0 = 6 \times 10^{-5}$ and $\alpha = 1/2$. The steep positive slope of the profile forms a trap [124], which prevent the inner planet, placed there, from the migration. The outer planet, located in the region with the negative surface density slope, migrates inward. Therefore, the convergent migration takes place from the beginning of the simulations. We note that the disk mass within r_1 can be approximately calculated as $\pi\Sigma_0$ in units of the mass of the central star. Therefore, for the mass of the central star equal to $1M_\odot$, we get $0.19M_{\rm Jup}$. For $r_1 = 1$ AU this is about five times smaller than expected for the minimum mass solar nebula.

In this part of the thesis, we also use the numerical code FARGO3D [25] to solve the governing hydrodynamical equations. In the simulations in which the equation of state is specified, the effects of turbulence is modeled by a constant kinematic viscosity ν taken to be 1.2×10^{-6} and the constant aspect ratio is adopted to be $h = 0.02$, which gives the viscosity parameter α equal to 0.003 [191]. The softening parameter b for smoothing the gravitational potential of the planets is assumed to be $0.6h$.

The computational domain in the radial direction extends from $r_{\min} = 0.2$ to $r_{\max} = 2.6$ and covers the whole 2π domain in azimuth. It is divided into 900 equal cells in the radial direction and 1800 equal cells in the azimuthal direction. We adopt a rotating frame that corotates with the Keplerian angular velocity at the initial location of the inner planet. The standard outflow

boundary conditions are applied at the inner and outer boundaries of the computational domain while the wave killing-zones [43] operate in the regions of $[0.2, 0.32]$ and $[2.36, 2.6]$.

We denote the masses of the inner and outer planets to be q_1 and q_2, where $q_i = m_i/M_*$ (with $i = 1, 2$ for inner and outer planets, respectively) is the planet-to-star mass ratio. For the disk parameters adopted in the simulations, the parameters $q_i^{1/3}/h \sim 1$, and $q_i/(40\nu) \sim 0.25$, which are related to the degree of non-linearity and the ratio of tidal to viscous torques, respectively. Therefore, both super-Earths in the simulations are expected to open a partial gap around their orbits [38, 105, 111]. This is the precondition for the effectiveness of the wave-planet repulsion mechanism given in [21].

5.3 Divergent migration of two super-Earths near the 3:2 resonance

In this section we present the orbital evolution of two super-Earths migrating in a thin protoplanetary disk in the vicinity of the 3:2 MMR obtained in our two-dimensional hydrodynamic simulations. Our aim is to answer the question whether the initial convergent migration of two super-Earths will become divergent as it has been observed in the system composed of an inner giant planet and an outer super-Earth [174] (Chapter 4) as well as the system consisting of two Saturn-like planets or two Uranus-like planets [21].

5.3.1 Migration of two super-Earths in a disk with a power-law surface density profile

We consider two super-Earths with $q_1 = 1.3 \times 10^{-5}$ and $q_2 = 1.185 \times 10^{-5}$ embedded in a protoplanetary disk. As mentioned before, both planets are able to open a partial gap in the disk with the parameters, which we adopted in the simulations ($h = 0.02$ and $\nu = 1.2 \times 10^{-6}$). The planets are originally put in circular orbits with $r_2/r_1 = 1.48$ and thus their initial orbital period ratio is 1.8, which is larger than the 3:2 commensurability. In this case, we take the initial surface density profile as a power-law in the form of $\Sigma = \Sigma_0 r^{-\alpha}$, where $\Sigma_0 = 8 \times 10^{-5}$ and $\alpha = 0.5$. There is no need for the modification of the surface density distribution given in Equation (5.1) to establish initially convergent migration of the planets.

The evolution of the orbital period ratio, the semi-major axes, the eccentricities of two planets and the 3:2 mean-motion resonance angles are shown in Figure 5.1. Both planets migrate inward during the whole calculation. The system migrate convergently and arrives near the 3:2 MMR at $t \sim 6000$ orbits. When planets are close to the 3:2 commensurability, both eccentricities increase and the 3:2 resonance angles begin to librate. The maximum value of e_1 is around 0.0011 while that of e_2 is approximately equal to 0.0012. Soon after $t \sim 6000$ orbits, the convergent migration of two planets changes to be divergent. The orbital period ratio is increasing and both eccentricities are decreasing. At $t \sim 6500$ orbits, the migration becomes convergent again and the eccentricities are slightly increased. At $t \sim 7500$ orbits, the relative migration of two planets changes back to be divergent. A similar behavior of orbital evolution takes place again around $t \sim 9000$ orbits. However, the general trend of the relative migration is obviously divergent from $t \sim 6000$ orbits till the end of the calculation.

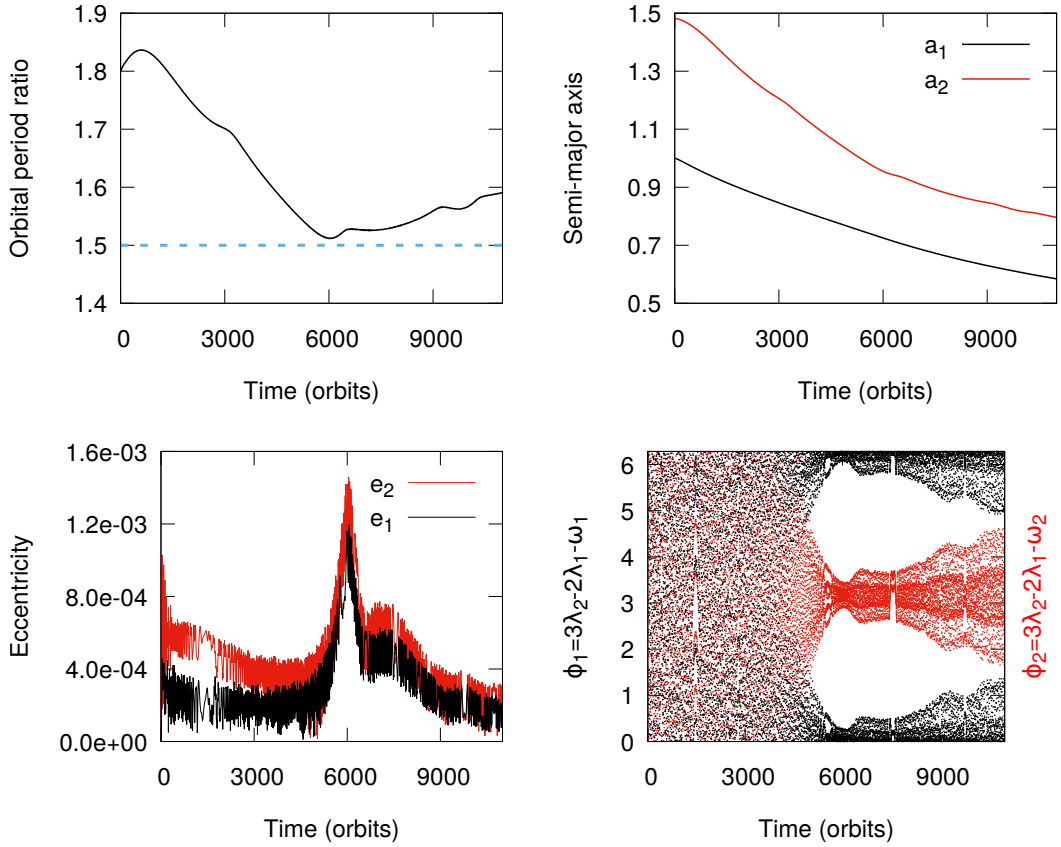

Figure 5.1: Results of the simulation of two super-Earths in the disk with a power-law surface density profile - The masses of the inner and outer planets are $q_1 = 1.3 \times 10^{-5}$ and $q_2 = 1.185 \times 10^{-5}$. The initial disk surface density is taken to be $\Sigma(r) = 8 \times 10^{-5} r^{-1/2}$. The evolution of the planets' orbital period ratio (top-left), the semi-major axes (top-right), the eccentricities (bottom-left) and the 3:2 resonance angles (bottom-right) are shown. The horizontal dashed blue line in the top-left panel indicates the position of the 3:2 commensurability.

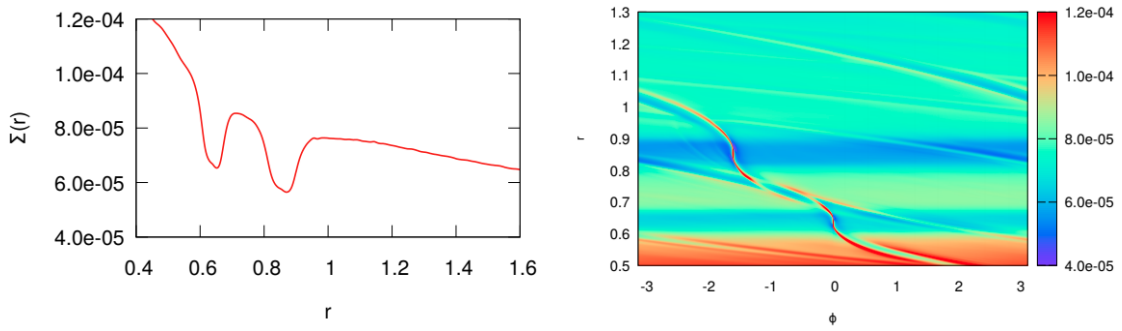

Figure 5.2: Partial gaps formed in the simulation of two super-Earths in the disk with a power-law surface density profile - The azimuthally averaged surface density profile and the contour plot of the disk surface density in the vicinity of two planets at $t \sim 8560$ orbits in the simulation of two super-Earths with $q_1 = 1.3 \times 10^{-5}$ and $q_2 = 1.185 \times 10^{-5}$ in the disk with the initial surface density profile in the form: $\Sigma = 8 \times 10^{-5} r^{-1/2}$.

In Figure 5.2 we illustrate the azimuthally averaged disk surface density profile and the corresponding contour plot in the vicinity of two planets in the simulation at $t \sim 8560$ orbits. Both planets open a partial gap in their co-orbital regions as we expected and the gaps are well separated.

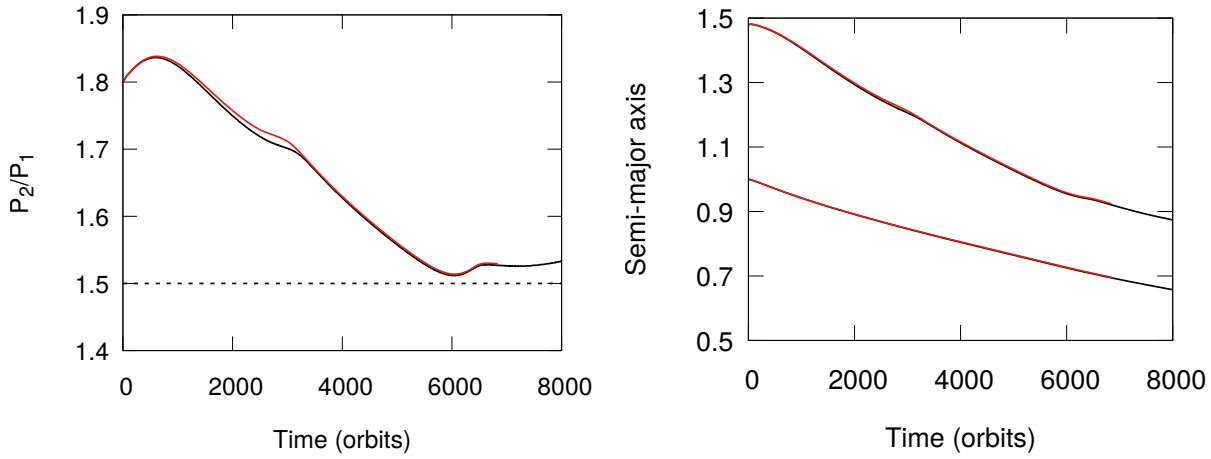

Figure 5.3: The results of the simulations of two super-Earths with and without planet-planet interactions - Evolution of the period ratio and the semi-major axes of two super-Earths with $q_1 = 1.3 \times 10^{-5}$ and $q_2 = 1.185 \times 10^{-5}$ in the simulation without calculating the interactions between planets (red line) and the one presented already in Figure 5.1 (black line).

We rerun the simulation by switching off the planet-planet interactions, as we did for the case with an inner giant planet in Section 4.3.1, to separate the effects of the disk-planet interactions from that caused by the planet-planet interactions. The results of this simulation is presented in Figure 5.3 denoted by the red line together with the results already shown in Figure 5.1 (black line). The comparison performed in the figure allows to conclude that the occurrence of the divergent migration in the simulation shown in Figure 5.1 is not related to the direct gravitational interactions of two planets with each other but to the disk planet interactions.

5.3.2 Migration of two super-Earths in a disk with a central cavity

To understand better the mechanism responsible for the repulsion between planets observed in Figure 5.1, we need to extend the study towards a wider range of the mass ratio of two planets. We would like to be able to follow the evolution of the planetary pairs also when the inner planet is more massive than 1.3×10^{-5}, used in the already presented calculation. The convergent migration cannot be easily achieved in the disk with a simple power-law surface density profile, if the inner low-mass planet is significantly more massive than the outer one. Therefore, we adopt the particular profile given by Equation (5.1) with a central disk cavity to guarantee the convergent migration in the early evolution stage. For checking whether the results of the simulation will be changed by adopting different $\Sigma(r)$, we run the simulation with the same disk parameters as in the previous case but taking the initial surface density profile to be Equation (5.1) with $\Sigma_0 = 6 \times 10^{-5}$.

5.3.2.1 Orbital evolution of the planets

The results of the simulations with the initial $\Sigma(r)$ given in Equation (5.1), taking $\Sigma_0 = 6 \times 10^{-5}$ are shown in Figure 5.4. At the beginning of the calculations, the planets migrate convergently. During this early stage, the outer planet migrates inward and the inner planet halts around its initial orbit due to the specific initial surface density profile adopted in the simulation. This results in the relative migration rate of the planets, which is faster than that in the previous case, and the planets approach the 3:2 resonance earlier. At approximately $t \sim 3000$ orbits, when the pair is getting closer to the 3:2 resonance, both eccentricities increase while the 3:2 resonance angles begin to librate. As the effect of the resonance capture, the inner planet leaves the trap and both planets migrate slowly inward together. At $t \sim 5000$ orbits, the orbital period of the planets is very close to the 3:2 commensurability. The eccentricities reach their maximal values: $e_1 \sim 8.5 \times 10^{-4}$ and $e_2 \sim 1.0 \times 10^{-3}$. After that, the orbital period ratio increases and the planets leave the 3:2 MMR. From this point on the eccentricities decrease and the amplitudes of the 3:2 resonance angles increase. In this phase, the outer planet migration slows down and after $t \sim 8000$ orbits, the outer planet begins to migrate outwards. At the same time, the inward migration rate of the inner planet decrease till the end of the calculation.

The comparison of the orbital period ratio evolution in two simulations by adopting different initial disk surface density profiles is illustrated in Figure 5.5. The convergent migration rate in the case with the initial disk surface density distribution given in Equation (5.1) is faster than in the previous case with a simple power law profile. However, after $t \sim 6000$ orbits, the divergent migration occurs in both cases and the further evolution of the period ratios is very similar. Therefore we confirm that the results in two simulations with these two different initial surface densities are qualitatively the same. As we have already anticipated, we have introduced the disk with a central cavity in order to have more flexibility in the choice of the masses of the planets for further investigations, so this case will serve as a reference for other simulations presented in this chapter. Here we have shown that adopting the disk with a cavity we have got the same outcome of the simulations as in the disk without it.

5.3.2.2 Evolution of the disk surface density

We have just described the orbital evolution of the planets embedded in the disk and show that the repulsion between the planets is in operation. In this simulation, we adopted a specific initial disk surface density profile with an inner cavity, which halts the inward migration of the inner planet and thus leads to the convergent migration in the early stage of the evolution. The presence of the planets inevitably modifies the surface density profile during the planets migration. This modification in turn, affects the orbital evolution of planets in the disk. Hence, it is of interest to have a look at the evolution of the disk surface density, when the planets are present and when they are absent. For that purpose, we draw the azimuthally averaged surface density profiles $\Sigma(r)$ at different moments of time in the left panel of Figure 5.6.

When the planets are present in the disk, the surface density profile is dominated by the partial gaps around the planetary orbits. The modification of the initial profile is pronounced. The initial negative slope of the surface density distribution at the outer planet position changes slowly and finally becomes a positive one at $t \sim 4777$ orbits. In addition, the local maximum of

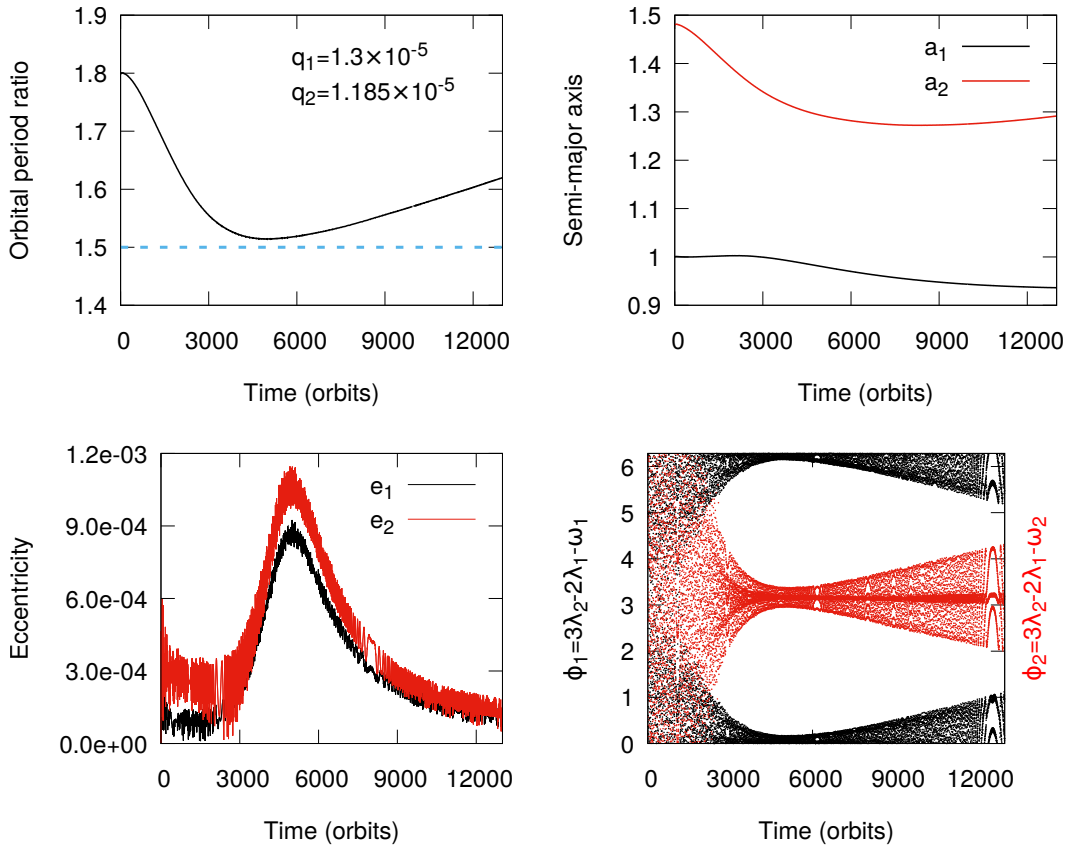

Figure 5.4: Results of the simulation of the evolution of two super-Earths in the disk with a central cavity - The masses of the inner and outer planets are $q_1 = 1.3 \times 10^{-5}$ and $q_2 = 1.185 \times 10^{-5}$. The initial surface density has the form given in Equation (5.1) with $\Sigma_0 = 6 \times 10^{-5}$ and $\alpha = 0.5$. The evolution of the planets' orbital period ratio (top-left), the semi-major axes (top-right), the eccentricities (bottom-left) and the resonance angles (bottom-right) are shown. The horizontal dashed blue line in the top-left panel indicates the position of the 3:2 resonance commensurability.

the disk surface density that resides between the planets moves slightly inwards along with the migration of two planets.

It is difficult not to noticed the analogy with the operation of the horseshoe drag at a planet trap, where we expect that a positive surface density slope at the location of the outer planet might lead to a slowing down of its migration. The slope of $\Sigma(r)$ changes to be positive at almost the same time when the divergent migration of two planets takes place. However, this effect is not ultimately responsible for the divergent migration, as it occurs also in the disk with the initial power law density profile which does not exhibit a positive slope (compare Figure 5.2 and Figure 5.6).

The evolution of the surface density $\Sigma(r)$ obtained at the same moments, but without planets embedded in the disk is illustrated in the right panel of Figure 5.6. The surface density maximum value moves outwards under the effects of the disk viscosity (see the trajectory indicated by the green dashed-dotted line). As a consequence, the surface density profile tends to be flatter as the evolution in time proceeds.

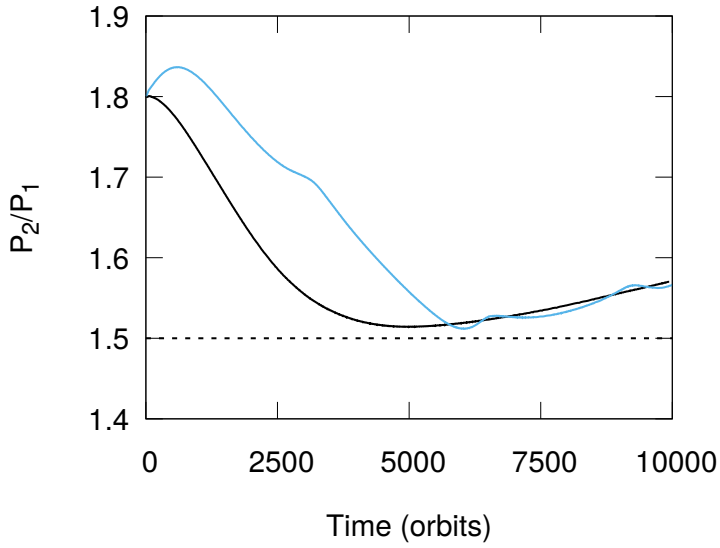

Figure 5.5: Evolution of the period ratio in the simulations with different initial surface density profiles - The comparison between the period ratio evolution of two super-Earths with $q_1 = 1.3 \times 10^{-5}$ and $q_2 = 1.185 \times 10^{-5}$ in the disk with the two different initial surface density profiles: $\Sigma = 8 \times 10^{-5} r^{-1/2}$ (light blue) and the one given in Equation (5.1) with $\Sigma_0 = 6 \times 10^{-5}$ and $\alpha = 0.5$ (black line).

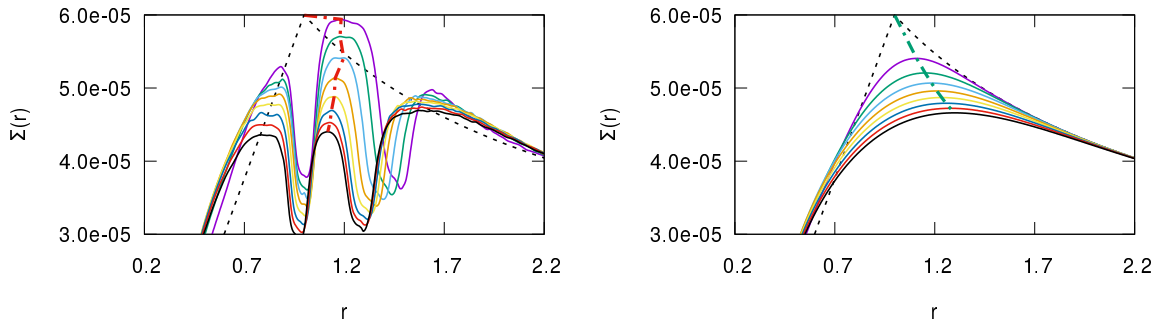

Figure 5.6: Disk evolution with and without super-Earths - The evolution of the surface density in the disk with a central cavity with the planets embedded in it with $q_1 = 1.3 \times 10^{-5}$ and $q_2 = 1.185 \times 10^{-5}$ (left panel) and without planets (right panel). The initial surface density profile (dashed black line) is described by Equation (5.1) with $\Sigma_0 = 6 \times 10^{-5}$ and $\alpha = 0.5$. The solid lines show the surface density profiles at $t = 0, 796, 1592, 2389, 3185, 3981, 4777, 5573$ and 6369 orbits (from the purple solid line to the black solid line). The red dashed-dotted line in the left panel indicates the position of the local maximum of the surface density profile between the planet positions. The green dashed-dotted line in the right panel shows the position of the maximum value of Σ in the disk surface density profile.

We have shown, in this section, that two super-Earths migrating towards the 3:2 mean-motion resonance, instead of being locked in the commensurability, evolve away from it, due to the divergent migration. We are going to demonstrate that the mechanism responsible for such a behavior is the repulsion between the planets caused by the wave-planet interactions. We have already pointed out some conditions, which are essential for this mechanism to work, as for example the formation of the partial gaps, but before providing a full explanation, we need to consider in detail how an isolated, capable to form a partial gap, super-Earth migrates in the disk. We dedicate the next section to this topic.

5.4 Migration of an isolated super-Earth capable to form a partial gap

In this section, we study the evolution of the outer super-Earth ($q = 1.185 \times 10^{-5}$) without the presence of the inner planet in the disk. The super-Earth is able to form a partial gap. We have chosen the disk parameters and the planet mass to arrange for that. In our simulations, presented in the previous section, we verified that it is indeed the case. So, how does such a planet migrate? Is type I migration a good approximation for its evolution in the disk?

The knowledge about the migration of the isolated outer planet will allow for a proper interpretation of the two-planet case. However, to use this knowledge in a meaningful way we need to have roughly the same physical conditions in both cases. As we have already mentioned and illustrated in Figure 5.6, when two planets are present in the disk, the slope of the surface density profile at the outer planet location evolves during the whole simulation, starting from the initial slope with $\alpha = 0.5$, passing through the flat profile ($\alpha = 0.0$) and ending with the positive slope ($\alpha \sim -0.3$). Therefore, we perform three simulations placing an isolated super-Earth initially in the circular orbit at $r = 1.48$ in the disk in exactly the same configuration as the outer planet in the two-planet case described in Section 5.3.2.1. The following disk parameters are the same in all three calculations: $h = 0.02$, $\nu = 1.2 \times 10^{-6}$ and $\Sigma_0 = 6 \times 10^{-5}$. The only difference is in the adopted slope of the surface density distribution. We choose $\alpha = 0.5$ for the initial profile with the negative slope, $\alpha = -0.067$ for the almost flat distribution and $\alpha = -0.3$ for the final profile with the positive slope.

5.4.1 A close look at the vicinity of an isolated super-Earth migrating in the disk

The evolution of the surface density $\Sigma(r)$ in the vicinity of the isolated super-Earth in the simulations with different α is shown in Figure 5.7. We note that the depth of the partial gap opened by the planet increases fast during the first 900 orbits of the evolution in all three cases. After that, the shape of the partial gap does not change significantly, and we can say that it is quasi-stationary. In the bottom right panel of Figure 5.7, we illustrate the comparison of the $\Sigma(r)$ at $t = 1000$ orbits in each simulation. This comparison is done at the time when the formation process of the partial gap can be considered completed. The full width at half maximum gap depth is larger than the disk aspect ratio h and the value of the surface density

at the position of the planet r_p in the bottom of the partial gap is about 68% of the unperturbed value, in all simulations.

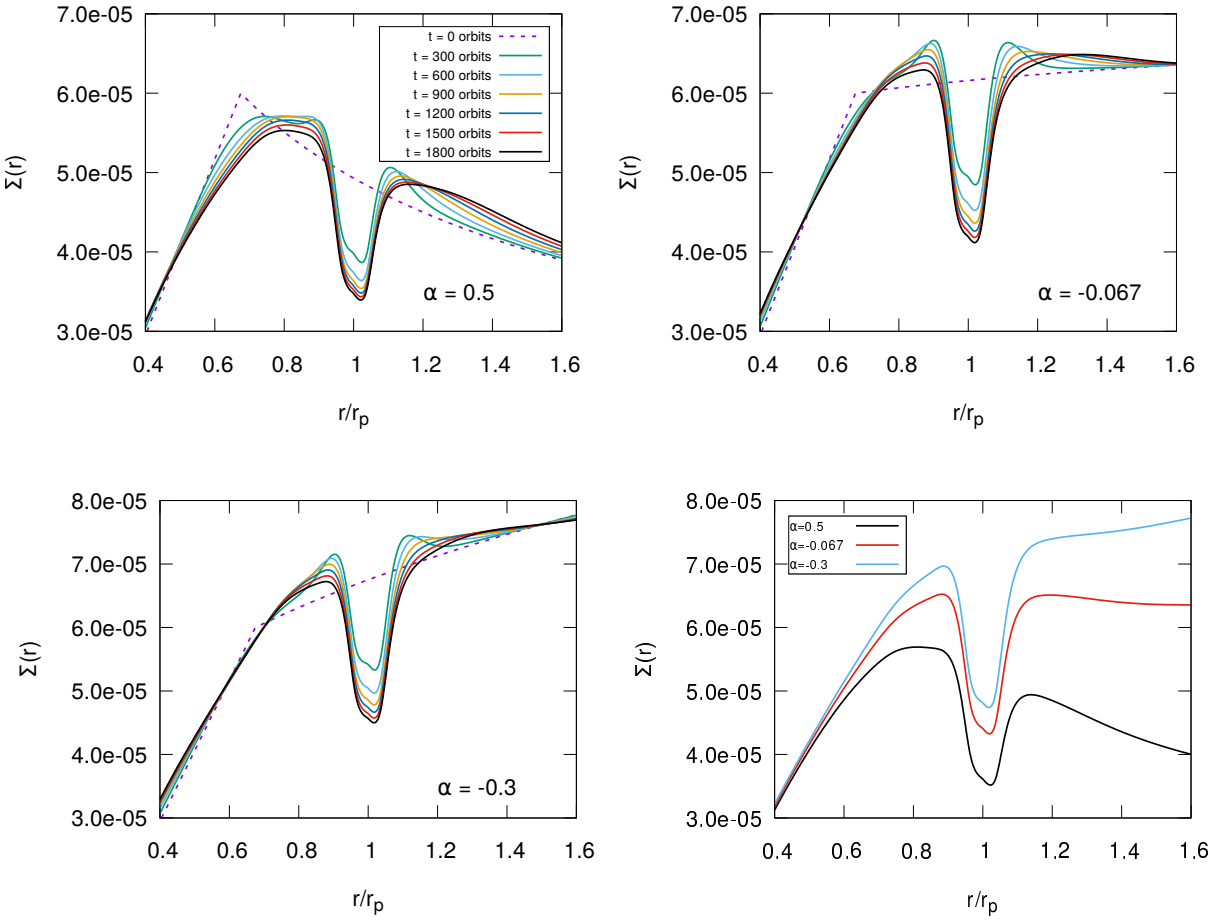

Figure 5.7: Evolution of the partial gap formed in the disk by the isolated super-Earth in the simulations with the different slopes of the surface density profile - The azimuthally averaged surface density around the planet as a function of r/r_p obtained at different moments of time in the simulation for the single planet cases with initial $\alpha = 0.5$ (top left), -0.067 (top right) and -0.3 (bottom left). The disk surface densities at $t = 1000$ orbits in each simulation are illustrated in the bottom right panel.

In order to understand better how the disk-planet interactions operate, it is helpful to consider the relevant length-scales in our calculations. The Hill radius, at the planet position r_p, can be evaluated as $r_H = (q/3)^{1/3} r_p = 0.0158 r_p$. Therefore, it is comparable to the local thickness of the disk, which is $H = h r_p = 0.02 r_p$ in the simulations. The half-width of the horseshoe region, x_s/r_p, can be determined from the topology of the gas flow in the vicinity of the planetary co-orbital region. Considering the low mass planets with small q and the softening parameter b comparable to h in the simulations, [149] estimated $x_s \sim r_p\sqrt{q/h}$. To verify this estimation, we draw in Figure 5.8 the contour plots of the disk surface density in the calculations for the isolated planet cases with $\alpha = 0.5, -0.067$ and -0.3 in the vicinity of the planet, together with the gas

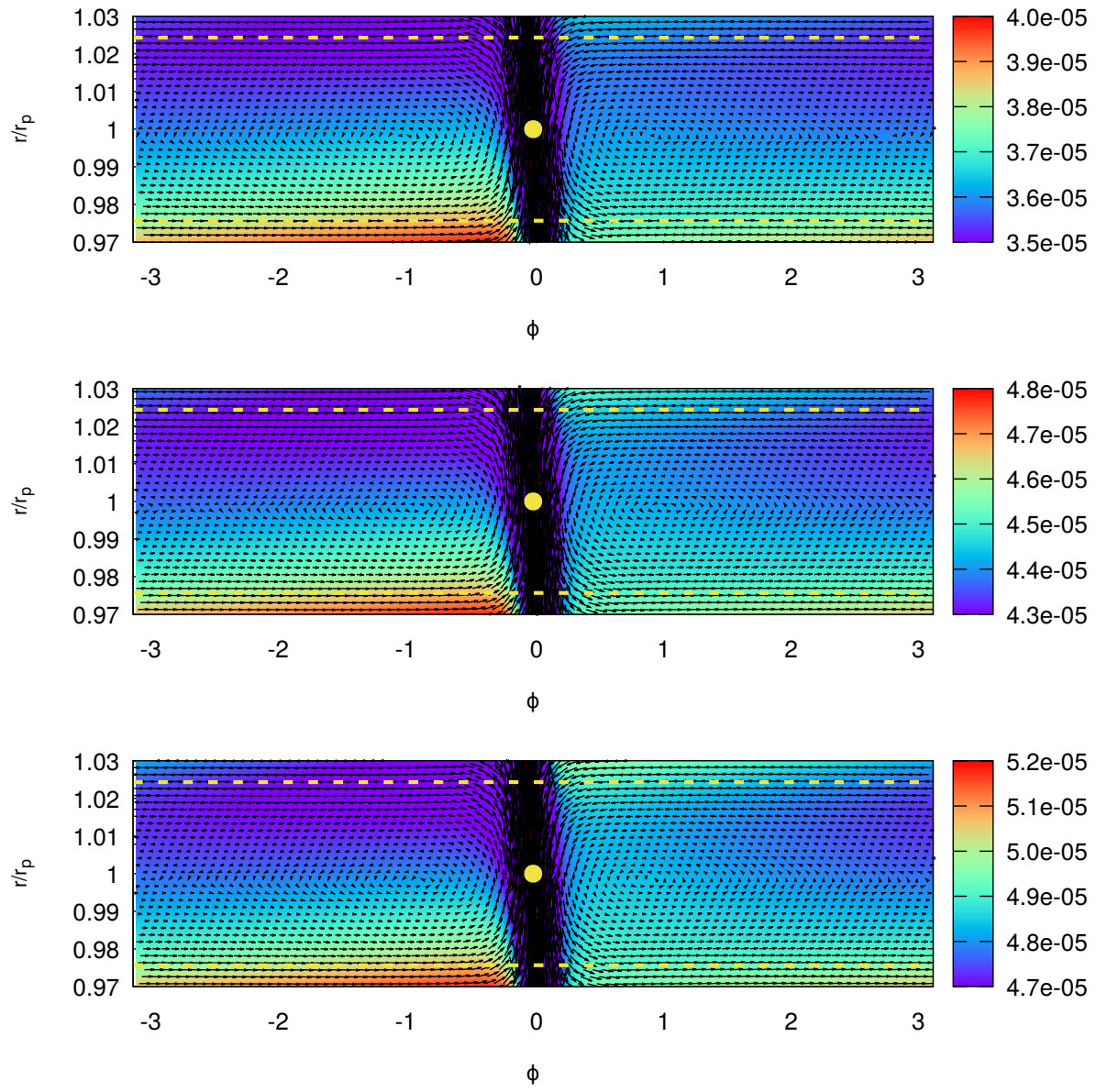

Figure 5.8: Horseshoe region of the super-Earth in the disk with different power-law surface density profiles - The snapshot of the surface density and the velocity of gas flow in the vicinity of the planet at $t = 1000$ orbits in the single super-Earth simulation with $\alpha = 0.5$. The yellow solid circle indicates the position of the planet and the dashed horizontal yellow lines show the position of the separatrix at $r = r_p \pm r_p\sqrt{q/h}$. From top to bottom, the values of α in the initial power-law surface density profiles are taken to be $0.5, -0.067$ and -0.3, respectively.

flow velocity field at t=1000 orbits. From the trend of the gas velocity indicated by the arrows in the disk, we can confirm that the horseshoe region extends approximately from $r = r_p - r_p\sqrt{q/h}$ to $r_\mathrm{p} + r_p\sqrt{q/h}$, as indicated by the dashed yellow lines. Therefore, the half-width of the region x_s is

$$x_s = r_p\sqrt{\frac{q}{h}} = 0.0243 r_p. \tag{5.2}$$

Another interesting quantity to be considered is $2H/3$, related to the positions of $r = r_p \pm 2H/3$, where the Lindblad resonances pile up. These locations are also the regions from where the density waves are first launched in the disk [73]. In our simulations, we have $2H/3 = (2/3)hr_p = 0.013 r_p$.

The last potentially relevant length scale we would like to mention is the non-linear shocking length l_{sh} which is the distance from the planet where its density waves become nonlinear and shocks. It can be calculated as [45]

$$\frac{l_{sh}}{r_p} \approx 0.8 \left(\frac{\gamma+1}{12/5}\frac{m_p}{M_{th}}\right)^{-2/5} h \tag{5.3}$$

with $M_{th} = c_s^3/(\Omega_p G)$ while m_p and γ denote the mass of the planet and the adiabatic index, respectively. In our simulations, we have $l_{sh} = 0.0147 r_p$, which is smaller than x_s and very close to $2H/3$. Therefore the density waves can be treated as nonlinear when they are launched.

In Figure 5.9, we illustrate how the characteristic lengths mentioned above denoted by the different types of the vertical lines compare with the widths of the partial gaps formed by the isolated planet in each simulation. All those length scales are smaller than the widths of the gaps and are located in the bottom of the partial gaps.

5.4.2 Torque exerted by the disk on the isolated planet with a partial gap

Now we discuss the torques exerted by the disk on the isolated super-Earth that derive the planet migration. We confirmed that the super-Earth opens a partial gap in its orbit and that the opening process is completed in the first 900 orbits of the super-Earth evolution in the disk. Therefore, we plot in Figure 5.10, the total torque Γ_total from the disk acting on the super-Earth, obtained from the three hydrodynamical simulations, lasted for 1000 orbits each, with different initial surface density slopes, α. The total torques are indicated by the black lines.

Firstly, we compare the numerical torque obtained from the simulations with the torque calculated from the formula of the type I migration. As discussed in Section 2.3.1, the migration of the low-mass planet which cannot open a partial gap in the disk can be approximately treated as the type I migration. In this regime the Lindblad torque is calculated from the linear theory. Therefore, the total torque acting on the planet is the sum of the linear Lindblad torque and the corotation torque. The formulae for these two torques in a locally isothermal disk are obtained from Equation (2.35) and Equation (2.42) by taking $\gamma = 1, \beta = 1$ and $b/h = 0.6$, which have the following form [150]:

$$\Gamma_\mathrm{L}/\Gamma_0 = -3.15 + 0.075\alpha_p \tag{5.4}$$

$$\Gamma_\mathrm{C}/\Gamma_0 = 1.905 - 0.73\alpha_p \tag{5.5}$$

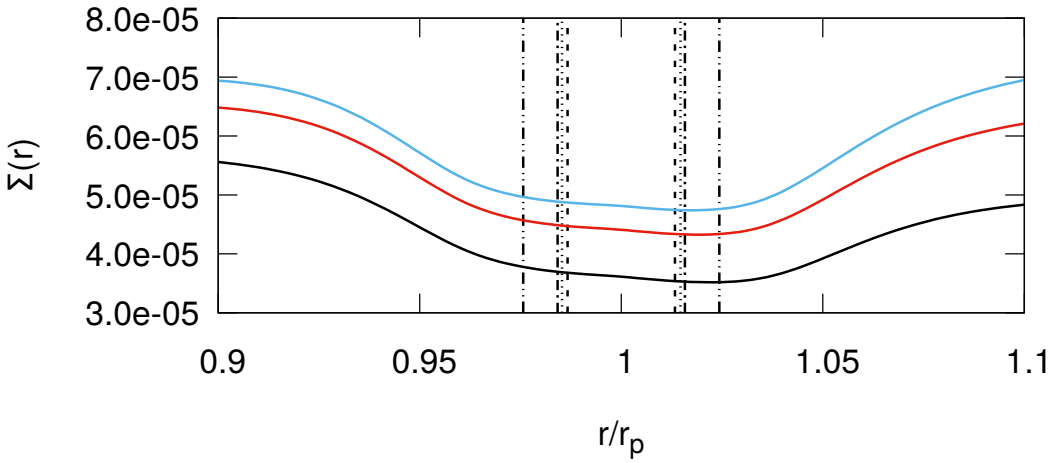

Figure 5.9: The characteristic length scales compared to the width of the partial gaps - The characteristic scales in three isolated super-Earth simulations, which are illustrated by the various types of the vertical lines, from the closest to the planet and proceeding to the furthest one indicate the scales of $2H/3$ (dashed), l_{sh} (dotted), r_H (dash-dotted) and x_s (dash double-dotted lines). The surface density profiles of the disk in the vicinity of the planet are taken at $t = 1000$ orbits, when the position of the planet is $r_p \sim 1.413$. The different colors of the profiles indicate the results of the simulations with α of 0.5 (black), -0.067 (red) and -0.3 (blue lines).

with

$$\Gamma_0 = (q/h)^2 \Sigma_{p,un} r_p^4 \Omega_p^2 \tag{5.6}$$

where α_p and $\Sigma_{p,un}$ are the density slope and the unperturbed surface density at the position of the planet, respectively while Ω_p is the angular velocity of the planet. Therefore, the total torque for type I migration in a locally isothermal disk is as follows:

$$\frac{\Gamma_{\rm total}}{\Gamma_0} = \frac{\Gamma_{\rm L}}{\Gamma_0} + \frac{\Gamma_{\rm C}}{\Gamma_0} = -1.245 - 0.655\alpha_p. \tag{5.7}$$

Based on this formula, we calculate the type I migration torque for the isolated super-Earth in each simulation, which is indicated by the orange asterisks in Figure 5.10. The parameters used for each of the three cases are given in Table 5.2. It is important to stress that α_p is measured by fitting the azimuthally averaged surface density in the region of $[r_p - x_s, r_p + x_s]$ with the formula of $\Sigma(r) \propto r^{-\alpha_p}$. Since the horseshoe region of the super-Earth is located inside the partial gap (see Figure 5.9), the density slope α_p is taken at the bottom of the gap and not at the background disk.

The comparisons shown in Figure 5.10 indicate that the torques calculated by Equation (5.7) (indicated by the orange asterisks) agree quite well with the numerical torques obtained from the simulation with $\alpha = 0.5$ for the negative slope of the initial surface density profile. In two other simulations, with the flat initial profile ($\alpha \sim 0$) and the positive slope of the initial profile ($\alpha < 0$), the agreement is not so good. It means that the corotation and Lindblad torques are affected by the existence of the partial gap.

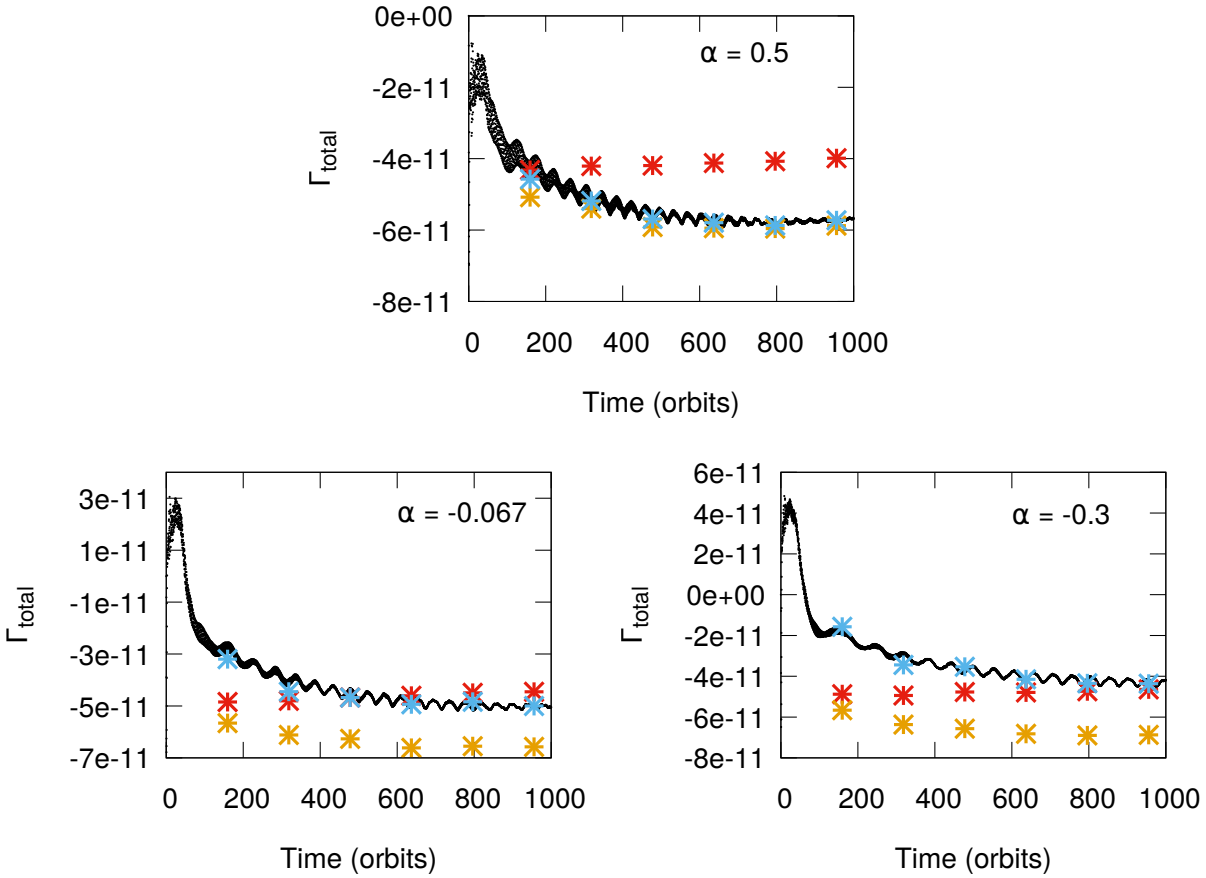

Figure 5.10: Theoretical and numerical torques from the disk acting on the isolated super-Earth - The total torque from the disk acting on the planet in the simulations with different values of α. The orange asterisks show the torques calculated from the formula of the type I migration for the planet embedded in the locally-isothermal disk. The red and blue asterisks indicate the torque calculated from Equation (5.9) and Equation (5.11).

Next, we make an attempt to modify the type I formula to take into account the effect of the presence of the partial gap around the super-Earth orbit. During the gap formation, the slope of the surface density profile in the vicinity of the planet changes in time and becomes different from the initial value (see Table 5.2). Moreover, the surface density at the planet position changes in time and is lower than the unperturbed value. In light of the surface density depression in the partial gap, we rescale the above expressions for the corotation torque and the Lindblad torque as follows

$$\begin{aligned} \Gamma'_{\rm C}/\Gamma_0 &= (\Sigma_{p,min}/\Sigma_{p,un})(\Gamma_{\rm C}/\Gamma_0) \quad \text{and} \\ \Gamma'_{\rm L}/\Gamma_0 &= (\Sigma_{p,min}/\Sigma_{p,un})(\Gamma_{\rm L}/\Gamma_0), \end{aligned} \tag{5.8}$$

where $\Sigma_{p,min}$ is the surface density at the position of the planet at the bottom of the partial gap. Therefore, the total torque is evaluated as:

$$\frac{\Gamma'_{\rm total}}{\Gamma_0} = \left(\frac{\Gamma_{\rm L}}{\Gamma_0} + \frac{\Gamma_{\rm C}}{\Gamma_0}\right)\frac{\Sigma_{p,min}}{\Sigma_{p,un}} = (-1.245 - 0.655\alpha_p)\frac{\Sigma_{p,min}}{\Sigma_{p,un}}. \tag{5.9}$$

We compare the torque calculated from this modified formula (indicated by red asterisks) with our numerical results in Figure 5.10. It is clear that the fit is not good either. Such discrepancy is expected since the Lindblad torque originates from beyond the partial gap and may not be well represented by linear theory.

Table 5.2: Numerical parameters for the torque calculation in the isolated super-Earth cases

$\alpha = 0.5$				
Time (orbits)	α_p	$\Sigma_{p,un}$ $(\cdot 10^{-5})$	$\Sigma_{p,min}$ $(\cdot 10^{-5})$	r_p
159	1.098	5.00	4.25	1.4729
318	1.258	5.08	3.96	1.4630
478	1.386	5.39	3.82	1.4519
637	1.437	5.38	3.73	1.4403
796	1.477	5.37	3.67	1.4284
955	1.471	5.35	3.63	1.4165
$\alpha = -0.067$				
Time (orbits)	α_p	$\Sigma_{p,un}$ $(\cdot 10^{-5})$	$\Sigma_{p,min}$ $(\cdot 10^{-5})$	r_p
159	0.783	6.21	5.32	1.4776
318	0.986	6.27	4.92	1.4701
478	1.047	6.33	4.72	1.4613
637	1.108	6.59	4.59	1.4514
796	1.113	6.56	4.50	1.4412
955	1.155	6.54	4.43	1.4308
$\alpha = -0.3$				
Time (orbits)	α_p	$\Sigma_{p,un}$ $(\cdot 10^{-5})$	$\Sigma_{p,min}$ $(\cdot 10^{-5})$	r_p
159	0.564	6.75	5.82	1.4801
318	0.809	6.93	5.38	1.4747
478	0.841	7.10	5.16	1.4675
637	0.937	7.16	5.03	1.4595
796	0.978	7.18	4.93	1.4509
955	0.997	7.15	4.83	1.4421

In order to obtain the formula to calculate the total torque in a good agreement with the numerical torques obtained in our simulations, we perform a fit to derive values of $\Gamma_{\rm total}$ at t = 1000 orbits for each of the three numerical simulations that were carried out with different initial profiles of the surface density in the disk. The choice of the moment of time (t = 1000 orbits) to be used for this procedure is justified by the requirement that the partial gap formed in the disk is to a good approximation stationary.

The fitted formula has the same form as Equation (5.9), but with two constant coefficients C_1 and C_2 introduced to rescale the contributions of the corotation and Lindblad torques, respectively. Therefore, the fitted formula has the form

$$\frac{\Gamma''_{\rm total}}{\Gamma_0} = \left(C_1 \frac{\Gamma_{\rm L}}{\Gamma_0} + C_2 \frac{\Gamma_{\rm C}}{\Gamma_0} \right) \frac{\Sigma_{p,min}}{\Sigma_{p,un}}. \tag{5.10}$$

We find that the best fit to the numerical results can be obtained for $C_1 = 2.2003$ and $C_2 = 4.2310$, which gives

$$\frac{\Gamma''_{\rm total}}{\Gamma_0} = (1.129 - 2.924\alpha_p)\frac{\Sigma_{p,min}}{\Sigma_{p,un}}. \tag{5.11}$$

This fit reduces the contribution of the Lindblad torque relative to the corotation torque, which is consistent with the expectation that here the Lindblad torque should be smaller than that estimated from the linear theory.

Using Equation (5.11) we calculate the total torque at few moments of time and the results are indicated by the blue asterisks in Figure 5.10. The comparison shows that after 200 orbits, the torque from the fitted formula is consistent with the numerical torques in all three cases. We emphasize that this fitting procedure is not available for a general case and Equation (5.11) can only be used in the limited parameter range determined by those three simulations on which it has been based.

In this section, we have analyzed the migration of the isolated super-Earth capable to form a partial gap in the disk. We have demonstrated that the migration of such a planet is not that of the type I and we have derived the phenomenological formula, which approximately reproduce the torque exerted by the disk on the planet. In the next section we come back to the two-planet system and its evolution described in Section 5.3. Our attention will be directed to examining how the presence of the second super-Earth in the interior orbit in this system, influences the migration of the outer super-Earth.

5.5 Migration of two super-Earths capable of forming partial gaps in the disk: Torque exerted by the disk on the outer planet

In the previous section, we have derived a phenomenological formula, which allow to calculate the torque from the disk acting on an isolated super-Earth migrating in the disk. Now we apply this formula to describe the migration of the outer planet in the case when there is another super-Earth in the disk, which is also able to form a partial gap around its orbit. Our aim here is to find out how the presence of the second low-mass planet in the disk affects the migration described in the previous section. This is a crucial step in understanding the nature of the divergent migration observed in Section 5.3.

In Figure 5.11, we plot the numerical torque $\Gamma_{\rm total-outer}$ exerted from the disk on the outer planet in the simulation for the reference case (black line). Using our phenomenological formula given in Equation (5.11), we calculate the torque acting on the planet, which is expected from the isolated planet case displayed in the same figure (blue asterisks). For completeness we illustrate also results for the torques obtained from Equation (5.7) (orange asterisks) and Equation (5.9) (red asterisks) for the isolated outer planet. All the parameters adopted in the reference case necessary to calculate the torques are given in Table 5.3. Considering that our phenomenological formula is obtained from the simulations for the isolated super-Earth case, in which α_p is in the range of [0.564, 1.477] (see Table 5.2), it can only be applied to get the torques for the outer planet after 3000 orbits, when α_p is exactly in that range.

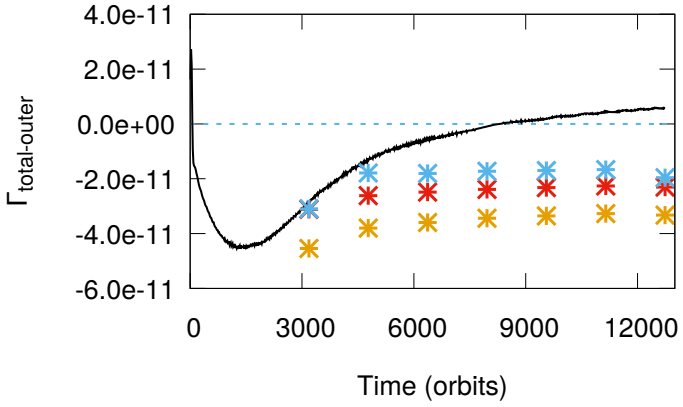

Figure 5.11: The torque exerted from the disk on the outer planet in two super-Earth case - The total torque from the disk acting on the outer planet in the simulation of two super-Earths for the reference case (the results are shown in Figure 5.4). The orange asterisks indicate the torques calculated from the classical type I migration formula for the outer planet embedded in the locally-isothermal disk. The red and blue asterisks represent the torques calculated from Equation (5.9) and Equation (5.11), respectively.

Table 5.3: Numerical parameters for the torque calculation in two super-Earth case

Time (orbits)	α_p	$\Sigma_{p,un}$ $(\cdot 10^{-5})$	$\Sigma_{p,min}$ $(\cdot 10^{-5})$	r_p
3185	1.0416	5.03	3.45	1.3349
4777	0.7997	4.72	3.25	1.2968
6369	0.8302	4.48	3.10	1.2782
7962	0.8289	4.31	2.99	1.2719
9554	0.8349	4.19	2.90	1.2734
11146	0.8375	4.06	2.81	1.2798
12739	0.9249	3.97	2.75	1.2896

From the comparison shown in Figure 5.11, we infer that if there is no inner planet in the disk, the torque acting on the outer planet should be negative during the whole calculation and thus it should migrate inwards. However, we notice that starting from $t \sim 5000$ orbits, when the divergent migration occurs (see Figure 5.4), the torque calculated from our phenomenological formula for the isolated super-Earth case becomes less than the numerical torque in the case of two super-Earths. Moreover, after 9000 orbits, the torque acting on the outer planet in the case of two super-Earths becomes positive and the outer planet begins to migrate outwards. This comparison shows that there must be a mechanism operating in the system, by which angular momentum is transferred between the planets, providing an additional torque acting on the outer planet. The angular momentum transfer can take place through direct gravitational interaction between planets, and/or indirectly, first to the horseshoe region of the outer planet and then to the planet itself. The direct gravitational interaction between planets is going to be relevant very close to the positions of the mean-motion resonances. However, already [21] found that the mechanism still works when gravitational interaction between the planets was switched off in their simulations. We have confirmed this finding in our simulations concerned with two

super-Earths, shown in Figure 5.3. The conclusion is clear, something more is needed to explain the divergent migration of the planets. The nature of the repulsion mechanism mentioned as the second possibility is connected with the wave-planet interactions, discussed in Chapter 4, and will be explored in the next Section in detail.

5.6 Criteria for the effective repulsion between two planets resulting from wave-planet interactions

In this section, we investigate the repulsion between two low-mass planets resulting from the wave-planet interactions and derive the conditions, which must be satisfied for the planets to repel each other effectively. The effective repulsion will change the convergent migration of two planets to divergent, and prevent the resonance capture. According to the scenario of the wave-planet repulsion mechanism, the angular momentum is transferred, in the first place, by the density waves excited by one planet (a wave emitter) to the horseshoe region of the second planet (a receiver), and then to the planet itself through the horseshoe drag. The analysis of each phase of the mechanism operating in the disk will give us a criterion for the effectiveness of the repulsion between planets. First, we consider the dissipation of the outward propagating density waves in the co-orbital region of the receiver and next we discuss the action of the horseshoe drag.

5.6.1 The angular momentum deposited in the planet's horseshoe region by the propagating density waves: Criterion 1

For convenience, we assume that the inner planet is a wave emitter and that the density waves excited by the inner planet transfer the angular momentum to the co-orbital region of the outer planet. The angular momentum transport in the opposite direction, in the situation when the outer planet is an emitter and the inner one is a receiver, can be analyzed in the same way.

We start our deduction from a simple expression of the linear Lindblad torque. Considering that the Lindblad torque is insensitive to the background surface density profile of the disk, the Lindblad torque induced by the unperturbed disk with background surface density Σ_{un} can be expressed as

$$\Gamma_L = -3.075 q^2 \Sigma_{un} r^4 \Omega^2 h^{-2} \tag{5.12}$$

which is obtained from Equation (5.4) with the slope of a representative value $\alpha_p = 1$.

As mentioned in Section 2.3.1.1, the net Lindblad torque is the sum of the one-sided Lindblad torques separately induced by the outer disk beyond the planet and the inner disk interior to it. For the inner planet, the outer one-sided Lindblad torque can be approximately given by $\Gamma_{L(1s)} = \Gamma_L/(5.7h)$ [159]. Therefore, we adopt

$$\Gamma_{L(1s)} = -0.54 q_1^2 \Sigma_{un} r^4 \Omega^2 h^{-3} \tag{5.13}$$

where q_1 is the mass of the inner planet, which is treated here as a wave emitter.

Considering that the outer planet is approaching to the inner one due to the convergent migration, the outward propagating density waves excited by the inner planet dissipate in the

co-orbital region of the outer planet. During this process, some of the angular momentum carried by the density waves can be transferred into the horseshoe region and then to the outer planet itself through the horseshoe drag. Assuming that a fraction of the angular momentum flow, namely $2\lambda x_s/r_p$, is transferred to the horseshoe region of the outer planet, we estimate the effective angular momentum transfer rate into the horseshoe region of the outer planet to be $|\Gamma_{L(1s)}|2\lambda x_s/r_p$. Here λ is a dimensionless constant, which is expected to be of order unity. Taking $x_s = r_p\sqrt{q/h}$ (Equation (5.2)), we obtain

$$|\Gamma_{L(1s)}|2\lambda\sqrt{q_2/h} \sim 1.08\lambda\sqrt{q_2}q_1^2\Sigma_{un}r^4\Omega^2h^{-7/2}, \tag{5.14}$$

where q_2 is the mass of the outer planet, or in general of the receiver. In order to make the repulsion of the outer planet significant, the effective angular momentum transfer rate, given in Equation (5.14), should exceed the torques responsible for convergent migration, which we estimate to be of magnitude $f|\Gamma_L|$ for the inner planet (a wave emitting planet), where f is a dimensionless constant that can be of order but usually less than unity. Therefore, we require $|\Gamma_{L(1s)}|2\lambda\sqrt{q_2/h} \gtrsim f|\Gamma_L|$, which gives

$$\frac{q_2}{h^3} \gtrsim 8.1\left(\frac{f}{\lambda}\right)^2. \tag{5.15}$$

When $f \sim \lambda/3$, the right hand side of this inequality is around unity and the criterion given in Equation (5.15) has the same form as the thermal condition for the disk response to the planet gravity being nonlinear and the gap formation [157]. Thus the first condition for the efficient repulsion mechanism due to wave-planet interactions, just derived, is that the planet is able to form a partial gap.

To be more rigorous, we add here few comments, which extend the validity of the derived criterion to the more general physical situation. In the discussion above, we consider only the angular momentum carried by the density waves to the horseshoe region of the outer planet. However, the angular momentum can be also supplied to the planet by the material just exterior to the horseshoe region through scattering. This may be taken into account by adopting a larger value for λ, which would make this condition easier to satisfy.

Another cause of concern is that we used linear Lindblad torques to derive our criterion, whereas as illustrated in Figure 5.9 x_s/r_p is larger than $2h/3$ for our simulations so, we expect the torques to have been over estimated. We allow for this in an approximate manner by replacing h by $3x_s/(2r_1)$ with $x_s/r_1 = \sqrt{q_1/h}$, where r_1 is the orbital radius of the inner planet, when calculating Γ_L and $\Gamma_{L(1s)}$. In this way, the inequality (5.15) becomes

$$\frac{q_2}{q_1} \gtrsim 18.3\left(\frac{f}{\lambda}\right)^2 \tag{5.16}$$

which will be satisfied for sufficiently slow convergent migration. Apparently, it seems that this criterion has nothing to do with the formation of the partial gap. However, we recall that this criterion was derived under the condition of $x_s > 2H/3$. If it is satisfied together with (5.16), we must have

$$\frac{q_2}{h^3} > 8.1\left(\frac{f}{\lambda}\right)^2. \tag{5.17}$$

Hence, we have recovered the condition implying the existence of a partial gap as before.

Now we discuss the quantity λ which appears in the condition (5.15). It was introduced in the definition of the fraction of the angular momentum flux produced by the inner planet that is absorbed in the horseshoe region of the outer planet, given in the form $2\lambda\sqrt{q_2/h}$. If $\lambda = 1$, it corresponds to the case such that the angular momentum flux is absorbed uniformly over a scale of the orbital radius of the outer planet r_2 and the amount of absorption in any radial interval is proportional to its extent. However, the angular momentum flux is likely to decrease more rapidly with the increased distance x from the planet emitting the density waves. In [45], it has been suggested that the flux is $\propto x^{-5/4}$, which implies that the fraction absorbed in the horseshoe region is $2.5\sqrt{q_2/h}(r_2/x)(L/x)^{5/4}$. Here, L denotes the distance from the emitting planet beyond the place where the power law drop off is valid. By assuming $L = 2x_s$, which roughly corresponds to the gap width (see Figure 5.9), the fraction absorbed in the horseshoe region is $5.2^{1/4}\sqrt{q_2/h}(r_2/x)(x_s/x)^{5/4}$. This gives $\lambda = 5.2^{-3/4}(r_2/x)((x_s/x)^{5/4}$. Taking $x_s/r_1 = 0.0243$ (see Equation (5.2)) and a separation corresponding to the 3:2 MMR, we obtain $\lambda \sim 0.56$. Therefore, λ is plausibly of order unity for the parameters considered here.

5.6.2 The angular momentum transfer from the planet's horseshoe region to the planet itself through horseshoe drag: Criterion 2

In Section 5.6.1 we have obtained one condition, namely (5.15), which tells us that to make the repulsion between planets effective the planet should be able to form a partial gap along its orbit. This condition has been derived from the requirement that the effective angular momentum transfer rate between the propagating density wave and the material in the horseshoe region must exceed the torques responsible for convergent migration.

The final phase of the repulsion mechanism is the transfer of the deposited, in the planet's horseshoe region, angular momentum to the planet itself through horseshoe drag. To make the repulsion between planets effective, also this phase need to lead to the effective transfer of angular momentum. Therefore, the first condition must be satisfied, which means that the planet formed the partial gap and the material in the horseshoe region now in the gap region can transport the angular momentum deposited by waves to the planet through the horseshoe drag. Due to the strong density perturbation in the gap, our approach must differ from that appropriate for the situation where there is no gap. The question is when the horseshoe drag is most effective. This is when it only works on one side of the planet. In the case considered here, namely when the angular momentum is transferred by the outward propagating density waves towards the outer planet, this will be the leading side of the planet. On the trailing side we suppose that material approaching the planet absorbs angular momentum from the waves causing the horseshoe turn to occur at significant distances from the planet.

The one-sided horseshoe drag results in

$$\Gamma_{hsl} = \frac{1}{2}\Sigma_{min}\Omega^2 r x_s^3 = \frac{1}{2}\Sigma_{min}\Omega^2 r^4 (q_2/h)^{3/2}, \tag{5.18}$$

where r and Ω are evaluated at the position of the outer planet while Σ_{min} is the minimum surface density at the bottom of the partial gap. The effective angular momentum transfer to

the outer planet can take place if

$$\Gamma_{hsl} > |\Gamma_{L(1s)}| 2\lambda \sqrt{q_2/h}, \tag{5.19}$$

where $\Gamma_{L(1s)}$ is the one-sided Lindblad torque of the inner planet. Taking its form from Equation (5.13), we obtain

$$\left(\frac{\Sigma_{min}}{\Sigma_{un}}\right)_2 > \left(\frac{2.16\lambda q_1^2}{q_2 h^2}\right)\left(\frac{(\Sigma_{un} r^4\Omega^2)_1}{(\Sigma_{un} r^4\Omega^2)_2}\right), \tag{5.20}$$

where the parameters inside the brackets with the subscripts of 1 and 2 are calculated at the locations of the inner and outer planets, respectively. We remark that we have used the linear Lindblad torque which, being an overestimate, will not disturb conclusions obtained from the above condition.

As we have mentioned, the material slightly exterior to the horseshoe region may also transfer the angular momentum brought in by the density waves through scattering, and this can be incorporated by choosing a larger value of λ in condition (5.15). In this situation, less angular momentum transport from the horseshoe region to the planet would be required than it is assumed here. Accordingly, if the criterion (5.20) is satisfied, we can be assured that it will be able to sustain the required transport.

At this point we have completed the derivation of the conditions for effective planet repulsion. We have formulated two conditions and they are given in (5.15) and (5.20). Here, the wave emitting planet has mass ratio q_1 and the receiving planet mass ratio q_2, but the roles may be easily reversed. It is sufficient to interchange q_1 and q_2 and the subscripts 1 and 2 in these conditions. While doing this we assume that the value of λ remains the same. The two criteria, after reversing the roles of the emitter and the receiver can be written as follows

$$\frac{q_1}{h^3} \gtrsim 8.1\left(\frac{f}{\lambda}\right)^2 \tag{5.21}$$

and

$$\left(\frac{\Sigma_{min}}{\Sigma_{un}}\right)_1 > \left(\frac{2.16\lambda q_2^2}{q_1 h^2}\right)\left(\frac{(\Sigma_{un} r^4\Omega^2)_2}{(\Sigma_{un} r^4\Omega^2)_1}\right). \tag{5.22}$$

Now we can check, if the derived conditions are satisfied in our calculations with $q_1 = 1.3 \times 10^{-5}$ and $q_2 = 1.185 \times 10^{-5}$. The first condition $q_2/h^3 = 1.48 > 8.1(f/\lambda)^2$ is satisfied for $f \lesssim 0.43\lambda$. The second criterion is also fulfilled, because it is sufficient that $(\Sigma_{min}/\Sigma_{un})_2 > 0.052\lambda$, which is exactly the case if λ does not exceed a factor of ~ 4. If we apply the two criteria to the inner planet as a receiving planet, than we obtain that the first criterion $1.6 > 8.1(f/\lambda)^2$ is satisfied for $f \lesssim 0.44\lambda$ while the second one requires $(\Sigma_{min}/\Sigma_{un})_1 > 0.059\lambda$, which is also satisfied for λ not exceeding a factor of ~ 4 as above. This means that in our simulations with $q_1 = 1.3 \times 10^{-5}$ and $q_2 = 1.185 \times 10^{-5}$, we should expect the effective repulsion between planets. We have shown that the effective angular momentum transfer between the planets resulting from wave-planet interactions, both from inner to outer planet and outer to inner planet can readily occur, particularly for slow enough convergent migration. We can say even more, namely reversing the planet positions, placing the inner one at the position of the outer planet and vice versa will lead to the same conclusion. In the next sections we will verify our prediction.

5.6.3 The wave-planet repulsion mechanism at work in two super-Earths case

We have derived the criteria for the effectiveness of the repulsion between two super-Earths due to the wave-planet interactions and found that they are satisfied in our simulation with $q_1 = 1.3 \times 10^{-5}$ and $q_2 = 1.185 \times 10^{-5}$ (shown in Figure 5.4). Now we take a closer look at this mechanism to demonstrate that the repulsion between the planets observed in our simulations is indeed of the postulated here nature. In other words, we demonstrate that the angular momentum carried by the waves is transferred to the horseshoe region and then to the planet itself through horseshoe drag.

To do so, we start from the calculation of the angular momentum flux carried by the density waves excited by the inner planet and propagating towards the outer planet. The wave angular momentum flux as a function of r, which represents the angular momentum flow across a circle of radius r, can be calculated as follows

$$F_{\rm wave} = r^2 \bar{\Sigma} \int_0^{2\pi} (v_\phi - \bar{v}_\phi)(v_r - \bar{v}_r) d\phi \tag{5.23}$$

where $\bar{\Sigma}$ is the azimuthally averaged surface density defined as $\bar{\Sigma} = \frac{1}{2\pi} \int_0^{2\pi} \Sigma d\phi$ while $\bar{v}_\phi$ and $\bar{v}_r$ are the azimuthally averaged velocity in the azimuthal and radial directions, respectively. This is correct to second-order in perturbations around the background state and should be adequate for the small amplitude waves considered. The wave angular momentum flux in the simulation for our reference case, calculated based on Equation (5.23), is indicated by the black line in the left panel of Figure 5.12. It might be helpful to recall here the characteristics of our reference case, which was presented in Section 5.3.2.1. The reference case is a system of two super-Earths with $q_1 = 1.3 \times 10^{-5}$ and $q_2 = 1.185 \times 10^{-5}$ evolving in the disk with $h = 0.02$, $\nu = 1.2 \times 10^{-6}$, the initial surface density profile with a central cavity, $\Sigma_0 = 6 \times 10^{-5}$ and the slope $\alpha = 0.5$.

It should be noticed that the wave angular momentum flux $F_{\rm wave}$ illustrated in the panel has contributions from the density waves of both planets in the disk and what we actually need is the flux carried by the waves excited only by the inner planet. To extract the density contribution of the inner planet, first, we rerun the simulation for the reference case, removing the outer planet from the disk. Hereafter, we will refer to this calculation as the single planet case. In addition, following [73], we evaluate the angular momentum flux carried by the density wave constituting the wake of a planet in a non-self-gravitating disk, using the following expression

$$F_{\rm J}(r) = \frac{c_s^3 r_p^2}{|(r - r_p) r d\Omega/dr| \Sigma_0} \int_{-\pi}^{\pi} (\Sigma - \Sigma_0)^2 d\phi \tag{5.24}$$

where Σ_0 denotes the unperturbed surface density.

The angular momentum fluxes calculated by Equation (5.23) and Equation (5.24) at $t = 1000$ orbits in the single planet case are presented in the right panel of Figure 5.12. A very good agreement between the fluxes, shown in this figure, indicates that the wave angular momentum flux generated by a single planet can be well described by Equation (5.24).

Now, we are well prepared to come back to our reference case and perform the analysis of the angular momentum transfer in the two planet system. We calculate the angular momentum fluxes expected to be generated by the inner and outer planet separately using Equation (5.24)

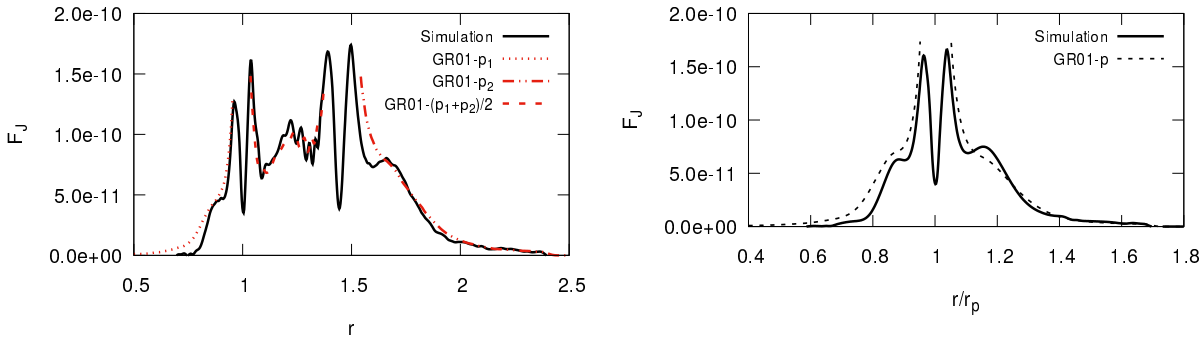

Figure 5.12: Theoretical and numerical angular momentum flux carried by the density waves excited by the super-Earth in the disk - The comparison of the angular momentum flux calculated by Equation (5.23) and Equation (5.24) in the reference case (left panel) and the single planet case (right panel) at t = 1000 orbits.

and then combine them in a way that should represent the total angular momentum flux in a radial interval between the planets when the wakes do not interact. The expression used for that has the form

$$F_{\rm J}(r) = \left(\frac{r_1^2}{|r - r_1|} + \frac{r_2^2}{|r - r_2|} \right) \frac{c_s^3}{|2rd\Omega/dr|\Sigma_0} \int_{-\pi}^{\pi} (\Sigma - \Sigma_0)^2 d\phi \tag{5.25}$$

The total angular momentum flux, calculated in this way, is shown in the left panel of Figure 5.12 denoted by the red dashed line. In addition, the wave fluxes generated separately from the inner and outer planets, obtained from Equation (5.24), are presented in the same panel and they are indicated by the red dotted line and dashed double dotted line, respectively.

The comparison shown in the left panel of Figure 5.12 allows to conclude that:

1. In the inner part of the disk ($r < r_1$), the wave angular momentum flux calculated by Equation (5.23) and the angular momentum flux carried by the density wave constituting the wake of a planet obtained from Equation (5.24) applied to the inner planet, agree with each other. This is because in this region, the disk is mainly perturbed by the interior wake of the inner planet.

2. In the central part of the disk ($r_1 < r < r_2$), the wakes of both planets perturb the disk with similar strength. The wave angular momentum flux is consistent with the contribution from the two planets expressed by Equation (5.25). Based on this comparison, we confirm that the angular momentum fluxes calculated from Equation (5.24) and Equation (5.25) as applicable, which are based on the theoretical consideration of the effects arising from the planetary wakes, agree with the values of the angular momentum flux seen in our simulations.

3. In the outer part of the disk ($r > r_2$), the wave angular momentum flux calculated by Equation (5.23) and the angular momentum flux carried by the density wave constituting the wake of a planet obtained from Equation (5.24) applied to the outer planet, also agree with each other. This is because in this region, the disk is mostly disturbed by the exterior wake of the outer planet.

The repulsion between planets requires the presence of an additional torque acting on the planets, which is absent in the case of the single planet evolving in the disk. We have postulated and then demonstrated that the theoretical consideration of the effects arising from the planetary wakes, agree with the values of the angular momentum flux seen in our simulations. Now, we provide next strong argument in favor of our interpretation of the repulsion mechanism by estimating the additional torque acting on the outer planet generated by the angular momentum flux transferred into its horseshoe region via density waves emitted by the inner planet. The transfer of the angular momentum to the horseshoe region was expressed in terms of the angular momentum flow induced by a planet towards the other planet. Considering the angular momentum transfer from the inner planet to the horseshoe region of the outer planet, we recall the expression for it given by the left hand side of Equation (5.14) in the form

$$\Gamma_{12hs} = |\Gamma_{L(1s)}| 2\lambda \sqrt{q_2/h} \tag{5.26}$$

where $|\Gamma_{L(1s)}|$ can be estimated from the flux generated by the inner planet when isolated illustrated in Figure 5.12 (right panel). From this figure, we can see that the total angular momentum flux produced is $\sim 1.7 \times 10^{-10}$ in the code units. This gives an estimate of Γ_{12hs} as follows $\Gamma_{12hs} \sim 0.83\lambda \times 10^{-11}$. Moreover, from the same figure we can read out the angular momentum flux at the location $r = 1.31 r_1$, corresponding to the location of a 3:2 resonance, which is $\sim 2 \times 10^{-11}$. Referring back to Figure 5.11 which indicates the torque deficit between the actual torque and the expected type I torque acting on the outer planet in the two planet system, we see that this is also $\sim 2 \times 10^{-11}$. Thus we see there is consistency with the picture presented here of this deficit being supplied by the inner planet if the emitted flux that reaches the horseshoe region is mostly absorbed there and $\lambda \sim 2.4$, being of order unity. Now, it is time to move on and present how the repulsion mechanism depends on the mass of the planets and properties of the disk in which they are embedded.

5.7 How the effectiveness of the repulsion between two super-Earths depends on the mass of the planets and disk properties

In previous sections, we have discussed in full detail the evolution of two planets with masses of $q_1 = 1.3 \times 10^{-5}$ and $q_2 = 1.185 \times 10^{-5}$ embedded in the disk. We have used two initial disk surface density profiles in the simulations for this case, which have the following forms: the simple power law $\Sigma = 8 \times 10^{-5} r^{-1/2}$ and the power law with a central cavity described by Equation (5.1) with $\alpha = 0.5$ and $\Sigma_0 = 6 \times 10^{-5}$. By taking the second profile with an inner disk cavity, we are able to extend our study to the systems with a range of mass ratios. In this section, we will investigate the effectiveness of the wave planet-repulsion mechanism in the systems of migrating super-Earths with the variety of mass ratios and disk properties.

5.7.1 Our sample of the super-Earth pairs with the predicted effectiveness of the repulsion between planets

In order to determine how the effectiveness of the repulsion between two super-Earths depends on the mass of the planets and disk properties, we perform a series of the simulations taking on the different masses of the planets and different initial disk surface densities. The parameters adopted in each simulation are given in Table 5.4.

Table 5.4: List of the performed simulations

Case	q_1 (M_*)	q_2 (M_*)	Initial $\Sigma(r)$ [1]	Symbol in Figure 5.13
1	1.3×10^{-5}	1.185×10^{-5}	$\Sigma(r) = 8 \times 10^{-5} \cdot r^{-0.5}$	black empty circle
2	1.3×10^{-5}	1.185×10^{-5}	$\Sigma_0 = 6 \times 10^{-5}, \alpha = 0.5$	black cross
3	1.185×10^{-5}	1.185×10^{-5}	$\Sigma_0 = 6 \times 10^{-5}, \alpha = 0.5$	dark blue cross
4	1.95×10^{-5}	1.185×10^{-5}	$\Sigma_0 = 6 \times 10^{-5}, \alpha = 0.5$	green cross
5	2.6×10^{-5}	1.185×10^{-5}	$\Sigma_0 = 6 \times 10^{-5}, \alpha = 0.5$	red cross
6	1.185×10^{-5}	1.3×10^{-5}	$\Sigma_0 = 6 \times 10^{-5}, \alpha = 0.5$	purple cross
7	1.185×10^{-5}	1.3×10^{-5}	$\Sigma_0 = 4.5 \times 10^{-5}, \alpha = 0.5$	orange triangle
8	4.4×10^{-5}	4×10^{-5}	$\Sigma(r) = 8 \times 10^{-5} \cdot r^{-0.5}$	purple asterisk
9	4.4×10^{-5}	4×10^{-5}	$\Sigma(r) = 3 \times 10^{-5} \cdot r^{-0.5}$	green empty square

[1] For the cases for which only Σ_0 and α are given in the table, the initial $\Sigma(r)$ is taken to be described by Equation (5.1).

In Section 5.6, we have obtained the criteria for the occurrence of the effective repulsion between two planets migrating in a protoplanetary disk. When two conditions are satisfied for both planets in the disk, we expect that the system eventually undergoes divergent migration. It is convenient to present the predictions of the outcome of our simulations listed in Table 5.4 in the following planes:

$$\left[\frac{q_1}{h^3}, \frac{h^2 q_1}{\pi q_2^2}\left(\frac{\Sigma_{min}}{\Sigma_{un}}\right)_1\right]$$

for the inner planet with the mass of q_1 receiving the angular momentum carried by the density waves of the outer planet (left panel of Figure 5.13) and

$$\left[\frac{q_2}{h^3}, \frac{h^2 q_2}{\pi q_1^2}\left(\frac{\Sigma_{min}}{\Sigma_{un}}\right)_2\right]$$

for the outer planet with the mass of q_2 absorbing the angular momentum transferred through the density waves excited by the inner planet (right panel of Figure 5.13). The masses of planet pairs and the initial surface density profile adopted in each case are given in Table 5.4, together with the symbols denoting each case in the figure. The top right regions surrounded by the blue dashed lines which extend to large distances from the origin in each panel are the locations where the wave-planet repulsion mechanism is expected to be effective for both planets in the system.

To justify why we have chosen these particular planes for the illustration of our results, we remark that the counterpart of the criterion given by Equation (5.15) that is applicable to the inner planet will be satisfied for $f/\lambda < 0.35$ if $q_1/h^3 > 1$ indicating enough supply to it as receiver to

enable the halting of convergent migration. Similarly the criterion $(h^2 q_2/(\pi q_1^2))(\Sigma_{min}/\Sigma_{un})_1 > \lambda$ recalling that we expect λ to be of order unity, ensures that the condition (5.20) which indicates the effectiveness of the horseshoe drag for the inner planet is satisfied and the planets are near to the 3:2 resonance. Similar remarks apply to the case with the role of the planets reversed and with q_1/h^3 and $(h^2 q_2/(\pi q_1^2))(\Sigma_{min}/\Sigma_{un})_1$ being respectively replaced by q_2/h^3 and $(h^2 q_1/(\pi q_2^2))(\Sigma_{min}/\Sigma_{un})_2$.

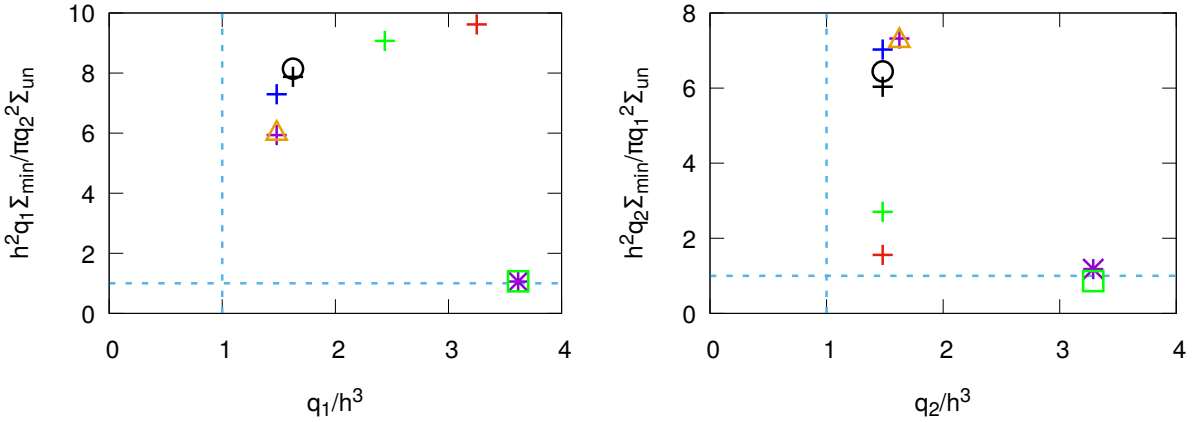

Figure 5.13: Effectiveness of the repulsion between the planets due to wave-planet interactions in the hydrodynamical simulations, according to our analytical criteria - The left panel gives information about the case in which the inner planet with the mass ratio q_1 is viewed as a receiver of waves emitted by the outer planet. The right panel gives information when the role of the planets in the pair is reversed, namely the outer planet is regarded as a receiver of waves emitted by the inner planet. The information about the simulations and the represented symbols are given in Table 5.4. See text for more details.

In Figure 5.13, the black empty circle and black cross in each panel indicate the results of the simulations for the case 1 and 2 described in Section 5.3 with $q_1 = 1.3 \times 10^{-5}$ and $q_2 = 1.185 \times 10^{-5}$. The small difference in the location of the planets in these two cases is caused by the different depths of the partial gaps. The dark blue, green and red crosses show the cases 3, 4 and 5 which only differ in the mass of the inner planet. We note that as the mass of the inner planet increases, the depth of the inner partial gap becomes larger while the depth of the outer partial gap decreases, even though the mass of the outer planet in all three cases is the same. The orange triangle and the purple cross (cases 6 and 7) are very close (left panel) or even overlapping (right panel) each other. In these two cases the only difference is in the adopted value of Σ_0. This difference resulted in a slightly different depth of the gap along the inner planet orbit and the same depth of the gap made by the outer planet.

We can conclude that the position of the points in the planes is mainly determined by the planet-to-star mass ratios of the planets. In the left panel, we can see that the location of the dark blue, green and red crosses increases from the left to the right following the increasing mass ratio of the inner planet. In the right panel, the same three crosses are located along a vertical line, because for all of them q_2 is the same. Those with larger q_1 are located below those with smaller q_1. The above results indicate that as q_1 increases for fixed q_2, the horseshoe drag

on the inner planet is increasingly able to sustain the wave-planet interaction. On the other hand, the increasing Lindblad torques it produces make it harder for the outer planet to sustain the interaction at fixed q_2. However, the reaction to this is likely to be that the disk-planet interaction can be sustained with the planets being further apart.

Based on our criteria, we have shown and illustrated in Figure 5.13 that the planet pairs (cases 1-7 in our hydrodynamic simulations) should eventually migrate divergently if they approach close enough to each other and the convergent migration causing this is sufficiently slow.

In Section 5.1 we have revealed our motivation to perform the study presented in this chapter and now, we would like to come back to two particular calculations from the paper of [21]. In one of those two calculations, two planets with comparable masses, namely the pair of the Uranus-like planets repel each other during their migration in the gaseous disk and failed being locked in the 3:2 mean-motion resonance. The same planets evolving in the lower surface density disk become locked in the 2:1 commensurability and do not show signs of divergent migration. Could our criteria be helpful in the interpretation of their results? To find the answer, we have recalculated the migration of two planets with mass ratios of $q_1 = 4.4 \times 10^{-5}$ and $q_1 = 4 \times 10^{-5}$, which have been investigated in [21]. The parameters adopted in these two simulations are given in Table 5.4 (cases 8 and 9) and the results are also plotted in Figure 5.13 indicated by purple asterisk and green empty square, respectively. The first criterion given in (5.15) and its counterpart corresponding to exchanging the planets are easily satisfied in both runs. Both planets form a partial gap. The second criterion matching $1.9\lambda q_1^2/q_1 h^2$ with $\lambda = 1$ and its counterpart corresponding to interchanging the planets are only just satisfied in the case eventually undergoing divergent migration (case 8) with the criterion for the outer planet to be an effective receiver marginally failing when $\lambda = 1$ for the case that retained convergent migration (case 9). So the results of a previous study are fully consistent with the picture presented here.

5.7.2 Divergent migration of two super-Earths in a protoplanetary disk

On the basis of our analytical criteria based on the magnitude of wave fluxes and the potential of the horseshoe drag to communicate the angular momentum transported to the planet, we conclude that all the cases considered in the previous section (cases 1-7) were likely to exhibit effective repulsion due to wave-planet interaction. We have already shown that it is indeed the outcome of the simulations in the cases 1 and 2 (Section 5.3.2.1). In this section, we verify this prediction for cases (3-7) in our hydrodynamic simulations, make the comparison with the reference case (case 2) and investigate how the repulsion between two planets depends on the convergent migration rate, planet-to-star mass ratio of the inner planet and the initial disk surface density.

5.7.2.1 Dependence on the convergent migration rate

First, we compare three cases (cases 2, 3 and 6) which differ from each other in the rate of initial convergent migration. The aim is to confirm the effectiveness of the repulsion between planets in these runs and, if successful, determine how the location where the transition between convergent and divergent migration occurs depends on the rate of initial convergent migration.

The case 2 is our reference run, discussed in Section 5.3.2.1 with the inner planet more massive than the outer one (the lowest rate of initial convergent migration of the three). In the case 3 (the intermediate rate of initial convergent migration), both planets have the same mass and in the case 6, the inner planet is less massive than the outer one (the highest rate of initial convergent migration of the three). In all cases the adopted initial surface density is given by Equation (5.1) with $\alpha = 0.5$ and $\Sigma_0 = 6 \times 10^{-5}$.

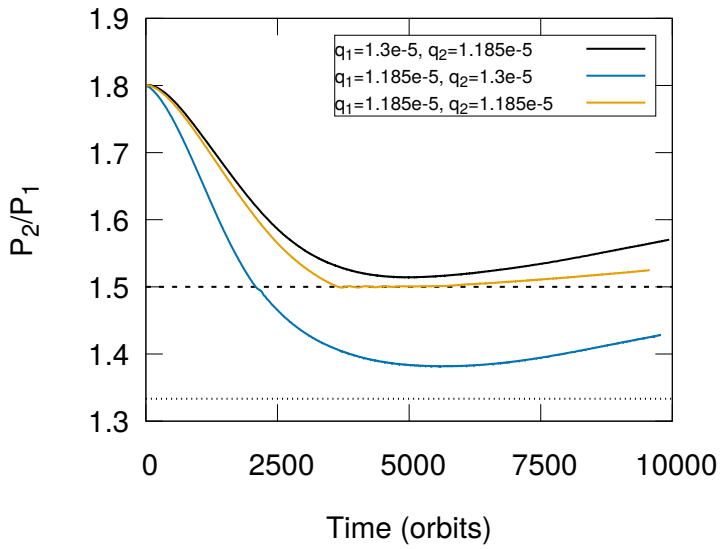

Figure 5.14: Evolution of the period ratio of planet pairs with different mass ratios - Evolution of the period ratio in the simulations for the cases with $q_1 = q_2 = 1.185 \times 10^{-5}$ (case 3, orange), $q_1 = 1.185 \times 10^{-5}$, $q_2 = 1.3 \times 10^{-5}$ (case 6, dark blue) and $q_1 = 1.3 \times 10^{-5}$, $q_2 = 1.185 \times 10^{-5}$ (case 2, black). The dashed and dotted horizontal lines indicate the positions of the 3:2 and 4:3 commensurabilities, respectively.

The evolution of the period ratio of two planets in these simulations is presented in Figure 5.14. In the case of the lowest rate of initial convergent migration (case 2, black line), the planets migrate towards the 3:2 MMR and at some point leaves the vicinity of the commensurability as a result of divergent migration. In the equal mass case (case 3, the intermediate rate) indicated by the orange line in Figure 5.14, the planets arrive at the 3:2 MMR and stay there for a longer period of time as compared to the previous case and eventually leaves the resonance with a slower divergent migration rate. In the simulation with $q_2 > q_1$ (case 6, the highest rate) denoted by the dark blue line in Figure 5.14, the relative migration of two planets is so fast that the system passes through the 3:2 MMR, but before arriving at the 4:3 MMR, the migration starts to be divergent. This result infers that being close to a strict commensurability is not necessary for the occurrence of the divergent migration, even though the 4:3 MMR could have some effects on the migration of planets (see the bottom panels in Figure 5.15).

The evolution of the period ratios, semi-major axes, eccentricities of two planets and the 3:2 or 4:3 resonance angles in these simulations is shown in Figure 5.15. For completeness, in the uppermost row, we present also the results already displayed in Figure 5.4.

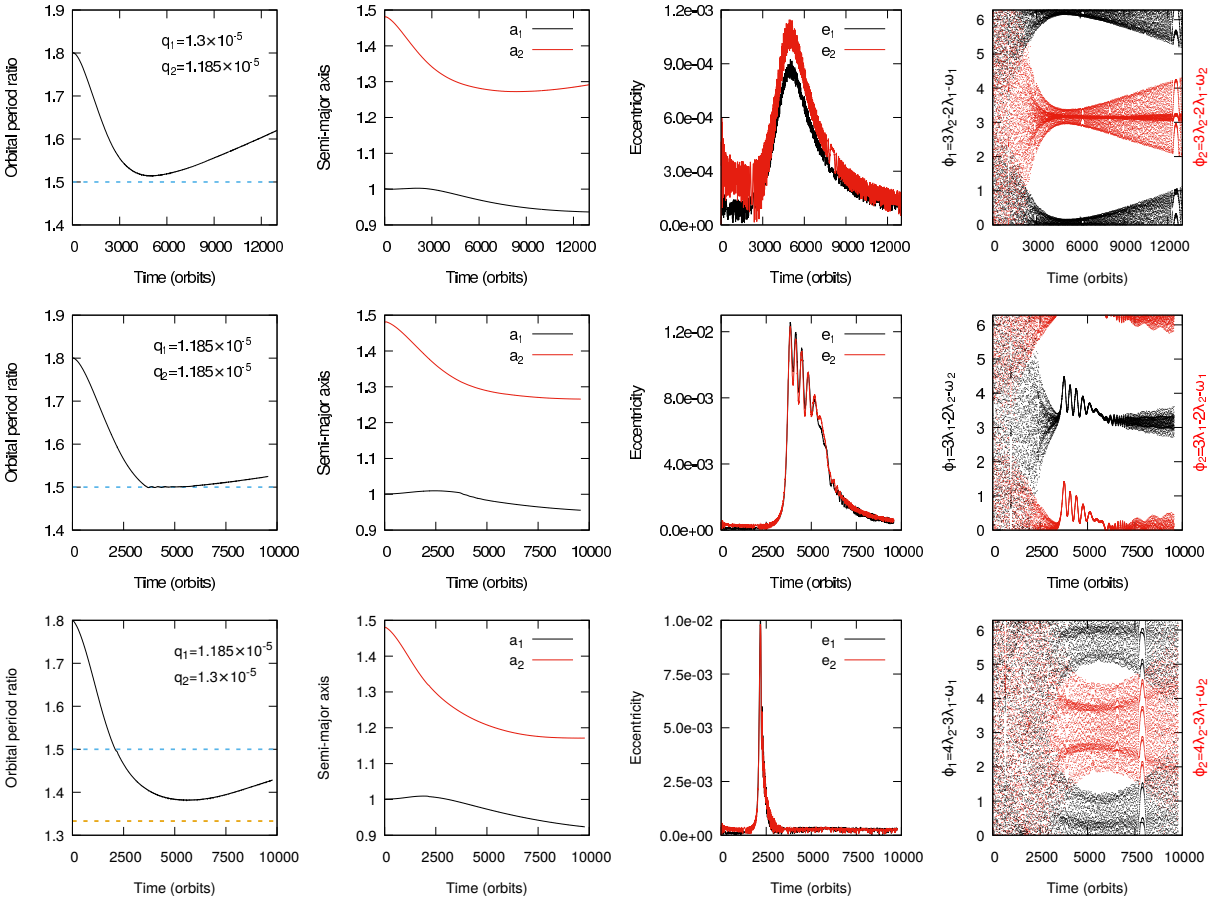

Figure 5.15: Results of simulations of two super-Earths with different convergent migration rates - Each row shows the results of the simulations with the same disk parameters but different masses of two planets, bringing about the different rates of initial convergent migration: first row – case 2 (lowest rate), second row – case 3 (intermediate rate) and third row – case 6 (highest rate). The panels in every row show, from left to right, the evolution of the planets' orbital period ratio, semi-major axes, eccentricities and the resonance angles in each simulation. The horizontal dashed blue line in the first left panel in each row indicates the position of the 3:2 commensurability. The horizontal dashed yellow line indicates the position of the 4:3 resonance.

From the results of the simulation for two equal-mass case shown in the second row of the figure, we can see that at the early stage of the evolution, the inner planet migrates outwards on account of the particular surface density profile adopted in the simulation, while the outer planet migrates inwards. As a consequence, the planets undergo the convergent migration and arrive to the 3:2 MMR at $t \sim 3500$ orbits. Then, their orbital period ratio stays at around 1.5 till $t \sim 6000$ orbits. During this period of time both planets migrate inwards, their eccentricities are excited to ~ 0.012 at $t \sim 4000$ orbits and subsequently decrease. The 3:2 resonance angles begin to librate at around 3500 orbits with mean values slightly above π and zero, respectively, and then decreasing in time. After $t \sim 6000$ orbits, the divergent migration occurs, which means that the orbital period ratio of the planets is increasing slowly while the eccentricities continue to decrease. The amplitudes of the 3:2 resonance angle libration increase with time, which

indicates that the planets are leaving the 3:2 MMR.

The last case (case 6) shown in the bottom row of the figure presents the situation when the mass ratios of the two planets in the simulation illustrated in the uppermost row (case 2) are interchanged. In this case, the convergent migration rate is significantly faster than in the other two cases and the planets pass through the 3:2 MMR at $t \sim 2400$ orbits. After that, they continue migrate convergently till 6000 orbits and then the divergent migration occurs, before the planets arrive to the 4:3 MMR. Both 4:3 resonance angles begin to librate with the large amplitudes at the same time. As we have already mentioned, the 4:3 resonance may play a significant role. Note that the distance from strict commensurability and the large amplitude librations of the resonance angles which occur around 6000 orbits indicate a relatively weak effect though this could be enough to affect the evolution.

In summary, the results of the simulations illustrated in Figures 5.14 and 5.15 allow us to determine the dependence of the effectiveness of the repulsion between planets on the rate of initial convergent migration. We conclude that, an increased rate is found to enable the pair to approach each other more closely before the relative migration reverses.

5.7.2.2 Dependence on the planet-to-star mass ratio of the inner planet

Next, we explore how the evolution of two super-Earths in the disk depends on the mass of the inner planet. To this aim, we consider a sequence of four simulations (cases 3, 2, 4 and 5), in which the outer planet has the fixed mass ratio $q_2 = 1.185 \times 10^{-5}$ with the inner planet respectively having the increasing mass ratio q_1. For all of these cases the initial surface density distribution was given by Equation (5.1) with $\alpha = 0.5$ and $\Sigma_0 = 6.0 \times 10^{-5}$. A comparison of the period ratio evolution in these cases is illustrated in Figure 5.16 and more details of the results are presented in Figure 5.17.

It can be noticed from Figure 5.16 that the initial relative migration rates in all four simulations are very similar but with a tendency to decrease as q_1 increases. This occurs because the surface density decreases sharply in the inner region of the disk, which tends to halt inward migration exactly where the inner planet is placed. However, for the inner planet with larger mass the inward migration cannot be halted entirely in this way and such a planet can still slowly migrate inward. That is the reason for which, there is a trend that the relative migration rate is slightly decreasing with the increasing values of q_1 (see the panels in second column of Figure 5.17).

In Figure 5.16, we can see that for the case with the lowest mass of the inner planet q_1 indicated by the orange line, the super-Earths have convergent migration and arrives at the position of the 3:2 resonance, where the resonance capture actually takes place. However, this capture is only temporary, as the planet after some time leave the commensurability. It is clear from the evolution of the planets' eccentricities illustrated in the top row of Figure 5.17, which shows that after being rapidly excited in the proximity of the resonance, the eccentricities decrease as the planets begin to undergo divergent migration. Increasing the mass of the inner planet q_1 results in slower initial convergent migration. This leads to divergent migration sooner at a higher period ratio. Indeed, in the case 4 and 5, indicated by the purple and green lines, the planets do not have a close approach to the 3:2 resonance. The migration of the outer planet

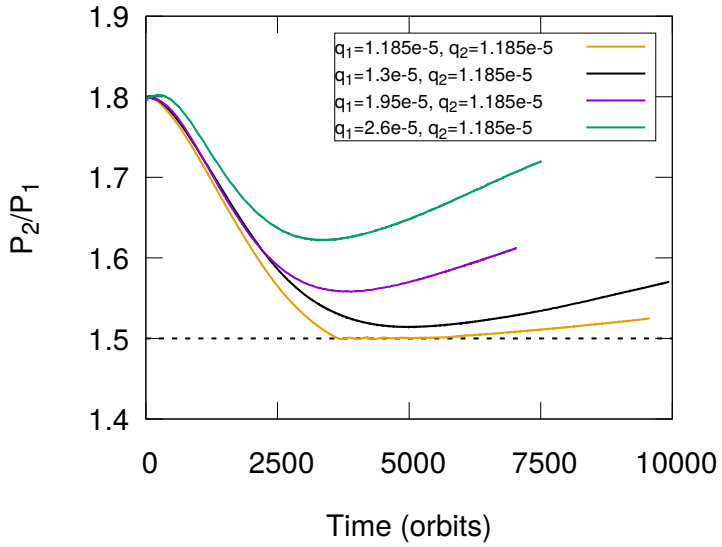

Figure 5.16: Period ratios of planet pairs in the simulations with different inner planet-to-star mass ratio - Evolution of the period ratio in the simulations for the cases with $q_1 = 1.185 \times 10^{-5}$ (case 3, orange), 1.3×10^{-5} (case 2, black), 1.95×10^{-5} (case 4, purple) and 2.6×10^{-5} (case 5, green). The dashed and dotted horizontal lines indicate the position of the 3:2 commensurability.

in all cases except the equal mass simulation (case 3), at some point reverses direction bringing the planet further away from its host star (see the second column of Figure 5.17). It is likely that this would also happen in the simulation with two equal planets if we had continued the simulation for a longer time.

We have confirmed the prediction, based on the criteria for the effectiveness of the wave-planet repulsion mechanism, that the divergent migration should take place in all the systems of two super-Earths embedded in the disk, discussed here. However, we can do more than that, namely we can perform a quantitative analysis of the divergent migration obtained in our simulations and its dependence on the mass of the inner planet. There are few interesting questions, we can make an attempt to answer here. One of the characteristic properties of the evolution is the value of the semi-major axis ratio of two planets at the moment of time at which the transition from convergent to divergent migration takes place, which we denote as follows $a_{\rm min} = (a_2/a_1)_{\rm min}$. Another relevant quantity is the divergent migration rate defined as

$$\dot{a}_{\rm div} = \left(\frac{d(a_2/a_1)}{dt} \right)_{\rm div} . \tag{5.27}$$

The value of $\dot{a}_{div}$ can be calculated as an average over the last 1500 orbits of the evolution. These two quantities are given in Table 5.5 for each simulation. From this table we can see that when q_1 is larger, also $a_{\rm min}$ and $\dot{a}_{\rm div}$ are larger, which means that a higher mass inner planet leads to a faster divergent migration rate even though the earlier convergent migration rate was slower. This is a natural expectation on account of the expected larger wave flux produced by a planet with larger q_1, resulting in a stronger repulsion between planets.

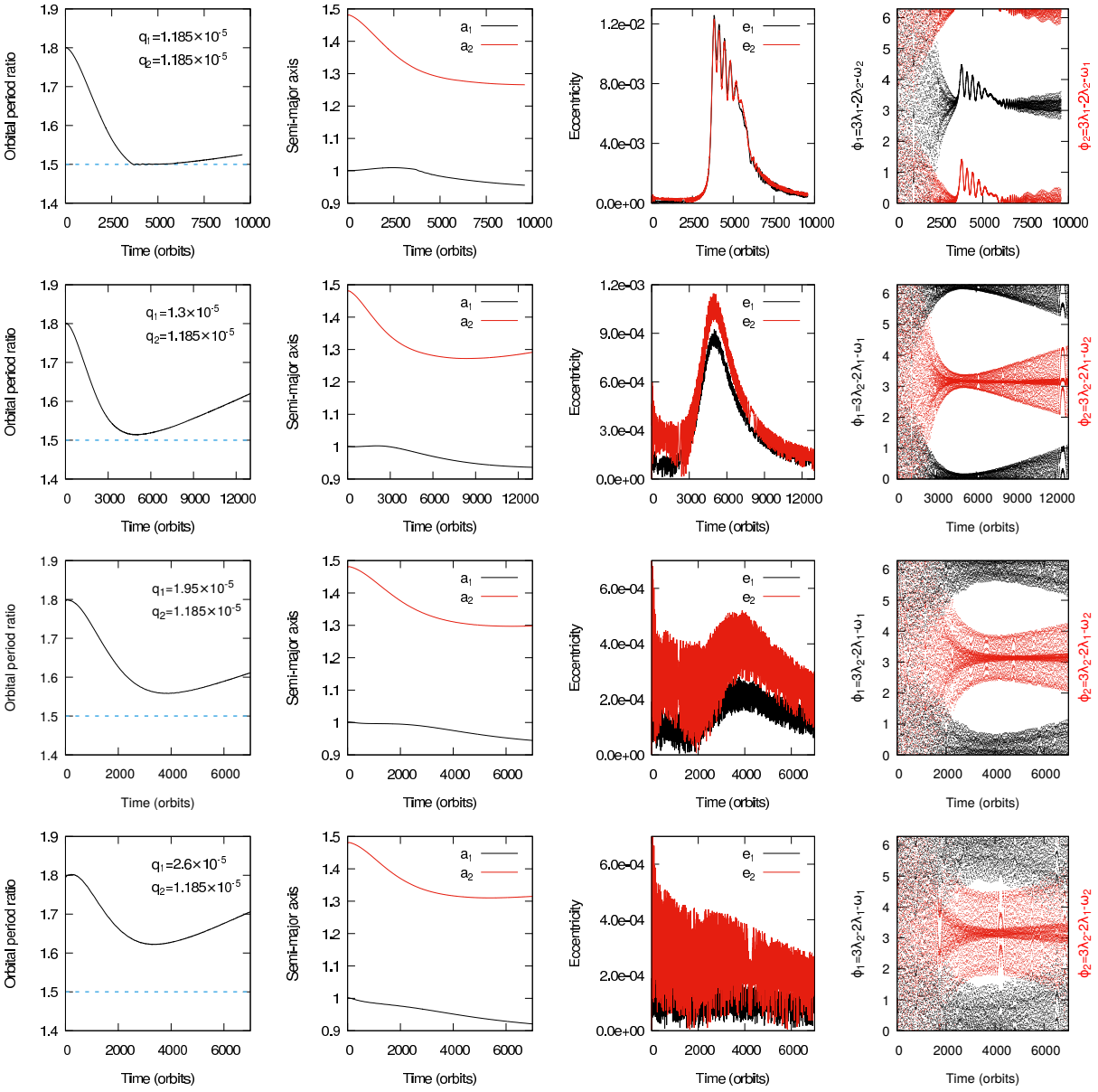

Figure 5.17: Results of the simulations of two super-Earths with different inner planet-to-star mass ratio - Each row shows the results of the simulations with the same disk parameters but a different mass of the inner planet. The panels in each row show the evolution of the planets' orbital period ratio, semi-major axes, eccentricities and the resonance angles from left to right for each simulation. The horizontal dashed blue line in the first left panels indicates the position of the 3:2 commensurability.

Table 5.5: The results of a quantitative analysis of the divergent migration of two planets in the simulations with different q_1 and fixed q_2.

q_1 (M_*)	$a_{\min}$	$\dot{a}_{\rm div}$ $({\rm yr}^{-1})$
1.185×10^{-5}	1.310	3.954×10^{-6}
1.3×10^{-5}	1.319	9.263×10^{-6}
1.95×10^{-5}	1.344	1.235×10^{-5}
2.6×10^{-5}	1.381	1.627×10^{-5}

5.7.2.3 Dependence on the initial disk surface density

Now we explore the effect of reducing the initial convergent migration rate by reducing the surface density scale. To this aim, we consider an additional simulation (case 7), for which the planets have mass ratios the same as in already discussed case 6, but taking the lower surface density scale with $\Sigma_0 = 4.5 \times 10^{-5}$ instead of 6×10^{-5} as in case 6. In case 6 the migration was fast enough for the planets to be able to pass through the 3:2 resonance (see the bottom panels in Figure 5.15).

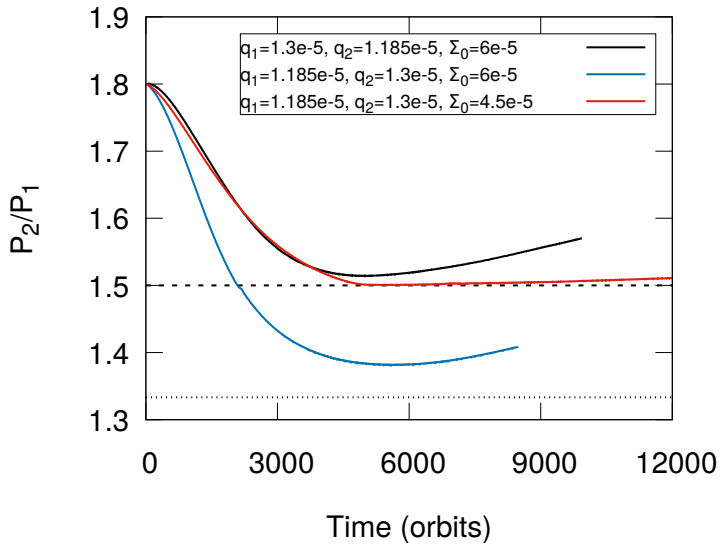

Figure 5.18: Period ratios of planet pairs in the simulations with different initial surface density scale - The results of the hydrodynamical simulations of two super-Earths with $q_1 = 1.185 \times 10^{-5}$ and $q_2 = 1.3 \times 10^{-5}$ migrating in a protoplanetary disk with $\Sigma_0 = 6 \times 10^{-5}$ (case 6, dark blue line) and $\Sigma_0 = 4.5 \times 10^{-5}$ (case 7, red line). The black line indicates the results of the simulation for our reference case (case 2). The dashed and dotted horizontal lines indicate the positions of the 3:2 and 4:3 resonance commensurabilities, respectively.

Our main motivation in performing the simulation with reduced surface density scale was to investigate the situation in which the outer planet is more massive than the inner one, and the relative migration rate is not too fast for 3:2 resonance capture to take place. Moreover, we choose Σ_0 in such a way that the convergent migration rate of the planets is approximately the same as for the evolution of the planets in our reference run (case 2). The comparison of

the period ratio in the simulations for the two cases 6 and 7 with different Σ_0 is illustrated in Figure 5.18. In addition, we also display the result in the simulation for the case 2 in the same figure, to show that indeed we succeeded in making the convergent migration rate of the planets in case 7 (indicated by the red line) approximately the same as in case 2 (indicated by the black line). Our choice of Σ_0 for case 7 gave the expected result and the planets have been trapped in the 3:2 commensurability due to their relative convergent migration.

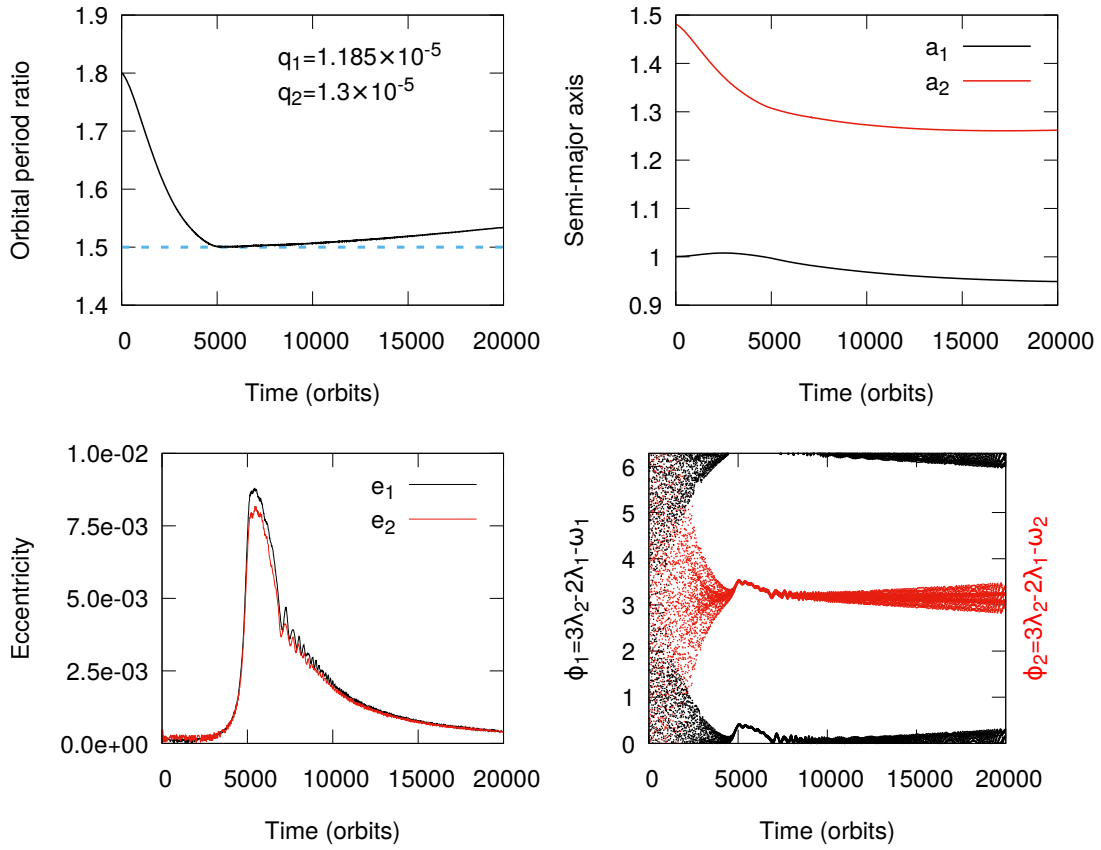

Figure 5.19: Results of the simulation with lower initial disk surface density (case 7) - Results of the simulation of two super-Earths with masses of $q_1 = 1.185 \times 10^{-5}$ and $q_2 = 1.3 \times 10^{-5}$ migrating in a protoplanetary disk with the initial surface density $\Sigma_0 = 4.5 \times 10^{-5}$. Evolution of the planets' period ratio, semi-major axis, eccentricities and the resonance angles is shown in the panels from left to right. The horizontal dashed blue line in the first left panel indicates the position of the 3:2 commensurability.

More details of the results in the case with $\Sigma_0 = 4.5 \times 10^{-5}$ (case 7) are shown in Figure 5.19. We can see in this figure that the planets undergo convergent migration from the beginning of the evolution till the time $t \sim 5000$ orbits, when the period ratio decreased to close to 1.5 and the planets enter the 3:2 commensurability, while the eccentricities of the planets reach their maximum values $e_1 = 8.0 \times 10^{-3}$ and $e_2 = 9.0 \times 10^{-3}$. Both 3:2 resonance angles start to librate with a small amplitude. The divergent migration takes place at $t \sim 7000$ orbits and then the eccentricities decrease while the amplitude of the libration of both resonance angles increase.

As a result, the system leaves the 3:2 MMR. The outer planet starts to migrate outwards at $t \sim 16000$ orbits and continues to do so till the end of the simulation.

In summary, we found that in case 7 the planets enter into the 3:2 MMR, stay there for a couple of thousand of orbits and then slowly (slower than in case 2), moves away from the resonance, due to the divergent migration. This performance is consistent with the notion that while the system remains close to the 3:2 commensurability the convergent migration is halted by the resonant interaction with the wave-planet interaction not being strong enough to separate the planets. However, this changes as the migration rates slow down at later times and separation from the resonance can take place.

5.8 Effect of a uniform surface density reduction on the migration of two super-Earths

In Section 5.7.2.3, we have described the migration of two super-Earths with $q_1 = 1.185 \times 10^{-5}$ and $q_2 = 1.3 \times 10^{-5}$ in the disk with two different surface density scales, namely 6×10^{-5} and 4.5×10^{-5}. Reducing the initial surface density scale from 6×10^{-5} to 4.5×10^{-5}, we obtain a slower relative migration rate of two planets and thus the relative migration rate was not too fast for the 3:2 resonance capture to take place. The reduction of the initial surface density has been done explicitly for that purpose, as we wanted to explore the repulsion between the planets locked at the 3:2 commensurability. We have found that such a modest change in the value of the initial surface density scale (a factor of 1.33) did not changed qualitative outcome of the simulation, which means that the divergent migration took place and the planets left the resonance.

Here, we continue our investigations of the dependence of the effectiveness of the repulsion between planets on the surface density in a disk, but this time our motivation is different and the values of the surface densities will be much different compared to those considered up to now. In the final stages of the evolution, during the dispersal of the protoplanetary disk, the surface density is expected to decrease to significantly smaller values than foreseen for the MMSN. Will the repulsion between planets be present also in a disk with the surface density scaled down 4 or even 16, not just 1.33 times?

5.8.1 Practical approach to answer the question about the efficiency of the repulsion between planets in a very low surface density disk

It is computationally expensive to calculate the complete orbital evolution of two planets in a disk with a very low surface density. Therefore, we need to do something else in order to answer the question about the efficiency of the repulsion between planets, due to wake-planet interactions, in a very low surface density disk. The idea is to start new calculations with a rescaled surface density profile taken from one of our already performed simulations. The best choice is to rescale the surface density profile from our reference simulation, namely from case 2. The form and direction of the orbital evolution may then be checked at different stages and then pieced together.

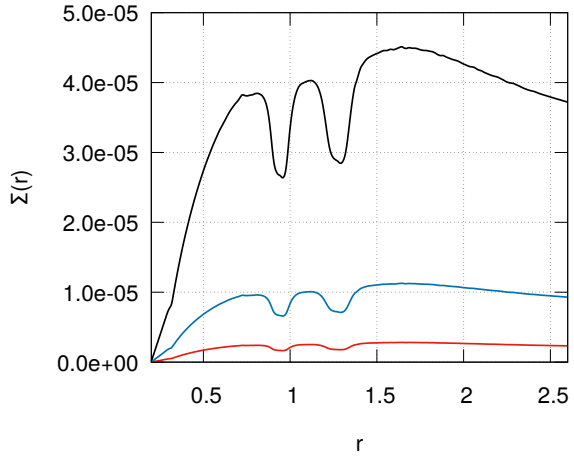

Figure 5.20: Disk surface density reduced by different factors - The azimuthally averaged surface density at $t = 10000$ orbits in the simulation for case 2 illustrated in Figure 5.4 (black line) and in the restarted ones with Σ reduced by a factor of 4 (dark blue line) and by a factor of 16 (red line).

Following our approach, we select the surface density profile at $t = 10000$ orbits in the reference simulation (case 2) and reduce Σ at each grid point by a constant factor and then use such a density profile as the initial one for a new simulation. The moment of time for restarting our calculation was determined by the need to start the evolution when the torque from the disk acting on the outer planet is already positive (see Figure 5.11). We performed two new simulations, one with the surface density uniformly scaled down by a factor of 4 and another by a factor of 16. The initial surface density profiles in those two simulations are illustrated in Figure 5.20 together with the original $\Sigma(r)$ from which they have been obtained (indicated by the black line).

5.8.2 Super-Earth migrating in the disk with reduced surface density

Here, we show the results of the restarted runs with the reduced surface density uniformly scaled down by a factor of 4 and 16 described in the previous section. In Figure 5.21, we present the evolution of the period ratios (top panel) of the two planets, semi-major axes of the inner (middle panel) and outer (bottom panel) planets. The results of the simulations with the surface density reduced by a factor of 4 (dark blue line) are given in the second column, and those with the surface density reduced by a factor of 16 (red line) in the third column. In the first column of the figure, we show also, for comparison, the results of the simulation in the reference case (case 2) indicated by the black line. The outer planet in all cases migrates outwards and the inner one migrates inwards resulting in divergent migration. As expected the orbital evolution is four (sixteen) times faster in the case for which the initial surface density is reduced by a factor of four (sixteen). Already at this stage we can conclude that the evolution of planets in the disk with the surface density reduced by a factor of 4 and that with the surface density reduced by a factor of 16 is divergent just as it was in the original one shown in Figure 5.4.

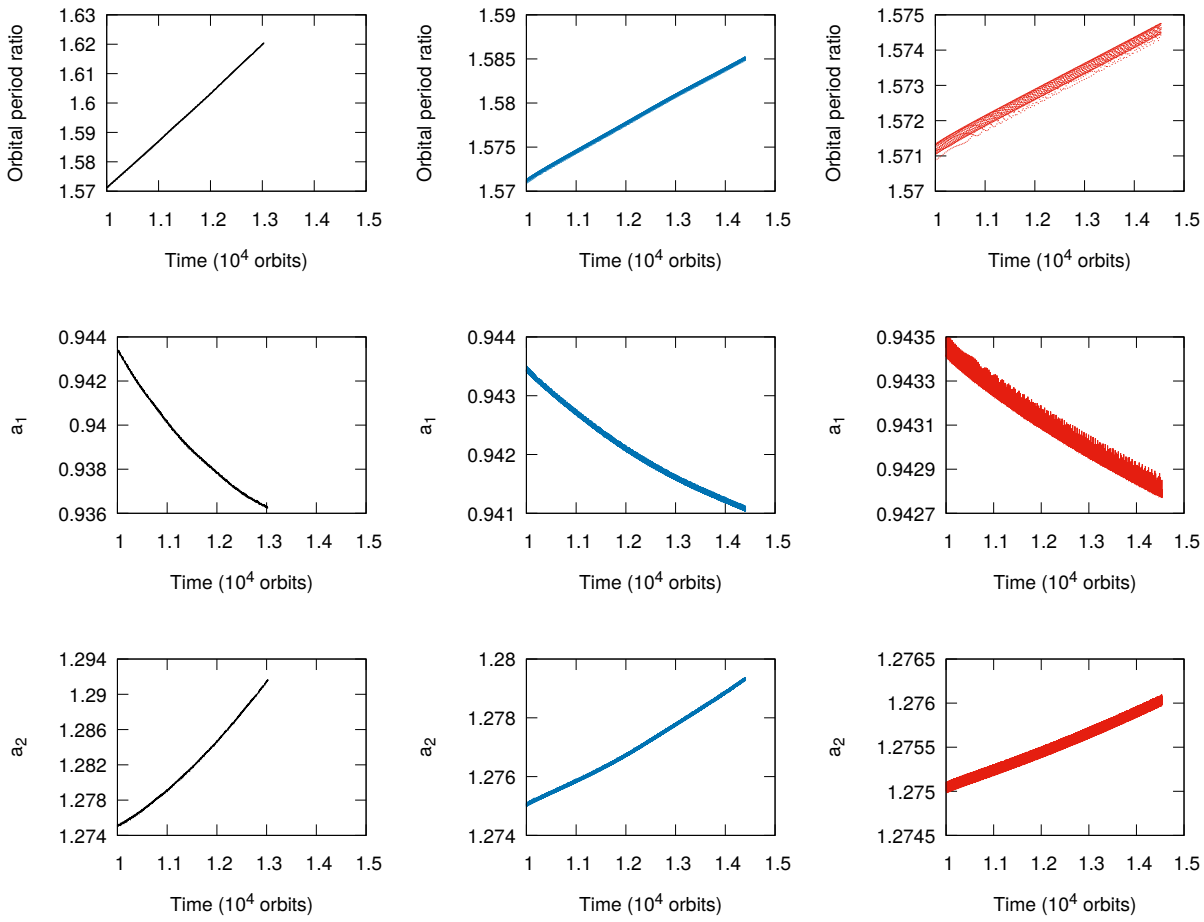

Figure 5.21: Results of the simulations with the surface density profile reduced by different factors - Evolution of the period ratios and semi-major axes of two super-Earths in the simulations with the surface density reduced by a factor of 4 (dark blue line) and 16 (red line) as well as in the simulation for the reference case (case 2) (black line).

However, as a final argument to demonstrate the efficiency of the planet repulsion due to the wave-planet interaction in the disk with a substantially reduced surface density, we present a comparison of the relevant torques in our simulations in Figure 5.22. In the left panel of this figure, we display the average torque in the run with the 4 times lower surface density (dark blue solid line) and the one expected from the scaling procedure (dashed purple line) applied to the original calculation shown in Figure 5.4. The scaling procedure consists in decreasing the total torque by a factor of 4 and increasing the time scale of the orbital evolution by the same factor, as this time scale should scale inversely with the surface density. In addition, in order to compare the same phases of the evolution in both calculations the initial time for the lower density run is shifted to t = 40000 orbits. The two torques are in very good agreement.

In the right panel of Figure 5.22, we compare the torque from the disk acting on the outer planet in the simulations with the surface density reduced by a factor of 16 (red solid line) with the torque (denoted by the dashed yellow line) expected from the scaling procedure described

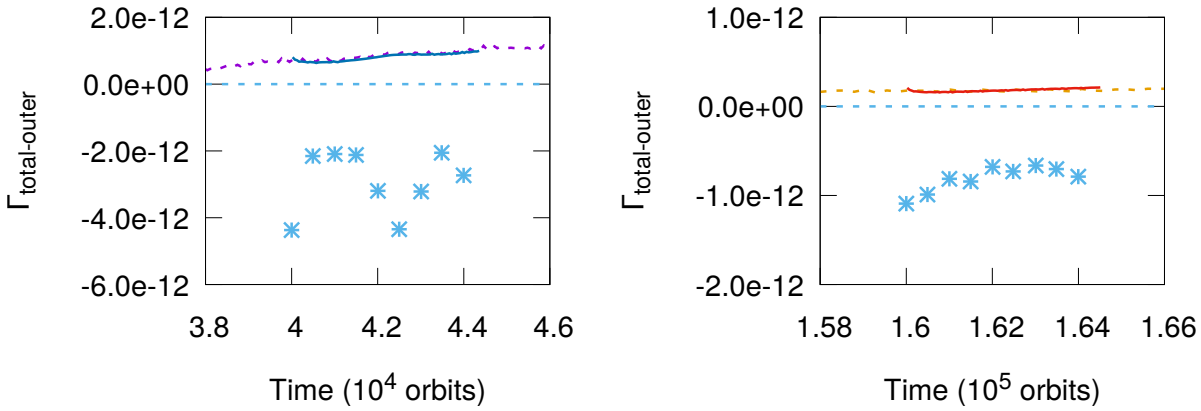

Figure 5.22: The torques in the simulations by taking the initial and reduced surface density profiles - The locally time averaged total torque from the disk acting on the outer planet in the restarted simulations with the surface density respectively scaled down by a factor of 4 (dark blue solid line in left panel) and 16 (red solid line in right panel). The dashed yellow and purple lines represent the scaled total torques exerting on the outer planet derived from the original simulation for the reference case. The blue asterisks indicate the torques calculated from Equation (5.11).

Table 5.6: Numerical parameters for torque calculation in simulations by taking the reduced surface density profile

shifted time (orbits)	α_p	$\Sigma_{p,un}$ $(\cdot 10^{-5})$	$\Sigma_{p,min}$ $(\cdot 10^{-6})$	r_p
$f = 4$				
40000	0.851	1.051	7.185	1.1749
40500	0.617	1.046	7.126	1.2755
41000	0.612	1.036	7.084	1.2757
41500	0.618	1.027	6.983	1.2764
42000	0.737	1.018	6.949	1.2768
42500	0.867	1.013	6.895	1.2771
43000	0.744	1.003	6.852	1.2775
43500	0.617	0.992	6.786	1.2783
44000	0.695	0.989	6.740	1.2788
$f = 16$				
160000	0.851	0.263	1.795	1.2749
160500	0.811	0.260	1.780	1.2751
161000	0.739	0.259	1.761	1.2753
161500	0.755	0.257	1.748	1.2753
162000	0.685	0.255	1.737	1.2757
162500	0.710	0.252	1.723	1.2756
163000	0.683	0.250	1.710	1.2756
163500	0.703	0.248	1.697	1.2759
164000	0.744	0.247	1.684	1.2757

above. Here the initial time for the low density calculation has been shifted to t = 160000 orbits. Also in this case the torques are in a very good agreement.

Besides that, we illustrate in both panels of Figure 5.22,the torques calculated from Equation (5.11) and indicated by the blue asterisks. The parameters used to calculate those torques are given in Table 5.6.

Based on these results, we conclude that the repulsion of the planets is also effective in the disk with a substantially reduced surface density relative to that adopted in previous simulations.

5.9 How robust are our results?: A particular choice of the equation of state of the disk material and the omission of the disk self-gravity

In previous section, we have confirmed that the divergent migration of two super-Earths can take place when the criteria for the effectiveness of the wave-planet repulsion mechanism are satisfied. However, as we have already discussed in Section 5.2, in our simulations we have used a simple disk model with the locally isothermal equation of state and without taking into account the self-gravity of the disk material. We have anticipated that we will come back to this point and now it is a good moment to do so and to check whether and how those assumptions might affect our conclusions.

5.9.1 Migration of two super-Earths in an adiabatic disk

In all previous simulations, the evolution of two super-Earths has been calculated assuming that the planets are embedded in a locally isothermal disk. One of the problems connected with the adoption of the locally isothermal equation of state might be that there is no strict conservation of wave action for small amplitude waves in this case [134]. Moreover, the co-orbital torques can differ on account of different behavior of the state variables within the horseshoe region.

In order to check the influence of the equation of state on the results of our simulations, we have performed a simulation adopting an adiabatic equation of state, for which there is no problem with the conservation of wave action for small amplitude waves. The adiabatic equation of state has the form

$$P = (\gamma - 1)e\Sigma \tag{5.28}$$

where P is the vertically integrated pressure, γ is the adiabatic index and e is the specific internal energy. To explore the effect related to the strict wave action conservation for linear waves discussed in [134], we take the same value of the adiabatic index as in their work, namely $\gamma = 1.001$. In view of being close to unity, this has the effect that the equation of state approaches the limit in which the temperature is conserved on fluid elements. Physically in this limit the temperature does not change on account of the very large number of degrees of freedom within the gas. In this limit the temperature does not change in a Lagrangian sense in comparison with the locally-isothermal equation of state for which it does not change in an Eulerian sense. The planet masses and the initial disk surface density profile are the same as in our reference run

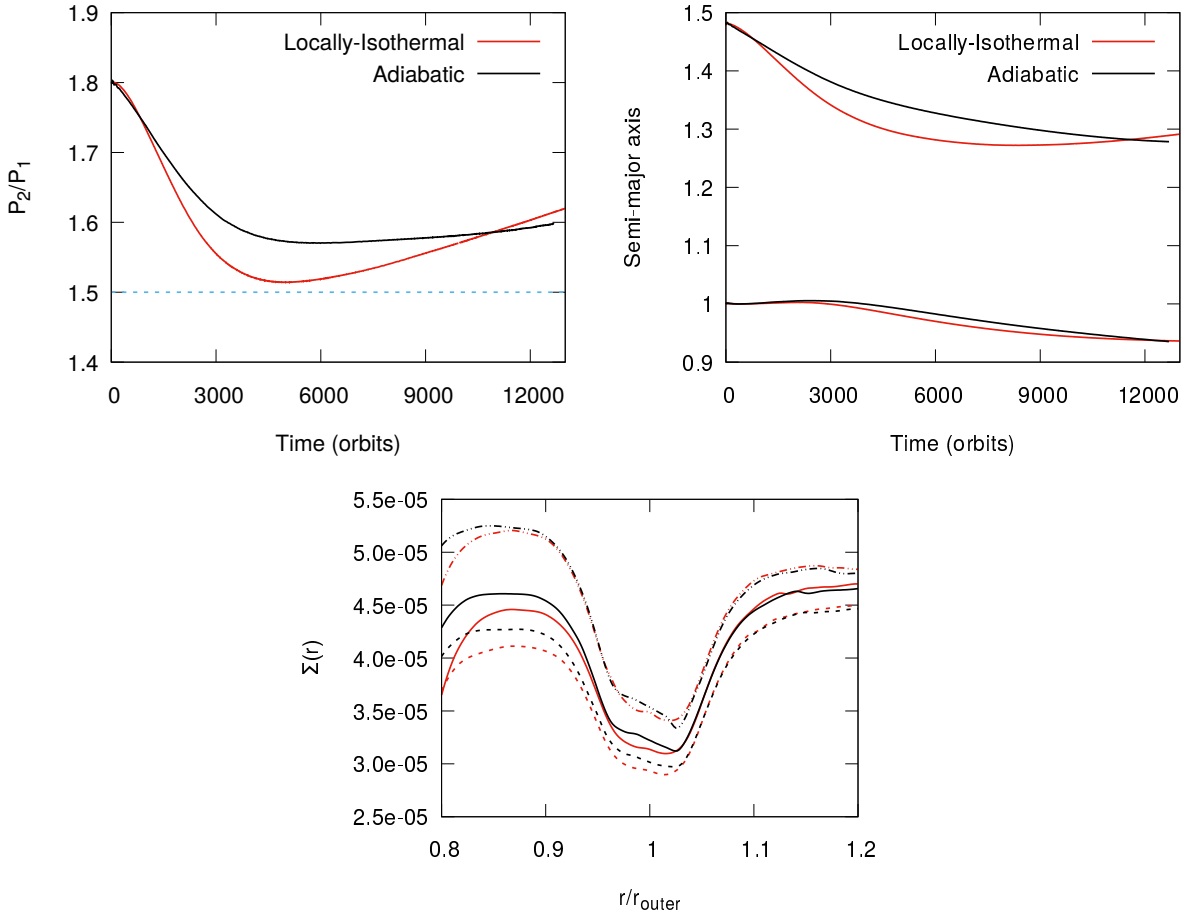

Figure 5.23: Comparison of the results obtained in the simulations with the locally-isothermal and adiabatic equations of state - Top: Evolution of the period ratio and semi-major axes of two planets in the locally-isothermal and adiabatic disks. Bottom: The surface density profile in the vicinity of the outer planet in the simulations with the locally-isothermal disk (red lines) and the adiabatic disk (black lines) at $t = 3000, 6000$ and 9000 orbits, which are indicated by the dashed-dotted lines, solid lines and dashed lines, respectively.

(case 2) (see Section 5.3.2.1). The killing-zone treatment near the boundaries of the disk is not used in this case.

The evolution of the period ratio, semi-major axes of two planets in the simulations with the locally-isothermal and adiabatic equations of state is shown in the top panels of Figure 5.23. We can see, that in the adiabatic case (indicated by the black lines), the planets undergo convergent migration in the early stage of the evolution till $t \sim 6000$ orbits. In comparison, in the locally-isothermal case (denoted by the red lines), the planets migrate convergently for a shorter period of time and already at $t \sim 5000$ orbits they migrate divergently. Moreover, in the adiabatic disk, the divergent migration occurs when the distance between two planets is larger than in the locally-isothermal disk. In the top right panel of the figure, we note that the migration of the inner planet in both cases is similar and it is not the case for the outer planet. The migration

rate of the outer planet is slower in the adiabatic disk than in the locally-isothermal one. In the adiabatic case, the outer planet migrates inwards till the end of the simulations, although at that stage it is very slow. While in the locally-isothermal case, it migrates outwards at the final stage of the calculation.

In the bottom panel of Figure 5.23, we illustrate the azimuthally averaged disk surface density profiles at $t = 3000, 6000$ and 9000 orbits in two cases. It is clear that at t=3000 orbits, the surface density profiles in the vicinity of the outer planet in both simulations are similar, though their forms at the bottom of the partial gap opened by the planet differ slightly. The gap is slightly deeper in the locally isothermal case with difference between that and the adiabatic case being larger in the inner region of the gap. This is most noticeable at $t = 6000$ orbits, when the divergent migration starts and at $t = 9000$ orbits, in the adiabatic case, the maximum deviation of the surface density in the partial gap from that found in the locally-isothermal case still occurs in the inner region.

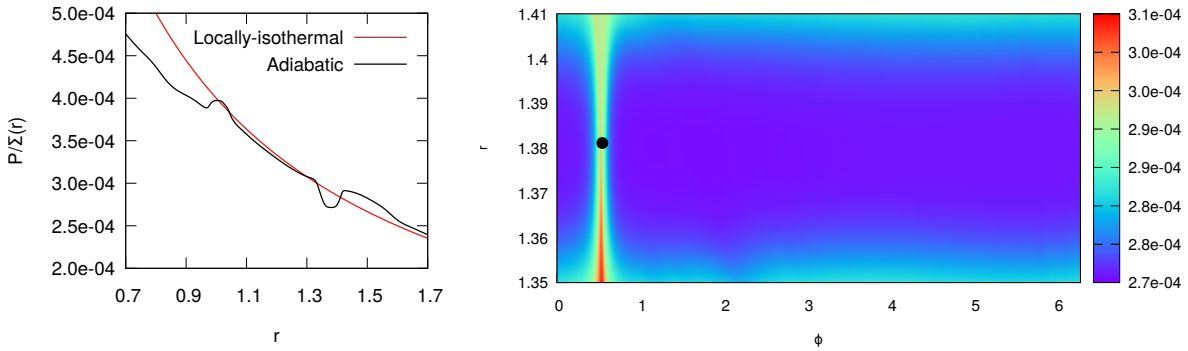

Figure 5.24: Temperature distribution in the vicinity of the planets in the adiabatic case - Left: The temperature profile in the vicinity of two planets at $t = 3000$ orbits in the simulations with a locally-isothermal and an adiabatic equations of state. Right: A contour plot of the temperature in the horseshoe region of the outer planet at $t = 3000$ orbits in the simulation with an adiabatic equation of state. The position of the planet is indicated by the black solid circle.

The differences, just described, in the evolution of planets in the disks with different equations of state, indicate differing behavior in the co-orbital region associated with different temperature profiles (see the top panel of Figure 5.24). In the locally isothermal case, the temperature profile is simply determined by location. Instead, in the adiabatic case, in the limit $\gamma \to 1$, it depends on the history of the material and possibly affected by phase mixing. The explicit comparison between those two cases at $t = 3000$ orbits is shown in the left panel of Figure 5.24. When the adiabatic equation of state is adopted, the temperature in the gaps is reduced below the background. This is expected if the planet migrates inwards dragging its horseshoe region with it. Another feature of the temperature profile, present beyond the outer gap edge, namely the increase of the temperature above the background, is due to the inner material passage through the separatrix to the outer disk. In the right panel of Figure 5.24, we present a contour plot of the temperature in the horseshoe region of the outer planet at $t = 3000$ orbits. The conditions in the gap are very smooth indicating that viscous and numerical diffusion have dealt well with phase mixing in the horseshoe region making the temperature quite uniform. The features in the

co-orbital dynamics, described here, which are the consequences of the conservation of entropy lead to differences in the horseshoe drag that are not easy to determine and in turn to a different torque that we calculate. Indeed such effects seem to slow down the convergent migration of the system at an early stage in the adiabatic case leading to an onset of divergent migration at larger period ratios.

The comparison of the results in two simulations indicate that the general picture obtained from the simulations with the locally isothermal equation of state remains unchanged by adopting the adiabatic equation of state. This means that the repulsion between two planets due to wave-planet interaction is effective in both cases.

5.9.2 Migration of two super-Earths with the disk self-gravity taken into account

In the simulations described up to now, the self-gravity of the disk has not been included. We have a very good argument to choose this approximation for our studies here, which is that the surface densities of the gas used in our simulations are relatively low corresponding to a Toomre Q value ~ 20. However, as it has been pointed out by [13, 20] one of the effects of including disk self-gravity is to cause a shift of the location of Lindblad and corotation resonances, which leads to changes in the torques acting on a planet, and in turn affecting its migration. The best way to check whether the self-gravity can affect our findings is to perform additional simulations.

Ideally, we could run the simulation with the disk self-gravity taken into account in the code explicitly. There are two reasons that we decided to do something else. First, we were concerned about the computational time, second, we were quite confident that it is unlikely that self-gravity will have a significant influence on the results of our simulations. Therefore, instead of running the simulation in the self-gravitating disk, we apply the method given in [25] who found that it is possible to take account of the effect of self-gravity by removing the azimuthally averaged surface density from the density of each cell prior to the calculation of the force due to self-gravity acting on the planet. This ensures that the background forces acting on the background rotating disk and planets are applied in a consistent manner.

To check how the self-gravity can affect our results, we run another simulation, in which all the numerical parameters are the same as adopted previously in the case of a single planet with $q = 1.185 \times 10^{-5}$ in a locally isothermal disk with the initial surface density profile adopted according Equation (5.1) with $\Sigma_0 = 6 \times 10^{-5}$ and $\alpha = 0.5$, $h = 0.02$ and $\nu = 1.2 \times 10^{-6}$ (see the top panel of Figure 5.10). In this case the difference is that the forces acting on the planet are evaluated according to the procedure of [25] outlined above. The evolution of the semi-major axis and the torque acting on the planet in this run is shown in Figure 5.25 indicated by the blue lines in both panels. For comparison, the results of the simulation for the single planet case with $\alpha = 0.5$ shown in Figure 5.7 are also shown in this figure (indicated by the black lines).

From Figure 5.25 (left panel), it is clear that after applying the procedure to account for self-gravity, the migration of the planet in the disk is slightly slower than in the previous case. The total torque from the disk acting on the planet after 700 orbits is $\Gamma_{\rm total} \sim -5 \times 10^{-11}$ while in the case without the correction the total torque is around -6×10^{-11}. From this comparison, we see that the effect of introducing the new procedure is similar to what would be attained by

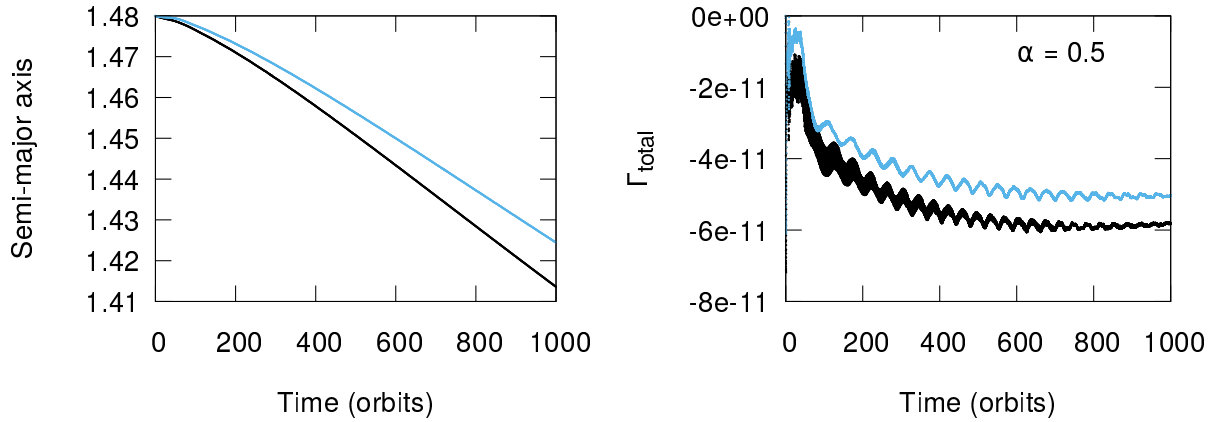

Figure 5.25: The results of the simulations of the single planet in the non-self-gravitating disk with and without the correction to allow for the effect of the disk self-gravity - Left: The evolution of the semi-major axis of the single planet in the non-self-gravitating disk (black line) and with the correction for the effect of the disk self-gravity (blue line). Right: The torque from the disk acting on the planet in both cases.

reducing the background surface density by a modest amount and thus could be compensated for by increasing it (see the discussion Section 5.7.2.3).

After investigating the effect of disk self-gravity on the migration of a single planet we are quite confident that taking into account this effect in the two-planet case will not change qualitatively the outcome of our calculations. To demonstrate this, we perform the simulations for our reference run (case 2) (see Section 5.3.2) again, but this time implementing the same procedure as described above for a single planet. The results are shown in Figure 5.26 (blue line) together with the original reference case (black line). In this figure, we show a comparison of the evolution of the orbital period ratios (left panel) and the semi-major-axes of the planets (right panel) in both simulations. It is clear that the divergent migration occurs later when the self-gravity is taken into account. In addition, the divergent migration takes place when the distance between two planets is larger than in the disk without self-gravity included. Moreover, in the right panel, we can see that the migration rates of two planets are slower than that in the simulation without considering the disk self-gravity, as we found from the comparison for the single planet case discussed above. The observed effect of disk self-gravity is similar to that obtained by reducing the background surface density, as illustrated in Figure 5.18 and discussed in Section 5.7.2.3.

Therefore, from the results presented here, we confirm our expectation that it is unlikely that self-gravity will have a significant influence on the results of our simulations.

5.10 Migration of super-Earths in a viscous disk with local balance between heating and cooling

We have investigated the process of repulsion between planets arising from wave-planet interaction for a range of super-Earth masses and a range of values for the characteristic magnitude

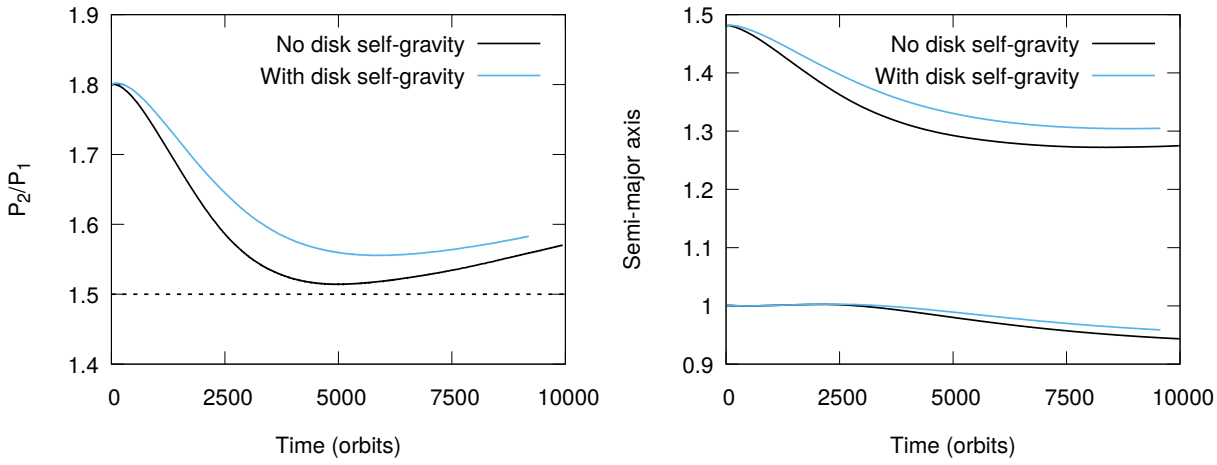

Figure 5.26: The results of the simulations of two planets in the non-self-gravitating disk with and without the correction to allow for the effect of the disk self-gravity- Left: Evolution of the period ratio in the simulations of two planets in the non-self-gravitating disk with and without the correction to allow for the effect of the disk self-gravity. Right: Evolution of the semi-major axes of two planets in both simulations.

of the disk surface density. However, so far only a locally isothermal equation of state has been extensively considered, though in Section 5.9.1, we have discussed also the migration of two super-Earths in the protoplanetary disk by adopting the adiabatic equation of state with $\gamma = 1.001$. The calculation with the adiabatic equation of state has been done just to check whether the general picture obtained from the simulations with the locally isothermal equation of state remains unchanged. In order to show that the repulsion between planet is not limited to this particular physical situation, we extend our study to an initial disk model in which the balance between local heating and cooling determines the local disk temperature. This is very different from a local isothermal prescription and could potentially lead to substantially different dynamics in the vicinity of gaps induced by orbiting planets. The adopted here disk model is viscous while initially supporting a constant angular momentum flux. One of the possible physical scenarios, which justifies the consideration of such a model is when the inner disk interacts with a magnetosphere of the central star prior to dispersal [9], which might be associated with a protoplanet trap.

5.10.1 A viscous disk model with local balance between heating and cooling

We start from considering a model with constant angular momentum flux F, which has the form

$$F = 3\pi\nu\Sigma\sqrt{GM_*r}. \tag{5.29}$$

We adopt the general power law scalings with

$$\Sigma \propto r^{-\beta_1}, \;\; h \propto r^{-\beta_2} \;\; \text{and} \;\; \nu \propto r^{-\beta_3}$$

where β_i for i=1, 2 and 3 are constants. To provide scalings for these quantities, we set

$$\Sigma = 6.0 \times 10^{-5} f_\Sigma (M_*/R^2)(r/R)^{-\beta_1}, \tag{5.30}$$

$$h = 0.02 f_h (r/R)^{-\beta_2} \ , \tag{5.31}$$

and

$$\nu = 1.2 \times 10^{-6} f_\nu \sqrt{GM_* R} (r/R)^{-\beta_3} \tag{5.32}$$

where we adopt the fixed parameters $M_* = 1 M_\odot$ and $R = 0.1$ AU while f_h, f_Σ and f_ν are the dimensionless scaling constants that are expected to be of order unity. The characteristic disk mass within radius R with the above specifications is $6 \times 10^{-5} \pi f_\Sigma M_*$. To have an idea how it compares to the disk mass extrapolated for the MMSN, we perform the evaluation for $R = 0.1$ AU, $M_* = 1 M_\odot$ and $f_\Sigma = 1$, and we get the disk mass which is about 1.5 times smaller than derived from the MMSN. It can be mentioned here that the disk mass may be reduced by scaling down the surface density. According to the discussion in Section 5.8, we might expect that under appropriate conditions and scaling, the interactions between the disk and the planet would be preserved with the reduced disk mass. As we consider here the model with constant angular momentum flux, so $\beta_1 + \beta_3$ must be equal to 1/2. Assuming a constant kinematic viscosity we have $\beta_3 = 0$ and thus $\beta_1 = 1/2$. Inserting Equations (5.30) and (5.32) into Equation (5.29) and taking $M_* = M_\odot$ and $R = 0.1$ AU, we obtain

$$\begin{aligned} \frac{F}{\sqrt{GM_* R}} &= 6.79 \times 10^{-10} f_\nu f_\Sigma M_\odot \sqrt{GM_\odot} R^{-3/2} \\ &= 6.79 \times 10^{-10} f_\nu f_\Sigma M_\odot (2\pi \cdot (10)^{3/2} \cdot \mathrm{yr}^{-1}) \\ &= 1.35 \times 10^{-7} f_\nu f_\Sigma M_\odot \cdot \mathrm{yr}^{-1}. \end{aligned} \tag{5.33}$$

At this stage the model is not yet complete. We did not constrain the value of β_2. To complete the model we will use the energy balance. Once we provide the energy equation we will be able to get another relationship between the β_i and find out the missing β_2. We start by considering the properties of the opacity that is mostly due to grains as can be seen from [57]. They showed that, for the parameter ranges of interest the grain opacity, κ, is approximately constant and scales with metal abundance, Z, so that $\kappa \sim (Z/0.02)$. This scaling holds down to very small Z as when $Z = 0$, $\kappa \sim 10^{-8}$, which is associated with Rayleigh scattering due to Hydrogen molecules. Thus if there is significant unknown grain depletion as a result of the planet formation process, the opacity is highly uncertain, which may translate to the uncertainty in the disk models.

Next, for our fixed parameters, namely $M_* = M_\odot$ and $R = 0.1$ AU, we evaluate the surface density given by Equation (5.30). It has the form

$$\Sigma = 53333 f_\Sigma (r/R)^{1/2}. \tag{5.34}$$

For standard metallicity without considering the grain depletion, this indicates that the disk is very optically thick with $\tau = 5 \times 10^4 f_\Sigma$ at $r = R$. In such an optically thick case, the rate of cooling per unit mass Q^- is given by

$$Q^- = (2\sigma T_e^4)/\Sigma \tag{5.35}$$

where σ is the Stefan-Boltzmann constant and T_e is the effective temperature which has to be related to the mid-plane temperature. Here, we assume that radial diffusion of heat is not important. Our assumption is reasonable for disturbances on a radial scale exceeding the scale height with smaller scales being smoothed by physical and numerical viscosity. The rate of viscous heating per unit mass Q^+ is given by

$$Q^+ = \nu r^2 \left(\frac{d\Omega}{dr}\right)^2 = 2.7 \times 10^{-6} f_\nu (GM_*)^{3/2} R^{-5/2} (r/R)^{-3}. \tag{5.36}$$

The balance between the rates of the cooling and viscous heating, it means when Q^- is equal to Q^+, allows to determine the effective temperature T_e, which is expressed by

$$T_e^4 = \frac{7.2}{\sigma} \times 10^{-2} f_\nu f_\Sigma (GM_*)^{3/2} R^{-5/2} (r/R)^{-7/2} \tag{5.37}$$

or

$$T_e = 917.8 (f_\nu f_\Sigma)^{1/4} (r/R)^{-7/8} \text{ K}. \tag{5.38}$$

Next, we deduce the expression of h. Assuming that the temperature of the mid-plane is $T = f_T T_e$, where f_T is a scaling parameter, we have

$$h = \frac{\sqrt{\mathcal{R}T/\mu}}{r\Omega} = 0.019 (f_T)^{1/2} (f_\nu f_\Sigma)^{1/8} (r/R)^{1/16} \tag{5.39}$$

where $\mathcal{R}$ is the gas constant and μ is the mean molecular weight. Here we adopt $\mu = 2.35$ corresponding to the predominantly molecular Hydrogen [61] .

The determination of f_T depends on the way in which the energy is transported from the disk mid-plane to the surface. This is highly uncertain since the optical depth is affected by uncertain grain depletion and the turbulent transport due to the magnetorotational instability operates. However, we remark that the simulations in [61] indicate only modest mean vertical variation of the temperature for models with optical depth less than ~ 100. Accordingly, we shall assume appropriate grain depletion and adopt $f_T = 1$ in order to have a working model.

This was the last specification needed in order to complete the initial model for a viscous protoplanetary disk with local balance between heating and cooling. Now, the model can be described as follows

$$\Sigma = 6.0 \times 10^{-5} f_\Sigma (M_*/R^2)(r/R)^{-1/2}, \tag{5.40}$$

$$h = 0.019 f_T^{1/2} (f_\nu f_\Sigma)^{1/8} (r/R)^{1/16} \tag{5.41}$$

and

$$\nu = 1.2 \times 10^{-6} f_\nu \sqrt{GM_* R}. \tag{5.42}$$

For practical purposes, we will set all the scaling factors of f_Σ, f_ν and, as already mentioned, f_T equal to unity.

5.10.2 Numerical setup

We run the simulations to follow the evolution of two super-Earths migrating in the disk with constant angular momentum flux, described by Equations (5.40 – 5.42). As mentioned before, the units of length and mass are taken to be $R = 0.1$ AU and $M_* = M_\odot$. The energy equation solved in the simulations has the form

$$\frac{\partial e}{\partial t} + \nabla \cdot (e\vec{u}) = -P\nabla \cdot \vec{u} + Q^+\Sigma - Q^-\Sigma \tag{5.43}$$

where e is the internal energy per unit area, $\vec{u}$ is the gas velocity, P is the integrated pressure, Q^- and Q^+ are the heating and cooling functions, respectively, defined in Equations (5.35) and (5.36). An ideal equation of state is adopted to close the hydrodynamic equations, so the vertically integrated pressure satisfies the relation

$$P = \frac{\mathcal{R}}{\mu}\Sigma T. \tag{5.44}$$

Thus the internal energy per unit area is related to the temperature through

$$e = \frac{\mathcal{R}}{\mu}\frac{\Sigma T}{\gamma - 1} \tag{5.45}$$

where γ is the adiabatic index taken to be $9/7$.

We adopted the initial disk model with constant angular momentum flux, F, for which the inner and outer boundaries of the computational domain, correspond to imperfectly slippery rigid boundaries. At the boundaries the constant flux is respectively transported away from and towards by viscous stresses. This comes down to the boundary condition with the form

$$F = -2\pi\nu\Sigma r^3 \frac{d(v_\phi/r)}{dr}, \tag{5.46}$$

where v_ϕ is the gas velocity in the azimuthal direction. In our simulations we retain this boundary condition when the planets are put into the disk. In doing so we remark that the boundary conditions may evolve in a long time scale as physical conditions at the boundaries change.

Before doing actual simulations, which consists in placing the planets in the disk and following their evolution, we need to perform test calculations. The disk model, we have just described, should converged to the expected steady state before adding the planets to it. To check, whether it is indeed the case, we run a simulation in which the empty disk has been evolved for 800 orbits. The evolution of the unperturbed surface density profile without planets in the disk is shown in the left panel of Figure 5.27. It can be seen clearly that during the calculation, which lasted for 800 orbits, $\Sigma(r)$ does not change significantly from its initial profile. In the right panel of Figure 5.27, we present the temperature profile of the disk at different moments, together with the analytic value given by Equation (5.38). After 800 orbits, the comparison indicates a very good agreement. Therefore, we conclude that the test calculation was successful and that the disk relaxation for 800 orbits in order to ensure convergence to the expected steady state is sufficient.

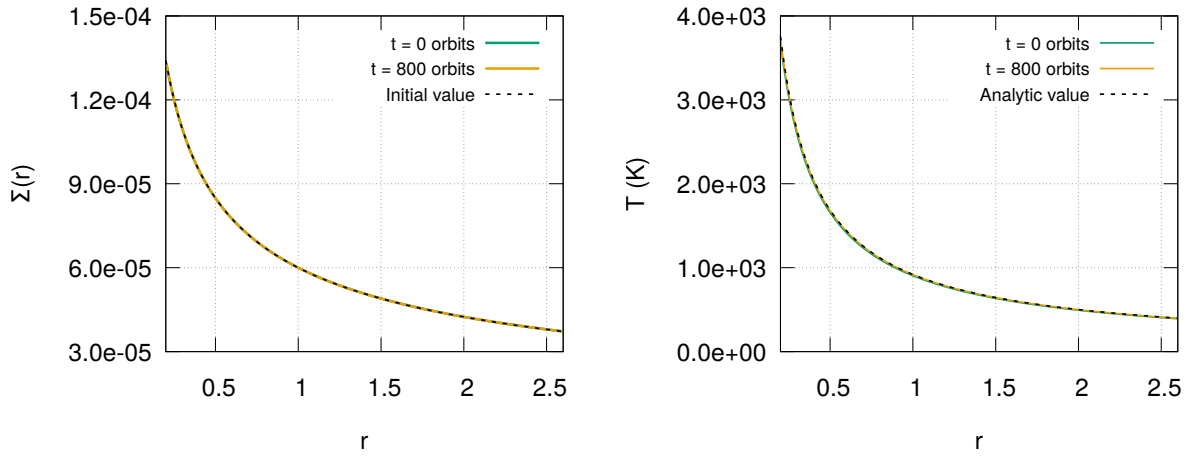

Figure 5.27: Evolution of the radial profiles of the surface density and temperature in a viscous disk with local balance between heating and cooling - Left: Disk surface density profile $\Sigma(r)$ at $t = 0$ and 800 orbits. The black dashed line indicates the initial surface density profile given in Equation (5.40). Right: Disk temperature profile T at $t = 0$ and 800 orbits. The black dashed line denotes its analytic value given in Equation (5.38).

5.10.3 Results of hydrodynamic simulations

In this section we investigate the migration of two super-Earths in a protoplanetary disk by adopting the disk model described above. The disk was relaxed for 800 orbits in order to ensure that the steady state is attained before putting the planets into it. The inner and outer planets are initially located in the circular orbits with the positions of $r_1 = 1.0$ and $r_2 = 1.36$, respectively. Here we consider two planet pairs, which differ with regard to the mass of the inner planet. The first one has $q_1 = q_2 = 2.6 \times 10^{-5}$ (both planets have the same mass) while the second one has $q_1 = 1.3 \times 10^{-5}$ and $q_2 = 2.6 \times 10^{-5}$ (the inner planet has its mass smaller than the outer one by a factor of two).

5.10.3.1 A case with the equal mass planets

Here, we study the migration of two super-Earths in the simulation for the equal mass case. The evolution of the period ratio, semi-major axes, eccentricities of the planets and the 3:2 resonant angles is shown in Figure 5.28. We can see that both planets migrate inwards during the whole calculation. After a short period of divergent migration at the initial stage of the evolution, the planets undergo convergent migration till $t \sim 900$ orbits when they arrive at the 3:2 MMR. At this time, the eccentricities of two planets are excited to $e_1 \sim 0.012$ and $e_2 \sim 0.013$ while the 3:2 resonant angles begin to librate. When $t \sim 1300$ orbits, the divergent migration takes place and the planets leave the 3:2 MMR with the increased period ratio. After that, both eccentricities decrease and the 3:2 resonant angles start to circulate.

From the results of the simulation shown above, we note that the 3:2 MMR has a significant effect on the relative migration of two super-Earths. In order to exclude this influence, which arises from the gravitational interactions between two planets, we rerun the simulation without

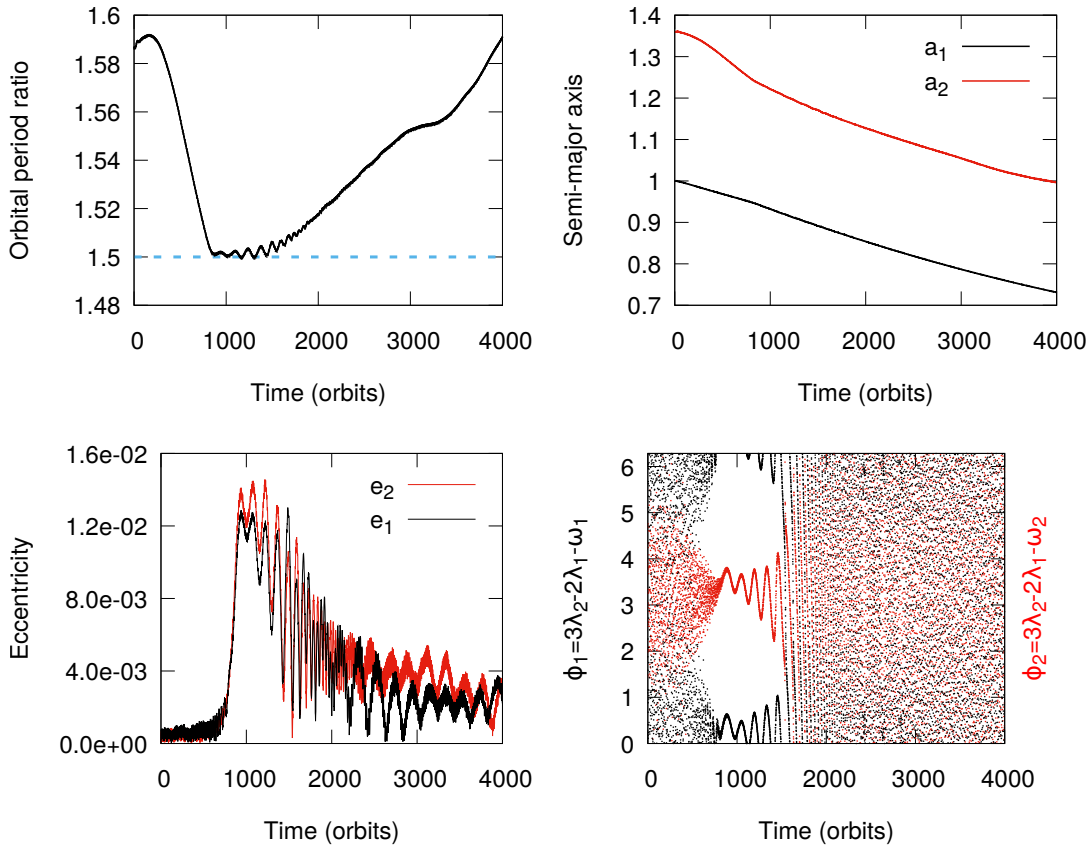

Figure 5.28: Results of the simulation of two equal-mass super-Earths migrating in the disk with local heating and cooling - Evolution of the period ratio, semi-major axes, eccentricities and the 3:2 resonance angles in the simulation are shown in each panel, respectively. The masses of two planets are taken to be $q_1 = q_2 = 2.6 \times 10^{-5}$. The horizontal dashed blue line in the top left panel indicates the position of the 3:2 resonance commensurability.

computing the planet-planet interactions. The orbital period ratio and the semi-major axes of two planets in this simulation are given in Figure 5.29. They are indicated by the blue solid and dashed lines in the left and right panels, respectively. In this way, we observe the effects caused only by the interaction of planets with the gas in the disk structured by the wakes they produce. And indeed, also in this case, the divergent migration took place. The planets did not stop at the position of the resonance, because the planets do not feel the direct gravitational interaction between each other. Instead, they evolve convergently a little bit further than in the previous case and then, at around $t \sim 2500$ orbits, the migration changes into the divergent one. From those two calculations we can conclude that, even if the MMR may play a role in the way the repulsion mechanism operates, but by no means it is necessary for the effect to take place.

We have already mentioned few times in this thesis, that it is essential to know how a single planet capable to open a partial gap migrate in the disk. In principle it could happen that the effect we observe here is caused by the intrinsic migration of the planets. To check this, we run two simulations in which only an isolated planet with $q = 2.6 \times 10^{-5}$ is initially put into the relaxed disk. The first one with the planet at the position $r = 1.0$ and the second one with the

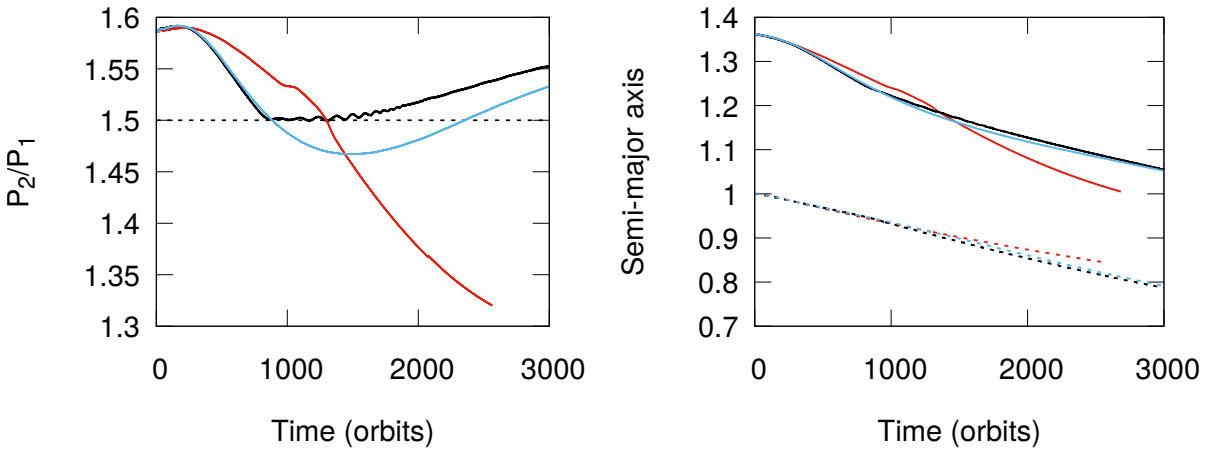

Figure 5.29: Results in the simulations of two equal-mass super-Earths with and without planet-planet interaction in the disk with local heating and cooling - Left: The period ratio evolution in the simulation of two super-Earths with $q_1 = q_2 = 2.6 \times 10^{-5}$ with (black solid line) and without (blue solid line) the planet-planet interactions. The red solid line represents the period ratio calculated from the results of single planet runs for $q = 2.6 \times 10^{-5}$ starting from the initial positions $r = 1.0$ and $r = 1.36$. Right: Evolution of the semi-major axes of the two planets in the simulations shown in the left panel. The results of the simulations with and without the planet-planet interaction are indicated by the black solid and dashed lines and the blue solid and dashed lines, respectively. The red dashed and solid lines represent the result of the single planet simulations initiated with $r = 1.0$ and $r = 1.36$, respectively.

planet at $r = 1.36$. The evolution of the semi-major axis of the single planet in two simulations is shown in the right panel of Figure 5.29 (red solid and dashed lines). For comparison, we illustrate P_2/P_1 calculated from the orbital periods of the single planets in these two cases in the left panel of Figure 5.29 (red solid line).

From the results shown in the figure, we can see that the single planet in both simulations with different initial positions migrates inwards. Moreover, the planet initiated at $r = 1.36$ migrates faster than the one with the initial position of $r = 1.0$. Therefore, the relative migration of a pair of such planets is expected to be convergent, which is confirmed by the ratio of the planetary orbital periods in these two cases illustrated in the left panel of Figure 5.29. Here we remark that the variations of temperature and surface density in the disk alone could make divergent migration through their effect on the disk-planet interaction [119]. But this is not the case in our simulations. On the other hand, we found that in the simulation for two planets cases indicated by the black solid line, the convergent migration only persists for roughly 1000 orbits till when the planets enter into the 3:2 MMR. The planets are captured into the 3:2 MMR, but they do not stay in there for a long time and eventually migrate divergently. In the case, in which the planet-planet interaction is not present in the simulation (blue solid line), the convergent migration is retained till 1500 orbits. The divergent migration occurs after that and must be produced by the interaction between the planets and the perturbed disk.

In addition, we have performed a simulation with $q_1 = q_2 = 1.95 \times 10^{-5}$ and shown its outcome in Figure 5.30. The results of this simulation are similar to the simulation with $q_1 =$

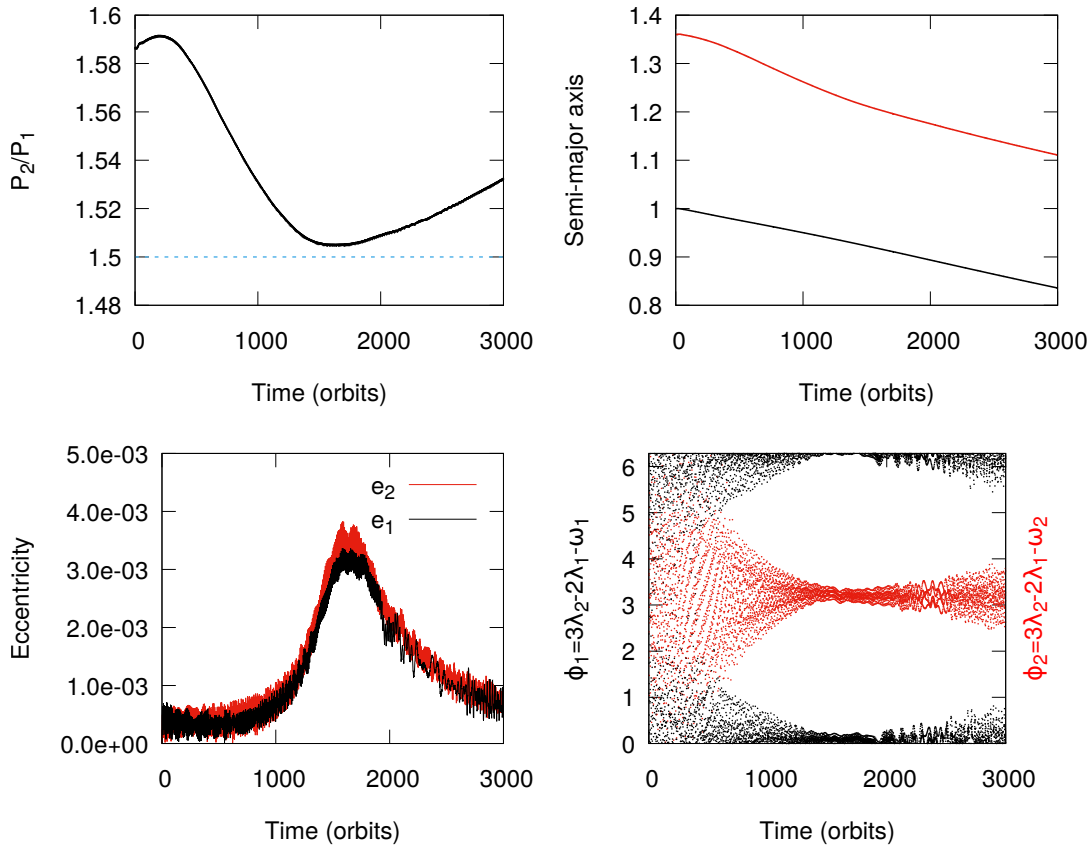

Figure 5.30: Results of the simulation of two equal-mass super-Earths ($q_1 = q_2 = 1.95 \times 10^{-5}$) migrating in the disk with local heating and cooling - Evolution of the period ratio, semi-major axes, eccentricities of two planets and the 3:2 resonant angles is shown in each panel, respectively. The horizontal dashed blue line in the top left panel indicates the position of the 3:2 commensurability.

$q_2 = 2.6 \times 10^{-5}$ presented in Figure 5.28, except that the initial convergent relative migration rate of two planets is slower. In this case, the divergent migration occurs around $t \sim 1600$ orbits before the planets arrive at the 3:2 MMR. The detailed discussion will be given in a summary at the end of this section.

5.10.3.2 A case with the unequal-mass planets

Now we consider the case of a pair of the unequal mass planets migrating in the disk with local balance between heating and cooling. In order to ensure the initial convergent migration, we choose the inner planet mass to be smaller than the mass of the outer one. The mass of the inner planet is taken to be $q_1 = 1.3 \times 10^{-5}$ and the initial position that of $r_1 = 1.0$. The outer planet mass has the value of $q_2 = 2.6 \times 10^{-5}$ and the initial location of the planet is $r_2 = 1.36$. The disk was relaxed for 800 orbits before adding the planets into the calculation.

In Figure 5.31, we show the evolution of the period ratio, semi-major axes, eccentricities of two planets and the 4:3 resonance angles. We can see that the relative convergent migration

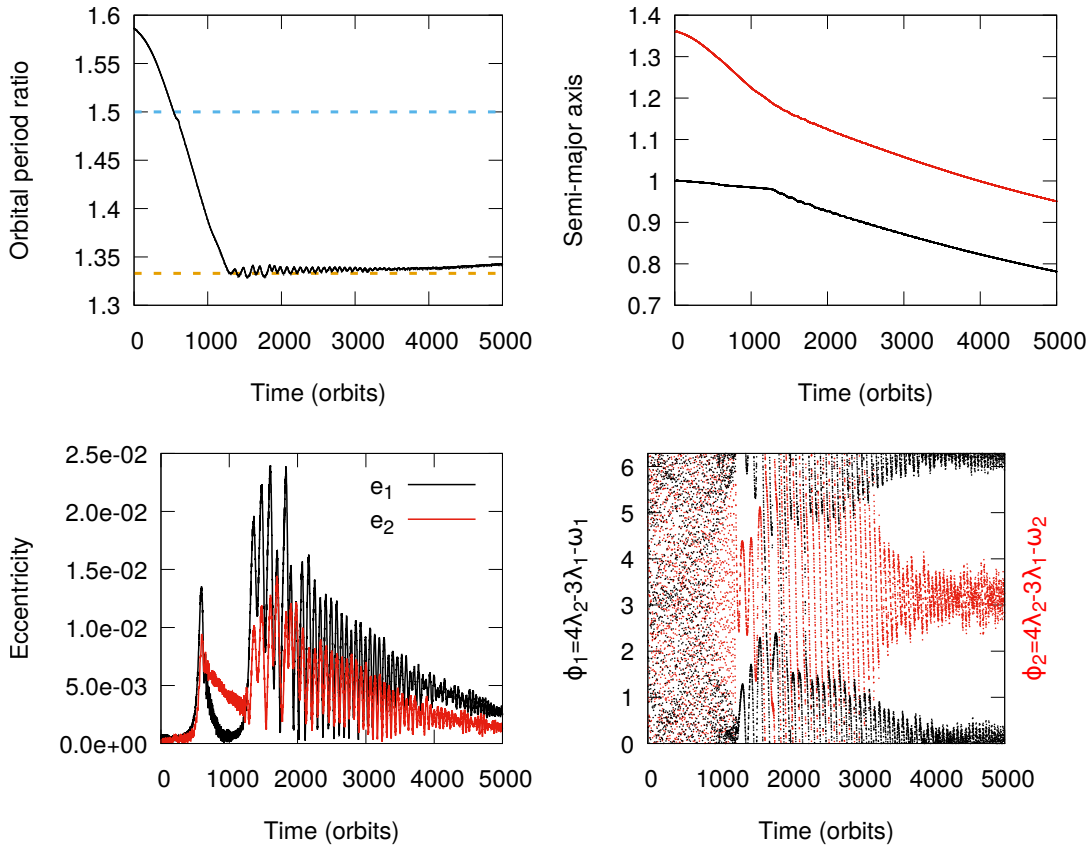

Figure 5.31: Results of the simulation of two unequal-mass super-Earths migrating in the disk with local heating and cooling - Evolution of the period ratio, semi-major axes, eccentricities and the 4:3 resonance angles is shown in each panel, respectively. The masses of the inner and outer planets are taken to be $q_1 = 1.3 \times 10^{-5}$ and $q_2 = 2.6 \times 10^{-5}$. The horizontal dashed blue and yellow line indicate the positions of the 3:2 and 4:3 commensurabilities, respectively.

of the planets is much faster than in the equal mass planet case. As a consequence, they passed through the 3:2 MMR at $t \sim 500$ orbits and arrive at the 4:3 MMR at $t \sim 1200$ orbits. The eccentricities of two planets are excited twice, the first time when the planets are passing through the 3:2 MMR and the second one when arriving at the 4:3 MMR. After 3000 orbits, the divergent migration takes place with the period ratio slowly increasing and the eccentricities slowly decreasing. Both 4:3 resonant angles librate till the end of the simulation. During the whole calculation, both planets migrate inwards in the disk.

As in the study of the equal-mass planet migration, we run another simulation in which the planet-planet interaction is switched off during the entire calculation. The orbital period ratio and the semi-major axes of the two planets in this simulation are shown in Figure 5.32, which are respectively indicated by the blue solid line in the left panel and the blue solid and dashed lines in the right panels. We also run simulations for the isolated planet with $q = 1.3 \times 10^{-5}$ and the initial position $r = 1.0$ as well as with $q = 2.6 \times 10^{-5}$ and the initial position $r = 1.36$ in the relaxed disk, respectively. The evolution of the semi-major axes of the isolated planets in these two simulations is shown in the right panel of Figure 5.32. The red dashed and solid

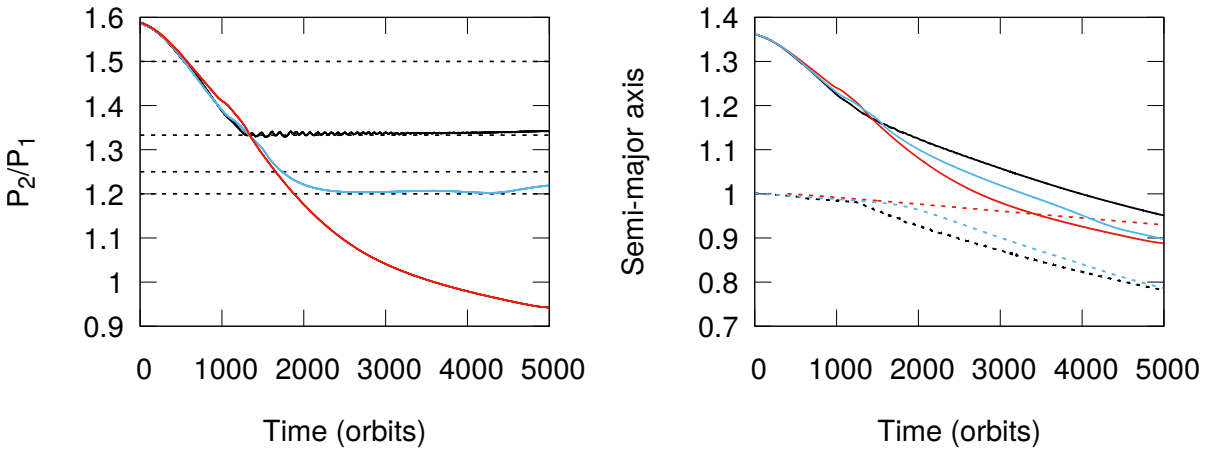

Figure 5.32: Results of the simulations of two unequal-mass planets with and without planet-planet interaction in the disk with local heating and cooling - Left: Period ratio of planets in the simulations of the evolution of two super-Earths with $q_1 = 1.3 \times 10^{-5}$ and $q_2 = 2.6 \times 10^{-5}$ migrating in a disk with local heating and cooling with and without the planet-planet interaction, which are respectively indicated by the black and blue solid lines. The red solid line represents the period ratio based on results from the single planet cases with $q = 1.3 \times 10^{-5}$ initiated at $r = 1.0$ and $q = 2.6 \times 10^{-5}$ initiated at $r = 1.36$. The dashed horizontal lines indicate the positions of the 3:2, 4:3, 5:4 and 6:5 resonances from top to the bottom. Right: Evolution of the semi-major axes of two planets in the simulations illustrated in the left panel. The results from the simulations with and without the planet-planet interaction are respectively denoted by the black and blue dashed and solid lines. The red dashed and solid lines show the results of the single planet simulations with $q = 1.3 \times 10^{-5}$ and $q = 2.6 \times 10^{-5}$ respectively.

lines represent respectively, the evolution of the isolated inner and outer planets. Based on the planetary orbital periods in two single planet cases, we calculate the period ratio P_2/P_1 and plot it in the left panel of Figure 5.32 indicated by the red solid line.

The migration of the isolated planet placed at the position of the outer planet is much faster than the isolated planet evolving from the position of the inner planet. Therefore, the convergent migration is expected, if we can ignore any effects due to the presence of two planets in the disk. It is illustrated in the left panel of Figure 5.32 (red solid line). After switching off the planet-planet interaction, the planets pass through the 4:3 and 5:4 commensurabilities during the convergent migration. However, when they approach to the 6:5 commensurability, the migration became divergent and the period ratio subsequently slowly increased. This evolution is similar to that in the equal mass case mentioned above.

5.10.3.3 Effectiveness of repulsion between planets in a disk with local heating and cooling

In our simulations we have demonstrated the repulsion between planets with a mass in the super-Earth range. The reason for this to happen is the disturbance in the disk induced by one planet interacting with the other. As waves are launched by the planets in this interaction we describe this as wave-planet interactions. The repulsion was found to be very strong between

planets with equal mass as can be clearly noticed in Figure 5.33.

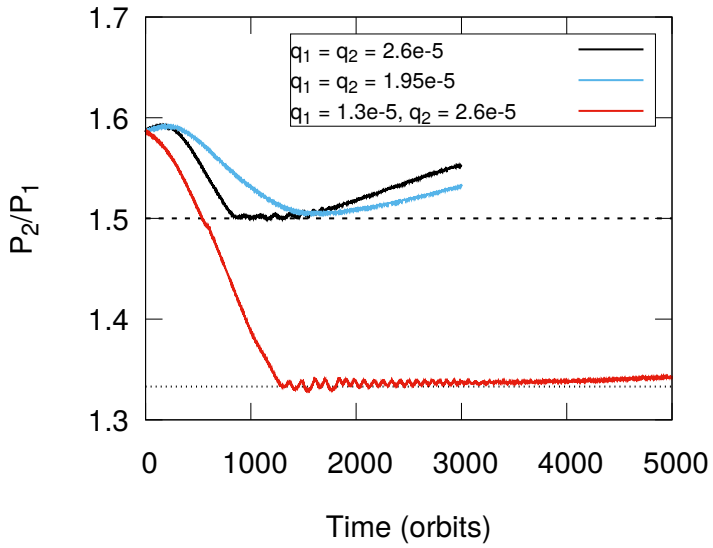

Figure 5.33: Comparison of the period ratio evolution in the simulations of two super-Earths in the equal- and unequal-mass cases in the disk with local heating and cooling - Evolution of the period ratios of two planets in the simulations of two super-Earths with mass ratios of $q_1 = q_2 = 2.6 \times 10^{-5}$ (black line), $q_1 = q_2 = 1.95 \times 10^{-5}$ (blue line) and $q_1 = 1.3 \times 10^{-5}$, $q_2 = 2.6 \times 10^{-5}$ (red line) migrating in a disk with local heating and cooling. The horizontal dashed and dotted lines indicate the locations of the 3:2 and 4:3 resonances, respectively.

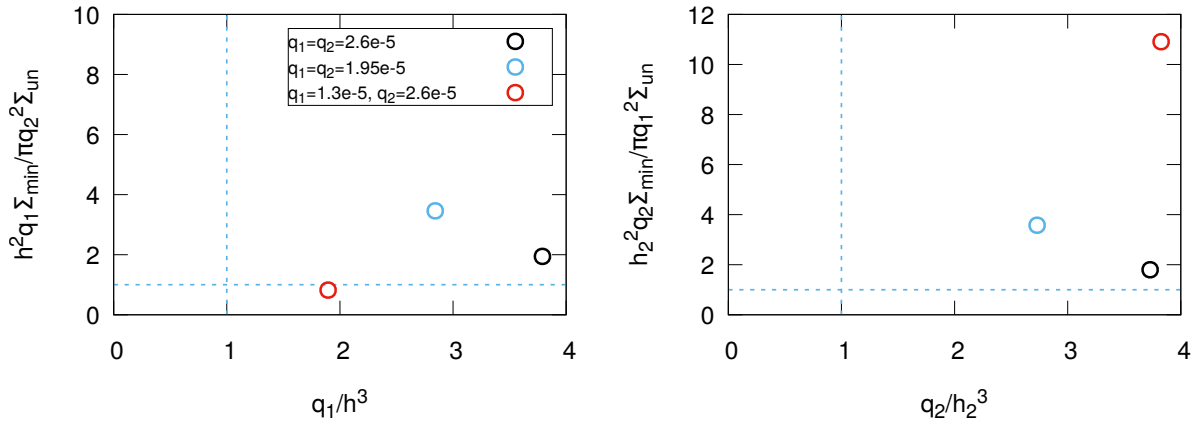

Figure 5.34: Effectiveness of the repulsion due to wave-planet interactions in the system of two super-Earths migrating in the disk with local heating and cooling - The results of the simulations of two super-Earths, in the equal- and unequal-mass cases, are plotted in the planes used to indicate the effectiveness of the repulsion due to wave-planet interactions as was done for our previous simulations in Figure 5.13 (see the discussion in Section 5.7).

In this figure, we draw the evolution of the period ratios in the simulations of two equal-mass cases (blue and black lines) and the unequal mass case (red line). The initial relative migration

in the equal-mass cases is slow favoring the mechanism at work.

Now, we can check whether the criteria for the effectiveness of the repulsion derived in Section 5.6, applied already to our previous simulations, and plotted in Figure 5.13, are satisfied in the three simulations discussed here. The results are shown in Figure 5.34. The black and blue open circles, which correspond to the two equal-mass cases, are located in the regions in which the occurrence of the efficient repulsion between two planets in the system due to the wave-planet interactions is expected. Instead, the red open circle representing the unequal-mass case in the left panel is not located in this region, which infers that the repulsion mechanism does not work efficiently on the inner planet and in consequence the repulsion between two planets is not as strong as in other two cases. Based on that, we confirm that the results of the simulations are consistent with the predictions obtained from the criteria we derived for the repulsion mechanism to work.

5.11 Summary of the main results

In this chapter we have demonstrated that wave-planet repulsion can be effective in converting convergent migration to divergent one as two planets in the super-Earth range, embedded in a thin low viscosity gaseous protoplanetary disk, approach a first-order commensurability. The effective repulsion between planets found in our simulations prevent the permanent capture into this commensurability. Moreover, we have derived the criteria, which must be satisfied for the effective wave-planet repulsion to take place.

The most important specific results obtained in this chapter are summarized as follows:

- We found (Section 5.3) that effective repulsion between planets takes place in the case of a pair of super-Earths with the masses of inner and outer planets taken to be respectively $q_1 = 1.3 \times 10^{-5}$ and $q_2 = 1.185 \times 10^{-5}$, embedded in a protoplanetary disk with the aspect ratio $h = 0.02$ and kinematic viscosity $\nu = 1.2 \times 10^{-6}$. The repulsion between two planets is present both in the simulation with a power-law surface density profile, taken in the form $\Sigma(r) = 8 \times 10^{-5} \cdot r^{-0.5}$ and the one with an inner cavity described in Equation (5.1). Moreover, it operates also in the simulation with the planet-planet interactions between two super-Earths switched off (see Figure 5.3).

- One of the important steps in uncovering the nature of the repulsion between planets was to separate the effects arising only in a presence of two planets in the disk from those which are there also in the case of an isolated planet. To made this step, we explored the migration of an isolated super-Earth capable to form a partial gap in a gaseous protoplanetary disk, which is exactly this type of planet we have in our simulations with two super-Earths (Section 5.4). We demonstrated that standard type I migration does not apply to this case even when scaled with the surface density in the gap. For that reason, we developed a new fit to the migration rate, given in Equation (5.11), which is applicable to local power-law surface density profiles. Using our new torque formula, derived in this way, we succeeded in showing the presence of an additional torque acting on the outer planet of the two planet system embedded in the disk. We identified the additional torque as

being due to wave-planet interactions (see Figure 5.11), and characterized its magnitude (Section 5.5).

- We developed a simplified description of wave-planet interactions, based on density waves emitted by one planet being absorbed in the horseshoe region of the other and then transmitted to it (Section 5.6). In this way the density waves are able to supply an additional torque needed to change from convergent to divergent migration, the presence and magnitude of which we have determined in our simulations. We formulated the approximate conditions for the wave-planet interactions to be effective (inequalities (5.15) and (5.20) and their counterparts for the other planet). These criteria describe clearly that the planets should be massive enough to make a partial gap but that this should not be so deep that there is inadequate material in horseshoe regions to be able to transfer the angular momentum transported by waves to the associated planet. We verified the criteria for our simulations in Section 5.7.1 and Section 5.7.2 for a range of mass ratios $(1.185 \times 10^{-5}, 2.6 \times 10^{-5})$ adopted for both planets. We showed that when the two conditions are satisfied for both planets the repulsion between planets is effective and divergent migration takes place, preventing the planets from being trapped into MMRs.

- We found that increasing the initial rate of convergence, which can be achieved by increasing the disk surface density or the mass of the outer planet relative to the inner one, resulted in the planets approaching each other more closely before switching to divergent migration (see Figure 5.16).

- We checked that the angular momentum being transported between the planets was consistent with theoretical expectation in the case of density waves generated by the planets' interaction with the disk (Section 5.6.3). It was also shown that this was consistent with the magnitude of the torque required to convert from convergent to divergent migration.

- We we established the robustness of the mechanism to changes of the form of the surface density profile, changes to the equation of state and a correction to allow for the effect of self-gravity (Sections 5.9). In addition, we investigated the effects of significant changes to the magnitude of the surface density in the disk in which the planets are embedded by considering reductions in this by more than an order of magnitude obtained through application of a uniform scaling factor (Section 5.8).

- We demonstrated the effectiveness of the repulsion between planets in a viscous disk in which the temperature was determined by a local balance between heating and cooling (Section 5.10). We confirmed that the conclusions obtained from the simulations with this particular disk model are consistent with the results of calculations with a locally isothermal disk model (see Figure 5.33 and Figure 5.34).

In this chapter, we have investigated the mechanism underlying the repulsion between two super-Earths migrating in a protoplanetary disk that enables to change the convergent migration to be divergent. Our findings in this thesis provide one of the possible reasons why there are not so many planet pairs observed to be locked in the mean-motion resonances, as it could be

inferred from the predictions taking into account only standard type I migration. To have a definitive solution to this problem it is necessary to incorporate the entire final stages of the evolution of proptoplanetary disks that also includes the formation of the planets and requires an extensive further studies. More thoughts for the extension of our study and perspective for the future will be discussed in the final chapter of this thesis.

Chapter 6

Summary and Conclusion

In this thesis we have investigated the robust features observed in many planetary systems (including our Solar System), namely the mean-motion resonances, linking together the characteristic frequencies of the orbital motions of two or more objects (planets, dwarf planets, asteroids or satellites) in the system. Mean-motion resonances carry important information about the formation processes taking place in the planetary systems. They intrigued people for centuries and they continue to do so. To decipher at least a small part of the information encrypted in mean-motion resonances, we have concentrated on the early stages of the planetary system evolution, during which forming or already formed planets are still embedded in a gaseous protoplanetary disk. This allowed us to find out how the commensurabilities may form under the effect of disk-planet interactions, and even more importantly as we showed in Chapters 4 – 5, how disk-planet interactions can prevent the resonance from forming or being maintained. In recent years, a large number of extrasolar planets have been discovered, which makes the exoplanet research bursting with vitality and new ideas. The statistics shows that the majority of known exoplanets are the super-Earths (or mini-Neptunes or both) with radii between the radius of the Earth and Neptune, detected mostly by the transit method (see Figure 1.1). That is exactly why we have chosen for our studies low-mass planets in the super-Earth mass range. They are simply numerous. In Chapter 4, however, we have considered also higher mass planets (for example Jupiter-like planet) but they were always accompanied by a super-Earth.

The mean-motion resonances are interesting features by themselves, but here we have employed them mainly to test the migration processes due to the interactions between the disk and planets embedded in it. The observed frequency of the resonance occurrence should be consistent with the way in which the commensurabilities are formed and evolve. It has been noticed that the occurrence of the resonances between low-mass exoplanets residing in known protoplanetary systems is not as common, as could be inferred from the assumption that those planets migrate with type I migration, while still embedded in a gaseous protoplanetary disk. The question about the reason for that is not an easy one. Between the early stage of the evolution of the planetary system and the mature system as for example our own Solar System, there are many intermediate stages, which are far from being understood. The commensurability born at the early stage will be affected by the disk dispersal, interactions with the planetesimals, star-planet interactions and so on. Our approach here is to question whether we really expect so many

resonances to form due to the disk-planet interactions in the early stages. This should provide a good starting point for considering the consequent stages of the planetary system evolution.

In our studies we have had a closer look at the migration of the low-mass planets embedded in a gaseous protoplanetary disk, using the full two-dimensional hydrodynamic simulations. We follow the formation and evolution of mean-motion resonances as a result of the orbital migration of the planets. This brought us to the important conclusions which we have presented in Chapters 3 – 5 and now we are going to summarize them.

6.1 Summary of the most significant results

There are two main contributions of this thesis to our understanding of the formation and evolution of mean-motion resonances in planetary systems. We have provided, for the first time, the conditions for the formation of a second-order mean-motion resonance based on full two-dimensional hydrodynamical simulations and we have discovered the effective repulsion mechanism due to wave-planet interactions, operating in the systems containing two super-Earths (planets with the masses less than 10 Earth's masses), and significantly affecting the formation and maintenance of mean-motion resonances.

1. Conditions for low-mass planets to be captured into the 9:7 mean-motion resonance

Motivated by the discovery of two low mass planets with period ratio extremely close to the strict 9:7 commensurability in Kepler-29 system, we have investigated the formation of the 9:7 MMR in a system of two equal mass super-Earths migrating in a protoplanetary disk. For the first time, a full two-dimensional hydrodynamic treatment of the disk-planet interactions has been applied to the formation of the second-order mean-motion resonance. The hydrodynamic calculations allow to follow the migration of the planets in the best possible way. The previous research has been performed in the framework of the restricted three-body problem and N-body simulations (e.g. [133, 138, 176, 217]). We have found conditions (the disk properties) for the 9:7 resonance capture. Moreover, we have uncovered an interesting fact, that the capture occurs during the convergent migration of planets if their resonance angle at the moment of arrival at the commensurability assumes values in a certain range (inside a window of capture). Similar property has been found in [62] for the 3:1 resonance by the analytical methods. If the relative migration rate is slow, the window is wide and the capture will take place with high probability, in particular, it can be certain. We have succeeded in confirming the analytic and N-body results for very slow convergent migration of planets by hydrodynamical calculations. For faster relative migration, the window becomes narrower, and for sufficiently high migration rate it will be entirely closed. In this last case the capture will not take place. However, the width of the window depends not only on the relative migration rate but also on the circularization rate. Both quantities are determined by the disk parameters. Moreover, we have also shown how the 9:7 resonance window of capture is affected by the initial eccentricities and the initial orbits of the planets.

2. Repulsion mechanism between two planets, embedded in a gaseous protoplanetary disk, due to wave-planet interactions

The second contribution of this thesis, discovery of the effective repulsion mechanism operating in the system of two planets with the masses less than 10 Earth's masses, is the main finding of our study. We have devoted to the detailed analysis of this mechanism two chapters, namely Chapter 4 and 5. In Chapter 4, we study the orbital evolution of a planet pairs with a super-Earth as an outer planet migrating in a thin protoplanetary disk in the presence of more massive planet on the inside.

First, we have considered a system with an inner giant planet ($m_1 = 1M_{\rm Jup}$) and an outer super-Earth ($m_2 = 5.5M_\oplus$). This system has exactly the same configuration as the one in which the repulsion mechanism has been identified for the first time by [173] and [174]. We have confirmed the results of those authors, showing that indeed, the capture into the 2:1 MMR did not take place, when expected, due to the action of the density wave excited by a Jupiter-like planet in the disk. It was important step to check whether our calculations are consistent with the conclusions drawn in the work of [174], mainly because we have used different numerical codes. We have utilized the FARGO3D code instead of NIRVANA which was applied by the previous authors. We have demonstrated the reproducibility of the results by performing these calculations. This allowed us to go on with further investigations.

Next we have extended our work to the systems composed of the inner planets with the masses less than the Jovian value, spanned the range of $8M_\oplus - 100M_\oplus$ and a super-Earth in the exterior orbit with the same mass as in our test calculations above. In order to guarantee the relative convergent migration of the planets, necessary for the resonance capture, we kept the inner planet on the fixed orbit. The outcome of our calculations demonstrated that the density waves excited by the inner planet is strong enough to prevent the resonance capture if the mass of the inner planet is larger or equal to $40M_\oplus$. Instead, if the mass of the inner planet is less or equal to $20M_\oplus$ than the capture occurred and the resonance was maintained till the end of the calculations. The conclusion is that the effectiveness of the repulsion mechanism depends on the mass of the inner planet. This mechanism can prevent the resonance capture if, for the particular disk model and the mass of the external super-Earth adopted in these calculations, the inner planet is more massive than $40M_\oplus$.

In Chapter 5, we continue to investigate the effectiveness of the repulsion mechanism, but this time between two low-mass planets (both planets with the masses less than 10 Earth masses) migrating in a thin gaseous protoplanetary disk. As we have already mentioned few times, the most numerous planets known till now are super-Earths and mini-Neptunes. Many multi-planet systems contain only low-mass planets. Does the repulsion mechanism operate also between them at the early stages of the evolution, when the gaseous disk is still present in the system? This question has been asked soon after the identification of the repulsion mechanism in the system containing the Jupiter and super-Earth. The common opinion was that the effect of the waves excited in the disk by the low-mass planets will not be sufficient to repel the planets from each other. In [21] it has been found out that the effect is still present if the masses of both planets are similar to Saturn or even to Uranus (they call the latter super-Earths, but it

should not be mistaken with the definition of a super-Earth, adopted in our study, as we have assumed that super-Earths have masses less than 10 Earth masses). The essential condition for the repulsion mechanism to work, formulated in their study, was that at least one of the planets should be able to open the partial gap along its orbit.

Using this condition as a guidance we have shown that the repulsion mechanism can be effective also for planets as small as 4 Earth masses. We have demonstrated it performing the simulations for a system of two planets with the masses of $m_1 = 4.3M_\oplus$ and $m_2 = 3.95M_\oplus$ orbiting the star with the mass equal to the mass of the Sun. Both planets are able to open a partial gap in their co-orbital regions in the disk model adopted in our simulations. The results show that the divergent migration of two super-Earths occurs before they arrive to the strict 3:2 resonance commensurability. The reason for this behavior has been analyzed in detail in Chapter 5 and we have concluded that it is due to the angular momentum transfer by the density waves excited by one planet to the co-orbital region of the other planet in the system and then to the planet itself through the horseshoe drag. We derive the approximate criteria for a planet being repelled efficiently due to the wave-planet interactions in the disk. They can be formulated as follows: the planet should be able to form a partial gap in the disk and there should be enough material in its horseshoe region for transferring angular momentum carried by the density waves of the other planet to itself efficiently. If the criteria are satisfied for both planets in the system, we expect that the divergent migration will take place and prevent the planets from being trapped into the MMRs. The predictions according to the derived criteria have been verified in all our simulations, including also the calculations performed for the systems studied in [21]. Next, the model assumptions have been relaxed in order to exclude the possibility that the mechanism under the study is limited to the particular physical conditions. We have investigated this mechanism in a wide range of disk surface densities, with two different equations of state: the locally isothermal and adiabatic ones. We have studied the repulsion between planets in the disk with and without the central cavity. We have checked also the effect of the disk self-gravity on the outcome of our calculations. All those numerical experiments were fully successful and the repulsion of the planets was present, as expected.

However, the models of the disk used here was still largely simplified. To go one step further, improving the physics treatment in our calculations, we have performed the additional study, namely we have considered a pair of super-Earths embedded in a viscous disk initially supporting a constant angular momentum flux, in which the balance between local heating and cooling determines the local disk temperature. The adopted disk model is very different from the one with a locally isothermal equation of state in which the repulsion between planets, as we showed, operated efficiently. It allowed us to find out whether the repulsion mechanism will operate also in the case in which substantially different dynamics in the vicinity of gaps induced by orbiting planets is expected. The calculations of the evolution of the super-Earths in the viscous disk resulted in the transition from the convergent to the divergent migration as in our previous simulations in the disk with the locally isothermal equation of state and are consistent with the criteria we derived for the repulsion mechanism to work. The repulsion was found to be particularly strong between planets with equal mass. In this thesis we have demonstrated

that the repulsion between two planets embedded in a gaseous protoplanetary disk due to wave-planet interactions is effective for a wide range of planetary masses and disk properties, therefore it should be taken into account in modeling the early phases of the planetary system evolution.

6.2 Directions for the future work

The formation and evolution of planetary systems is the subject of the intensive investigations (see Section 1.4). The numerous and high quality data provided by the state-of-the-art ground-based facilities as well as the space missions from one side, and the advanced computational techniques and powerful supercomputers from the other side, make these investigations become possible. Particular attention is directed towards the robust features observed in planetary systems, namely the mean-motion resonances. They may help in solving some of the formation puzzles. The observational, theoretical and numerical studies of the mean-motion resonances, as those presented in this thesis will contribute to our understanding of the planetary system formation processes. We still did not know how the observed mean-motion resonances are formed, how the planets migrate in the protoplanetary disks or what the structure and physical conditions of the disk forming planets are.

In this study we have employed the hydrodynamical simulations, extending the simple analytical considerations and N-body calculations towards more realistic physical models. These resulted in the identification of the discrete windows of resonance capture in the second-order commensurability 9:7 and the repulsion mechanism between low-mass planets migrating in the viscous disk with local heating and cooling. Based on these findings we can predict observational properties of planetary systems and accept or reject our model assumptions.

Despite the progress achieved in this field there are still important steps to be performed. The most obvious development is to drop the limitation of the two-dimensional disk model and consider more realistic three-dimensional disk structure. It is computationally challenging task, but with the recent progress in supercomputing, it begins to be feasible. As far as the repulsion mechanism in concerned, in which the horseshoe drag plays important role, the extension to the third dimension should preserve the qualitative picture found in this thesis. The argument for that is based on our analytical considerations and the encouraging results obtained by [128] on the horseshoe drag in three-dimensional globally isothermal disks. Following the migrating planets for the sufficiently long period of time, necessary for studying the formation and evolution of the second-order mean-motion resonances, in three dimensions will require almost prohibitive amount of computational time. So probably it is not the best direction to go, especially that there are more important questions to be answered first.

In this study we have considered the disk models in which the angular momentum is transported radially in the disk. However, there are more and more arguments that the angular momentum can be transported vertically away from the disk in a magnetized wind. The vertical transport has been found to be very efficient. If the accretion in the protoplanetary disk is driven by surface stress, and not as it is often assumed, by turbulence than the planets will migrate differently. How different the orbital migration will be, we still do not know. The first attempts to find out how the planets migrate in the two-dimensional wind-driven disks have

been performed and they show that the differences may be very significant [99]. An interesting extension of our work will be to verify whether the repulsion mechanism found in viscous disks operates also in wind-driven disks.

The knowledge about the properties of the protoplanetary disks is essential for studying disk-planet interactions and their consequences. There is a fast progress in modeling protoplanetary disks, for example the global models of protoplanetary disks have been presented by [108]. The high quality observations provide direct constraints on the structure of the disks showing rings and non-axisymmetric bumps, on turbulent velocity dispersion, magnetic field strength and topology, to name just few recent developments. The protoplanetary disks are cold and weakly ionized. Therefore in order to model them, the non-ideal MHD effects, namely Ohmic, Ambipolar and Hall effects should be properly treated in the calculations. However, the magnitude of the non-ideal effects depends strongly on the disk structure, composition and environment, which are not sufficiently well known at present. So, it is a bit too early for the very detailed disk modeling including chemical processes.

Also the knowledge about the properties of the planets and the planetary systems architectures are crucial to make progress in the understanding the disk-planet interactions. The observational data is rapidly increasing thanks to the ground-based facilities and new observational techniques as well as the space missions, as for example TESS and CHEOPS, which are operating now or PLATO to be launch in 2026 and ARIEL coming up in 2029. The progress happening in the observations, theoretical considerations and numerical calculations will lead to the answers to the most fundamental questions in the field of planetary system formation and evolution. The mean-motion resonances will contribute substantially to the process of finding those answers.

Appendix A

Hydrodynamic simulations presented in Chapter 3

Table A.1: Numerical parameters in simulations for the 9:7 resonance survey

$\Sigma_0(10^{-5})$	$\nu(10^{-6})$	$\phi_a(rad)$	$t_{\rm R}$(yr)	$\phi_{\rm entry}(rad)$	$\dot{a}/a(\mathrm{Myr}^{-1})$	$-\dot{e_1}/e_1(\mathrm{Myr}^{-1})$
2.0	1.0	41.09	2070	2.87	0.956	708.4
2.5	1.0	28.30	1273	3.10	1.210	482.3
3.0	1.0	21.52	955	3.60	1.460	596.5
3.5	1.0	16.56	637	2.28	1.715	708.4
4.0	1.0	14.02	557	4.82	1.964	816.4
4.5	1.0	11.48	446	1.08	2.219	916.9
5.0	1.0	9.95	382	2.61	2.469	1008.6
5.5	1.0	8.89	334	3.67	2.713	1090.2
6.0	1.0	8.00	318	4.56	2.955	1158.0
2.0	2.0	54.47	2229	2.05	0.865	358.0
2.5	2.0	38.07	1592	5.89	1.094	469.74
3.0	2.0	28.36	1274	3.04	1.322	581.53
3.5	2.0	21.89	955	3.23	1.550	690.80
4.0	2.0	17.03	717	1.81	1.779	797.56
4.5	2.0	12.34	637	4.24	2.007	896.78
5.0	2.0	11.98	478	0.58	2.235	989.73
5.5	2.0	10.22	398	2.34	2.458	1073.88
6.0	2.0	9.15	366	3.41	2.681	1145.47
2.5	3.0	45.41	1911	4.83	0.987	457.18
3.0	3.0	34.1	1592	3.58	1.195	566.46
3.5	3.0	25.97	1067	5.43	1.402	673.22
4.0	3.0	21.06	955	4.06	1.609	777.46
4.5	3.0	16.73	717	2.11	1.816	876.69
5.0	3.0	14.52	669	4.32	2.023	969.63
5.5	3.0	12.08	511	0.48	2.230	1055.04
6.0	3.0	10.36	457	2.20	2.432	1130.40
2.5	4.0	48.21	1943	2.03	0.190	448.39

Table A.1: Numerical parameters in simulations for the 9:7 resonance survey

$\Sigma_0(10^{-5})$	$\nu(10^{-6})$	$\phi_a(rad)$	$t_{\rm R}$(yr)	$\phi_{\rm entry}(rad)$	$\dot{a}/a(\mathrm{Myr}^{-1})$	$-\dot{e_1}/e_1(\mathrm{Myr}^{-1})$
3.0	4.0	36.29	1465	1.39	1.094	553.90
3.5	4.0	28.66	1223	2.74	1.285	659.40
4.0	4.0	22.93	968	2.19	1.476	761.14
4.5	4.0	19.23	796	5.89	1.667	859.10
5.0	4.0	15.94	717	2.90	1.858	952.05
5.5	4.0	13.99	615	4.85	2.044	1038.71
6.0	4.0	11.76	510	0.80	2.235	1116.58
2.5	5.0	51.30	2006	5.22	0.834	437.09
3.0	5.0	39.37	1608	4.59	1.014	540.08
3.5	5.0	30.59	1220	0.81	1.189	643.07
4.0	5.0	25.11	1006	0.01	1.370	743.55
4.5	5.0	21.12	939	4.00	1.545	840.26
5.0	5.0	17.39	725	1.45	1.720	933.21
5.5	5.0	15.19	686	3.65	1.901	1019.90
6.0	5.0	13.33	561	5.51	2.071	1099.00
2.5	6.0	53.27	2182	3.25	0.780	428.30
3.0	6.0	40.84	1672	3.12	0.945	530.03
3.5	6.0	32.89	1306	4.79	1.110	631.77
4.0	6.0	27.15	1131	4.25	1.279	730.99
4.5	6.0	22.19	936	2.93	1.444	826.45
5.0	6.0	19.00	764	6.12	1.609	919.39
5.5	6.0	16.13	696	2.71	1.773	1006.06
6.0	6.0	14.43	637	4.41	1.938	1087.70
2.5	7.0	54.26	2038	2.26	0.733	427.04
3.0	7.0	42.07	1672	1.89	0.887	527.52
3.5	7.0	34.28	1401	3.40	1.041	626.74
4.0	7.0	28.16	1167	3.24	1.200	724.71
4.5	7.0	23.41	924	1.71	1.354	820.17
5.0	7.0	20.56	857	4.56	1.513	911.86
5.5	7.0	17.21	701	1.63	1.667	999.78
6.0	7.0	15.26	669	3.58	1.821	1081.42
3.0	8.0	44.06	1640	6.18	0.834	523.75
3.5	8.0	35.31	1354	2.37	0.982	622.98
4.0	8.0	29.19	1131	2.21	1.131	719.69
4.5	8.0	24.88	971	0.24	1.279	813.89
5.0	8.0	21.46	909	3.66	1.428	905.58
5.5	8.0	18.50	745	0.34	1.571	992.24
6.0	8.0	16.02	678	2.82	1.720	1075.14
3.0	9.0	46.27	1831	3.97	0.791	518.73
3.5	9.0	36.73	1390	0.95	0.929	616.70
4.0	9.0	30.59	1174	0.81	1.072	712.15
4.5	9.0	26.41	1035	4.99	1.210	806.35
5.0	9.0	22.24	912	2.88	1.348	896.78

Table A.1: Numerical parameters in simulations for the 9:7 resonance survey

$\Sigma_0(10^{-5})$	$\nu(10^{-6})$	$\phi_a(rad)$	$t_{\rm R}$(yr)	$\phi_{\rm entry}(rad)$	$\dot{a}/a(\mathrm{Myr}^{-1})$	$-\dot{e_1}/e_1(\mathrm{Myr}^{-1})$
5.5	9.0	19.77	780	5.35	1.492	984.70
6.0	9.0	16.86	701	1.98	1.630	1067.60
3.0	10.0	47.17	1831	3.07	0.749	514.96
3.5	10.0	38.71	1449	5.25	0.881	610.42
4.0	10.0	32.25	1226	5.43	1.014	705.87
4.5	10.0	27.42	1139	3.98	1.147	798.82
4.75	10.0	25.25	968	6.15	1.216	844.03
5.0	10.0	23.10	920	2.02	1.285	889.25
5.25	10.0	21.78	908	3.34	1.343	933.21
5.5	10.0	20.70	852	4.42	1.417	975.91
5.75	10.0	19.32	764	5.80	1.481	1018.62
6.0	10.0	17.82	725	1.02	1.550	1060.06

Table A.2: Numerical parameters in simulations with initial $e_1 = 0.015$ and $e_2 = 0$

$\Sigma_0(10^{-5})$	$\nu(10^{-6})$	$\phi_a(rad)$	$\dot{a}/a(\mathrm{Myr}^{-1})$
4.5	1.0	9.91	0.387
4.75	1.0	6.89	0.403
5.0	1.0	6.33	0.419
5.25	1.0	5.95	0.433
5.5	1.0	5.75	0.445
5.75	1.0	5.52	0.456
6.0	1.0	5.35	0.466
4.5	2.0	10.48	0.362
4.75	2.0	10.19	0.378
5.0	2.0	9.89	0.393
5.25	2.0	6.42	0.407
5.5	2.0	6.08	0.419
5.75	2.0	5.79	0.429
6.0	2.0	5.50	0.439
4.5	3.0	10.94	0.337
4.75	3.0	10.55	0.353
5.0	3.0	10.33	0.367
5.25	3.0	10.12	0.381
5.5	3.0	6.66	0.392
6.0	3.0	5.92	0.413
4.5	4.0	11.20	0.317
5.0	4.0	10.72	0.346
5.25	4.0	10.47	0.359
5.5	4.0	10.24	0.371
5.75	4.0	6.80	0.382
6.0	4.0	6.40	0.391

Table A.2: Numerical parameters in simulations with initial $e_1 = 0.015$ and $e_2 = 0$

$\Sigma_0(10^{-5})$	$\nu(10^{-6})$	$\phi_a(rad)$	$\dot{a}/a(\mathrm{Myr}^{-1})$
4.5	5.0	11.67	0.300
4.75	5.0	11.27	0.315
5.0	5.0	11.00	0.329
5.25	5.0	10.81	0.342
5.5	5.0	10.49	0.354
5.75	5.0	10.29	0.364
6.0	5.0	6.82	0.374
4.5	6.0	12.11	0.286
5.0	6.0	11.31	0.314
5.5	6.0	10.77	0.339
6.0	6.0	10.29	0.359
5.0	6.0	11.61	0.302
5.5	6.0	11.03	0.325
6.0	6.0	10.60	0.346

Table A.3: Numerical parameters in simulations with initial $e_1 = 0.025$ and $e_2 = 0.015$

$\Sigma_0(10^{-5})$	$\nu(10^{-6})$	$\phi_a(rad)$	$\dot{a}/a(\mathrm{Myr}^{-1})$
1.5	1.0	13.04	0.147
2.0	1.0	10.02	0.196
2.2	1.0	9.08	0.215
2.5	1.0	7.37	0.244
3.0	1.0	6.06	0.290
3.5	1.0	5.15	0.335
4.0	1.0	4.48	0.377
2.0	3.0	11.80	0.167
2.5	3.0	9.38	0.208
3.0	3.0	7.14	0.248
3.5	3.0	5.93	0.288
4.0	3.0	5.14	0.325
2.0	5.0	15.66	0.139
2.5	5.0	11.34	0.174
2.8	5.0	9.96	0.194
3.0	5.0	9.24	0.208
3.2	5.0	8.59	0.221
3.5	5.0	7.09	0.242
4.0	5.0	5.94	0.274
2.0	6.0	16.69	0.127
2.5	6.0	12.18	0.160
3.0	6.0	10.07	0.192
2.0	8.0	19.26	0.109
2.5	8.0	15.48	0.138

Table A.3: Numerical parameters in simulations with initial $e_1 = 0.025$ and $e_2 = 0.015$

$\Sigma_0(10^{-5})$	$\nu(10^{-6})$	$\phi_a(rad)$	$\dot{a}/a(\mathrm{Myr}^{-1})$
3.0	8.0	11.62	0.166
3.5	8.0	9.83	0.193
4.0	8.0	8.29	0.221

References

[1] Agol E., Steffen J., Sari R., Clarkson W.. **On detecting terrestrial planets with timing of giant planet transits**. *MNRAS*, 2005. 359, 567. 3

[2] Andrè Q., Papaloizou J.C.B.. **On the orbital evolution of a pair of giant planets in mean motion resonance**. *MNRAS*, 2016. 461, 4406. 14

[3] Andrews S.M., Wilner D. J., Hughes A. M., et al.. **Protoplanetary disk structure in Ophiuchus**. *ApJ*, 2009. 700, 1502. 9

[4] Andrews S.M., Huang J., Pérez L.M., et al.. **The Disk Substructures at High Angular Resolution Project (DSHARP). I. Motivation, Sample, Calibration, and Overview**. *ApJL*, 2018. 869, L41. 6

[5] Andrews S.M., Terrell M., Tripathi A., et al.. **Scaling relations associated with Millimeter Continuum sizes in protoplanetary disks**. *ApJ*, 2018. 865, 157. 6

[6] Andrews S.M.. **Observations of protoplanetary disk structures**. *ARA&A*, 2020. 58, 483. 7, 10

[7] Ansdell M., Williams J.P.,van der Marel N. et al.. **ALMA survey of Lupus protoplanetary disks. I. Dust and gas masses**. *ApJ*, 2016. 828, 46. 8

[8] Ansdell M., Williams J.P., Trapman L. et al.. **ALMA survey of Lupus protoplanetary disks. II. Gas disk radii**. *ApJ*, 2018. 859, 21. 8

[9] Armitage P. J., Clarke C. J.. **Magnetic braking of T Tauri starts**. *MNRAS*, 1996. 280, 458. 129

[10] Armitage P.J.. **Lecture notes on the formation and early evolution of planetary systems**. *arXiv*, 2007. astro-ph/0701485v6. 11, 32

[11] Artymowicz P.. **On the wave excitation and a generalized torque formula for Lindblad resonances excited by external potential**. *ApJ*, 1993. 419, 155. 27, 28

[12] Ataiee S., Pinilla P., Zsom A.. **Asymmetric transition disks: vorticity or eccentricity?**. *A&A*, 2013. 533, L3. 6

[13] Ataiee S., Kley W.. **The role of disc torques in forming resonant planetary systems**. *A&A*, 2020. 635, 204. 23, 127

[14] Bae J., Zhu Z., Hartmann L.. **On the Formation of Multiple Concentric Rings and Gaps in Protoplanetary Disks**. *ApJ*, 2017. 850, 201. 6

[15] Baglin A., Chaintreuil S., Vandermarcq O.. **The CoRoT Legacy Book: II.1 The CoRoT observations**. *EDP Sciences*, 2021. 29. 1

[16] Bai X.N., Stone J.M.. **Wind-driven accretion in protoplanetary disks. I. Suppression of the magnetorotational instability and launching of the magnetocentrifugal wind**. *ApJ*, 2013. 769, 76. 10

[17] Balbus S.A., Hawley J.F.. **A powerful local shear instability in weakly magnetized disks. I. linear analysis**. *ApJ*, 1991. 376, 214 10, 15

[18] Barclay T., Rowe J., Lissauer J., et al.. **A sub-Mercury-sized exoplanet**. *Nature*, 2013. 494, 452. 37

[19] Barnes R., Jackson B., Raymond S. N., et al.. **The HD 40307 planetary system: super-Earths or mini-Neptunes?**. *ApJ*, 2009. 695, 1006. 3

[20] Baruteau, C., Masset F.. **On the corotation torque in a radiatively inefficient disk**. *ApJ*, 2008. 672,1054. 30, 127

[21] Baruteau C., Papaloizou J.C.B.. **Disk-planets interactions and the diversity of period ratios in Kepler's multi-planetary systems**. *ApJ*, 2013. 778, 7. 16, 17, 18, 83, 85, 88, 102, 112, 145, 146

[22] Batygin K., Morbidelli A.. **Dissipative Divergence of Resonant Orbits**. *AJ*, 2013. 145, 1. 5, 15

[23] Batygin K.. **Capture of planets into mean-motion resonances and the origins of extra-solar orbital architectures**. *MNRAS*, 2015. 451, 2589. 13

[24] Benítez-Llambay P., Masset F.S.. **FARGO3D: a new GPU-oriented MHD code**. *ApJS*, 2016. 223, 11. 24, 70

[25] Benítez-Llambay P., Ramos X.S., Beaugé C., et al.. **Long-term and large-scale hydrodynamical simulations of migrating planets**. *ApJ*, 2016. 826, 13. 87, 127

[26] Benz W., Broeg C., Fortier A., et al.. **The CHEOPS mission**. *Experimental Astronomy*, 2021. 51, 109. 1

[27] Bergin E. A., Cleeves L. I., Gorti U., et al.. **An old disk still cacpable of forming a planetary system**. *Nature*, 2013. 493, 644. 8

[28] Binney J., Tremaine S.. **Galactic dynamics**. *Princeton Univerisity Press*, 1987. 27

[29] Borsato L., Malavolta L., Piotto G., et al.. **HARPS-N radial velocities confirm the low densities of the Kepler-9 planets**. *MNRAS*, 2019. 484, 3233. 4

[30] Borucki W., Koch D., Batalha N., et al.. **KEPLER: Search for Earth-size planets in the habitable zone**. *IAU Symposium*, 2009. 253, 289. 1

[31] Borucki W., Koch D., Basri G., et al.. **Characteristics of planetary candidates observed by Kepler. II. Analysis of the first four months of data**. *ApJ*, 2011. 736, 19. 2

[32] Brandenburg A., Nordlund A., Stein R.F.. **The disk accretion rate for dynamo-generated turbulence**. *ApJ*, 1996. 458, 45. 15

[33] Brogan C.L., Pérez L.M., Hunter T.R., et al.. **The 2014 ALMA Long Baseline Campaign: First Results from High Angular Resolution Observations toward the HL Tau Region**. *ApJ*, 2015. 808, L3. 7

[34] Bryden G., Różyczka M., Lin D.N.C., et al.. **On the Interaction between Protoplanets and Protostellar Disks**. *ApJ*, 2000. 540, 1091. 35

[35] Calahan J.K., Bergin E., Zhang K., et al.. **The TW Hya Rosetta Stone Project. III. Resolving the Gaseous Thermal Profile of the Disk**. *ApJ*, 2021. 908, 8. 8

[36] Carter J., Agol E., Chaplin W.J., et al.. **Kepler-36: A pair of planets with neighboring orbits and dissimilar densities**. *Science*, 2012. 337, 556. 4, 86

[37] Cresswell P., Nelson R.P.. **On the evolution of multiple protoplanets embedded in a protostellar disc**. *A&A*, 2006. 450, 833. 14, 35

[38] Crida A., Morbidelli A., Masset F.. **On the width and shape of gaps in protoplanetary disks**. *Icarus*, 2006. 181, 587. 31, 32, 88

[39] Crida A., Sándor Z., Kley W.. **Influence of an inner disc on the orbital evolution of massive planets migrating in resonance**. *A&A*, 2008. 483, 325. 12, 14

[40] Deleuil M., Aigrain S., Moutou C., et al.. **Planets, candidates, and binaries from the CoRoT/Exoplanet programme. The CoRoT transit catalogue**. *A&A*, 2018. 619, 97. 1

[41] Delisle, J. B., Laskar, J. Correia A. C. M.. **Resonance breaking due to dissipation in planar planetary system**. *A&A*, 2014. 566, 137. 15

[42] Delisle, J. B., Laskar, J.. **Tidal dissipation and the formation of Kepler near-resonant planets**. *A&A*, 2014. 570, L7. 5, 15

[43] de Val-Borro M., Edgar R.G., Artymowicz P., et al.. **A comparative study of disc-planet interaction**. *MNRAS*, 2006. 370, 529. 23, 24, 70, 88

[44] Dodson-Robinson S. E., Salyk C.. **Transitional disks as signposts of young, multiplanet systems**. *ApJ*, 2011. 738, 131. 6

[45] Dong R., Rafikov R.R., Stone J.M.. **Density waves excited by low-mass planets in protoplanetary disks. II. High-resolution simulations of the nonlinear regime**. *ApJ*, 2011. 741, 57. 97, 105

[46] Dong R., Li S., Chiang E., et al.. **Multiple Disk Gaps and Rings Generated by a Single Super-Earth**. *ApJ*, 2017. 843, 127. 6

[47] Duffell P.C., MacFadyen A.I.. **Gap opening by extremely low-mass planets in a viscous disk**. *ApJ*, 2013. 769, 41. 32

[48] Duffell P.C., Haiman Z., MacFadyen A.I., et al.. **The migration of gap-opening planets is not locked to viscous disk evolution**. *ApJL*, 2014. 792, L10. 11, 33, 86

[49] Duffell P.C.. **A simple analytical model for gaps in protoplanetary disks**. *ApJL*, 2015. 807, L11. 32

[50] Dullemond C.P., Penzlin A.B.T.. **Dust-driven viscous ring-instability in protoplanetary disks**. *A&A*, 2018. 609, 50. 10, 11, 33

[51] Dürmann C., Kley W.. **Migration of massive planets in accreting disks**. *A&A*, 2015. 574, 52. 11, 33, 86

[52] Ercolano B., Pascucci I.. **The dispersal of planet-forming discs: theory confronts observations**. *Royal Society Open Science*, 2017. 170114. 7

[53] Eriksson L. E. J., Johansen A., Liu B.. **Pebble drift and planetesimal formation in protoplanetary discs with embedded planets**. *A&A*, 2020. 635, 110. 6

[54] Fabrycky D.C., Ford E.B., Steffen J.H, et al.. **Transit timing observations from Kepler. IV. confirmation of four multiple-planet systems by simple physical models**. *ApJ*, 2012. 750, 114. 17, 35

[55] Fabrycky D.C., Lissauer J.J., Ragozzine D., et al.. **Architecture of Kepler's multi-transiting systems. II. new investigations with twice as many candidates**. *ApJ*, 2014. 790, 146. 5

[56] Fendyke S.M., Nelson R.P.. **On the corotation torque for low-mass eccentric planets**. *MNRAS*, 2014. 437, 96. 24

[57] Ferguson J. W., Alexander D. R., Allard F., et al.. **Low-temperature opacities**. *ApJ*, 2005. 623, 585. 130

[58] Flaherty K.M., Hughes A.M., Rosenfeld K.A., et al.. **Weak turbulence in the HD 163296 protoplanetary disk revealed by ALMA CO observation**. *ApJ*, 2015. 813, 99. 10

[59] Flaherty K.M., Hughes A.M., Rose S.C., et al.. **A three-dimensional view of turbulence: constraints on turbulent motions in the HD 163296 protoplanetary disk using** DCO^+. *ApJ*, 2017. 843, 150. 10

[60] Flaherty K.M., Hughes A.M., Teague R., et al.. **Turbulence in the TW Hya disk**. *ApJ*, 2018. 856, 117. 10

[61] Flaig M., Ruoff P., Kley W., Kissmann R.. **Global structure of magnetorotationally turbulent protoplanetary discs**. *MNRAS*, 2012. 420, 2419. 131

[62] Folonier H.A., Roig F., Beaugé C.. **Capture probability in the 3:1 mean motion resonance with Jupiter: an application to the Vesta family**. *Celestial Mechanics and Dynamical Astronomy*, 2014. 119, 1. 38, 39, 50, 66, 144

[63] Fressin F., Torres G., Charbonneau D., et al.. **The false positive rate of Kepler and the occurrence of planets**. *ApJ*, 2013. 766, 81. 3

[64] Fulton B. J., Petigura E. A., Howard A. W., et al.. **The California-Kepler Survey. III. A gap in the radius distribution of small planets**. *AJ*, 2017. 154, 109. 3

[65] Fulton B. J., Petigura E. A.. **The California-Kepler Survey. VII. Precise planet radii leveraging Gaia DR2 reveal the stellar mass dependence of the planet radius gap**. *AJ*, 2018. 156, 264. 3

[66] Fung J., Shi J.M., Chiang E.. **How empty are disk gaps opened by giant planets?**. *ApJ*, 2014. 782, 88. 32

[67] Gillon M., Triaud A.H.M.J., Demory B., et al. . **Seven temperate terrestrial planets around the nearby ultracool dwarf star TRAPPIST-1**. *Nature*, 2017. 542, 456. 4

[68] Ginzburg S., Schlichting H.E., Sari R.. **Core-powered mass-loss and the radius distribution of small exoplanets**. *MNRAS*, 2018. 476, 759. 3

[69] Goldreich P., Peale S.J.. **More on spin-orbit coupling in the solar system**. *AJ*, 1966. 71, 856. 13

[70] Goldreich P., Tremaine S.. **The excitation of density waves at the lindblad and corotation resonances by an external potential**. *ApJ*, 1979. 233,857. 10, 27, 28, 29

[71] Goldreich P., Tremaine S.. **Disk-satellite interactions**. *ApJ*, 1980. 241, 425. 6, 10, 12, 27, 28

[72] Goldreich P., Sari R.. **Eccentricity evolution for planets in gaseous disks**. *ApJ*, 2003. 585, 1024. 31

[73] Goodman J., Rafikov R.R.. **Planetary torques as the viscosity of protoplanetary disks**. *ApJ*, 2001. 552, 793. 27, 97, 107

[74] Goździewski K., Migaszewski C., Panichi F., et al.. **The Laplace resonance in the Kepler-60 planetary system**. *MNRAS*, 2016. 445, 104. 4

[75] Gupta A., Schlichting H.E.. **Suplting the valley in the radius distribution of small exoplanets as a by-product of planet formation: the core-powered mass-loss mechanism**. *MNRAS*, 2019. 487, 24. 3

[76] Hadden S., Lithwick Y.. **Densities and eccentricities of 139 Kepler planets from transit time variations**. *ApJ*, 2014. 787, 80. 37

[77] Hadden S., Lithwick Y.. **Numerical and analytical modeling of transit timing variations**. *ApJ*, 2016. 828, 44. 86

[78] Hadden S., Lithwick Y.. **Kepler Planet masses and eccentricities from TTV analysis**. *AJ*, 2017. 154, 5. 86

[79] Haisch K.E.Jr., Lada E.A., Lada C.J.. **Disk frequencies and lifetimes in young clusters**. *ApJL*, 2001. 553, 153. 7

[80] Harsono D., Bjerkeli P., van der Wiel M.H.D., et al.. **Evidence for the start of planet formation in a young circumstellar disk**. *Nature Astronomy*, 2018. 2, 646. 7

[81] Hartmann L., Calvet N., Gullbring E., et al.. **Accretion and the evolution of T Tauri disks**. *ApJ*, 1998. 495, 385. 10

[82] Hawley J.F., Gammie C.F., Balbus S.A.. **Local three-dimensional simulations of an accretion disk hydromagnetic dynamo**. *ApJ*, 1996. 464, 690. 15

[83] He M.Y, Ford E.B., Ragozzine D.. **Architectures of exoplanetary systems - I. A clustered forwad model for exoplanetary systems around Kepler's FGK start**. *MNRAS*, 2019. 490, 4575. 3

[84] Holczer T., Mazeh T., Nachmani G., et al. **Transit timing observations from Kepler.IX. catalog of the full long-cadence data set**. *ApJS*, 2016. 225,9. 4, 35

[85] Holman M. J., Murray N. W. **The use of transit timing to detect terrestrial-mass extrasolar planets**. *Science*, 2005. 307, 1288. 3

[86] Howell S. B., Sobeck C., Haas M., et al.. **The K2 mission: characterization and early results**. *Publications of the Astronomical society of the pacific*, 2014. 126, 398. 1

[87] Huang J., Andrews S. M., Dullemond C. P., et al.. **The disk substructures at High Angular Resolution Project(DSHARP). II. Characteristics of annular substructures**. *ApJL*, 2018. 869, L42. 6

[88] Hueso R., Guillot T.. **Evolution of protoplanetary disks: constraints from DM Tauri and GM Aurigae**. *A&A*, 2005. 442, 703. 7, 10

[89] Hughes A.M., Wilner D.J., Andrews S.M., et al.. **Empirical constraints on turbulence in protoplanetary accretion disks**. *ApJ*, 2011. 727, 85. 10

[90] Ivanov P. B., Papaloizou J. C. B., Polnarev A. G.. **The evolution of a supermassive binary caused by an accretion disk**. *MNRAS*, 1999, 307, 79. 11, 32

[91] Izidoro A., Ogihara M., Raymond S.N., et al.. **Breaking the chains: hot super-Earth systems from migration and disruption of compact resonant chains**. *MNRAS*, 2017, 470, 1750. 5

[92] Jontof-Hutter D., Ford E.B., Rowe J.F., et al.. **Secure mass measurements from transit timing: 10 Kepler exoplanets between 3 and 8 $M_\oplus$ with diverse densities and incident fluxes**. *ApJ*, 2016. 820, 39. 17, 35, 36, 86

[93] Jontof-Hutter D., Wolfgang A., Ford E.B., et al.. **Following up the Kepler field: masses of targets for transit timing and atmospheric characterization**. *AJ*, 2021. 161, 246. 4, 36

[94] Kama M., Trapman L., Fedele D., et al.. **Mass constraints for 15 protoplanetary discs from HD 1-0**. *A&A*, 2020. 634, 88. 8

[95] Kanagawa K.D., Muto T., Tanaka H., et al.. **Mass estimates of a giant planet in a protoplanetary disk from the gap structures**. *ApJL*, 2015. 806, L15. 32

[96] Kanagawa K.D., Tanaka H., Szuszkiewicz E.. **Radial migration of gap-opening planets in protoplanetary disks. I. The case of a single planet**. *ApJ*, 2018. 861, 140. 11, 33, 86

[97] Kanagawa K.D., Szuszkiewicz E.. **Radial migration of gap-opening planets in protoplanetary disks. II. The case of a planet pair**. *ApJ*, 2020. 894, 59. 16, 86

[98] Keppler M., Benisty M., Müller A., et al.. **Discovery of a planetary-mass companion within the gap of the transition disk around PDS 70**. *A&A*, 2018. 617, 44. 6

[99] Kimmig C.N., Dullemond C.P., Kley W.. **Effect of wind-driven accretion on planetary migration**. *A&A*, 2020. 633, 4. 10, 148

[100] Kley W., Peitz J., Bryden G.. **Evolution of planetary systems in resonance**. *A&A*, 2004. 414, 735. 35, 40

[101] Kley W., Dirksen G.. **Disk eccentricity and embedded planets**. *A&A*, 2006. 447, 369. 6

[102] Kley W., Crida A.. **Migration of protoplanets in radiative discs**. *A&A*, 2008. 487, 9. 39

[103] Kley W., Nelson R.P.. **Planet-disk interaction and orbital evolution**. *ARA&A*, 2012. 50, 211. 6, 11, 12, 27

[104] Kley W.. **Planet formation and disk-planet interactions**. *Arxiv*, 2017. 1707.07148. 25

[105] Korycansky D.G., Papaloizou J.C.B.. **A method for calculations of nonlinear shear flow: application to formation of giant planets in the Solar nebula**. *ApJS*, 1996. 105, 181. 88

[106] Lee M.H., Peale S.J.. **Dynamics and origin of the 2:1 orbital resonances of the GJ 876 planets**. *ApJ*, 2002. 567, 596. 5, 13

[107] Lee M.H., Fabrycky D.F., Lin D.N.C.. **Are the Kepler near-resonance planet pairs due to tidal dissipation?**. *ApJ*, 2013. 774, 52. 5, 15

[108] Lesur G.. **Magnetohydrodynamics of protoplanetary discs**. *Cambridge University Press*, 2020. 148

[109] Lin D.N.C., Papaloizou J.C.B. **Tidal torques on accretion disks in binary systems with extreme mass ratios**. *MNRAS*, 1979. 186, 799. 6, 10, 28

[110] Lin D.N.C., Papaloizou J.C.B. **On the tidal interaction between protoplanets and the protoplanetary disk. III. Orbital migration of protoplanets**. *ApJ*, 1986. 309, 846. 6

[111] Lin D.N.C., Papaloizou J. C. B.. **Protostars and Planets III**. *Univ. of Arizona Press, Tucson, AZ*, 1993. 749. 28, 31, 88

[112] Lissauer J.J., Ragozzine D., Fabrycky D.C., et al.. **Architecture and dynamics of Kepler's candidate multiple transiting planet systems**. *ApJS*, 2011. 197, 8. 5

[113] Lithwick Y., Wu Y.. **Resonant repulsion of Kepler planet pairs**. *ApJL*, 2012. 756, L11. 5, 15

[114] Lithwick Y., Xie J., Wu Y.. **Extracting Planet Mass and Eccentricity From TTV Data**. *ApJ*, 2012. 761, 122. 3

[115] Long F., Pinilla P., Herczeg G.J., et al.. **Gaps and rings in an ALMA survey of disks in the Taurus star-forming region**. *ApJ*, 2018. 869, 17. 6

[116] Lopez E.D., Fortney J.J.. **The role of core mass in controlling evaporation: the Kepler radius distribution and the Kepler-36 density dichotomy**. *ApJ*, 2013. 776, 2. 3

[117] Luger R., Sestovic M., Kruse E., et al.. **A seven-planet resonant chain in TRAPPIST-1**. *Nature Astronomy*, 2017. 1, 129. 4

[118] Marcy G.W., Isaacson H., Howard A.W., et al.. **Masses, Radii, and Orbits of Small Kepler Planets: The Transition from Gaseous to Rocky Planets**. *ApJS*, 2014. 210, 20. 37

[119] Marzari F., D'Angelo G.. **Dust distribution around low-mass planets on converging orbits**. *A&A*, 2020. 641, 125. 135

[120] Masset F.S.. **FARGO: A fast eulerian transport algorithm for differentially rotating disks**. *A & AS*, 2000. 141, 165. 24

[121] Masset F.S.. **On the co-orbital corotation torque in a viscous disk and its impact on planetary migration**. *ApJ*, 2001. 558, 453. 31

[122] Masset F.S.. **The co-orbital corotation torque in a viscous disk: Numerical simulations**. *A&A*, 2002. 387, 605. 31

[123] Masset F.S., Papaloizou J.C.B.. **Runaway migration and the formation of hot Jupiters**. *ApJ*, 2003. 588, 494. 11, 33

[124] Masset F.S., Morbidelli A., Crida A., et al.. **Disk surface density transitions as protoplanet traps**. *ApJ*, 2006. 642, 478. 87

[125] Masset F.S., D'Angelo G.D., Kley W.. **On the migration of protogiant solid cores**. *ApJ*, 2006. 652, 730. 24, 30

[126] Masset F.S., Casoli J.. **On the horseshoe drag of a low-mass planet. II. migration in adiabatic disks**. *ApJ*, 2009. 703, 857. 30

[127] Masset F.S., Casoli J.. **Saturated torque formula for planetary migration in viscous disks with thermal diffusion: recipe for protoplanet population synthesis**. *ApJ*, 2010. 723, 1393. 24

[128] Masset F.S., Benitez-Llambay P.. **Horseshoe drag in three-dumensional globally isothermal disks**. *ApJ*, 2016. 817, 19. 147

[129] Mayor, M., Queloz, D.. **A jupiter-mass companion to a solar-type star**. *Nature*, 1995. 378, 355. 3

[130] McClure M.K., bergin E.A., Cleeves L.I., et al.. **Mass measurements in protoplanetary disks from hydrogen deuteride**. *ApJ*, 2016. 831, 167. 8

[131] Migaszewski C.. **On the migration of two planets in a disc and the formation of mean motion resonances**. *MNRAS*, 2015. 453, 1632. 15

[132] Migaszewski C., Goździewski K., Panichi F.. **The origin and 9:7 MMR dynamics of the Kepler-29 system**. *MNRAS*, 2017. 465, 2366. 36

[133] Migaszewski C.. **On the migration-induced formation of the 9:7 mean motion resonance**. *MNRAS*, 2017. 469, 1131. 4, 14, 17, 38, 65, 66, 144

[134] Miranda R., Rafikov R.R.. **On the planetary interpretation of multiple gaps and rings in protoplanetary disks seen by ALMA**. *ApJL*, 2019. 878, L9. 124

[135] Monnier J.D., Millan-Gabet R.. **On the interferometric sizes of young stellar objects**. *American Astronomical Society*, 2002. 34, 1260. 7

[136] Morton T., Bryson S., Coughlin J., et al.. **False positive probabilities for all Kepler objects of interest: 1284 newly validated planets and 428 likely false positives**. *ApJ*, 2016. 822, 86. 37

[137] Murray C.D., Dermott S.F.. **Solar System Dynamics**. *Cambridge University Press, Cambridge, UK*, 1999. 42, 43, 44, 45, 58

[138] Mustill A.J., Wyatt M.C.. **A general model of resonance capture in planetary systems: first- and second-order resonances**. *MNRAS*, 2011. 413, 554. 13, 14, 37, 54, 55, 56, 65, 66, 144

[139] Nelson R.P., Papaloizou J.C.B., Masset F., et al.. **The migration and growth of protoplanets in protostellar discs**. *MNRAS*, 2000. 318, 18. 40

[140] Nelson R.P., Papaloizou J.C.B.. **Possible commensurabilities among pairs of extrasolar planets**. *MNRAS*, 2002. 333, 26. 14, 35, 40, 41

[141] Nelson R.P., Papaloizou J.C.B.. **The interaction of giant planets with a disc with MHD turbulence - IV. Migration rates of embedded protoplanets**. *MNRAS*, 2004. 350, 849. 15

[142] Ofir A., Dreizler S., Zechmeister M., et al.. **An independent planet search in the Kepler dataset. II. An extremely low-density super-Earth mass planet around Kepler-87**. *A&A*, 2014. 561, 103. 4

[143] Ogihara M., Morbidelli A., Guillot T.. **A reassessment of the in situ formation of close-in super-Earths**. *A&A*, 2015. 578, 36. 5

[144] Ogihara M., Kokubo E., Suzuki T.K. et al.. **Formation of close-in super-Earths in evolvuing protoplanetary disks due to disk winds**. *A&A*, 2018. 615, 63. 5

[145] Ogilvie G. I., Lubow S. H.. **Saturation of the corotation resonance in a gaseous disk**. *ApJ*, 2003. 587, 398. 31

[146] Owen J., Wu Y.. **Kepler planets: A tale of evaporation**. *ApJ*, 2013. 775, 105. 3

[147] Owen J.E., Wu Y.. **The Evaporation Valley in the Kepler Planets**. *ApJ*, 2017. 847, 29. 3

[148] Paardekooper, S.J., Papaloizou J.C.B.. **On disc protoplanet interactions in a non-barotropic disc with thermal diffusion**. *A&A*, 2008. 485, 877. 30, 31

[149] Paardekooper, S.J., Papaloizou J.C.B.. **On corotation torques, horseshoe drag and the possibility of sustained stalled or outward protoplanetary migration**. *MNRAS*, 2009. 394, 2283. 40, 47, 95

[150] Paardekooper S.J., Baruteau C., Crida A. et al.. **A torque formula for non-isothermal type I planetary migration - I. Unsaturated horseshoe drag**. *MNRAS*, 2010. 401, 1950. 29, 30, 33, 97

[151] Paardekooper S.J., Baruteau C., Kley W.. **A torque formula for non-isothermal Type I planetary migration - II. Effects of diffusion**. *MNRAS*, 2011. 410, 293. 31

[152] Paardekooper S.J., Rein H., Kley W.. **The formation of systems with closely spaced low-mass planets and the application to Kepler-36**. *MNRAS*, 2013. 434, 3018. 15, 24

[153] Paardekooper S.J.. **Dynamical corotation torques on low-mass planets**. *MNRAS*, 2014. 444, 2031. 34

[154] Panichi F., Migaszewski C., Goździewski K.. **Two super-Earths in the 3:2 MMR around KOI-1599**. *MNRAS*, 2019. 485, 4601. 4

[155] Papaloizou J.C.B., Lin D.N.C.. **Theory of Accretion Disks I: Angular Momentum Transport Processes**. *ARA&A*, 1995. 33, 505. 21

[156] Papaloizou J.C.B., Larwood J.D.. **On the orbital evolution and growth of protoplanets embedded in a gaseous disc**. *MNRAS*, 2000. 315, 823. 28

[157] Papaloizou J.C.B., Nelson R.P., Snellgrove M.D.. **The interaction of giant palnets with a disc with MHD turbulence - III. Flow morphology and conditions for gap formation in local and global simulations**. *MNRAS*, 2004. 350, 829. 104

[158] Papaloizou J.C.B., Szuszkiewicz E.. **On the migration-induced resonances in a system of two planets with masses in the Earth mass range**. *MNRAS*, 2005. 363, 153. 5, 14, 35

[159] Papaloizou J.C.B. Nelson R. P., Kley W., et al.. **Protostars and Planets V**. *University of Arizona Press, Tucson*, 2007. 655. 27, 103

[160] Papaloizou J.C.B., Terquem C.. **On the dynamics of multiple systems of hot super-Earths and Neptunes: tidal circularization, resonance and the HD 40307 system**. *MNRAS*, 2010. 405, 573. 15, 68, 86

[161] Papaloizou J.C.B.. **Tidal interactions in multi-planet systems**. *Celestial Mechanics and Dynamical Astronomy*, 2011. 111, 83. 15, 68, 86

[162] Papaloizou J.C.B.. **Planet Migration**. *ArXiv*, 2021. 2107.07269. 11

[163] Peale S.J.. **Orbital resonance in the solar system**. *ARA&A*, 1976. 14, 215. 13

[164] Pecaut M.J., Mamajek E.E.. **The star formation history and accretion-disc fraction among the K-type members of the Scorpius-Centaurus OB association**. *MNRAS*, 2016. 461, 794. 7

[165] Perraut K., Labadie L., Bouvier J., et al.. **The GRAVITY Young Stellar Object survey. VII. The inner dusty disks of T Tauri stars**. *A&A*, 2021. 655, 73. 7

[166] Petigura E.A., Howard A.W., Marcy G.W.. **Prevalence of Earth-size planets orbiting Sun-like stars**. *Proceedings of the National Academy of Science*, 2013. 110, 19273. 3

[167] Pichierri G., Morbidelli A., Crida A.. **Capture into first-order resonances and long-term stability of pairs of equal-mass planets**. *Celestial Mechanics and Dynamical Astronomy*, 2018. 130, 54. 13

[168] Pierens A., Nelson R.P.. **Constraints on resonant-trapping for two planets embedded in a protoplanetary disc**. *A&A*, 2008. 482, 333. 14

[169] Pierens A., Baruteau C., Hersant F.. **On the dynamics of resonant super-Earths in disks with turbulence driven by stochastic forcing**. *A&A*, 2011. 531, 5. 15

[170] Pierens A., Raymond S. N., Nesvorny D., et al.. **Outward migration of Jupiter ans Saturn in 3:2 or 2:1 resonance in radiative disks: implications for the Grand Tack and Nice models**. *ApJL*, 2014. 795, L11. 14

[171] Pierens A.. **Fast migration of low-mass planets in radiative discs**. *MNRAS*, 2015. 454, 2003. 34

[172] Pinte C., Dent W.R.F., Ménard F., et al.. **Dust and gas in the disk of HL Tauri: surface density, dust settling, and dust-to-gas ratio**. *ApJ*, 2016. 816, 25. 10

[173] Podlewska-Gaca E., Szuszkiewicz E.. **A super-Earth caught in a trap**. *MNRAS*, 2009. 397, 1995. 18, 71, 83, 145

[174] Podlewska-Gaca E., Papaloizou J. C. B., Szuszkiewicz E.. **Outward migration of a super-Earth in a disc with outward propagating density waves excited by a giant planet**. *MNRAS*, 2012. 421, 1736. 15, 17, 18, 68, 69, 70, 71, 79, 83, 85, 88, 145

[175] Powell D., Murray-Clay R., Schlichting H.E.. **Using ice and dust lines to constrain the surface densities of protoplanetary disks**. *ApJ*, 2017. 840, 93. 8

[176] Quillen A.C.. **Reducing the probability of capture into resonance**. *MNRAS*, 2006. 365, 1367. 37, 65, 144

[177] Quillen A.C., Bodman E. and Moore A.. **Origin scenarios for the Kepler 36 planetary system**. *MNRAS*, 2013. 435, 2256. 15

[178] Rafikov R.R.. **Planet migration and gap formation by tidally induced shocks**. *ApJ*, 2002. 572, 566. 31

[179] Ragusa E., Rosotti G., Teyssandier J., et al.. **Eccentricity evolution during planet-disc interaction**. *MNRAS*, 2018. 474, 4460. 11, 32

[180] Rajpaul V. M., Buchhave L. A., Lacedelli G., et al.. **A HARPS-N mass for the elusive Kepler-37d: a case study in disentangling stellar activity and planetary signals**. *MNRAS*, 2021. 507, 1847. 37

[181] Rein H., Papaloizou J.C.B.. **On the evolution of mean motion resonances through stochastic forcing: fast and slow libration modes and the origin of HD 128311**. *A&A*, 2009. 497, 595. 15

[182] Ribeiro R.S., Morbidelli A., Raymond S. N., et al.. **Dynamical evidence for an early giant planet instability**. *Icarus*, 2020. 339, 113605. 5

[183] Ricker G.R., Winn J.N., Vanderspek R., et al.. **Transiting exoplanet survey satellite (TESS)**. *Journal of Astronomical Telescopes, Instruments and Systems*, 2015. 1, 014003. 1

[184] Rivera E.J., Laughlin G., Butler R.P., et al.. **The Lick-Carnegie Exoplanet Survey: a Uranus-mass fourth planet for GJ 876 in an extrasolar Laplace configuration**. *ApJ*, 2010. 719, 890. 4

[185] Robert C. M. T., Crida A., Lega E., et al.. **Toward a new paradigm for Type II migration**. *A&A*, 2018. 617, 98. 11, 33

[186] Robertson P., Endl M., Cochran W. D., et al.. **The McDonald Observatory Planet Search: New long-period giant planets and two interacting Jupiters in the HD 155358 system**. *ApJ*, 2012. 749, 39. 4

[187] Rosenthal L.J., Fulton B.J., Hirsch L.A., et al.. **The California Legacy Survey. I. A catalog of 178 planets from precision radial velocity monitoring of 719 neary by stars over three decedes**. *ApJS*, 2021. 255, 8. 4

[188] Ruden S.P., Lin D.N.C.. **The global evolution of the primordial solar nebula**. *ApJ*, 1986. 308, 883. 39

[189] Saad-Olivera X., Martinez C.F., Costa de Souza A., et al.. **A super-Earth and a mini-Neptune around Kepler-59**. *MNRAS*, 2020. 491, 5238. 86

[190] Scardoni C.E., Rosotti G.P., Lodato G., et al.. **Type II migration strkes back - an old paradigm for planet migration in discs**. *MNRAS*, 2020. 492, 1318. 11

[191] Shakura N.I., Sunyaev R.A.. **Black holes in binary systems. Observational appearance**. *A&A*, 1973. 24, 337. 10, 20, 87

[192] Snellgrove M.D., Papaloizou J.C.B., Nelson R.P.. **On disc driven inward migration of resonantly coupled planets with application to the system around GJ876**. *A&A*, 2001. 374, 1092. 13, 35

[193] Steffen J.H., Fabrycky D.C., Agol E., et al.. **Transit timing observations from Kepler - VII. Confirmation of 27 planets in 13 multiplanet systems via transit timing variations and orbital stability**. *MNRAS*, 2013. 428, 1077. 4

[194] Süli A., Érdi B., And Pál A.. **A new method to determine the derivatives of the Laplace coefficients**. *Celestial Mechanics and Dynamical Astronomy*, 2004. 88, 259. 44

[195] Syer D., Clarke C.J.. **Satellites in discs: regulating the accretion luminosity**. *MNRAS*, 1995. 277, 758. 11, 32

[196] Szuszkiewicz E., Podlewska-Gaca E.. **Migration-induced architectures of planetary systems**. *Origin of Life and Evolution of Biospheres*, 2012. 42, 113. 12

[197] Tanaka H., Takeuchi T., Ward W.R.. **Three-dimensional interaction between a planet and an isothermal gaseous disk. I. corotation and Lindblad torques and planet migration**. *ApJ*, 2002. 565, 1257. 27, 28, 29, 39, 47

[198] Teague R., Guilloteau S., Semenov D., et al.. **Measuring turbulence in TW Hydrae with ALMA: methods and limitations**. *A&A*, 2016. 592, 49. 10

[199] Teague R., Henning T., Guilloteau S.. **Temperature, mass, and turbulence: a spatially resolved multiband non-LET analysis of CS in TW Hya**. *ApJ*, 2018. 864, 133. 8, 10

[200] Terquem C., Papaloizou J.C.B., Nelson R.P.. **Disks, Extrasolar Planets and Migration**. *Space Science Reviews*, 2000. 92, 323. 39

[201] Terquem C., Papaloizou J.C.B.. **Migration and the formation of systems of hot super-Earths and Neptunes**. *ApJ*, 2007. 654, 1110. 5

[202] Trapman L., Miotello A., Kama M., et al.. **Far-infrared HD emission as a measure of protoplanetary disk mass**. *A&A*, 2017. 605, 69. 8

[203] Van Eylen V., Agentoft C., Lundkvist M.S., et al.. **An asteroseismic view of the radius valley: stripped cores, not born rocky**. *MNRAS*, 2018. 479, 4786. 3

[204] Varniére P., Quillen A.C., Frank A.. **The evolution of protoplanetary disk edges**. *ApJ*, 2004. 612, 1152. 31

[205] Venturini J., Guilera O.M., Haldemann J., et al.. **The nature of the radius valley: Hints from formation and evolution models**. *A&A*, 2020. 643, 1. 3

[206] Veras D., Ford E.B.. **Identifying non-resonant Kepler planetary systems**. *MNRAS*, 2012. 420, 23. 5

[207] Vissapragada S., Jontof-Hutter D., Shporer A., et al.. **Diffuser-assisted infrared transit photometry for four dinamically interacting kepler systems**. *AJ*, 2020. 159, 108. 4, 36, 37, 86

[208] Ward W.R.. **Horseshoe orbit drag**. *Abstracts of the Lunar and Planetary Science Conference*, 1991. 22, 1463. 30

[209] Ward W.R.. **Disk-protoplanet interactions: torques from the coorbital zone**. *Annals of the New York Academy of Sciences*, 1992. 675, 314. 30

[210] Ward W.R.. **Protoplanet Migration by Nebula Tides**. *Icarus*, 1997. 126, 261. 11, 27, 28

[211] Williams J.P., Cieza L.A.. **Protplanetary disks and their evolution**. *ARA&A*, 2011. 49, 67. 7

[212] Winn J.N., Fabrycky D.C.. **The occurrence and architecture of exoplanetary systems**. *ARA&A*, 2015. 53, 409. 4

[213] Wolfgang A., Rogers L.A., Ford E.B.. **Probabilistic mass-radius relationship for sub-Neptune-sized planets**. *ApJ*, 2016. 825, 19. 68

[214] Wright J.T., Veras D., Ford E.B., et al. . **The California Planet Survey. III. A possible 2:1 resonance in the exoplanetary triple system HD 37124**. *ApJ*, 2011. 730, 93. 4

[215] Xiang-Gruess M., Papaloizou J.C.B.. **Evolutionary outcomes for pairs of planets undergoing orbital migration and circularization: second-order resonances and observed period ratios in Kepler's planetary systems**. *MNRAS*, 2015. 449, 3043. 14, 38, 40, 41, 42, 45

[216] Xie J.W.. **Asymmetric orbital distribution near mean motion resonance: application to planets observed by Kepler and radial velocities**. *ApJ*, 2014. 786, 153. 5

[217] Xu W., Lai D.. **Migration of planets into and out of mean motion resonances in protoplanetary discs: analytical theory of second-order resonances**. *MNRAS*, 2017. 468, 3223. 13, 14, 38, 56, 65, 144

[218] Xu W., Lai D., Morbidelli A.. **Migration of planets into and out of mean motion resonances in protoplanetary discs: overstability of capture and nonlinear eccentricity damping**. *MNRAS*, 2018. 481, 1538. 13

[219] Yoder C.F. . **Diagrammatic theory of transition of pendulum-like systems**. *Celestial Mechanics*, 1979. 19, 3. 13

[220] Yoder C.F., Peale S.J.. **The tides of Io**. *Icarus*, 1981. 47, 1. 13

[221] Yorke H.W., Bodenheimer P., Laughlin G.. **The formation of protostellar disks. I. 1 M sub sun**. *ApJ*, 1993. 411, 274. 7

[222] Zhu W., Nelson R.P., Hartmann L., et al.. **Transitional and pre-transitional disks: gap opening by multiple planets?**. *ApJ*, 2011. 729, 47. 6

[223] Zhu Z., Stone J.M., Rafikov R.R., et al.. **Particle concentration at planet-induced gap edges and vortices. I. inviscid three-dimensional hydro disks**. *ApJ*, 2014. 785, 122. 6

[224] Zhu W., Wu Y.. **The super Earth - Cold Jupiter relations**. *AJ*, 2018. 156, 92. 3

[225] Ziegler U.. **NIRVANA: An adaptive mesh refinement code for gas dynamics and MHD**. *Computer Physics Communications*, 1998. 109, 111. 24, 40